

AN ABSTRACT OF THE DISSERTATION OF

Wassanai Wattanutchariya for the degree of Doctor of Philosophy in Industrial Engineering presented on April 29, 2002.

Title: Application of Buckling Behavior to Evaluate and Control Shape Variation in High-Temperature Microlamination.

Redacted for Privacy

Abstract approved: _____

Brian K. Paul

The miniaturization of energy, chemical and biological systems for distributed and portable applications, known as process intensification, is realized by the enhancement in heat and mass transfer performance within high surface-to-volume ratio microchannels. Fabrication of devices for process intensification is achieved in part by microlamination techniques. These techniques consist of patterning, aligning, and bonding thin layers of material into monolithic devices. Even though the fabrication techniques used in microlamination are generally accurate and consistent, small amounts of dimensional variation in microlaminated structures can strongly affect the device performance. One significant finding of this dissertation is that fin warpage, which is commonly induced during bonding, generally has more adverse device performance effects than misalignment. A heat exchanger that contains fin warpage as small as 25 percent of the microchannel height (on the order of 10 μm) needs to almost double the number of flow channels to gain the same thermal effectiveness as the uniform one. Therefore, the focus of this dissertation is to investigate, understand, and learn how to control the cause and effect of buckling warpage produced within microlaminated structures. The microlamination discussed in this dissertation is performed with a thermally-controlled registration process, which facilitates metallic bonding at elevated

temperatures. Another finding of this dissertation is that the tolerance limits of the fixture used in this registration process exceed the accuracy of the machine tools used to produce the fixture. Fixture tolerance limits on the order of 10 μm are necessary to align and bond laminae with thicknesses below 100 μm . An alternative technique based on the compliance of the fixture is proposed in order to improve these limits. This technique helps compensate for the excessive registration force due to over-constrained bonding, which extends the range of fixture tolerance limit to over 100 μm well within current process capability of machine tools. Another approach to controlling fin warpage, based on the induction of higher modes of fin buckling, is also discussed. An analytical evaluation shows that the effect of fin warpage is minor as the mode of buckling reaches mode 10. A preliminary experiment confirms that the induction of fin buckling into a higher mode can be achieved by constraining the fin at specific locations along the fin during microlamination.

©Copyright by Wassanai Wattanutchariya

April 29, 2002

All Rights Reserved

Application of Buckling Behavior to Evaluate and Control Shape Variation in
High-Temperature Microlamination

by

Wassanai Wattanutchariya

A DISSERTATION

submitted to

Oregon State University

in partial fulfillment of
the requirements for the
degree of

Doctor of Philosophy

Presented April 29, 2002
Commencement June 2002

Doctor of Philosophy dissertation of Wassanai Wattanutchariya presented on April 29, 2002.

APPROVED:

Redacted for Privacy

Major Professor, representing Industrial Engineering

Redacted for Privacy

Head of the Department of Industrial and Manufacturing Engineering

Redacted for Privacy

Dean of the Graduate School

I understand that my dissertation will become part of the permanent collection of Oregon State University libraries. My signature below authorizes release of my dissertation to any reader upon request.

Redacted for Privacy

Wassanai Wattanutchariya, Author

ACKNOWLEDGMENTS

The author acknowledges with gratitude the guidance and patience of my advisory committee. Special thanks are due to Dr. Brian K. Paul for his objective supervision and helpful discussions throughout the completion of this work. Recognition is also due to Dr. Rick Wilson, Dr. Bill Warnes, and Dr. Kevin Drost for many helpful comments and beneficial discussions. The author would like also to thank Dr. David Gobeli, not only for his role in graduate council representative but also some comments and suggestions. In addition, I would like to acknowledge Dr. John Shea (IME), Dr. Tom Plant (ECE), Dr. Richard Peterson (ME) and Dr. Deborah Pence (ME) for their suggestions on my works. My appreciation is also due to Mr. Steve Etringer for his help in device fabrication. In addition, the author would like to thank the Royal Thai Embassy and Chiangmai University, as well as Industrial and Manufacturing department, Oregon State University for support and financial assistance. Last but not least the author would like to express sincere appreciation to my friends, Duanghathai Katwibun, Wichai Chattinnawat, Kannapon Lopetcharat, among others, who have contributed to the conception of this work.

TABLE OF CONTENTS

	<u>Page</u>
CHAPTER 1 Introduction.....	1
1.1 MEMS VS. MECS.....	2
1.2 The Need for Meso-Scale.....	3
1.3 Microfluidic Systems.....	5
1.4 Meso-Scale Research.....	6
1.5 Fabrication of MECS Devices.....	7
1.6 Shape Variation in Microlamination.....	8
1.6.1 Shape Variation in Laminae Patterning.....	9
1.6.2 Shape Variation in Laminae Registration.....	13
1.6.3 Shape Variation in Laminae Bonding.....	14
1.7 Problem Statements and Dissertation Organization.....	16
1.7.1 Effect of Fin Warpage and Channel Misregistration on the Performance of Metallic Microlaminated Heat Exchangers.....	17
1.7.2 Use of Buckling Theory to Predict Bonding Fixture Tolerances for High-Temperature Microlamination.....	17
1.7.3 Use of Compliance in High-Volume Metal Microlamination to Reduce Shape Variation due to Fin Buckling.....	18
1.7.4 Use of Buckling Theory to Control Fin Warpage in Metallic Microlaminated Heat Exchangers.....	18
1.8 References.....	20
 CHAPTER 2 Effect of Fin Warpage and Channel Misregistration on the Performance of Metallic Microlaminated Heat Exchangers.....	 25
2.1 Abstract.....	25

TABLE OF CONTENTS (Continued)

	<u>Page</u>
2.2 Introduction	26
2.3 Theoretical Models.....	30
2.3.1 Fin Warpage Analysis	31
2.3.2 Misregistration Analysis	37
2.4 Case Study	38
2.4.1 Base Case Heat Exchanger Characteristics	38
2.4.2 Evaluation of Heat Transfer Performance Penalty and Pressure Drop Reduction	39
2.4.3 Transformation of Heat Transfer Performance Penalty into a Compensated Area	42
2.4.4 Determination of Channel Misalignment Effects on Heat Exchanger Performance	44
2.4.5 Comparison between Fin Warpage and Channel Misalignment	44
2.4.6 Effect of the Base Case NTU on the Device to the Penalty of Thermal Performance Due to Fin Warpage	45
2.4.7 The Relation between Aspect Ratio of a Flow Channel and the Penalty of Performance due to Channel Nonuniformity	46
2.5 Summary	47
2.6 References	49
CHAPTER 3 Use of Buckling Theory to Predict Bonding Fixture Tolerances for High-Temperature Microlamination	51
3.1 Abstract	51
3.2 Introduction	51
3.3 Theoretical Models	58
3.3.1 Fin Buckling Analysis.....	59
3.3.2 The Relationship between Fin Stiffness and the Critical Point of Buckling	61

TABLE OF CONTENTS (Continued)

	<u>Page</u>
3.4 Experimental	65
3.5 Results and Discussion	70
3.5.1 The Relation between Fixture Allowance and Fin Buckling	70
3.5.2 The Relation between Fixture Allowance and Channel Misalignment. 72	72
3.5.3 The Relationship of Both Fin Buckling and Channel Misalignment to Device Performance	77
3.6 Conclusions	79
3.7 References	80
CHAPTER 4 Use of Compliance in High-Volume Metal Microlamination to Reduce Shape Variation Due to Fin Buckling	83
4.1 Abstract	83
4.2 Introduction	84
4.3 Theoretical Models	88
4.3.1 Fin Warpage Analysis	89
4.3.2 The Compliance of the TEER Fixture	92
4.4 Experimental	94
4.5 Results and Discussion	98
4.5.1 The Relationship between Tolerance Limit and Fin Buckling	98
4.5.2 The Relationship between Fin Buckling and Device Performance	102
4.6 Conclusions	106
4.7 References	107

TABLE OF CONTENTS (Continued)

	<u>Page</u>
CHAPTER 5 Use of Buckling Theory to Control Fin Warpage in Metallic Microlaminated Heat Exchangers	109
5.1 Abstract	109
5.2 Introduction	110
5.3 Theoretical Models	116
5.4 Preliminary Experiment	118
5.4.1 Mode 1 and Mode 2 Buckling	118
5.4.2 Mode 10 Buckling	121
5.5 Results and Discussion	121
5.5.1 Analytical Results for Various Modes of Buckling	121
5.5.2 Experimental Results	123
5.6 Conclusions	127
5.7 References	128
 CHAPTER 6 Conclusions and Recommendations	 130
6.1 Summary	130
6.2 Recommendations for Future Work	132
 Bibliography	 135
 Appendices.....	 143

LIST OF FIGURES

<u>Figure</u>	<u>Page</u>
1-1	The microlamination scheme for fabricating (a) dual microchannel array, (b) two-fluid counter-flow microchannel array..... 7
1-2	Top view of the kerf width with representation of ejecta at the edge..... 10
1-3	Schematic of the pulsed laser-cutting process..... 11
1-4	Cross-sectional profile of channel patterned by EMM..... 11
1-5	Friction coefficient of flow channels as a function of aspect ratios..... 13
1-6	Misregistration of laminates..... 14
1-7	SEM micrograph of a microchannel heat exchanger with fin buckling shape variation..... 15
1-8	The plan view of the two-fluid counter-flow microchannel array comprised of microchannel and fin laminae..... 16
1-9	Cross-section of the device at cross-section AA in Figure 1-8..... 16
2-1	An exploded view illustrating a microlamination procedure in microchannel fabrication..... 26
2-2	SEM photo micrographs of Ni-Al Microchannel heat exchanger with nonuniform flow channels (a) before and (b) after fin buckling..... 27
2-3	Geometry of (a) uniform flow channels, (b) nonuniform flow channels due to fin warpage, (c) nonuniform flow channels due to channel misalignment..... 31
2-4	Geometry of (a) uniform flow channels, (b) nonuniform flow channels due to fin warpage..... 32
2-5	Fin buckling in higher modes: (a) Mode 2 (b) Mode 3 and (c) Mode 4..... 33

LIST OF FIGURES (Continued)

<u>Figure</u>	<u>Page</u>
2-6	Geometry of (a) uniform flow channels, (b) nonuniform fin buckling of Mode 1, and (c) nonuniform fin buckling of Mode 2.....34
2-7	Flow distribution of heat exchanger as a function of channel deviations....39
2-8	The relationship of channel deviation due to fin warpage and the heat exchanger performance in terms of average effectiveness and NTU..... 40
2-9	The impact of channel deviation on percent loss in NTU, percent gain in ΔP41
2-10	The relation of channel deviation and the number of channel needed and percent increase in area to compensate the loss in heat transfer performance..... 43
2-11	Relationship between the system NTU and the percent loss in NTU for Mode 1 and Mode 2 fin buckling 46
3-1	Microlamination scheme used to fabricate a dual microchannel array (arrows show direction of flow).....52
3-2	A SEM micrograph of an intermetallic microchannel device with shape variation..... 53
3-3	Cross-section of a micro-ball valve..... 54
3-4	(a) Micro gas turbine generator cross-section, (b) silicon turbine wheel.... 54
3-5	Schematic of fin buckling due to excess registration force..... 56
3-6	SEM micrographs of a microchannel heat exchanger with nonuniform flow channels (a) before and (b) after fin buckling..... 56
3-7	Graph of misalignment versus allowance between fixture and laminae at bonding temperature..... 57

LIST OF FIGURES (Continued)

<u>Figure</u>	<u>Page</u>
3-8	Geometry of (a) uniform flow channels, (b) nonuniform fin buckling.....58
3-9	Column buckling behavior for fixed-ended boundary condition.....59
3-10	Relationship between fin stiffness or thickness and the critical load..... 63
3-11	Relationship between fin stiffness or thickness and the allowable fin-fixture interference at the critical point of buckling.....64
3-12	Geometry of the test specimen for the experiment..... 65
3-13	Loading of the test specimen laminae onto the TEER fixture..... 66
3-14	Measuring misalignment at a window with a line marker..... 68
3-15	Magnitude of fin buckling versus the interference between fixture and laminae at bonding temperature with 95% confidence interval of standard deviation 71
3-16	Deflection profiles of laminate (a) prior to bonding (b) after bonding measured by Dektak3 surface profiler..... 72
3-17	Misalignment versus allowance between fixture and laminae at bonding temperature with 95% confidence interval of standard deviation..... 73
3-18	50X Optical Microscope images of (a) good alignment, (b) misaligned microlaminated structure..... 74
3-19	Measurement locations for misalignment analysis..... 74
3-20	Test specimen with adhesive tape on both sides.....76
3-21	Effect of fin buckling on a nominal heat exchanger performance in terms of (a) percent loss in NTU, (b) thermal effectiveness at different amounts of allowance between laminae and fixture at elevated temperature..... 78

LIST OF FIGURES (Continued)

<u>Figure</u>	<u>Page</u>
4-1	Microlamination scheme used to fabricate a dual microchannel array (arrows represent direction of flow)..... 85
4-2	Schematic of fin buckling due to excessive registration force..... 86
4-3	Microchannel heat exchanger with nonuniform flow channels due to fin buckling..... 86
4-4	A schematic of TEER fixture (a) original concept, (b) with the implementation of the compliance of fixture.....88
4-5	Geometry of (a) uniform flow channels, (b) nonuniform fin buckling.....89
4-6	Column buckling behavior for fixed-ended boundary condition..... 90
4-7	Geometry of the test specimen in this study..... 95
4-8	Loading of the test specimen laminae onto the TEER fixture..... 96
4-9	Magnitude of fin buckling versus interference between fixture and laminae at bonding temperature with 95% confidence interval of standard deviation 99
4-10	Deflection profiles of laminate (a) prior to bonding, (b) after bonding measured by Dektak3 surface profiler..... 101
4-11	Effect of fin buckling on a nominal heat exchanger performance in terms of (a) percent loss in NTU, (b) thermal effectiveness at different amounts of allowance between laminae and fixture at elevated temperature..... 103
4-12	Relationship between the pin deflection and tolerance limit for misalignment.....105
5-1	A schematic of microlamination procedure for two-fluid counter-flow microchannel array.....111

LIST OF FIGURES (Continued)

<u>Figure</u>		<u>Page</u>
5-2	Schematic of fin buckling due to excess registration force.....	112
5-3	SEM micrographs of a microchannel heat exchanger with nonuniform flow channels (a) before and (b) after fin buckling.....	113
5-4	First and second buckling modes (Shames, 1989).....	114
5-5	Formation of mode 3 buckling (Shames, 1989).....	115
5-6	Mode 2 buckling formation by external restraint (Hexiang, 1999).....	115
5-7	Geometry of fin warpage induced by buckling from mode 1 to mode 4...	116
5-8	Geometry of test specimen for rudimentary experiment.....	119
5-9	Loading of the test specimen laminae onto the TEER fixture.....	120
5-10	Magnitude of buckling of a fin layer at different amounts of clearance between the laminae and fixture.....	123
5-11	Photographs of laminate from (a) mode 1 and (b) mode 2 buckling.....	124
5-12	Deflection profiles of laminate from (a) mode 1 buckling, (b) mode 2 buckling.....	124
5-13	Photographs of laminate from mode 10 buckling	126
5-14	Deflection profiles of mode 10 buckling	126

LIST OF TABLES

<u>Table</u>	<u>Page</u>
1-1 Comparison of MEMS and MECS.....	3
2-1 Summary table of heat transfer performance and pressure drop at different buckling modes.....	42
2-2 The relation of aspect ratio and percent loss in NTU.....	46
3-1 The average misalignment measurements at four locations.....	75
3-2 Misalignment data from additional experiments.....	76
4-1 The average initial deflection of fin lamina of a variety of shim thickness...	100

LIST OF APPENDICES

<u>Appendix</u>	<u>Page</u>
A Aspect Ratio Limits in Microlamination Due to Machining Methods.....	144
B Derivation of Equations for LONDON MODEL and Implementation to Fin Warpage Nonuniformity.....	158
C Evaluation of Overall Number of Transfer Units and Transfer Areas.....	161
D Evaluation of the Heat Transfer Performance and Pressure Drop Relationship Based on Channel Deviation.....	163
E Evaluation of Channel Deviation Due to Fin Buckling.....	164
F Simpson Approximation for Calculation of Arc Length Equation.....	174
G Conversion of NTU into a Compensated Area or Number of Channels...	175
H Measuring Equipment, Test Specimen, and Fixture Configurations.....	176
I Experimental Procedure Details.....	181
J Nominal Evaluation for Original and Modified TEER.....	184
K Experimental Results of Fin Buckling and Channel Misalignment for Chapter 3.....	188
L Experimental Results of Fin Buckling for Chapter 4.....	193
M Statistical Evaluations.....	199
N Effect of Fixture Allowance on the Magnitude of Buckling and Misalignment and Device Performance.....	204
O Effect of Fin Stiffness or Thickness on Critical Point of Buckling.....	206
P Evaluation of Time Dependent (Creep) Deformation in Diffusion Bonding.....	207

NOMENCLATURE

- a = displacement used to evaluate channel deviation in mode 1 buckling (mm)
- A = cross-sectional of channel flow area (mm^2)
- Aa = cross-sectional of channel flow area only under buckled fin (mm^2)
- Ah = overall heat transfer area (mm^2)
- An = channel flow area for uniform channel (mm^2)
- A_f = cross-sectional area of fin (mm^2)
- A_{mp} = amplitude of lateral deflection due to buckling (mm)
- c_p = fluid specific heat at constant pressure (J/kg K)
- Cf = friction factor coefficient
- cn = uniform channel height or gap between fin (mm)
- d = displacement used to evaluate channel deviation in mode 2 buckling (mm)
- D = diameter of pin (mm)
- D_{max} = maximum deflection of the fin buckling (mm)
- E = modulus of elasticity (GPa)
- F = registration force (kN)
- f = fanning friction factor
- g_c = gravitational constant (1 kg m/N)
- h = convective heat transfer coefficient ($\text{W}/\text{m}^2 \text{K}$)
- H = height of laminae stack (mm)
- I = moment of inertia (mm^4)
- Inf = amount of interference at the bonding temperature (mm)
- k = conductive heat transfer coefficient ($\text{W}/\text{m K}$)
- K = stiffness (kg/s^2)
- L = characteristic length (mm)
- L_{ch} = channel flow length (mm)
- L_d = device width (mm)

- L_f = width of the fin, or channel width (mm)
 L_s = width of the fixture slot (mm)
 L_c = contact width between 2 misaligned channels (mm)
 n = number of flow passage or mode number
 NTU = number of transfer units
 Nu = Nusselt number
 P = wetted perimeter (mm)
 P_c = buckling critical load (kN)
 Pr = Prandtl number
 P_t = load due to thermal expansion (kN)
 q = heat transfer rate (W)
 rh = hydraulic radius (mm)
 Re = Reynolds number
 St = Stanton number
 T_{ci} = inlet temperature of cold-side fluid ($^{\circ}\text{C}$, K)
 T_{co} = outlet temperature of cold-side fluid ($^{\circ}\text{C}$, K)
 T_{diff} = temperature at diffusion point ($^{\circ}\text{C}$)
 T_{hi} = inlet temperature of hot-side fluid ($^{\circ}\text{C}$, K)
 T_{ho} = outlet temperature of hot-side fluid ($^{\circ}\text{C}$, K)
 t = fin thickness (mm)
 U = overall heat transfer coefficient ($\text{W}/\text{m}^2 \text{K}$)
 V = fluid velocity (m/s)
 W = fluid mass flow rate (kg/s)
 W_p = pumping power (W)
 x = misalignment (mm)
 X = displacement (mm)
 y = deflection displacement (mm)
 α = aspect ratio of channel cross-section
 α_g = linear coefficient of thermal expansion of graphite (K^{-1})

- α_{ss} = linear coefficient of thermal expansion of stainless steel (K^{-1})
 ρ = fluid density (kg/m^3)
 ε = heat transfer effectiveness
 δ = amount of pin deflection (mm)
 δ_c = channel deviation
 σ_c = buckling stress (MPa)
 σ_p = stress at proportional (elastic) limit (MPa)
 σ_y = yield stress (MPa)
 μ = viscosity ($kg/s\ m$) or a coefficient used in the evaluation of higher modes buckling
 ν = kinematic viscosity (m^2/s)
 ω = a ratio of flow distribution
 ΔP = pressure drop (kPa)
 ΔT = temperature difference (K)
 ΔT_{eff} = the effective temperature difference (K)
 ΔT_m = average mean temperature difference (K)
 Δx = number of subsection to be integrated by Simpson approximation

Subscripts and Superscripts

- $1, 2, n$ = subscripts relating to the channel number 1, 2, or a uniform channel (n)
 eff = a subscript on NTU denotes an effective NTU for the combination (1)-(2) channel system
 i = a subscript referring to either channel 1 or 2
 o = a subscript on NTU denotes an original status
 $'$ = a superscript referring to a status of the parameter at elevated temperature or a superscript for Ah denotes the contact area of fin after misalignment
 $*$ = a superscript referring the optimal value

DEDICATION

To the memory of my grandfather (1916-2002)

Dedicated to my grandmother, my parents, and my aunt, whose support and encouragement were invaluable

APPLICATION OF BUCKLING BEHAVIOR TO EVALUATE AND CONTROL SHAPE VARIATION IN HIGH-TEMPERATURE MICROLAMINATION

CHAPTER 1

INTRODUCTION

Microtechnology-based Energy and Chemical Systems (MECS) are bulk fluidic devices, which rely on embedded micro-scale features for their function (Paul, et al., 1999). These devices are used mainly to process bulk fluids in large quantities such as gasoline or river water. Quite often these fluids are not pure samples having both contamination and particulate matter which can make processing difficult. The overall size of MECS devices is meso-scopic ranging between microscale systems, such as Microelectromechanical Systems (MEMS), and macroscale systems such as automobile engines and vacuum pumps. These mesoscopic systems are expected to provide a number of important functions where a premium is placed on either mobility, compactness, or point application. The benefits of decentralized and portable energy and chemical systems are realized by the enhancement in heat and mass transfer performance within high surface-to-volume ratio microchannels. Other benefits of microchannels include rapid temperature changes, excellent temperature control, and the opportunity of operating at elevated pressures (Ameel, et al., 1997; Ameel, et al., 2000; Peterson, 2001). The implementation of MECS in heat transfer and chemical applications includes microelectronic cooling systems (Kawano, et al., 1998), chemical reactors (Martin, et al., 1999; Martin, et al., 1999; Matson, et al., 1999), fuel processing (Tonkovich, et al., 1998; Daymo, et al., 2000), and heat pumps (Drost, et al., 1997; Drost, et al., 2000) among others.

1.1 MEMS VS. MECS

Almost three decades ago, mechanical miniaturization was introduced with the seminal work of Angeli at Stanford (reference). Since then, the term microelectromechanical systems (MEMS) has been used to classify a suite of micro-scale sensors and actuators which take advantage of the electrical and mechanical integration possible at small scales with the use of bulk silicon micromachining, surface micromachining and microwelding technologies. MEMS refer to highly miniaturized devices or any array of devices that combines electrical and mechanical components within its microscale architecture, with nominal feature sizes between 1 and 100 micrometers. Fabrication of the mechanical portions of MEMS devices is compatible with integrated circuit (IC) fabrication techniques. Applications of MEMS in industry include various sensors and actuators (Pottenger, et al., 1997; Qin, et al., 1998; van den Berg, et al., 1998; French, 1999; Quan, 1999; Weigl, et al., 1999). With respect to MEMS applications, silicon, glass, and polymers are the common materials used for fabricating MEMS devices (Spearing, 2000).

While feature sizes in MEMS devices are microscale, MECS devices are classified as mesoscale devices indicating that critical feature sizes range from 25 to 200 μm . MECS devices are typically multi-scale fluidic devices requiring some type of microlaminated method for production involving the patterning and bonding of shim or sheet stock (Paul, et al., 1999). For MECS applications, metals and polymers are typically the preferred materials due to their thermal and chemical properties as well as their ability to form sheet stock for microlamination. Table 1-1 summarizes the technology of MEMS and MECS in terms of scale, benefits, fabrication, and type of application.

Table 1-1. Comparison of MEMS and MECS

	MEMS	MECS
Scale	Microscopic: feature size in the 1-100 micron range	Mesosopic: feature size on the order of several hundred microns
Preferred Material	Silicon and polymer	Metal and polymer
Fabrication	Silicon-based micromachining	Microlamination
Type of Application	Miniature Sensors Microfluidic systems Micromechanical devices	Decentralized and portable energy, chemical and biological systems - portable power generators - portable HVAC - microreactors and fuel processors - dechlorinators or solvent extractors - tissue-based biosensors
Benefits	Low-cost batch fabrication Integration of optical or electronics components	Range of materials - low thermal conductivity - high thermal conductivity - high temperature properties - corrosion resistance Bulk processing fluids

1.2 The Need for Meso-Scale

The main reasons that MECS devices are in the mesoscopic range can be categorized into four areas of requirements: 1) design; 2) material; 3) fabrication; and 4) functionality (Drost, 2001). MECS devices normally consist of a sequence of unit operations designed either for heat transfer or chemical processing. In order to get bulk fluid flows into the microchannels, a series of headers or plenums are

needed with each successive decrease in size. Another way of looking at it is that the headers connect the microchannels to the outside world. Since the major value-added function of MECS devices is carried out in microchannels, generally it is desirable to reduce the volume of the header with respect to the volume of the microchannel. As the width of the microchannels get smaller and smaller, the length of the channels also decreases. Given that the header volume stays the same size, at some point the overall header volume begins to dominate the overall device volume leading to awkward device configurations.

Another reason for working at the mesoscale is related to material requirements. Most MECS devices are large compared with MEMS devices. Because of the bulkiness of MECS devices, material costs, and fracture resistance are important. Therefore, it is desirable to stay away from expensive monocrystalline materials. Furthermore, many MECS devices require thermal or chemical properties not available in silicon architectures. Therefore, many MECS designers want to make use of engineering materials. Mesoscale dimensions are more convenient for processing engineering materials, thereby making MECS devices more economical.

From a fabrication perspective, as the size of devices shrink, tolerances have more effect on device performance. In other words, a 10 μm error will have more impact on fluid dynamics and heat transfer in a 50 μm -high channel than in a 500 μm -high channel. The tolerances of many conventional manufacturing processes have been found suitable at the mesoscale making the high volume production of bulky MECS devices more feasible. For example, it has been found that reasonable precision of microchannel heights can be achieved at mesoscale dimensions through the lamination of sheet stock. The advantage of this approach is that the precision tolerances are controlled by an economical, high-volume process such as rolling. In this case, channel height (the smallest feature) is dictated by the dimensions of the sheet stock which can normally be sourced down to 25 μm thick. Further, some results have shown that warpage (or some other

variation phenomena) produced during lamination of copper foils limits microchannel dimensions to no smaller than 80 μm (Krause, et al., 1994).

The final reason for working at mesoscale dimensions pertains to functionality. A key aspect of all MECS devices is the bulk processing of fluids. Particulates within bulk processed fluids present opportunities for channel blockage and clogging. For example, consider the separation of hydrogen from gasoline for fuel cell applications. Gasoline contains random particles that make bulk processing difficult in microchannels with heights below about 100 μm .

1.3 Microfluidic Systems

A rapidly growing application of microtechnology is microfluidic systems. Some applications in which microfluidic devices are needed include chemical analysis, chromatography, electronics chip cooling, flow sensors, micro separator, micro heater, micro heat exchanger, micro reactor, etc. Most of these devices include such components as fluidic microchannels, fluid mixers, micropumps, microvalves, and reaction chambers. The dimensions of the fluidic paths in these components are in the range between five and a few hundred micrometers. Therefore, microfluidic systems can be implemented as either MEMS or MECS, depending on the scale of the applications in which they are implemented and the material used for implementation. Microfluidic devices for MEMS mostly deal with the processing of small purified samples of fluid such as those in the laboratory. On the other hand, MECS devices are designed to process bulk fluids thereby capable of replacing large centralized fluidic processors with portable and decentralized systems. MECS provide the unique advantage associated with the decentralization and portability of energy, chemical and biological systems such as portable power generators, portable HVAC, microreactors and fuel processors, dechlorinators or solvent extractors, tissue-based biosensors, etc.

1.4 Meso-Scale Research

Examples of organization currently involved in MECS devices development and their fields of investigation are:

Pacific Northwest National Laboratory (PNNL)

- micro reactors in chemical and biological processing (Matson, et al., 1997; Martin, et al., 1999; Martin, et al., 1999; Matson, et al., 1999; Martin, et al., 2000);
- microchannel fuel processors (Tonkovich, et al., 1998; Daymo, et al., 2000);
- miniature heat pumps (Drost, et al., 1997; Drost, et al., 1999; Drost, et al., 1999; Drost, et al., 2000);

Oregon State University

- miniature dechlorinators and chemical reactors; (Jovanovic, 2001)
- mesoscale cryocooler, micro combustor, micro energy, heat transfer and fluid flow systems (Peterson, 2001; Peterson, et al., 2001);
- environmental testing and high-throughput screening devices; (Jovanovic, et al., 2001)
- microchannels and microvalves (Paul, et al., 2000; Paul, et al., 2000; Paul, et al., 2000; Wangwatcharakul, et al., 2001);

Massachusetts Institute of Technology (MIT)

- micro gas turbines (Ashley, 1997; McDonald, 2000);

Stanford University

- rapid prototyping of mesoscopic devices (Stampfl, et al., 2000).

1.5 Fabrication of MECS Devices

Unlike MEMS fabrication, manufacturing of MECS devices is not based on IC processing. One method for producing MECS devices is called microlamination. This fabrication technique consists of stacking and joining multiple patterned layers of material, called laminae, into three-dimensional devices. Microlamination involves three steps: 1) laminae patterning, 2) laminae registration, and 3) laminae bonding. An illustration of the microlamination process is shown in Figure 1-1. Figure 1-1 (a) is an exploded view of a dual microchannel array, which could be used as a skeleton for a catalytic microreactor, while Figure 1-1 (b) presents an exploded view of a two-fluid counter-flow microchannel heat exchanger.

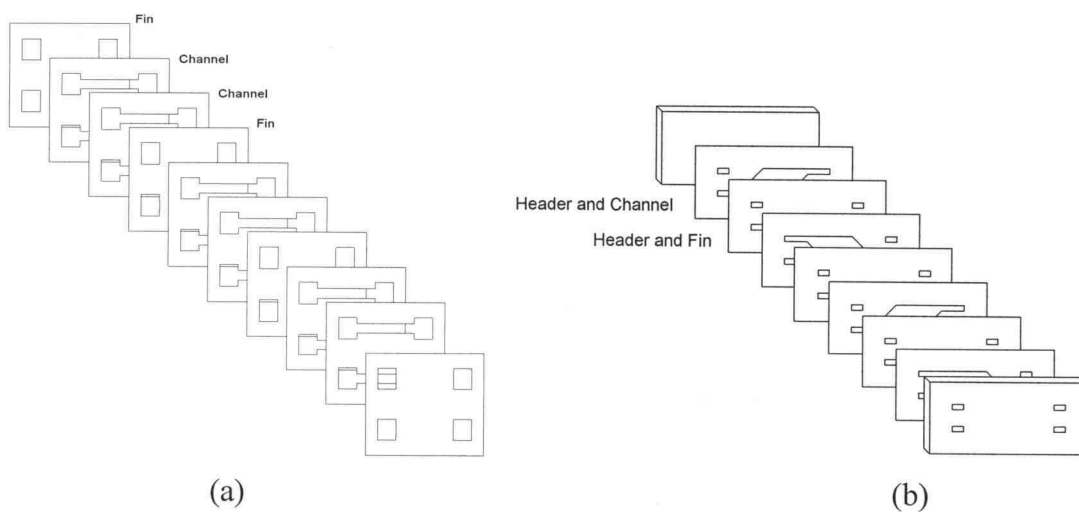


Figure 1-1. The microlamination scheme for fabricating (a) dual microchannel array, (b) two-fluid counter-flow microchannel array

In laminae patterning, sheet stock is converted into laminae by one of several methods including laser machining, chemical etching, wire EDM, and blanking. The second step involves laminae registration, where the patterned laminae are aligned and stacked in a clamping or bonding fixture prior to the bonding step. Techniques used for laminae registration can include pin alignment, edge alignment, or self-registration. Each has its advantage depending upon the bonding method. For high-temperature diffusion bonding applications, edge alignment methods have been found to provide superior levels of alignment accuracy (Thomas, 2001). After patterned laminae are stacked together in the bonding device, the entire system is put through a bonding cycle in order to produce a monolithic device. Common bonding techniques used in laminae bonding include diffusion bonding, diffusion brazing, diffusion soldering, ultrasonic welding, adhesive bonding and solvent welding, depending on the number of laminae and the lamina material. For bonding metallic laminae, diffusion bonding, diffusion brazing, and diffusion soldering are generally utilized. Microlamination has been used to construct MECS devices with a wide array of materials including copper, stainless steel, intermetallics and various polymers with features as small as tens of micrometers (Krause, et al., 1994; Martin, et al., 1998; Brooks, et al., 1999; Christenson, et al., 1999; Paul, et al., 1999; Wegeng, et al., 1999; Martin, et al., 2000; Paul, et al., 2000; Peterson, 2001; Wangwatcharakul, et al., 2001).

1.6 Shape Variation in Microlamination

A potential impediment to realizing the promise of MECS devices is the inability to control the microscale, internal geometries produced by microlamination methods. Shape variation is defined as any dimensional deviation or geometric imperfection (e.g. warpage, surface roughness, misregistration, etc.)

from the originally intended design geometry. Shape variation can have adverse effects on the performance of devices. As an example, it is well known that for laminar flows, the pressure drop, ΔP , across a fluid conduit of length, L , is directly related to the roughness of the conduit surface according to the following equation:

$$\Delta P = f \cdot \frac{L}{rh} \cdot \frac{V^2 \cdot \rho}{8 \cdot g} \quad (1)$$

where f is the fanning friction factor, rh is the hydraulic radius of the microchannel, V is the mean fluid velocity, ρ is the fluid density and g is the acceleration due to gravity. Under laminar fluid flow conditions, such as those experienced during forced convection through microchannels, the friction factor changes significantly with small changes in microchannel dimensions, resulting in greater pressure drop (Wu, et al., 1983; Pfahler, et al., 1990; Pfahler, et al., 1991; Cuta, et al., 1995).

As another example, consider the effects of warpage on a microchannel heat exchanger. Fin warpage within the microchannel array will cause some microchannels to be larger while others are smaller. As a result, this will cause some channels to have more fluid flow than others. In heat exchanger applications, this flow maldistribution across the microchannel array will cause some areas of the array to have greater heat transfer than others resulting in “hot spots” and reduced heat exchanger effectiveness. Below are presented the sources of known shape variation in microlamination.

1.6.1 Shape Variation in Laminae Patterning

Tolerances in the patterning process are generally not as significant as those in the bonding process (Kanlayasiri, et al., 2001). This is because feature size is generally larger in the patterned features than in the bonded features. Quite often, the patterned features are well above the millimeter-scale range while bonded features (e.g. the height of microchannel) are on the order of 100 μm . As

mentioned earlier, a number of micromanufacturing techniques exist for laminae patterning. For prototyping applications, one of the most common techniques is laser micromachining (LMM). It is generally accepted that lasers can remove material by one of two mechanisms: 1) thermal evaporation/sublimation; and 2) chemical ablation. In ablation, the chemical bonds between atoms are broken by the excess amount of laser energy absorbed by the valence electrons in the material. The advantage of chemical ablation is that since it is not a thermal process, it does not result in a heat-affected zone. However, most metals involve at least some level of thermal evaporation. As a result, the laser micromachining process generates ejected byproducts, such as slag, which deposit on the surface of the material which is being cut from ridges of recast material along the edges of the cut. These ejecta ridges act as burrs which can cause problems during bonding (Figure 1-2). Also, the molten material along the edge of the cuts can cause the sidewalls of the cut to be rough. Once bonded into a microlaminated device, these rough sidewalls establish endwalls or sidewalls of internal fluid conduits.

Another drawback to laser micromachining is that most lasers powerful enough to perform material removal are pulsed. As shown in Figure 1-3, one drawback of pulse-mode operation is the roughness of cut edges. This can also produce surface roughness on internal conduit walls.

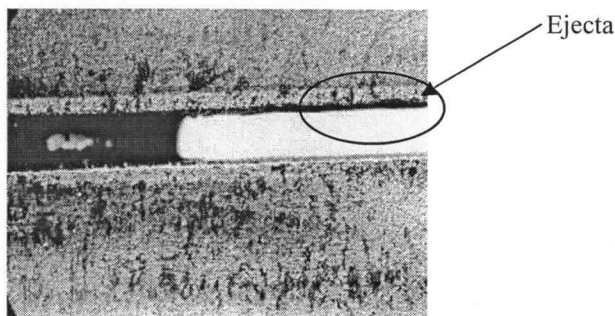


Figure 1-2. Top view of the kerf width with representation of ejecta at the edge

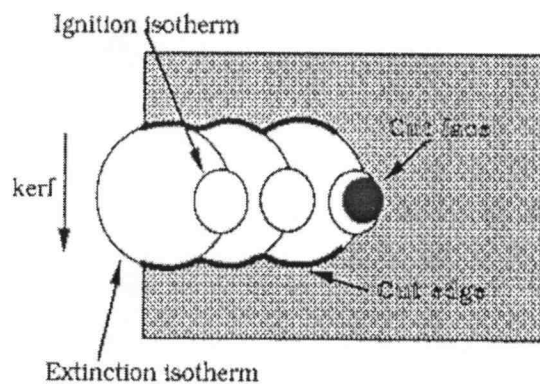


Figure 1-3. Schematic of the pulsed laser-cutting process

Another micromachining technique for lamina patterning of metals is through-mask electrochemical micromachining (EMM). EMM provides a smooth, burr-free cut, but the cross-sectional profile of the channel is not square as shown for Figure 1-4. This is largely due to the fact that some selectivity lateral etching is produced during processing.

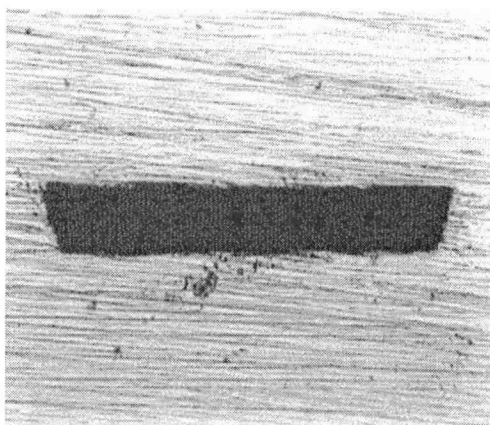


Figure 1-4. Cross-sectional profile of channel patterned by EMM

Wire Electrical Discharge Machining (EDM) is another fabrication technique that can be applied to pattern laminae. One advantage of wire EDM is its ability to process an entire stack of laminae at one time. Despite its capability for precision machining, this technique produces roughened surface with recast layers similar to the laser micromachined surfaces. In addition, for small quantities of laminae, it is a slow process (Matson, et al., 1997).

Other techniques for patterning include blanking or milling. Blanking methods permit high-volume processing, but burrs and unwanted bending can result. Milling can also produce burrs. Chips can cause problems in clogging microchannels if not completely removed. Recent ultraprecision mechanical micromachining processes have shown the ability to provide accuracy down to the submicron scale. Nonetheless, this process is expensive and generally slow (Weck, et al., 1999).

According to the previous investigation by the author and others, it was found that shape variation formed during lamina patterning by LMM and EMM have insignificant impact on the performance of typical MECS devices when the aspect ratio of the channel is over 10:1 (Kanlayasiri, et al., 2001). Figure 1-5 shows the theoretical and experimental results of the relationship between aspect ratios of the channel that is patterned by laser machining and EMM, and the corresponding friction coefficients. As shown in this figure, the friction coefficients of the flow from the microchannels that were fabricated by both techniques become constant, when their aspect ratios reach 9:1. The article of this investigation can be found in Appendix A.

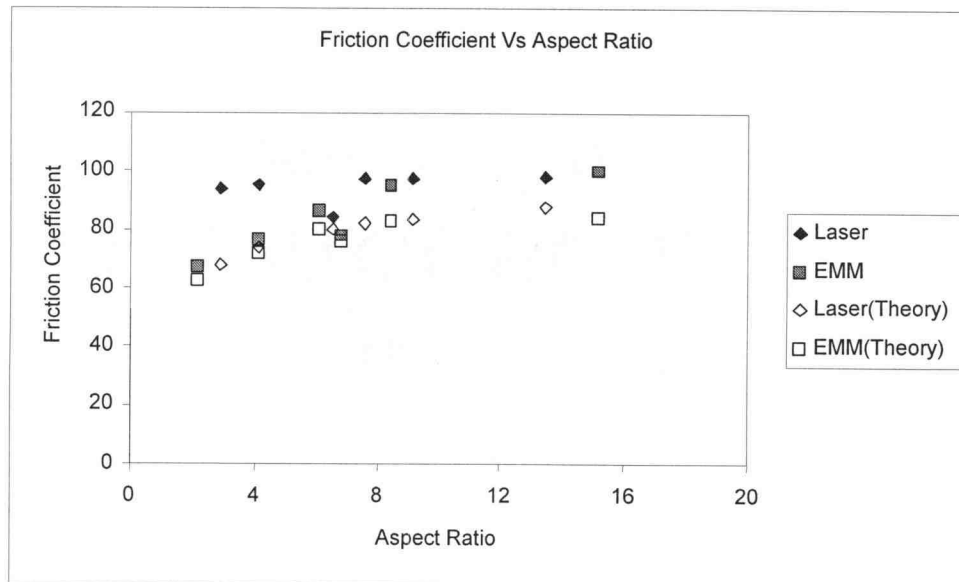


Figure 1-5. Friction coefficient of flow channels as a function of aspect ratios

1.6.2 Shape Variation in Laminae Registration

In microlamination, several registration techniques have been employed including pin, edge, and self-alignment. The technique used depends on the bonding process chosen. As mentioned earlier, MECS devices normally contain multiple laminae. Therefore, the main shape variation consideration is the layer-to-layer misalignment. For high temperature bonding processes, edge registration procedures have been found to be superior for minimizing misregistration. Figure 1-6 is a micrograph of multilayer structures with misregistration of fin and channel laminae.

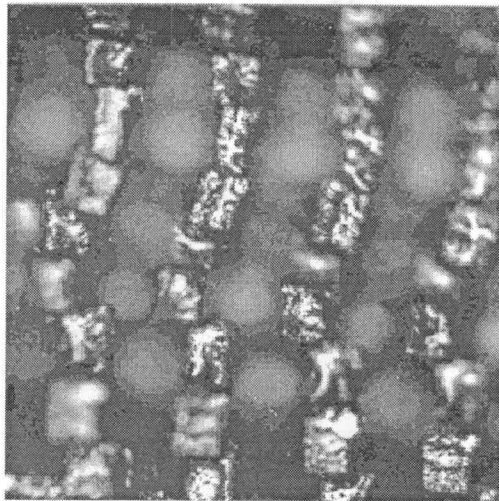


Figure 1-6. Misregistration of laminates

1.6.3 Shape Variation in Laminae Bonding

In the bonding step, laminae that are stacked and aligned together from the registration step are put in a vacuum oven to be diffusion-bonded into a monolithic structure. The bonding temperature for metallic materials is normally high (from a few hundred to over a thousand degrees Celsius). At this elevated temperature, the laminae will expand relative to their thermal expansion coefficient. In general, the bonding fixture used to hold these laminae during diffusion bonding has a lower coefficient of thermal expansion because the fixture is made from a refractory material that allows it to maintain its mechanical strength and stiffness at high temperature conditions. When the temperature is increased in the vacuum oven, the fixture can restrict the expansion of the metallic laminae. If the laminae are prevented from expanding freely, buckling will occur where the laminae are not constrained (Figure 1-7).

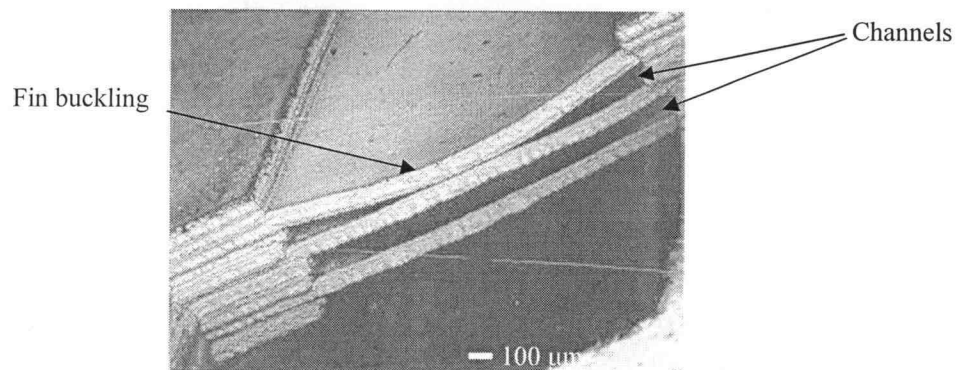


Figure 1-7. SEM micrograph of a microchannel heat exchanger with fin buckling shape variation

Another type of shape variation produced during laminae bonding is insufficient bonding. Insufficient bonding happens when the applied pressure and temperature do not meet the requirements of the bonding condition. This case includes situations where certain areas of the structure do not receive adequate pressure during diffusion bonding (Paul, et al., 2000). Figure 1-8 represents the plan view of the counter flow microchannel array from Figure 1-1 (b), and Figure 1-9 represents the cross sectional area of the same devices at cross-section AA. From Figure 1-9, area A and B of this geometry might not be bonded properly because there is no pressure directly transmitted to these areas. In addition, some researchers also found that fin bridging was resulted when copper foils had been used to produce microchannel cooler system with channel dimension below 80 μm, using microlamination technique (Krause, et al., 1994).

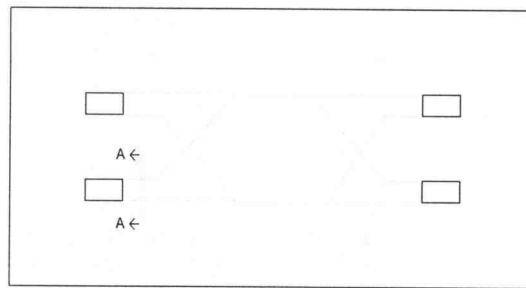


Figure 1-8. The plan view of the two-fluid counter-flow microchannel array comprised of microchannel and fin laminae

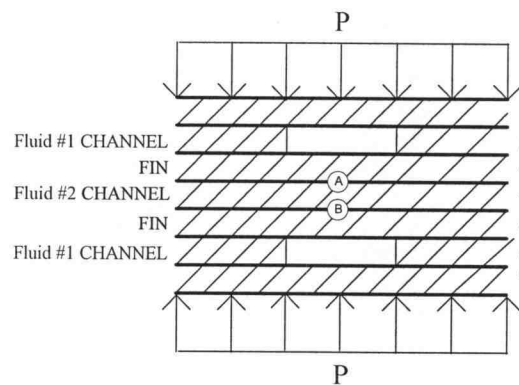


Figure 1-9. Cross-section of the device at cross-section AA in Figure 1-8

1.7 Problem Statements and Dissertation Organization

In order to overcome shape variation problems and understand their mechanisms, the effect of shape variation in microlamination registration and bonding are investigated, as well as the application of buckling theory to develop a predictive model for shape variation control. Therefore, the organization of this research is separated into four parts: 1) evaluation of the influence of misregistration and warpage on the performance of metallic devices; 2) use of

buckling theory to identify the tolerance limits of the bonding fixture for microlamination; 3) use of compliance of the bonding fixture to reduce shape variation due to fin buckling; and 4) use of preferential buckling to control shape variation due to fin warpage.

1.7.1 Effect of Fin Warpage and Channel Misregistration on the Performance of Metallic Microlaminated Heat Exchangers

In the first part of this study, the effects of misregistration and fin warpage are evaluated. The study includes theoretical analysis of heat exchanger performance based on these two modes of shape variation. The heat effectiveness and fluid flow behavior of the heat exchanger were used as the evaluation criteria of the device performance. This investigation is presented as Chapter 2 of this dissertation.

1.7.2 Use of Buckling Theory to Predict Bonding Fixture Tolerances for High-Temperature Microlamination

Buckling theory is used to investigate the behavior of the laminae during microlamination. The phenomenon of fin buckling and channel misalignment is studied and evaluated. Buckling theory is also used to verify the degree of variation and limitation of allowance between the laminae and the bonding fixture in terms of buckling interference and fin thickness. As a result, the tolerance limits of the fixture is established in order to prevent the shape variation due to fin warpage and misalignment in high-temperature microlamination. More information on buckling is presented in Chapter 3.

1.7.3 Use of Compliance in High-Volume Metal Microlamination to Reduce Shape Variation due to Fin Buckling

An alternative fixturing method based on the compliance of the fixture is introduced in Chapter 4. The technique modifies the original bonding fixture design shown in Chapter 3 to minimize the buckling behavior during high-temperature microlamination. Beam bending theory and buckling theory were implemented to evaluate the degree of variation and verify the limitation of allowance between the laminae and the bonding fixture in terms of buckling interference and fin thickness. Modification of the bonding fixture is discussed so that the predicted tolerance limits can be specified in order to achieve a buckle-free microlaminated device.

1.7.4 Use of Buckling Theory to Control Fin Warpage in Metallic Microlaminated Heat Exchangers

Based on the analysis performed in Chapter 2 and Chapter 3, research is presented for controlling fin warpage in MECS devices. The relationship between warpage geometry and the process parameters is studied in order to gain a better understanding about the formation of this nonuniformity. Chapter 5 illustrates the design methodology utilized in creating the novel microchannel heat exchanger with higher modes of buckling, which is presented for the purpose of minimizing the impact of shape variation on the heat transfer performance.

The corresponding objectives for this research can be stated as follows:

- (1) to evaluate the effect of fin warpage and channel misalignment on the performance of a stainless steel microchannel heat exchanger in terms of heat transfer penalties and pressure drop reduction;

- (2) to understand the tolerance limits of high-temperature microlamination based on registration allowance and fin buckling;
- (3) to develop a bonding fixture used in microlamination that can reduce shape variation due to fin buckling behavior; and
- (4) to establish the microlamination techniques to control fin warpage by inducing higher buckling modes in microchannel heat exchanger fins for the purpose of minimizing fin warpage in microchannel heat exchangers.

Finally, Chapter 6 will present the conclusions and future actions of this research, including a summary of the research contributions made in this dissertation.

1.8 References

- Ameel, T. A., Papautsky, I., Warrington, R. O., Wegeng, R. S., and Drost, M. K., "Miniaturization Technologies for Advanced Energy Conversion and Transfer Systems," *Journal of Propulsion and Power*, vol. 16, pp. 577-582, 2000.
- Ameel, T. A., Warrington, R. O., Wegeng, R. S., and Drost, M. K., "Miniaturization Technologies Applied to Energy Systems," *Energy Conversion and Management*, vol. 38, pp. 969-982, 1997.
- Ashley, S., "Turbines on a dime," *Mechanical engineering*, vol. 119, pp. 78-81, 1997.
- Brenchley, D. L. and Wegeng, R. S., "Status of Microchemical Systems Development in the United States of America," presented at AIChE 1998 Spring National Meeting, New Orleans, 1998.
- Brooks, K. P., Martin, P. M., Drost, M. K., and Call, C. J., "Mesoscale Combustor/Evaporator Development," presented at ASME IMECE Conference, Nashville, TN, 1999.
- Christenson, T. R. and Schmale, D. T., "A Batch Wafer Scale LIGA Assembly and Packaging Technique Via Diffusion Bonding," presented at The Twelfth IEEE international conference on Micro Electro Mechanical Systems, 1999.
- Cuta, J. M., Bennett, W. D., McDonald, C. E., and Ravigururaran, T. S., "Fabrication and Testing of Micro-Channel Heat Exchangers," presented at SPIE proceedings, 1995.
- Daymo, E. A., VanderWiel, D. P., Fitzgerald, S. P., Wang, Y., Rozmiarek, R. T., LaMont, M. J., and Tonkovich, A. L. Y., "Microchannel Fuel Processing for Man Portable Power," presented at AIChE 2000 Spring National Meeting, Atlanta, GA, 2000.
- Drost, M. K. *Personal Communication*, Nov 19, 2001.
- Drost, M. K. and Friedrich, M., "Miniature Heat Pumps for Portable and Distributed Space Conditioning Applications," presented at Proceedings of IECEC, 1997.

- Drost, M. K., Friedrich, M., Martin, C., and Martin, J., "Mesoscopic Heat-Actuated Heat Pump Development," presented at ASME IMECE Conference, Nashville, TN, 1999.
- Drost, M. K., Friedrich, M., Martin, C., Martin, J., and Cameron, R., "Recent Developments in Microtechnology-Based Chemical Heat Pumps," presented at 3rd International Conference on Microreaction Technology, Frankfurt, Germany, 1999.
- Drost, M. K., Wegeng, R. S., Martin, P. M., Brooks, K. P., Martin, J. L., and Call, C., "MicroHeater," presented at AIChE 2000 Spring National Meeting, Atlanta, GA, 2000.
- French, P. J., "Integration of MEMS devices," *Proceeding of SPIE -- the International Society for Optical Engineering*, vol. 3892, pp. 39-48, 1999.
- Jovanovic, G. "Chemical and Reactor-based Systems.", 2001 Available: www.me.orst.edu/research/mecs/projects/.
- Jovanovic, G., Chaplen, F., McFadden, P., Plant, T., Trempey, J., Paul, B. K., and Liburdy, J. "Environmental Testing and High-Throughput Screening Devices.", 2001 Available: www.me.orst.edu/research/mecs/projects/.
- Kanlayasiri, K., Wattanuchariya, W., and Paul, B. K., "ASPECT RATIO LIMITS IN MICROLAMINATION DUE TO MACHINING METHODS," *Journal of Manufacturing Science and Engineering (To be published)*, 2001.
- Kawano, K., Minakami, K., Iwasaki, H., and Ishizuka, M., "Micro Channel Heat Exchanger for Cooling Electrical Equipment," *ASME (HTD) -- Proceeding of the ASME Heat Transfer Division*, vol. 361-3, pp. 173-180, 1998.
- Krause, V., Treusch, H.-G., Loosen, P., Kimpel, T., Biesenbach, J., Kusters, A., Robert, F., Oestreicher, H., Marchiano, M., and DeOdorico, B., "Microchannel Coolers for High Power Laser Diodes in Copper Technology," *Proceeding of SPIE -- the International Society for Optical Engineering*, vol. 2148, 1994.
- Lohner, K. A., Chen, K.-S., Ayon, A. A., and Spearing, S. M., "Microfabricated Silicon Carbide Microengine Structures," *Proceeding of Material Resource Society Symposium*, vol. 546, pp. 85-90, 1999.
- Martin, P. M., Matson, D. W., and Bennett, W. D., "Microfabrication Methods For Microchannel Reactors and Separations Systems," *Chemical Engineering Communications*, vol. 173, pp. 245-254, 1999.

- Martin, P. M., Matson, D. W., Bennett, W. D., and Hammerstrom, D. J., "Fabrication of plastic microfluidic components," presented at Proceedings of SPIE, 1998.
- Martin, P. M., Matson, D. W., Bennett, W. D., Stewart, D. C., and Bonham, C. C., "Laminated Ceramic Microfluidic Components for Microreactor Applications," presented at AiChE 2000 Spring National Meeting, Atlanta, GA, 2000.
- Martin, P. M., Matson, D. W., Bennett, W. D., Stewart, D. C., and Lin, Y., "Laser Micromachined and Laminated Microfluidic Components for Miniaturized Thermal, Chemical and Biological Systems," presented at Proceeding of SPIE -- the International Society for Optical Engineering, 1999.
- Matson, D. W., Martin, P. M., and Bennett, W. D., "Laser micromachined microchannel solvent separator," presented at Proceedings of SPIE, 1997.
- Matson, D. W., Martin, P. M., Stewart, D. C., Tonkovich, A. L. Y., White, M., Zilka, J. L., and Roberts, G. L., "Fabrication of Microchannel Chemical Reactors Using a Metal Lamination Process," presented at Third International Conference on Microreaction Technology, Frankfurt, Germany, 1999.
- McDonald, C. F., "Low-cost compact primary surface recuperator concept for microturbines," *Applied Thermal Engineering*, vol. 20, pp. 471-497, 2000.
- Paul, B. K., Dewey, T., Alman, D., and Wilson, R. D., "Intermetallic Microlamination for High-Temperature Reactors," presented at 4th International Conference on Microreaction Technology, Atlanta, GA, 2000.
- Paul, B. K., Hasan, H., Thomas, J., Wilson, R. D., and Alman, D., "Limits on Aspect Ratio in Two-Fluid Micro-Scale Heat Exchangers," in *in press*, 2000.
- Paul, B. K. and Peterson, R. B., "Microlamination for Microtechnology-based Energy, Chemical, and Biological System," presented at ASME IMECE, Nashville, Tennessee, 1999.
- Paul, B. K. and Terhaar, T., "Comparison of two passive microvalve designs for microlamination architectures," *Journal of Micromechanical and Microengineering*, vol. 10, pp. 15-20, 2000.
- Peterson, R. B., "Small Package," in *Mechanical Engineering*, vol. June 2001, 2001.

- Peterson, R. B., Pence, D. B., Liburdy, J., and Welty, J. R. "Energy Systems, Heat Transfer, and Fluid Flow.", 2001 Available: www.me.orst.edu/research/mecs/projects/.
- Pfahler, J., Harley, J., and Bau, H., "Liquid Transport in Micron and Submicron Channels," *Sensors and Actuators A*, vol. 21-23, pp. 431-434, 1990.
- Pfahler, J., Harley, J., Bau, H., and Zemel, J. N., "Gas and Liquid Flow in Small Channels," *Micromechanical Sensors, Actuators, and Systems--Transaction of the ASME: DSC*, vol. 32, 1991.
- Pottenger, M. and Eyre, B., "MEMS: The maturing of a new technology," *Solid State Technology*, vol. 40, pp. 89-94, 1997.
- Qin, D., Xia, Y., Rogers, J. A., Jackman, R. J., Zhao, X.-M., and Whitesides, G. M., "Microfabrication, Microstructures and Microsystems," *Topics in Current Chemistry*, vol. 194, pp. 1-20, 1998.
- Quan, M., "Biochips: From Sci-Fi to Critical Tech," in *Electronic Engineering Times*, 1999, pp. 8.
- Spearing, S. M., "Materials Issues in Microelectromechanical Systems (MEMS)," *ACTA material*, vol. 48, pp. 179-196, 2000.
- Stampfl, J., Liu, H.-C., Nam, S. W., Kang, S., and Prinz, F. B., "Rapid Prototyping of Mesoscopic Devices," *Proceeding of Micromaterials 2000*, pp. 1-6, 2000.
- TeGrotenhuis, W. E., Cameron, R., Butcher, M. G., Martin, P. M., and Wegeng, R. S., "Microchannel Devices for Efficient Contacting of Liquids in Solvent Extraction," presented at AIChE 1998 Spring National Meeting, New Orleans, 1998.
- Thomas, J. "Establishing Thermally Enhanced Edge Registration (TEER) as a Feasible Alignment Technique for Metallic Laminated Devices." *M.S. Thesis*, Industrial Engineering: Oregon State University, 2001.
- Tonkovich, A. L. Y., Zilka, J. L., Jimenez, D. M., LaMont, M. J., and Wegeng, R. S., "Microchannel Chemical Reactors for Fuel Processing," presented at AIChE 1998 Spring National Meeting, New Orleans, 1998.
- van den Berg, A. and Lammerink, T. S. J., "Micro Total Analysis Systems: Microfluidic Aspects, Integration Concept and Applications," *Topics in Current Chemistry*, vol. 194, pp. 21-49, 1998.

- Wangwatcharakul, W. and Paul, B. K., "Development of Passive Micro-ball valve," in *in press*, 2001.
- Weck, M. and Fischer, S., "Manufacturing of Microstructures using Ultraprecision Machine Tools," presented at SPIE proceedings, 1999.
- Wegeng, R. S., Drost, M. K., and Brenchley, D. L., "Process Intensification Through Miniaturization of Chemical and Thermal Systems in the 21st Century," *Pacific Northwest National Laboratory*, 1999.
- Weigl, B. H. and Yager, P., "Microfluidic Diffusion-Based Separation and Detection," *Science*, vol. 283, pp. 346-347, 1999.
- Wu, P. and Little, W. A., "Measurement of the heat transfer characteristics of gas flow in fine channel heat exchangers used for microminiature refrigerators," *Cryogenics*, vol. 23, pp. 273-277, 1983.

CHAPTER 2

EFFECT OF FIN WARPAGE AND CHANNEL MISREGISTRATION ON THE PERFORMANCE OF METALLIC MICROLAMINATED HEAT EXCHANGERS

2.1 Abstract

This research investigates the theoretical effect of shape variation generated during the microlamination process on the performance of a parallel-plate microchannel heat exchanger. Fin warpage and channel misalignment are two types of shape variation evaluated in this study. The microchannel heat exchanger is comprised of alternating layers of channels, separated by fins, which allow two fluids to flow in opposite directions. A microlamination process is used to fabricate this device. During production, layers of fins and channels are laser-machined and diffusion-bonded to form a monolithic heat exchanger. During microlamination, fin warpage caused by mechanisms such as the difference in thermal expansion coefficients between the bonding fixture and the laminated material at elevated temperature can lead to nonuniform flow channels which affect the heat transfer effectiveness in these laminar flow channels. In a second case, when fin and channel layers are improperly registered to each other during microlamination, the heat transfer areas are reduced, lowering the thermal efficiency of the device.

Theoretical models of the heat transfer performance based on nonuniform flow channel and channel alignment are implemented in this study. The nonuniform flow channel model shows that warpage across the fin has a significant effect on the penalty in heat transfer performance but less on the flow friction behavior of the channel. On the other hand, the channel misalignment model shows only a slight effect on heat transfer performance and no effect on flow

behavior. In addition, it is found that by increasing the mode of buckling, the effect of fin warpage on the thermal performance of heat exchangers can be significantly reduced because higher mode buckling lowers the amount of channel width deviation.

2.2 Introduction

Microlamination is a fabrication technique for a parallel-plate heat exchanger, in which one of the channel dimensions is designated in the microscale to mesoscale (tens to hundreds of micrometer) (Martin, et al., 1999; Paul, et al., 1999; Peterson, 2001). In this process, thin layers of material, called laminae, are patterned upon different designs whether they are fins or channels, and then these laminae are bonded together into a monolithic device. In general, the process used for microlamination involves three major steps: 1) laminae patterning, 2) laminae registration, and 3) laminae bonding. Figure 2-1 shows an exploded view of a two-fluid counter-flow microchannel array, which could be used for mesoscale heat and mass transfer applications, illustrating the microlamination principle.

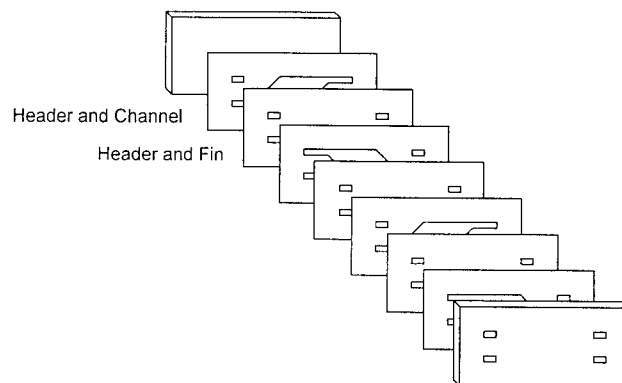


Figure 2-1. An exploded view illustrating a microlamination procedure in microchannel fabrication

In the bonding step of microlamination, laminae are held in a holding fixture normally made from a refractory material, and then put in a vacuum oven to diffusion-bond the laminae into a monolithic structure. However, interference between the fixture and the laminae caused by the difference in the coefficient of thermal expansion can apply a buckling load to the fins. As a result, nonuniform flow channels between the warpage fins are generated as shown in Figure 2-2. Because of the difference in the cross-section of flow channels due to this nonuniformity, the working fluid will normally flow at different rates between channels. More fluid tends to flow in the larger cross section channels and this larger flow fraction has a longer conduction path for heat transfer to or from the wall, resulting in a less effective heat transfer coefficient for the total surface area as well as overall heat transfer. This phenomenon is called flow maldistribution. In addition, other causes of warpage nonuniformity can include residual stresses that are relaxed during bonding, initial curvature of shim stock, mismatch of coefficient of thermal expansion of composite material, and delamination of composite laminae (Timoshenko, 1961; Shames, 1989; Fang, et al., 1994; Gere, et al., 1997; Ashby, 1999; Fang, et al., 1999; Popov, 1999; Paul, et al., 2000; Paul, et al., 2000).

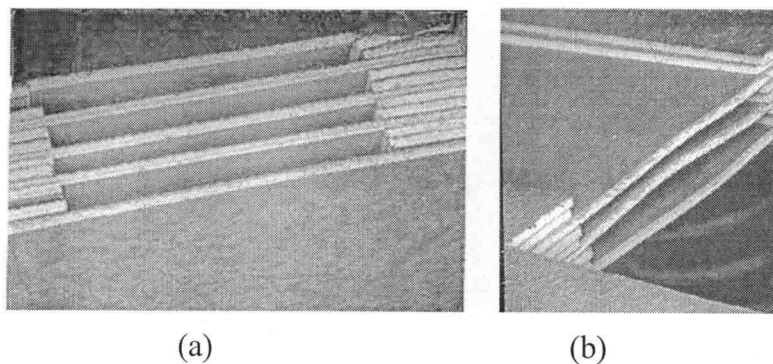


Figure 2-2. SEM photo micrographs of Ni-Al Microchannel heat exchanger with nonuniform flow channels (a) before and (b) after fin buckling

In 1970, London introduced an analytical method to determine the influence of nonuniformity of flow channels on the laminar regime surface characteristics. His investigations were based on nonuniformity models for both rectangular and triangular cross sections in a compact heat exchanger. Both of his models predicted the reduction of heat transfer effectiveness related to differences of flow distribution between channels (London, 1970). Later, the London model was generalized to combine the effect of fin curvature or bulginess during an investigation by Mondt (Mondt, 1977). In 1980, Shah and London reinvestigated the London model and included an additional investigation of gas-liquid heat transfer and thermal performance during the developing laminar flow scheme. Their results showed the influence of overall nonuniformities in flow channels on the heat transfer performance as well as the relationship of manufacturing tolerance and channel nonuniformity (Shah, et al., 1980).

Many researchers have found that flow maldistribution significantly affects the performance of heat exchangers. In 1985, Chowdhury and his colleagues showed that a passage-to-passage nonuniformity was considered to have a significant effect on heat transfer efficiency, but pressure drop was only slightly affected by flow maldistribution (Chowdhury, et al., 1985). A couple years later, Mueller and Chiou reviewed various types of flow maldistribution in heat exchangers and categorized them based on their causes. According to the authors, flow maldistribution in the heat exchangers consists of 4 categories: 1) mechanically caused maldistribution; 2) self-induced flow maldistribution; 3) two-phase flow maldistribution; and 4) fouling-caused maldistribution. Based on the shell and tube heat exchanger operating at turbulent flow, flow maldistribution results in a minor effect on the heat transfer performance at low NTU (less than 4), but large performance loss at high NTU (greater than 10) (Mueller, et al., 1988). Then in 1989, Kitto and Robertson stated that flow maldistribution can have a considerable effect on thermal performance of compact heat exchangers normally designed to yield a high effectiveness. However, flow maldistribution cannot be

easily identified because it is extremely difficult in practice to measure (Kitto, et al., 1989). Recently, Lalot, et al. demonstrated that flow maldistribution could lead to a 7% loss of effectiveness in condensers and counterflow heat exchangers, and up to 25% for cross-flow heat exchangers with velocity ratios up to 15 (Lalot, et al., 1999). These authors also investigated the relationship of flow distribution in electrical heaters to optimize the device performance.

Although there were several investigations on flow maldistribution in heat exchangers, most of them were performed either on a macroscale device or a compact heat exchanger (minimum dimension is above 500 μm), which is considerably larger than common heat exchangers for MECS devices (25-200 μm). Flow maldistribution based on fin warpage in mesoscopic counter-flow heat exchangers has yet to be explored.

In order to be able to utilize the full performance of microchannel heat exchangers for MECS applications, as well as to gain a better understanding of the microlamination process of making the devices, the effect of flow maldistribution due to fin warpage needs to be controlled. Therefore, the goal of this study is to explore the relationship of flow maldistribution and the performance of the microchannel heat exchanger when the device encounters deformation by fin warpage as well as misregistration of channel laminae. The impact of two modes of shape variation on the device performance is compared.

The following activities were used to investigate the influence of shape variation on the performance of microlaminated devices in this study:

- 1) Developing analytical models to evaluate the heat transfer penalty and pressure drop relations due to both fin warpage and laminae misregistration.
- 2) Using the model to determine the minimum levels of shape variation necessary in microlamination for high heat effectiveness and to predict how to reduce the effect of this variation on heat transfer performance.

2.3 Theoretical Models

This section presents the analytical models used to analyze the performance of a heat exchanger based on channel misregistration and fin warpage within laminated microchannel array. The heat exchanger in this study was based on a two-fluid counter-flow heat exchanger of hot and cold streams of air. The flow length and flow cross-sectional areas of both streams were the same. However, for the fin warpage case, the heat exchanger core consisted of two different channel cross sections where one channel area was smaller than another channel. Figure 2-3 is a diagram of the heat exchanger geometry used for the evaluation of the effect of flow maldistribution and reduction of heat transfer area in this chapter.

During this investigation, the following assumptions were made as a part of the evaluation of the impact of shape variation on the performance of the heat exchanger.

- The flow in the channel is fully developed.
- The heat transfer coefficient and friction factor along the channel length are constant.
- Entrance and exit losses are relatively small and can be neglected.
- Fluid properties such as density, viscosity, and specific heat are the same for all channels and may be treated as constants.
- The thermal boundary condition for this heat exchanger is a constant axial wall heat flux with constant peripheral wall temperature.
- The major source of warpage is due to a buckling load on the end of the fin.

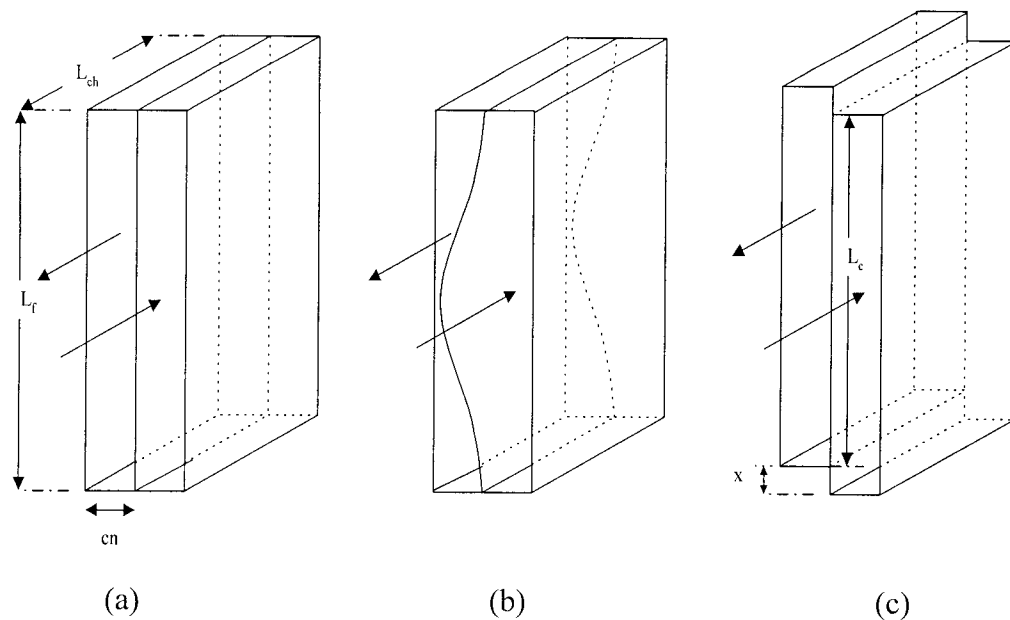


Figure 2-3. Geometry of (a) uniform flow channels, (b) nonuniform flow channels due to fin warpage, (c) nonuniform flow channels due to channel misalignment

2.3.1 Fin Warpage Analysis

Flow channels inside a microchannel array are deformed as a result of fin warpage, and the geometry of this nonuniformity is presented in Figure 2-3 (b). This section evaluates the impact of fin warpage nonuniformity on the performance of a counter flow heat exchanger based on both heat transfer performance and pressure drop. The characteristics of fin warpage are described, and the implementation of the London model for fin warpage is also presented.

2.3.1.1 Channel Deviation due to Fin Warpage (Fundamental Mode)

When a fin layer contains warpage, the flow channels between both sides of this fin are altered, as shown in Figure 2-3 (b). Channel deviation is a result of flow

channel fin warpage and nonuniformity. Two different rectangular cross section channels, as shown in Figure 2.4 (b), are used to represent the phenomenon.

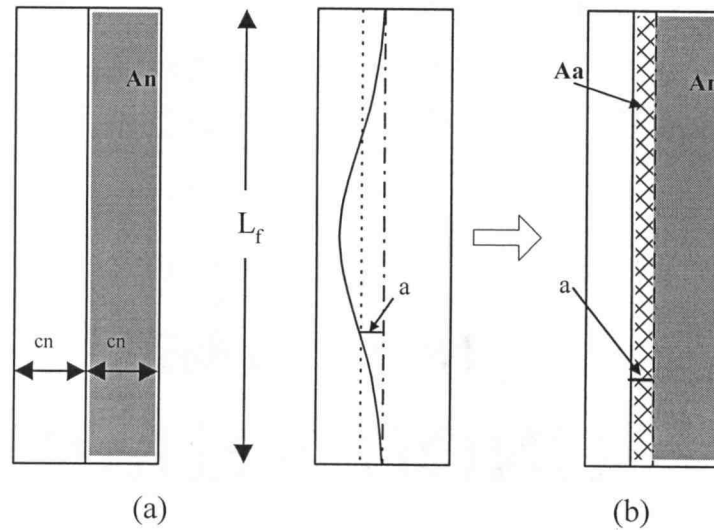


Figure 2-4. Geometry of (a) uniform flow channels, (b) nonuniform flow channels due to fin warpage

According to London (1970), the calculation of the channel deviation, or a deviation of flow channels (δ_c) is represented by:

$$\delta_c = \frac{a}{cn}. \quad (1)$$

The term “ a ” represents the distance from the expected position of the fin to achieve uniformity without warpage, to the average position of the warped fin, while “ cn ” is a channel height or a distance between fins. For fin warpage as shown in Figure 2-4 (b), “ a ” is specified as half the distance between the original position and the peak of the deflection. The cross-sectional area of each side of the uniform flow channels is “ An ”. However, when the flow channels encounter the fin warpage, the cross-sectional area will become either “ $An+Aa$ ” or “ $An-Aa$ ”, depending on what side of the channel they stand for, and the term “ Aa ” is the area

under the deflection after they convert into a rectangular shape (see Figure 2-4 (b) on the right side).

2.3.1.2 Channel Deviation and Fin Warpage at Higher Modes

From the previous section, the fin warpage was assumed to be in the fundamental mode, in which only one half-wave deflection was encountered. Figure 2-5 illustrates several other cases where a buckling load induces a higher mode of buckling in the fin.

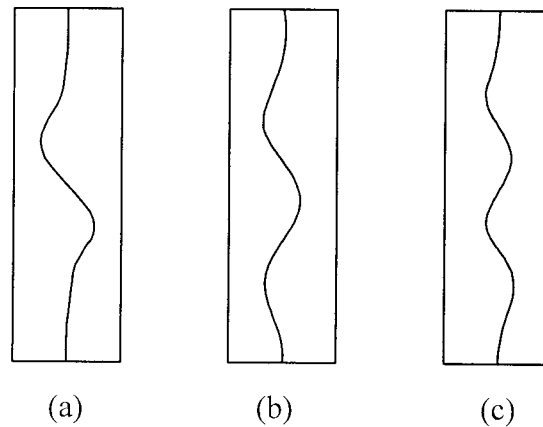


Figure 2-5. Fin buckling in higher modes: (a) Mode 2 (b) Mode 3 and (c) Mode 4

At the higher mode of buckling, the deflection amplitudes of the buckling become smaller. When the length of the fin stays constant, higher modes of buckling require the fin to form higher numbers of deflection peaks (mode number stands for the number of the peak), which lower the amplitude of each deflection peak, and lessen the average deviation of the flow channel.

In this study, the higher mode of fin buckling was evaluated to determine the relationship between the mode of buckling and channel deviation. Figure 2-6 (c) shows the geometrical characteristics important for describing mode 2 buckling, which was used to show this relationship.

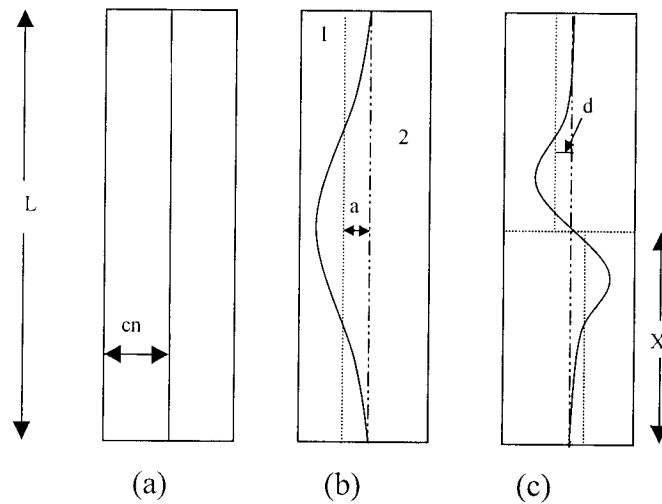


Figure 2-6. Geometry of (a) uniform flow channels, (b) nonuniform fin buckling of Mode 1, and (c) nonuniform fin buckling of Mode 2

At higher-mode fin warpage, the calculation of the channel deviation (δ_c)

can be stated as:

$$\delta_c = \frac{d}{cn}. \quad (2)$$

In mode 2, the distance “ d ” is used instead of “ a ” in the fundamental mode. This “ d ” distance is the distance from the centerline to an average position of the buckled fin either to the left or to the right side of the fin since the deflections are symmetrical. As the mode of buckling gets bigger, the term “ d ” gets smaller as well as δ_c .

2.3.1.3 The Relationship between Channel Deviation due to Fin Warpage and Performance of the Heat Exchanger

As mentioned previously, flow maldistribution between two sides of the counter-flow heat exchanger is a key to the performance of the device. The following summary demonstrates the implementation of the London model to evaluate the relationship between channel deviation and the performance of the heat exchanger in terms of heat transfer performance and pressure drop. Important equations are presented in this section; the transformation from one step to another and derivations of this relationship as well as the modification of the London model are provided in Appendix B.

In the case of fin warpage nonuniformity, one side of the channel becomes smaller than the other side. We define the channel with the smaller cross section to be channel 1, and the other side of the fin (a bigger cross section channel) to be channel 2. At the steady state, the pressure drop across both channels (1 and 2) is assumed to be the same, therefore:

$$\Delta P = f_1 \left[\rho \cdot \frac{(V_1)^2}{2 \cdot g_c} \right] \cdot \left(\frac{L}{r_{h,1}} \right) = f_2 \left[\rho \cdot \frac{(V_2)^2}{2 \cdot g_c} \right] \cdot \frac{L}{r_{h,2}} \quad (3)$$

When transforming the above equation in terms of mass flow rate, the ratio of flow distribution between channel 1 and 2 is

$$\frac{\omega_1}{\omega_2} = \frac{(fRe_2) \left(\frac{r_{h,1}}{r_{h,n}} \right)^2 \left(\frac{A_1}{A_n} \right)}{(fRe_1) \left(\frac{r_{h,2}}{r_{h,n}} \right)^2 \left(\frac{A_2}{A_n} \right)} \quad (4)$$

Then we convert equation (4) based on the buckling geometry to the flow distribution ratio:

$$\frac{\omega_1}{\omega_2} = \left(\frac{fRe_2}{fRe_1} \right) * \left(\frac{An - Aa}{An + Aa} \right)^3 \quad \text{where} \quad \omega_1 + \omega_2 = 1 \quad (5)$$

This equation can be transformed into the number of transfer units (NTU) based on the relationship between NTU and the Stanton number (see Appendix B). As a result, the ratio of NTU of any side ($i = 1$ or 2) of the channel over the NTU of a uniform channel is:

$$\frac{NTU_i}{NTU_n} = \left(\frac{Nu_i}{Nu_n} \right) \left(\frac{\omega_n}{\omega_i} \right) \left(\frac{A_i}{A_n} \right) \left(\frac{r_{h,n}}{r_{h,i}} \right)^2 \quad (6)$$

When substituting the warpage characteristics, this NTU ratio will change to:

$$\frac{NTU_i}{NTU_n} = \left(\frac{Nu_i}{Nu_n} \right) * \left(\frac{\omega_1}{\omega_2} \right) * \left(\frac{A_n}{A_i} \right) * \left(\frac{L_f + L_s + 2 * cn}{2 * L_s + 2 * cn} \right)^2 \quad (7)$$

From equation (7), the NTU for each channel can be calculated when the NTU_n is known. The effectiveness of each flow channel can be calculated individually by these equations:

$$\varepsilon_1 = \frac{NTU_1}{1 + NTU_1} \quad \varepsilon_2 = \frac{NTU_2}{1 + NTU_2} \quad (8)$$

Therefore, the average of heat transfer effectiveness is: $\varepsilon_{avg} = \omega_1 \cdot \varepsilon_1 + \omega_2 \cdot \varepsilon_2$ (9)

Then, the average effective number of transfer units based on the effectiveness-

$$NTU_{eff} = \frac{\varepsilon_{avg}}{1 - \varepsilon_{avg}} \quad (10)$$

NTU relations is:

As a result, the penalty in heat transfer performance in terms of the percent reduction of transfer units, $\%Loss_{NTU}$, is:

$$\%Loss_{NTU} = 1 - \frac{NTU_{eff}}{NTU_n} * (100\%) \quad (11)$$

As mentioned earlier, when fin warpage exists in a counter-flow heat exchanger, the cross-sectional area of the flow in one side of the channel becomes larger than the other one, and more fluid tends to flow in the larger cross sectional channel, resulting in a lower pressure drop for the overall heat exchanger. Based on the relation of pressure drop of both sides of the channel-equation (3), a ratio of

pressure drop between the nonuniform and uniform flow channels can be rewritten as:

$$\frac{\Delta P_i}{\Delta P_n} = \left(\frac{f_i}{f_n} \right) * \left(\frac{V_i}{V_n} \right)^2 * \left(\frac{r_{h_n}}{r_{h_i}} \right) \quad (12)$$

From the above equation, when converting the flow velocity into flow distribution, the ratio of pressure drop between the nonuniform flow channel and the uniform flow channel is:

$$\frac{\Delta P_i}{\Delta P_n} = \left(\frac{f Re_i}{f Re_n} \right) * \left(\frac{\omega_i}{\omega_n} \right) * \left(\frac{A_n}{A_i} \right) * \left(\frac{r_{h,n}}{r_{h,i}} \right)^2 \quad (13)$$

When nonuniformity occurs by fin warpage, the pressure drop ratio between any side of the channel over the pressure drop of the uniform channels becomes:

$$\frac{\Delta P_i}{\Delta P_n} = \left(\frac{f Re_i}{f Re_n} \right) * \left(\frac{\omega_i}{\omega_n} \right) * \left(\frac{A_n}{A_i} \right)^3 * \left(\frac{P_i}{P_n} \right)^2 \quad (14)$$

As a result, the friction behavior in terms of percent gain in pressure drop is:

$$\%Gain_{\Delta P} = 1 - \frac{\Delta P_i}{\Delta P_n} * (100\%) \quad (15)$$

2.3.2 Misregistration Analysis

When laminae misregistration develops, during the bonding process, the flow channels are not in line with each other, as shown in Figure 2-3 (c). From this figure, 'x' illustrates the amount of misalignment between the two consecutive flow channels. As a result, the contact width between these two channels, L_c , is equal to the original contact width (fin width), L_f , minus the amount of misalignment, x . The smaller the contact width, the smaller the heat transfer area assuming the heat exchanger length, L_{ch} , is constant. The flow distribution and hydraulic radius of these two consecutive channels are the same whether the channels are misaligned or not, because there is no change in the cross-sectional area. Similarly, the Nusselt

number (Nu) is also constant since the channel height does not change. The NTU of the channel is calculated from:

$$NTU = \frac{Nu}{Re} * \frac{L}{r_h} \quad \text{or} \quad NTU \propto Nu \cdot \frac{A}{\omega} \cdot \frac{1}{r_h^2} \quad (16)$$

According to equation (16), the NTU of the channels with misalignment is proportional to the heat transfer area or contact width between two consecutive channels. Correspondingly, the percent loss in NTU is proportional to the ratio of misalignment and the fin width or $\%Loss_{NTU} = \frac{x}{L_f}$ (17)

Nonetheless, misalignment shows no effect on the pressure drop because the cross-sectional area of the misaligned channels is still uniform.

2.4 Case Study

To evaluate the influence of shape variation on the performance of the parallel-plate heat exchanger (see Figure 2-3), a 20:1 aspect ratio heat exchanger was specified based on the following parameters:

L_{ch}	=	30	mm	T_{ci}	=	39	°C
cn	=	0.5	mm	k	=	30E-3	W/m K
L_s	=	10	mm	W	=	0.07	g/s
ΔT_m	=	3	°C	cp	=	1009	J/kg K
T_{hi}	=	100	°C	ε	=	0.95	

2.4.1 Base Case Heat Exchanger Characteristics

The base case selected for this experiment has its system characteristics and nominal geometry specified in Appendix C along with some useful geometrical relationships. According to Appendix C, the overall NTU of a specific system was 19, based on a 95% effectiveness of the nominal device. This also results in a total

heat transfer area of $11.43 \times 10^3 \text{ mm}^2$, or about 19-flow channels based on this hypothetical device. The overall NTU was used again to evaluate heat transfer performance penalties in later sections. The pressure drop based on this nominal device was 415 Pa (0.06 psi). The Reynolds number was 640 designating a laminar flow scheme. In addition, the system required 0.03 W of pumping power when assuming the flow rate of 70 mL/s.

2.4.2 Evaluation of Heat Transfer Performance Penalty and Pressure Drop Reduction

Theoretical models that were stated in section 2.2 were then implemented to calculate a percent loss in NTU for the nominal geometry specified when the microchannel encountered the deviation due to fin warpage. From equation (5), the graph illustrating the relationship between the flow distribution of channels and the channel deviation (δ_c) is presented in Figure 2-7.

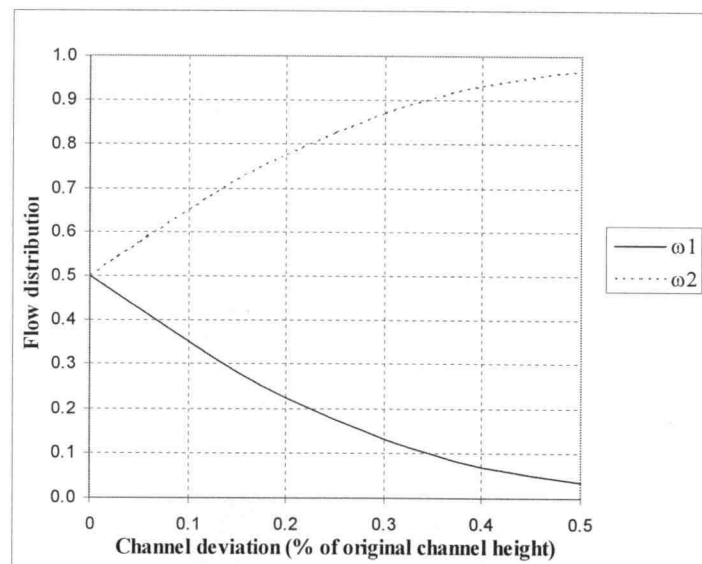


Figure 2-7. Flow distribution of heat exchanger as a function of channel deviations

Figure 2-8 represents the relation of channel deviation versus the effectiveness and NTU of the heat exchanger, while Figure 2-9 illustrates the impact of channel deviation on the percent loss in NTU and the gain in pressure drop. See numerical data in Appendix D.

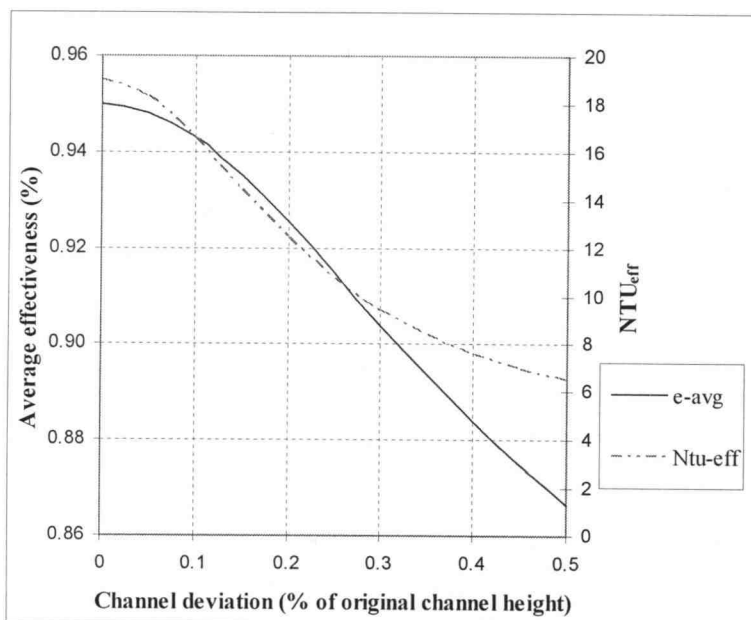


Figure 2-8. The relationship of channel deviation due to fin warpage and the heat exchanger performance in terms of average effectiveness and NTU

Appendix E represents an example of the evaluation of channel deviation based on a specific fin buckling. Based on a certain condition as specified in the Appendix, the fin was buckled due to the buckling load when the bonding fixture and laminae were interfered at bonding temperature, and produced a 45% channel deviation based on a fundamental mode warpage. So this deviation caused the NTU to drop from 19 to 7 (see Figure 2-8), which resulted in 63% loss of NTU, as in Figure 2-9. The pressure drop was decreased by 39%.

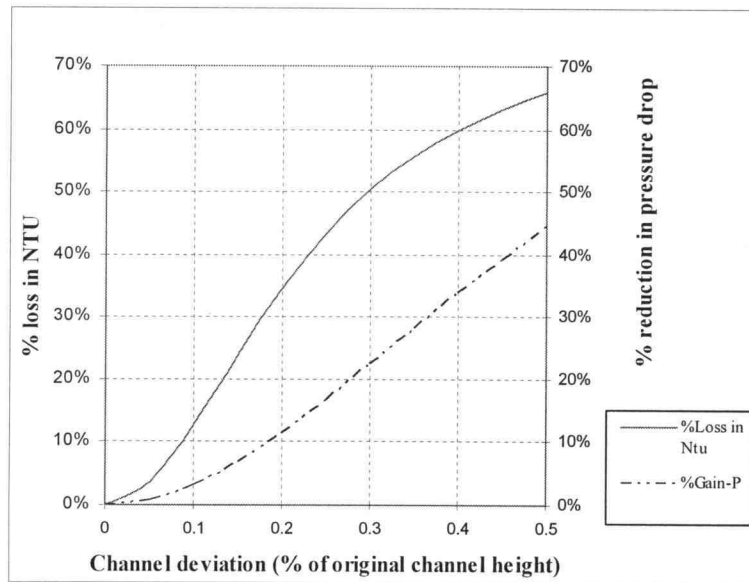


Figure 2-9. The impact of channel deviation on percent loss in NTU, percent gain in ΔP

The smaller the fin deflection, the lesser the flow maldistribution as well as the reduction of heat transfer performance. The initial analysis was based on mode 1 buckling only. It was expected that heat exchangers with higher modes of buckling would result in less flow maldistribution due to the reduction of channel deviation. According to Appendix E, when the fin with the same geometry as the previous discussion is induced to form mode 2 buckling, the maximum deflection of this mode was smaller than mode 1 by almost half, resulting in 24.5% channel deviation. Referring to Figure 2-8, the effect of 24.5% channel deviation produces a 42% loss in NTU, which is roughly 30% less than the loss in mode 1 buckling (63% loss in NTU).

2.4.3 Transformation of Heat Transfer Performance Penalty into a Compensated Area

In Figure 2-9, the result of flow maldistribution caused by fin warpage was evaluated in terms of the loss in NTU. However, in order for easy interpretation, the percent loss in NTU was transformed into the percent increase in heat exchanger area that was required to compensate the reduction of NTU. The calculation of compensated area from the cost of NTU in nonuniform flow channels is provided in Appendix G. Figure 2-10 illustrates the relationship of channel deviation and the compensated area as well as the number of channels required to satisfy the heat transfer performance when the channels are uniform.

A summary table of the maximum deflection, channel deviation, percent NTU reduction, pressure change, area compensation required, and number of compensated channel needed based on different modes of buckling is shown in Table 2-1.

Table 2-1. Summary table of heat transfer performance and pressure drop at different buckling modes

Buckling Mode	Maximum Deflection	Channel Deviation	% NTU Reduction	Pressure Change	Area Compensation Required	Number Channel Needed
Mode 1	0.45	0.45	63.2%	39.3%	172%	52
Mode 2	0.22	0.245	42.7%	16.1%	74%	33
Mode 3	0.15	0.191	32.9%	10.4%	49%	28
Mode 10	0.045	0.057	4.7%	1.0%	5%	20
∞	~ 0	~ 0	~ 0	~ 0	~ 0	19

For instance, for 45% deviation and 63% loss in NTU, the heat exchanger transfer area needs to be more than twice as large as the original heat transfer area (172%) to compensate for the loss in NTU caused by this deviation. Similarly, a heat exchanger that contains the same amount of channel deviation is needed to be

almost triple the number of flow channels to gain the same thermal effectiveness as the uniform one. It was evident that heat exchangers with fin buckling shape variation requires the entire device to be larger and heavier to have the same thermal effects as the originally designed units without this nonuniformity.

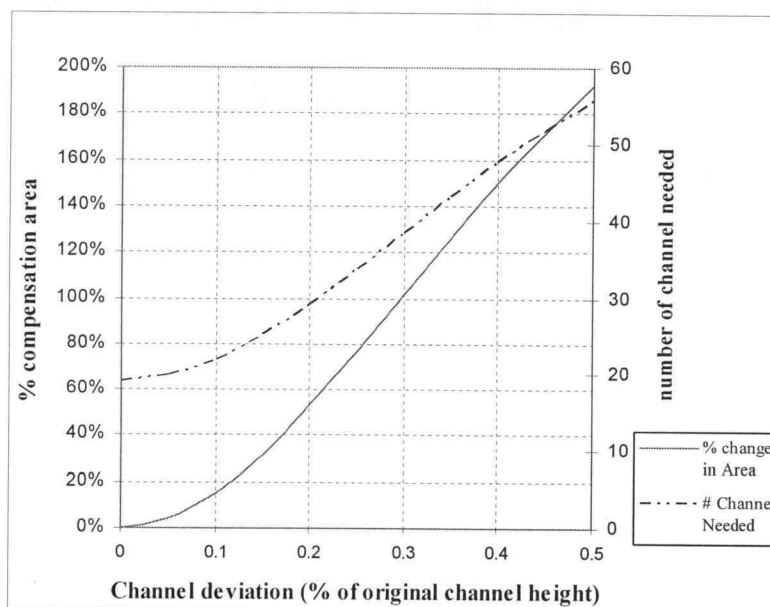


Figure 2-10. The relation of channel deviation and the number of channels needed and percent increase in area to compensate the loss in heat transfer performance

With respect to its lower channel deviation, mode 2 buckling contributed only 74% percent of the compensated area or a total of 33 channels, which is almost 100% reduction from mode 1 criteria.

It is expected that even higher modes of buckling would show further improvement in reducing the impact of flow maldistribution on heat exchanger performance. For example, with mode 10 buckling, the channel deviation was less than 6%, resulting in an insignificant 5% loss in NTU (see Table 2-1). This

suggests that a future research direction might be to experiment with preferential higher mode buckling in the foil. One possible advantage is that by stiffening the foil through preferential buckling, we could move toward thinner and thinner foils in order to maximize the heat transfer efficiency in the counter-flow heat exchanger.

2.4.4 Determination of Channel Misalignment Effects on Heat Exchanger Performance

As mentioned in section 2.2.2, the percent loss in NTU was proportional to the ratio of misalignment and the original contact width (equation 17). Appendix G also demonstrates the conversion of the percent loss in NTU for misalignment channel into a compensated area. For instance, if the channel is misaligned by 1 mm when the original channel width is 10 mm, the percent loss in NTU for this specific channel is 10% (from 1 mm divided by 10 mm). In the mean time, with 10% loss in NTU, the percent area to compensate the loss in NTU must be increased by 11.11%.

A typical misalignment error in the microchannel array of a mesoscale device was on the order of 5 to 50 μm (Thomas, 2001). Therefore, a nominal size of the heat exchanger in this case study can cause only 0.5% reduction in NTU, resulting in a negligible increase in the heat exchanger size of 0.5%.

2.4.5 Comparison between Fin Warpage and Channel Misalignment

As mentioned in the preceding section, a typical level of misalignment in a mesoscale counter-flow heat exchanger was mostly below 50 μm , which results in a negligible 0.5% of percent loss in NTU or compensated areas. Nonetheless, the level of warpage within this device has not been quantified. In the case of a

nominal dimension as stated in the case study, the fin warpage induced by fin buckling when the interference between the fin and laminae is 50 μm can cause up to 63% reduction in NTU. It appears that a tolerance of 50 μm has a more significant effect on a heat exchanger in terms of fin buckling than of misalignment.

2.4.6 Effect of the Base Case NTU on the Device to the Penalty of Thermal Performance Due to Fin Warpage

The relationship between the original NTU of a heat exchanger and the loss of performance due to channel deviation was investigated. Based on the case study, the evaluation was performed on a nominal device with an NTU of 19 or 95% effectiveness. When varying the NTU of the system, the impact of channel deviation on the thermal performance could be evaluated. This evaluation is illustrated in Figure 2-11, where NTU was varied from 0.1 up to 60 or about 9% – 98% thermal effectiveness. The calculation of percent loss in NTU for this section was based on the same nominal dimensions as was in the previous section.

This evaluation is in good agreement with Mueller and Chiou (1998), which stated that flow maldistribution results in minor performance reduction at nominal NTU, but has a greater performance loss at high NTU. Notice that when the value of NTU was over 10 (90% effectiveness), the percent losses in NTU of both modes of buckling are considerably constant.

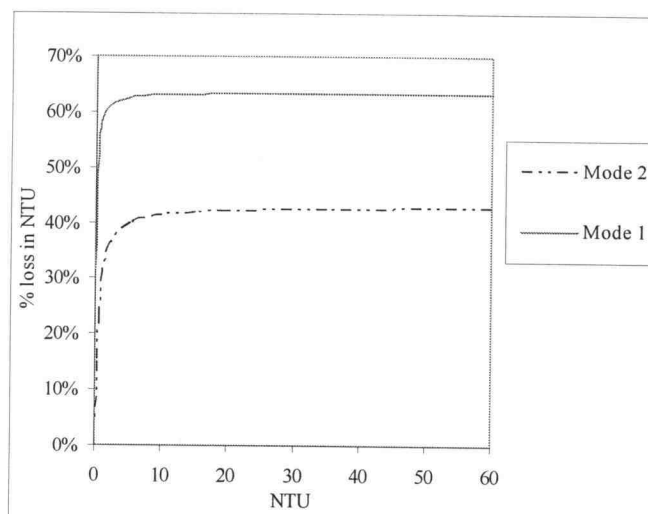


Figure 2-11. Relationship between the system NTU and the percent loss in NTU for Mode 1 and Mode 2 fin buckling

2.4.7 The Relation between Aspect Ratio of a Flow Channel and the Penalty of Performance due to Channel Nonuniformity

The aspect ratio of a flow channel was found to be a key design variable that can be varied for heat exchanger optimization. Consequently, the penalty of device performance due to channel nonuniformity can change as a function of aspect ratio. Either channel width or channel height must be changed when the aspect ratio is altered. Table 2 summarizes the percent loss in NTU as a function of aspect ratio when the device is encountered a 45% channel deviation.

Table 2-2. The relation of aspect ratio and percent loss in NTU

Aspect Ratio	ω_l	Nu_n	Nu_1	Nu_2	% Loss in NTU
20:1	0.048	7.462	8.011	7.661	63.18%
10:1	0.046	6.806	7.398	6.293	64.79%
5:1	0.043	5.782	6.704	5.100	66.88%

A general conclusion drawn from this comparison was that the penalty associated with a given nonuniformity magnitude, slightly increases as the aspect ratio decreases; therefore, at a fixed deviation, the higher the aspect ratio, the lower the loss in NTU, due to nonuniform flow through flow channels.

2.5 Summary

This investigation was carried out to study the effects of microchannel shape variation on microchannel heat exchanger performance. The implementation of the London model for evaluating the heat transfer penalty and pressure drop reduction based on fin buckling was studied. Misalignment of laminae in microlamination has also been evaluated. Warpage due to fin buckling has a significant effect on the performance of the device because it generates flow maldistribution between consecutive flow channels, which significantly reduces the number of transfer units. On the other hand, misalignment only impacts the reduction of heat transfer area, which has a slight effect on the number of transfer units based on a scale of misalignment encountered in a mesoscopic device. In contrast, fin warpage causes a slight decrease in pressure drop, which could lower the driven power for the system, but this is practically insignificant when compared to the loss of thermal effectiveness due to flow maldistribution.

One possible way to decrease the influence of buckling variation presented in this paper would be to preferentially buckle fins to higher modes of buckling to achieve smaller channel deviation and improved heat transfer performance. In a nominal heat exchanger design, changing from mode 1 to mode 2 buckling can reduce the compensation area or the amount of additional heat transfer area needed for the application from 172% to 74%. This suggests that higher mode buckling lowers the effects on heat transfer performance. Future research is needed to

develop economically feasible methods for higher modes of fin buckling in microlamination.

Finally, the impact of the channel nonuniformity due to fin buckling is a function of the aspect ratio of the microchannel. Flow maldistribution has a significant effect on the performance of heat transfer devices only when that device has a higher NTU (or the thermal effectiveness over 90%). Also, as the aspect ratio of flow passage increases, the penalty in heat transfer from nonuniformity becomes smaller, which results from the reduction in channel deviation.

2.6 References

- Ashby, M. F., *Materials selection in mechanical design*. Oxford; Boston: Butterworth-Heinemann, 1999.
- Chowdhury, K. and Sarangi, S., "Effect of Flow Maldistribution on Multipassage Heat Exchanger Performance," *Heat transfer engineering*, vol. 6, pp. 45-54, 1985.
- Fang, W., Lee, C.-H., and Hu, H., -H., "On the buckling behavior of micromachined beams," *Journal of Micromechanical and Microengineering*, vol. 9, pp. 236-244, 1999.
- Fang, W. and Wickert, J. A., "Post buckling of micromachined beams," *Journal of Micromechanical and Microengineering*, vol. 4, pp. 116-122, 1994.
- Gere, J. M. and Timoshenko, S. P., *Mechanics of materials*. Boston: PWS-KENT Pub. Co., 1997.
- Kitto, J. B. and Robertson, J. M., "Effects of Maldistribution of Flow on Heat Transfer Equipment Performance," *Heat transfer engineering*, vol. 10, pp. 18-25, 1989.
- Lalot, S., Florent, P., Lang, S. K., and Bergles, A. E., "Flow maldistribution in heat exchangers," *Applied Thermal Engineering*, vol. 19, pp. 847-863, 1999.
- London, A. L., "Laminar Flow Gas Turbine Regenerators--The Influence of Manufacturing Tolerances," *Transactions of ASME: Journal of Engineering for Power*, vol. 92, pp. 46-56, 1970.
- Martin, P. M., Matson, D. W., and Bennett, W. D., "Microfabrication Methods For Microchannel Reactors and Separations Systems," *Chemical Engineering Communications*, vol. 173, pp. 245-254, 1999.
- Mondt, J. R., "Effects of Nonuniform Passages on Deepfold Heat Exchanger Performance," *Transactions of ASME: Journal of Engineering for Power*, vol. 99, pp. 657-663, 1977.
- Mueller, A. C. and Chiou, J. P., "Review of Various Types of Flow Maldistribution in Heat Exchangers," *Heat transfer engineering*, vol. 9, pp. 36-50, 1988.

- Paul, B. K., Dewey, T., Alman, D., and Wilson, R. D., "Intermetallic Microlamination for High-Temperature Reactors," presented at 4th International Conference on Microreaction Technology, Atlanta, GA, 2000.
- Paul, B. K., Hasan, H., Thomas, J., Wilson, R. D., and Alman, D., "Limits on Aspect Ratio in Two-Fluid Micro-Scale Heat Exchangers," in *in press*, 2000.
- Paul, B. K. and Peterson, R. B., "Microlamination for Microtechnology-based Energy, Chemical, and Biological System," presented at ASME IMECE, Nashville, Tennessee, 1999.
- Peterson, R. B., "Small Package," in *Mechanical Engineering*, vol. June 2001, 2001.
- Popov, E. P., *Engineering mechanics of solids*. Upper Saddle River, N.J.: Prentice Hall, 1999.
- Shah, R. K. and London, A. L., "Effects of Nonuniform Passages on Compact Heat Exchanger Performance," *Transactions of ASME: Journal of Engineering for Power*, vol. 102, pp. 653-659, 1980.
- Shames, I. H., *Introduction to solid mechanics*. Englewood Cliffs, NJ: Prentice-Hall, 1989.
- Thomas, J. "Establishing Thermally Enhanced Edge Registration (TEER) as a Feasible Alignment Technique for Metallic Laminated Devices." *M.S. Thesis*, Industrial Engineering: Oregon State University, 2001.
- Timoshenko, S., *Theory of Elastic Stability*. New York, Toronto, London: McGraw-HILL Book Company, 1961.

CHAPTER 3

USE OF BUCKLING THEORY TO PREDICT BONDING FIXTURE TOLERANCES FOR HIGH-TEMPERATURE MICROLAMINATION

3.1 Abstract

Microtechnology-based Energy and Chemical Systems (MECS) devices are produced through the patterning and bonding of thin material sheets or laminae. Thermally-Enhanced Edge Registration (TEER) is a technique that is implemented to enable high precision alignment for the high temperature bonding of MECS devices. Shape variation due to misalignment or fin buckling during the TEER registration step can be encountered, which can lead to lower system performance or even functional failure. This research investigates tolerance limits allowable in a TEER fixture. A high-temperature buckling model is developed in order to predict the tolerance limits in a TEER fixture. Knowing the tolerance limits is necessary to minimize fin buckling and to attain precise alignment for MECS device produced by the microlamination procedure. This paper shows that within the tolerance limits, micron-scale channel-to-channel alignment can be achieved within monolithic MECS devices free of fin buckling. In addition, the relationship between the critical point of buckling and the device configuration is discussed so that the verification of fin buckling theory can be applied to different dimensions of device geometry.

3.2 Introduction

Microlamination is a process for fabricating a monolithic structure from thin layers of material, called laminae. This process is used to produce MECS

devices in which the embedded features are in the meso-scale range from 25 to 200 micrometers. Microlamination involves the patterning, registration and bonding of laminae to produce a monolithic structure. Figure 3-1 shows the lamination scheme for fabricating a dual microchannel array, which could be used as a heat exchanger in MECS applications.

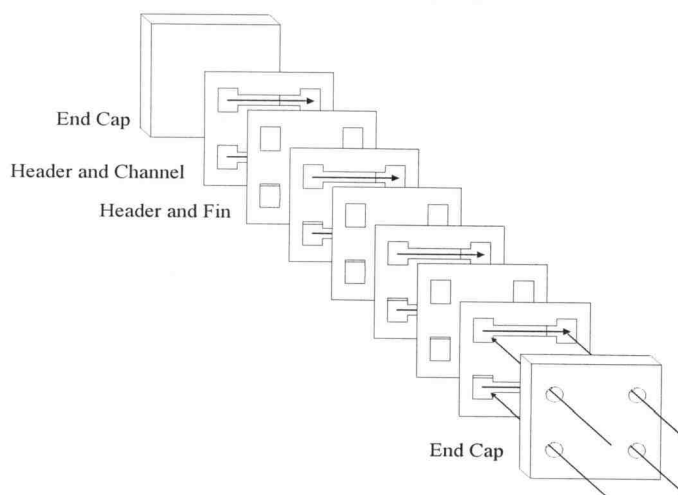


Figure 3-1. Microlamination scheme used to fabricate a dual microchannel array (arrows show direction of flow)

Microlamination techniques have been used to fabricate MECS devices for advanced climate control (Martin, et al., 1995), solvent separation (Matson, et al., 1997), chemical reactor (Martin, et al., 1999; Martin, et al., 2000), microcombustion (Brooks, et al., 1999), fuel processing (Tonkovich, et al., 1998; Daymo, et al., 2000), and thermal management (Drost, et al., 1997; Drost, et al., 1999; Drost, et al., 2000) among others. Several previous investigations have found that the registration and bonding step are the critical process in the microlamination (Ashley, 1997; Lohner, et al., 1999; Paul, et al., 2000; Wangwatcharakul, et al., 2001). Figure 3-2 presents the cross-section of a

microchannel device made from 100 μm thick NiAl shim (Paul, et al., 2000). This device encountered severe warpage. As can be seen, misalignment within the channel resulted in warpage within the channel.

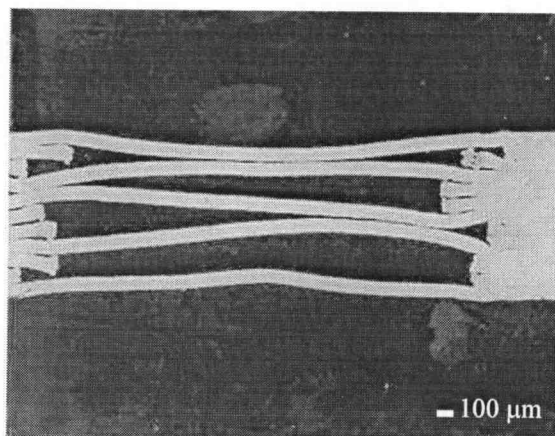


Figure 3-2. A SEM micrograph of an intermetallic microchannel device with shape variation

Microvalves are also another class of MECS unit operations that can suffer from misregistration. Figure 3-3 illustrates the cross-section of a micro-ball valve developed at Oregon State University. This multi-layered valve was developed for use in biological and microfluidic systems. The chamber is in the order of 100 μm in diameter. Laminae registration is crucial for the microvalve to perform well and have high diodicity (Wangwatcharakul, et al., 2001).

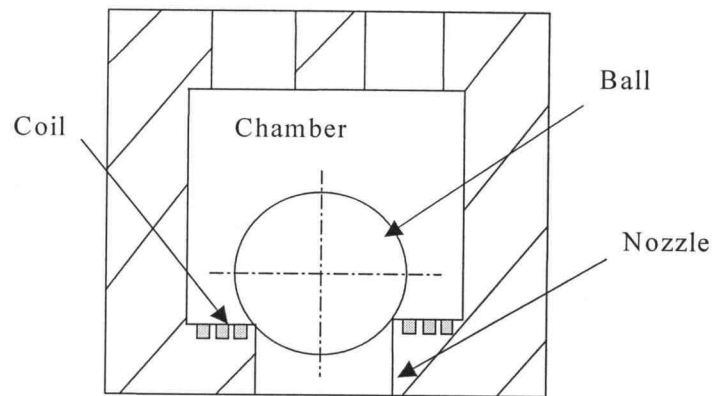


Figure 3-3. Cross-section of a micro-ball valve

Figure 3-4 presents a micro turbine generator developed by MIT. The fabrication of this device involves lamination of multiple layers of single crystal silicon to produce a turbine rotor and combustion chamber for the generator unit (Lohner, et al., 1999). The bearing gap of this turbine is on the order of $10\ \mu\text{m}$, precision alignment during lamination is critical to fabricating this device (Ashley, 1997).

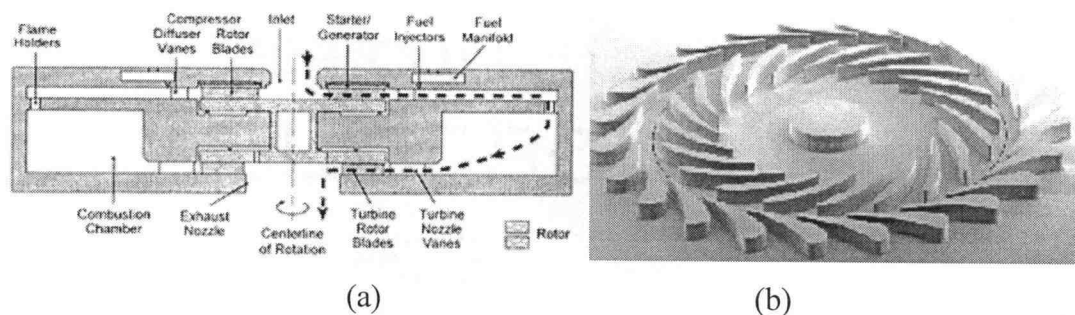


Figure 3-4. (a) Micro gas turbine generator cross-section, (b) silicon turbine wheel

In microlamination, several registration techniques have been employed including pin, edge, and self-alignment. The technique used depends on the bonding process chosen. As mentioned previously, alignment techniques are used to properly register layers of patterned shims prior to the bonding step. Aligning can be achieved mechanically through the use of pin or edge registration within a bonding fixture. The registration technique applied in this study is thermally-enhanced edge registration or TEER, developed at Oregon State University (Thomas, 2001). This technique can be used to register laminae during the high temperature diffusion bonding of polycrystalline metals and employs the difference in CTE between the bonding fixture and the laminated material to produce a registration force on the laminae at the bonding temperature. By making the bonding fixture from a material that has a lower CTE than the laminae, a clearance will exist between the tooling and the laminae at room temperature, which will make the loading of laminae easier than for other mechanical alignment methods. The benefits of TEER include high precision alignment, time and cost savings, because a larger number of laminae can be automatically registered in the fixture without the requirement of any specific aligning tool. At the same time, TEER is able to achieve an accuracy as small as 5 microns after bonding (Thomas, 2001).

During diffusion bonding, the metal laminae and the bonding fixture are heated up to a specific temperature, normally about 75% of the melting temperature of the base material. For metallic structures, this temperature can be as high as 1000 °C or higher. As the temperature is raised to the bonding temperature, the fixture and laminae will expand with respect to their CTE; then the difference in CTE between them will generate the registration force on the laminae. However, if this registration force is higher than the critical buckling load of the microchannel fin, buckling of the fin will occur. This is illustrated in Figure 3-5. When buckling develops, flow channels that are separated by the buckled fin are no longer uniform. Figure 3-6 shows nonuniform microchannels produced as a result of fin buckling.

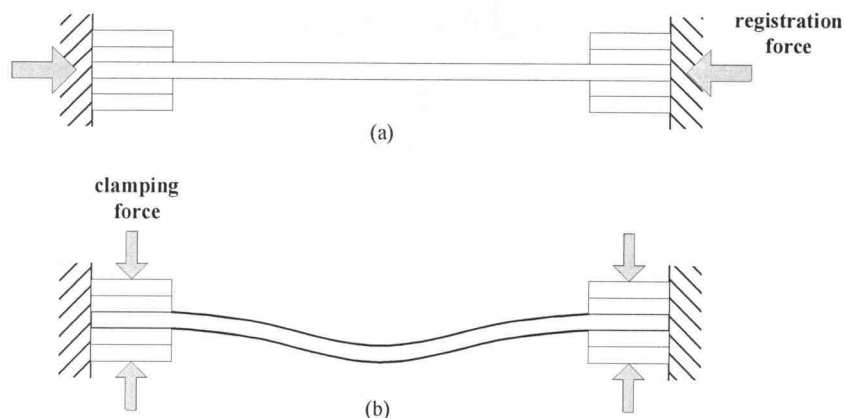


Figure 3-5. Schematic of fin buckling due to excess registration force

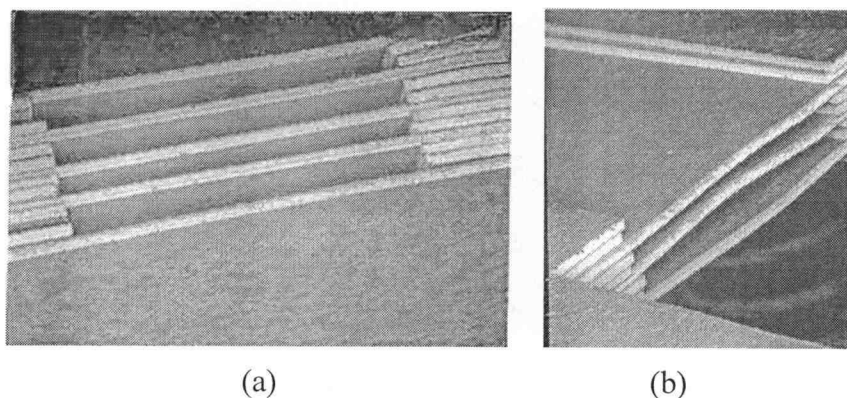


Figure 3-6. SEM micrographs of a microchannel heat exchanger with nonuniform flow channels (a) before and (b) after fin buckling

Figure 3-7 illustrates the result from the previous investigation conducted by Thomas (2001) on the TEER technique for microlamination. The graph shows the relationship between the allowance of the bonding fixture and laminae versus the amount of misalignment. This picture suggests that there is an interval of allowance between laminae and the bonding fixture, where the misalignment, typically remains constant. However, it was observed that once interference is

established the accuracy of registration is not improved any further. On the other hand, if this interference extends beyond a certain point, the fin will buckle. This indicates that interference should remain within a particular range. This range should constrain the allowable tolerance of the fixture, governed by the desired registration accuracy and the buckling of the laminae.

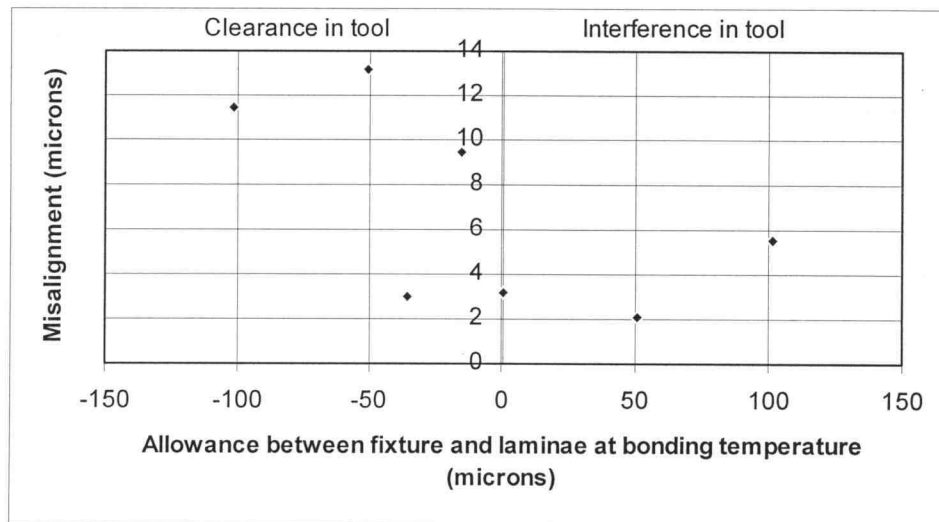


Figure 3-7. Graph of misalignment versus allowance between fixture and laminae at bonding temperature

The goal for this study is to predict the tolerance limits of TEER fixtures based on buckling theory and registration behavior. As a result, this study will improve the manufacturability of MECS devices through improved registration without fin buckling in high-temperature microlamination.

3.3 Theoretical Models

The following section provides an analysis of the buckling behavior of laminae during TEER. The schematic which illustrates the nonuniformity due to fin buckling is presented in Figure 3-8.

During the development of predictive model, the following assumptions were made as a part of the buckling evaluation.

- Before the load is applied, fin layer is perfectly straight.
- The buckling force is uniformly applied to the fin along the axis.
- The cross-section and the moment of inertia of the fin are assumed to be constant, thereby the fin buckling can be treated as a column buckling.
- Fin material is assumed to be linearly elastic and the elastic limit is constant for every fin sample.
- The scope of investigation in fin buckling is still under small deflection conditions.
- With the clamping force applied to both ends of the fin layer, the mode shape of fin buckling is derived from fixed-ended support condition.
- The bonding fixture is assumed to have a perfect rigidity when the placement of the sample is at the bottom level.

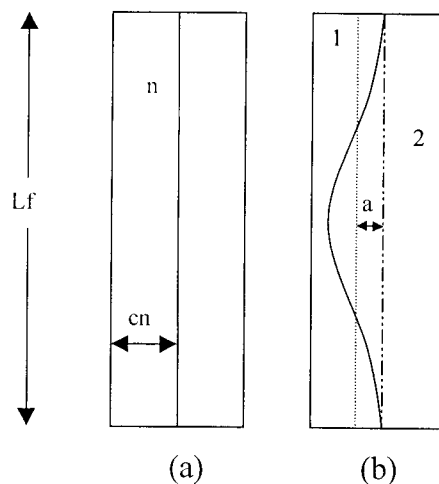


Figure 3-8. Geometry of (a) uniform flow channels, (b) nonuniform fin buckling

3.3.1 Fin Buckling Analysis

According to London (1970) and Mondt (1977), the calculation of the deviation of the flow channels (δ_c) due to fin buckling is $\delta_c = \frac{a}{cn}$, where a in Figure 3-9 (b) is the distance from the original position of the fin before buckling to the average position of the fin after buckling. The support boundary condition for the bonding step using the TEER process is a fixed-ended, as shown in Figure 3-6. With respect to this support condition, “ a ” will be half the distance between the original position and the peak of the deflection (London, 1970; Mondt, 1977). This distance can be used to calculate the impact on heat exchanger effectiveness as discussed in Chapter 2.

To determine if a fin will buckle, the mode of failure needs to be confirmed by calculating the critical buckling stress. If this critical stress is smaller than the yield stress of the fin material, the fin will yield in compression before it buckles (Gere, et al., 1997). For the fixed-ended boundary condition, the critical buckling

stress can be calculated from:

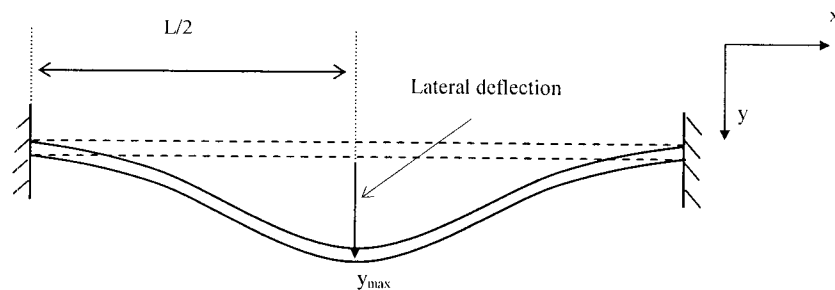
$$\sigma_c = \frac{P_c}{A} = \frac{4 \cdot \pi^2 \cdot E \cdot I}{A \cdot L^2} \quad (1)$$


Figure 3-9. Column buckling behavior for fixed-ended boundary condition

The second consideration is the force due to thermal expansion (P_t). As long as P_t is larger than the critical buckling load (P_c), the fin layer will buckle. The force due to the difference in CTE can be calculated from:

$$P_t = A \cdot E \cdot (\alpha_1 - \alpha_2) \cdot \Delta T \quad (2)$$

In this investigation, α_1 is the CTE of stainless steel and α_2 is the CTE of graphite, while ΔT is the different between room temperature and process temperature.

As the thermal stress caused by the temperature changes exceeds both P_c and the elastic limit of the base material, the fin will be permanently buckled. When permanent buckling happens, the geometry of the buckling deflection is used to evaluate the variation in flow passage and ultimately the impact on device performance. The deflection function of a fundamental mode of buckling is described by:

$$y = A_{mp} \cdot \left(1 - \cos\left(\frac{2 \cdot \pi \cdot x}{L}\right) \right) \quad (3)$$

The maximum deflection caused by fin buckling can be calculated from the amplitude (A_{mp}) of the buckling deflection function. The arc length formula is applied to solve for the amount of buckling amplitude as a function of the fin width and the fixture slot at the elevated temperature. The arc length equation is:

$$L1 = \int_0^{L/2} \sqrt{1 + \left(\frac{dy}{dx}\right)^2} dx \quad (4)$$

The fin deflection function from equation (3) will be substituted into the equation (4) to solve for the amplitude. However, since the buckling form of the substituted equation does not have a closed-form anti-derivation, an approximation method is applied to solve the equation. In this study, two approximation techniques have been implemented and compared. The first approximation technique used was the Simpson approximation, where the arc length is estimated from the length of subsection, and amplitude is substituted by trial and error (Stewart, 1995). The second approximation technique applies the equation:

$$L1 = \int_0^{L2} \sqrt{1 + \left(\frac{dy}{dx}\right)^2} dx \approx \int_0^{L2} \left\{ 1 + \frac{\left(\frac{dy}{dx}\right)^2}{2} \right\} dx \quad (5)$$

Both approximation techniques found the calculated amplitude to be within 1% of each other; therefore, the second approximation method was applied to evaluate the amplitude in this study because with equation (5) the amplitude could be calculated directly from the equation without trial and error. The details of these calculations and more description on both approximation techniques are presented in Appendices E and F.

When substitute the mode shape of fin buckling from equation (3) into

equation (5), we gets $L1 = L2 + \frac{\pi^2 \cdot A_{mp}^2}{L2}$, so the final maximum deflection ($2 \cdot A_{mp}$)

is:

$$D_{\max} = \frac{2}{\pi} \cdot \sqrt{L2 \cdot (L1 - L2)} \text{ or } \frac{2}{\pi} \cdot \sqrt{L2 \cdot Inf} \quad (6)$$

where $L2$ is the width of the fixture slot at the bonding temperature and $L1 - L2$ is the amount of the interference between the laminae and the fixture at the bonding temperature, Inf .

3.3.2 The Relationship between Fin Stiffness and the Critical Point of Buckling

In this section, the relation of fin thickness and stiffness to the critical load and the critical interference is derived to indicate the limitation of allowance where the fin buckling can be avoided during laminae bonding. In this case, the stiffness, K , which refers to the ability of the structure to resist changes in shape (Gere, et al., 1997), is the load applied per unit of deformation, or $K = \frac{P_c}{\delta}$. (7)

The term ' P_c ' represents the buckling load due to thermal expansion during the diffusion bonding cycle, and ' δ ' is a change in length of the lamina or laminae.

Since this δ can be written as:

$$\delta = \frac{P_c L}{AE} \quad (8)$$

then the stiffness equation becomes

$$K = \frac{AE}{L} = \frac{L_{ch} \cdot t \cdot E}{L_f} \quad (9)$$

Assuming a constant material, stiffness is directly proportional to the thickness (t) and fin length (L_{ch}), but inversely proportional to the width of the fin (L_f). When any of these variables change in value, the fin stiffness will be changed with respect to the amount of that dimensional change(s).

To determine the limit of the interference where buckling does not exist in the bonding geometry, we start with the force due to thermal expansion which must be lower or equal to the critical load of buckling, P_c .

The force due to the thermal expansion is $P_t = A_f * E * (\alpha_{ss} - \alpha_g) * \Delta T_{eff}$ (10)

where ΔT_{eff} is equal to the change in temperature once the laminae touch the fixture. The force that is required to cause the fin to buckle is

$$P_c = \frac{4 * \pi^2 * E * I}{L_s^2} \quad (11)$$

By definition $\Delta T_{eff} = \Delta T - \Delta T'$, where ΔT is the change in temperature from room temperature to the bonding temperature, and $\Delta T'$ is the change in temperature from room temperature to the point where the laminae touch the fixture, which can be

calculated from:

$$\Delta T' = \left(\frac{L_s - L_f}{\alpha_{ss} * L_f - \alpha_g * L_s} \right) \quad (12)$$

Substituting equation (11) into equation (10): $\Delta T_{eff} = \frac{P_c}{A_f * E * (\alpha_{ss} - \alpha_g)}$ (13)

If the critical load of buckling is less than the elastic limit, the buckling limit

becomes constrained by $P_p = \sigma_p * A_f$ (14)

Substituting equation (14) into equation (10): $\Delta T_{eff} = \frac{\sigma_p}{E * (\alpha_{ss} - \alpha_g)}$ (15)

As we know ΔT_{eff} either from equation (13) or (15), we can solve for the fin width and the fin stiffness from equation (12) and (9), respectively.

To evaluate the fin stiffness in terms of the interference between the laminae and the bonding fixture, Inf , the following equation is implemented:

$$Inf = L'_f - L'_s = L_f \cdot (1 + \alpha_{ss} \Delta T) - L_s \cdot (1 + \alpha_g \Delta T) \quad (16)$$

Figure 3-20 illustrates the relationship of the fin stiffness and thickness to the critical load that fin buckling can be avoided in the test specimen. According to this graph, if the elastic limit is larger than the critical buckling load up to the stiffness of $2 \times 10^7 \text{ kg/s}^2$, or at the thickness of 0.11 mm, then the critical buckling load is dominate over the buckling consideration. As a result, the interference limit in which the fin buckling will be formed in the device, based on the result in Figure 3-10, is presented in Figure 3-11.

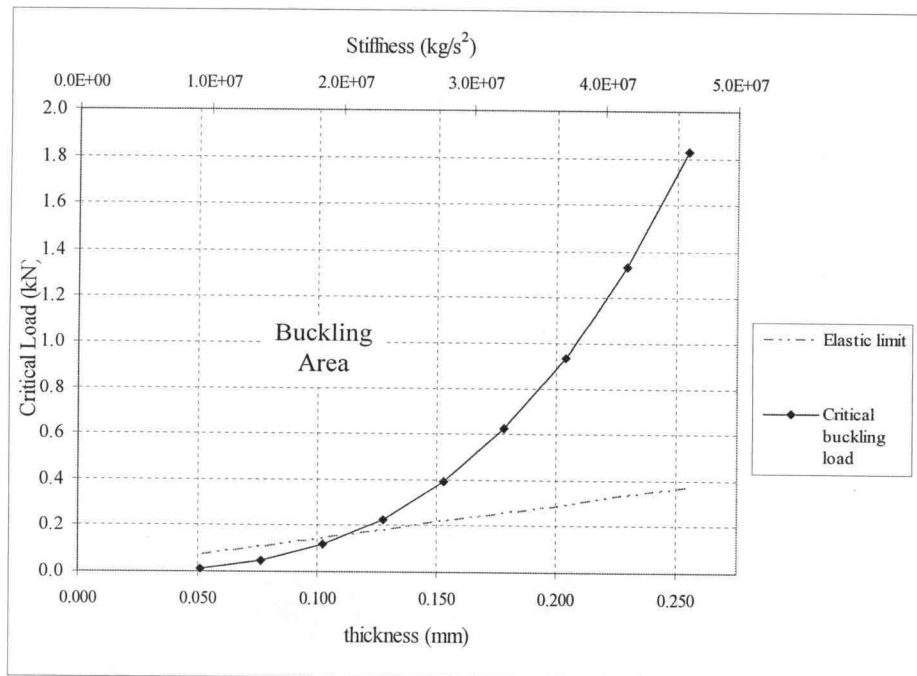


Figure 3-10. Relationship between fin stiffness or thickness and the critical load

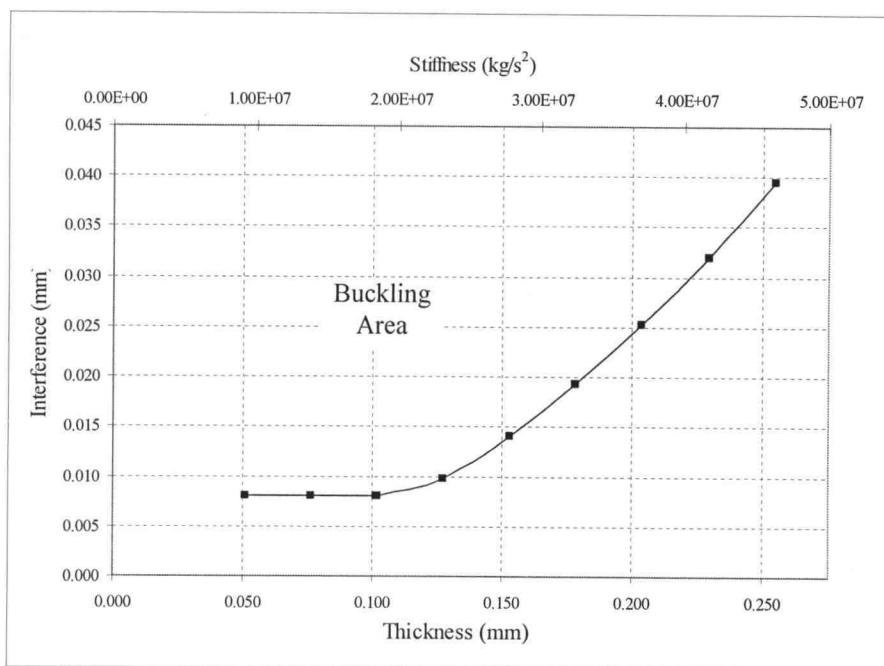


Figure 3-11. Relationship between fin stiffness or thickness and the allowable fin-fixture interference at the critical point of buckling

The model in this figure can be used to evaluate the tolerance limits of the bonding fixture to avoid fin buckling for different stiffness of fin layers. This relation also shows that as a fin layer becomes stiffer, it is unlikely that buckling exists in the structure because the interference limit in the stiffer fin is allowed to be greater.

Physical and thermal properties of the ISO-63 graphite and 304 stainless steel used in this experiment can be found in reference: (Chavez, et al., 1994; Toyo Tanso USA, Inc., 2002; The Online Materials Information Resource, 2002) and additional information of graphite and stainless steel are also referred from (ALSC, 1956; ASTM, 1965; Mantell, 1968; ASTM, 1969; ASM, 1976)

3.4 Experimental

The test specimen used in this experiment consisted of two-channel layers and a fin layer, as shown on Figure 3-12. All layers were made from a 304 stainless steel shim. A Nd:YAG laser operating at the fourth harmonic (266 nm) was used to pattern the shims of three different thicknesses (0.0508 mm, 0.0762 mm and 0.1016 mm). The hashed area in this picture represents the area that might encounter buckling if the force caused by difference in CTE between the laminae and the fixture exceeds the elastic limit. Figure 3-13 represents the loading of test coupons onto the TEER fixture. The amount of clearance between the laminae and the TEER fixture at room temperature can be seen in the difference between the width of specimen and the fixture slot. This permits easy loading of the laminae.

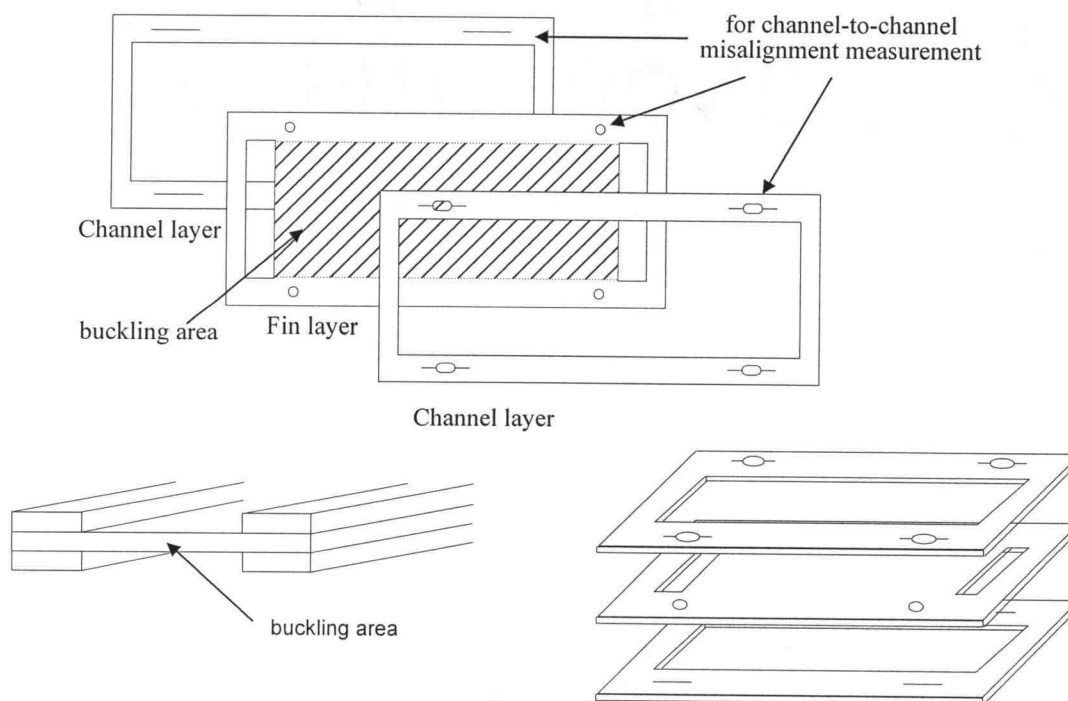


Figure 3-12. Geometry of the test specimen for the experiment

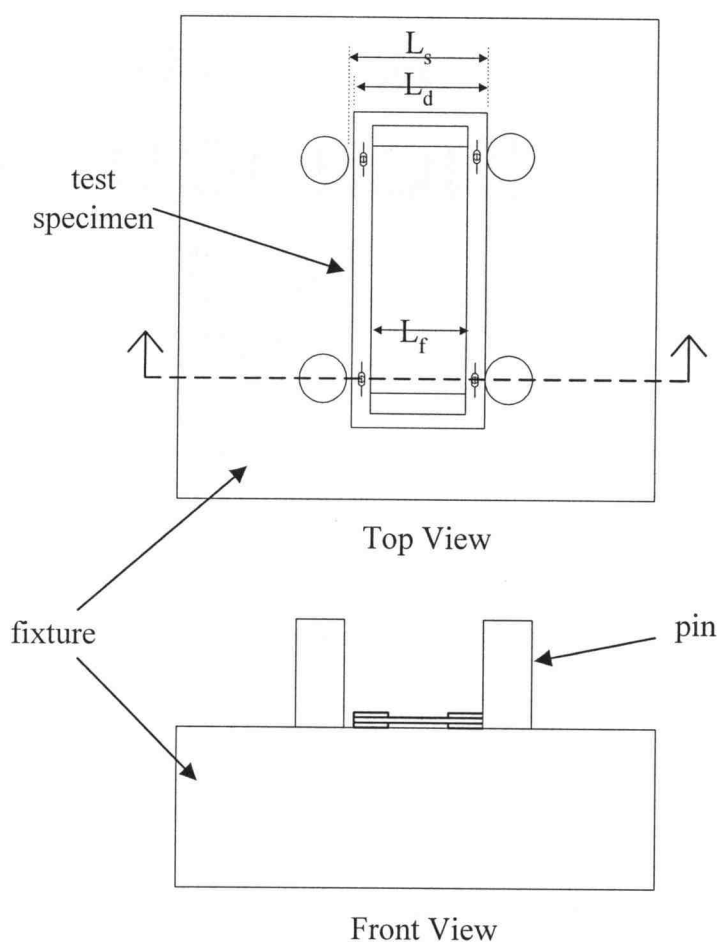


Figure 3-13. Loading of the test specimen laminae onto the TEER fixture

After patterning, all laminae were polished with an ultra fine 3M Scotch-Brite hand pad and cleaned with a 50% concentration of Citranox in an ultrasonic cleaner for 20 minutes to remove slag and ejecta which resulted from the laser machining process. Next, the fin lamina was measured by a Dektak3 surface profiler to record the initial flatness characteristics. This profiler is capable of making vertical measurements up to 2 mm with a 1 nm, standard deviation for step height repeatability. A 12.5- μm diamond-tipped stylus was used to perform surface topography measurements. Flatness measurements were taken at four locations for

each fin specimen: from the left end to the right end. Before bonding, all laminae were rinsed with Acetone, Ethanol, and De-ionized water (AED) to remove grease or any other residues on the surfaces so that a sound diffusion-bonded joint could be formed.

The fixture assembly was then put in a vacuum hot press chamber, and the bonding cycle began. The first step in the bonding process involved pumping down the chamber to achieve a satisfactory vacuum (approximately 10^{-4} mbar). This level was achieved by using both a mechanical pump for rough pumping, and a diffusion pump for high vacuum pumping. The system was then heated up to the appropriate bonding temperature. Once the bonding temperature was reached, clamping pressure was applied to the fixture to induce the diffusion bond. At the end of the bonding phase, the clamping pressure was removed so that the laminate could contract uniformly without inducing residual stress. The bonding conditions for this experiment were set up at 750 °C with 5 MPa applied pressure and a one hour dwell period.

After the system cooled down, the laminate was taken out to check for possible characteristics of fin deflection using the Dektak3 surface profiler. Similar to the initial flatness measurements, warpage measurements were also taken at four points from left to right for the post-bonding characterization. The average deflection and standard deviation of each sample were calculated and were used for theoretical comparisons.

The allowance between fin width and the fixture slot was varied in order to evaluate the relationship between the fixture allowance and both types of shape variation. Fins with thicknesses ranging from 0.0508 mm to 0.1016 mm were used in this study. In general, the critical point of buckling is proportional to the thickness of the fin layer, as derived in equation (1). The thicker the material, the greater the strength and the greater amount of interference needed before the fin starts buckling. However, this critical buckling load also needs to exceed the proportional limit of yield strength (or elastic property) to cause the fin to be

permanently deformed after bonding. For laminae with thicknesses below 0.1016 mm, the load at the proportional limit is found greater than the critical point of buckling; therefore, all specimens in this experiment should have the same buckling behavior, as shown in Figures 3-10 and 3-11.

The first experimental set up was designed to evaluate the effect of fin thickness on the buckling behavior of the fin. Since the buckling behavior of all fins in this experiment was supposed to be the same, each thickness was only tried at each 2 allowances. The significance of the thickness was checked using an analysis of variance (ANOVA). An additional test was performed to evaluate the difference between the theoretical and the experimental results. A paired t-test was used to verify this comparison based on the null hypothesis that the mean of the difference in theoretical data and experimental results is zero with alpha equal to 0.05. If both theoretical and experimental results are equal, a 95% confidence interval for the mean difference must include zero.

To assess channel misalignment, a technique for measuring channel-to-channel misregistration was developed by modifying a technique from a prior investigation (Thomas, 2001). By generating a line marker on the *bottom channel layer*, a reference line and window on the *top channel*, and only a window on the *fin layer*, channel-to-channel misalignment can be evaluated. The distance between the two lines is the measure of this misalignment, as illustrated in Figure 3-14.

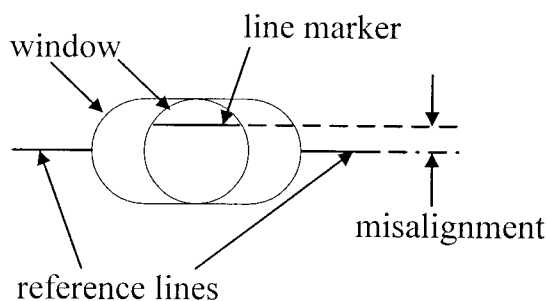


Figure 3-14. Measuring misalignment at a window with a line marker

The measurement of channel-to-channel misalignment was performed at 200X on a LEICA DML optical microscope with a video measurement system (VIA-100) and submicron resolution. This microscopy technique has provided reliable results which are statistically comparable to using a scanning electron microscope (Thomas, 2001). Reproducibility of the measurements was also evaluated by comparing the measurement results from two different inspectors and using an ANOVA to analyze the significance of the factor. Additional information about the measuring techniques implemented in this study can be found in Appendix H.

For misalignment analysis, a test was designed so to evaluate main effects such as fin thickness and allowance on the amount of misalignment. This evaluation was analyzed by a multifactor ANOVA (Type III Sums of Squares) under the condition that the p-value for a significant factor must be smaller than 0.05.

Before any experiments were run, a number of preliminary tests were conducted to calibrate the high temperature dimensions of the test fixture. The most important feature of the test fixture to be determined was the slot width at elevated temperature. A variety of test coupons with different width span were tested on the bonding fixture to identify where interference started relative to the expansion of both stainless steel and the graphite fixture. A number of runs were conducted at the same specimen dimensions to assess the repeatability of the experiments and the consistency of test results. It was found that the test fixture used in this experiment caused buckling in stainless steel laminae beyond 14.81 mm in width (at room temperature), as verified by measurement with Dektak3 surface profiler.

3.5 Results and Discussion

Upon variation of fixture allowance, the laminae and fixture are either over-constrained or under-constrained. Buckling was found when the laminae were over-constrained. In this case, the width of laminae was longer than the slot size at the diffusion temperature. The mechanism of this fin buckling occurs when the force, due to the difference in CTE between the stainless steel laminae and the graphite fixture, exceeds the critical point of buckling and elastic limit. The magnitude of fin buckling at different amounts of interference can be calculated from equation (5).

On the other hand, when the device was under-constrained, the width of laminae was shorter than the slot size at the bonding temperature, resulting in channel misalignment. The maximum misalignment was evaluated by looking at the actual clearance between fin width and slot size at the bonding temperature.

3.5.1 The Relation between Fixture Allowance and Fin Buckling

Figure 3-15 illustrates the magnitude of maximum deflection of warpage due to fin buckling with respect to the fixture allowance at the diffusion temperature from both theoretical prediction and experimental data. As can be seen from the graph, buckling begins for all three fin thickness at 10 μm of interference. The magnitude of warpage also increases as the interference increases. According to the ANOVA, it was concluded that there is no statistical evidence that the magnitude of warpage depends on the thickness of the shim under the scope of this experiment (p -value = 0.50). Furthermore, there was conclusive evidence that the mean warpage from the experimental data and the theoretical result were equal (t -stat = 1.42, df = 8). Its 95% confidence interval ranged from -0.01 to 0.05, which includes zero. Additional information on statistical evaluation can be found in Appendix M.

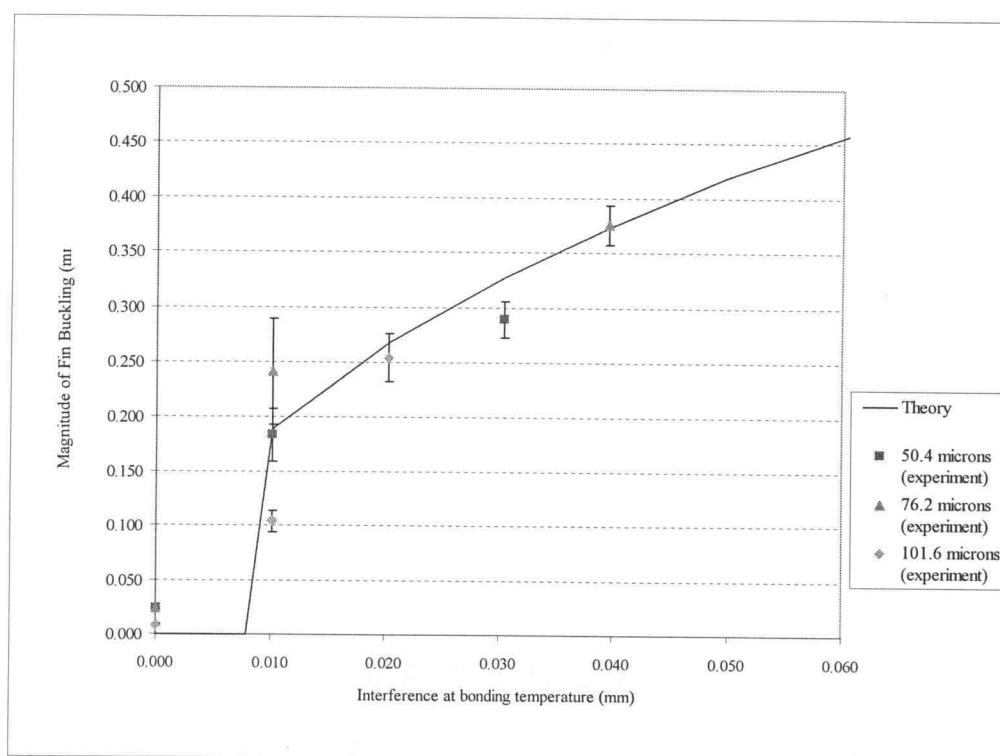


Figure 3-15. Magnitude of fin buckling versus the interference between fixture and laminae at bonding temperature with 95% confidence interval of standard deviation

The error bars shown in Figure 3-15 are 95% confidence interval of the measured warpage. Each side of the interval is equal to $2 \cdot S_m$, where S_m is the standard error calculated from the variation of the warpage measurement at 4 locations. As can be seen from the graph, there are some variations of experimental results from the theory. Sources of error for this experiment might include the deviation of fin width from the patterning step either due to variation of beam diameter or the residual ejecta. Although the accuracy of laser micromachining is down to the scale of a few microns, this variation could lead to the deviation in warpage magnitude. Furthermore, the materials that were used in this experiment are thin shims which might contain residual stress from a cold work processing that could play a key role in this variation. Figure 3-16 presents deflection

characteristics of a 0.0508-mm thick fin before and after buckling at 10- μm interference. Notice that the fin already contained some amount of deflection prior to the experiment as shown on Figure 3-16 (a). This amount of pre-warpage was removed from the post bonding warpage prior to plotting Figure 3-15. This pre-warpage might also have reduced the magnitude of the critical load for buckling causing additional deviations from theoretical.

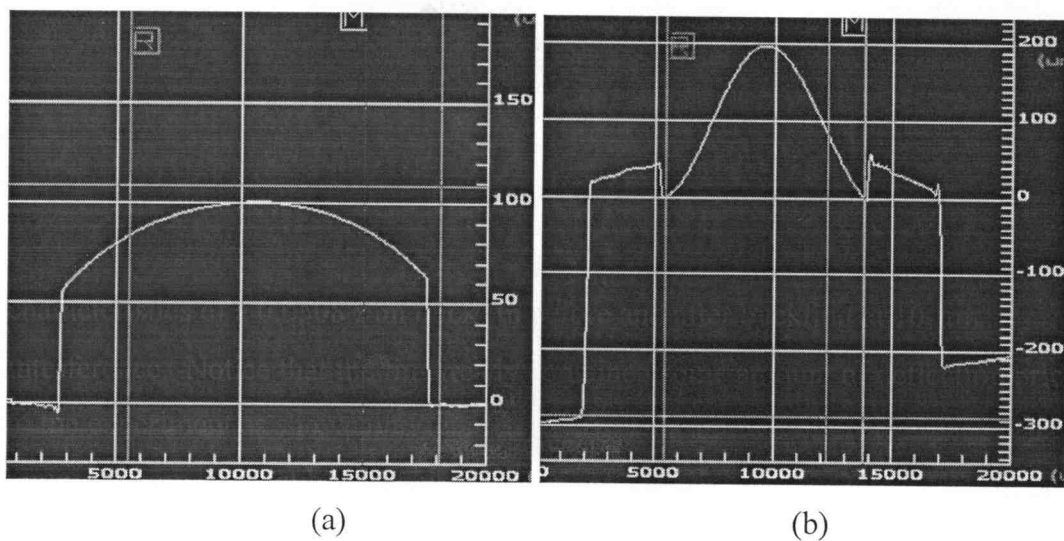


Figure 3-16. Deflection profiles of laminate (a) prior to bonding (b) after bonding measured by Dektak3 surface profiler

3.5.2 The Relation between Fixture Allowance and Channel Misalignment

Figure 3-17 displays the results for the misalignment analysis. Similar to Figure 3-15, this figure also presents the error bar based on the 95% confidence interval of the misalignment readings at 4 locations on the specimen. The test included the alignment analysis for both the under-constrained and over-constrained cases. With respect to this figure, precision alignment is achieved only

in the area close to the exact constraint. As can be seen, the average and standard deviation for misalignment increases with clearance, and it also increases as the fin begins to buckle. Therefore, tight tolerance is required in order to attain a well-aligned channel.

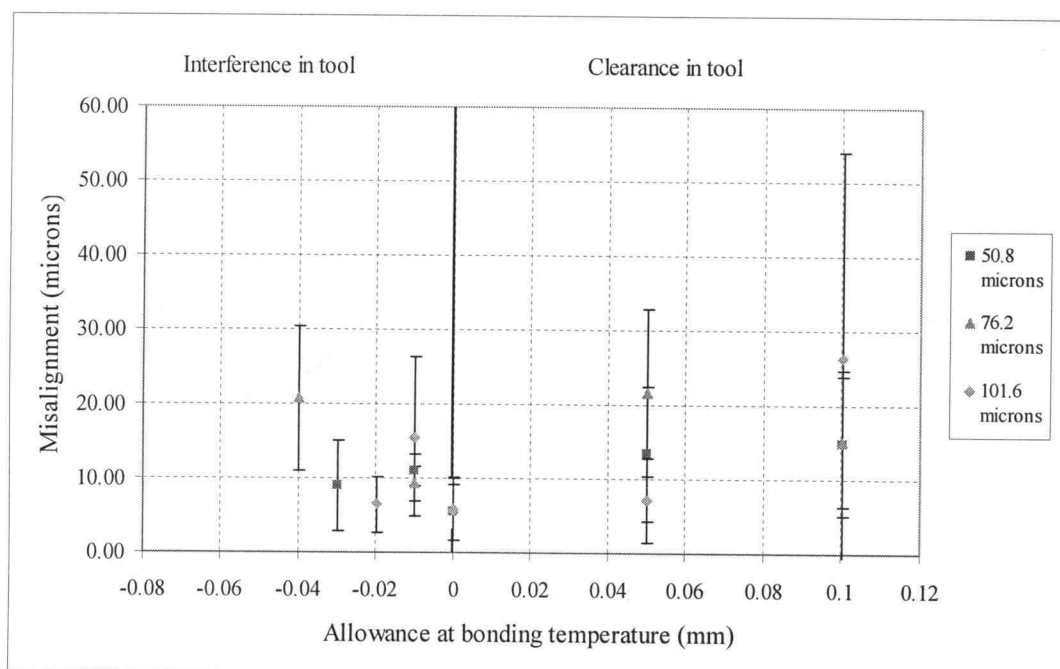


Figure 3-17. Misalignment versus allowance between fixture and laminae at bonding temperature with 95% confidence interval of standard deviation

Figure 3-18 presents two pictures taken from the specimen (a) with misalignment under $5\ \mu\text{m}$, and (b) with over $20\ \mu\text{m}$ misalignment. Table 3-1 summarizes the data collection on the misalignment at different allowances between the laminae and fixture at bonding temperature conducted by two different inspectors. Window columns depict the location where the measurement was inspected, as shown in Figure 3-19.

With respect to the ANOVA, the inspector factor was found to be not significant on misalignment (p-value = 0.9180) indicating a reproducible measurement technique. On the other hand, there is statistical evidence that misalignment depends on the allowance and window location (p-value < 0.05).

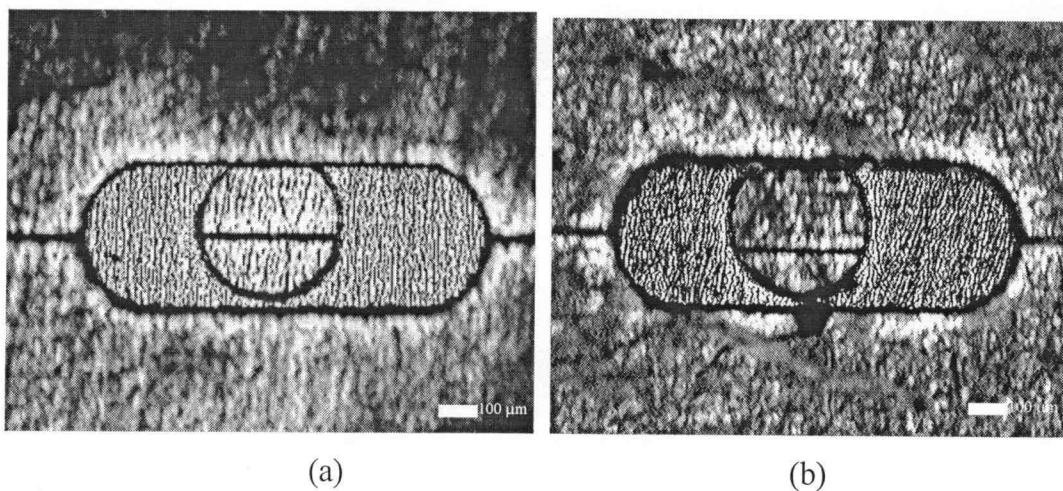


Figure 3-18. 50X Optical Microscope images of (a) good alignment, (b) misaligned microlaminated structure

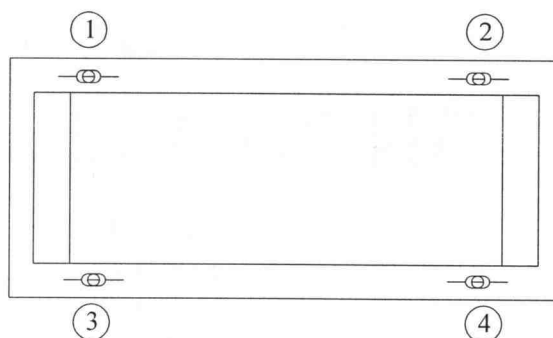


Figure 3-19. Measurement locations for misalignment analysis

Table 3-1. The average misalignment measurements at four locations

Thickness (micron)	Allowance (micron)	Window				Average Misalignment	Standard Deviation
		1	2	3	4		
50.8	0	9.70	7.10	3.72	1.25	5.44	3.71
	50	5.60	24.53	6.50	17.03	13.41	9.04
	100	5.00	28.53	12.20	13.98	14.93	9.86
	-10	11.65	11.38	13.25	8.20	11.12	2.11
	-30	4.60	8.07	5.25	17.80	8.93	6.10
76.2	0	5.85	1.60	11.80	4.45	5.93	4.30
	50	9.93	23.38	16.73	36.43	21.61	11.30
	100	6.93	21.15	8.13	24.25	15.11	8.87
	-10	6.68	9.43	12.30	8.75	9.29	2.32
	-40	15.65	26.55	9.88	30.88	20.74	9.67
101.6	0	4.82	11.83	4.35	2.13	5.78	4.20
	50	10.78	13.15	2.50	1.95	7.09	5.71
	100	2.13	50.03	2.63	50.65	26.36	27.69
	-10	9.45	30.20	17.00	5.78	15.61	10.79
	-20	2.75	7.63	11.25	4.33	6.49	3.77
Average		7.43	18.30	9.17	15.19	12.52	

According to Table 3-1, it was found that there was some variation in misalignment among all four locations. Windows 2 and 4, which represent the window on the right end of the sample, contributed the greater amount of misalignment when compared to the other two windows on the left end. This observed variation indicated that the laminae were consistently rotated around the left end and suggests that perhaps the distance between pins on the right side of the fixture was greater than the distance on the left side.

To search for some possible solutions to reduce misalignment due to laminae rotation, additional experiments were conducted with the use of adhesive tape to secure all three laminae together, as shown in Figure 3-20. Laminae have prealigned to one another and secured with tape. The results of these experiments are shown in Table 3-2.

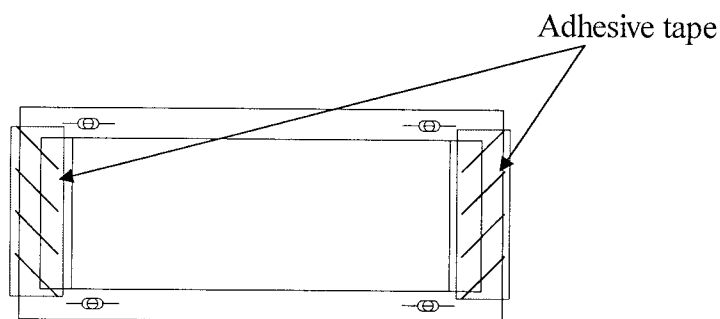


Figure 3-20. Test specimen with adhesive tape on both sides

Table 3-2. Misalignment data from additional experiments

Thickness (micron)	Allowance (micron)	Window				Average Misalignment	Standard Deviation
		1	2	3	4		
76.2	20	13.40	13.20	4.70	10.03	10.33	4.06
	50	11.83	6.00	20.15	21.80	14.94	7.39
	100	7.30	4.25	27.93	12.83	13.08	10.52
	> 100	6.20	7.55	9.85	5.73	7.33	1.85
	> 100	9.55	5.85	8.23	5.48	7.28	1.94
Average		9.66	7.37	14.17	11.17	10.59	2.85

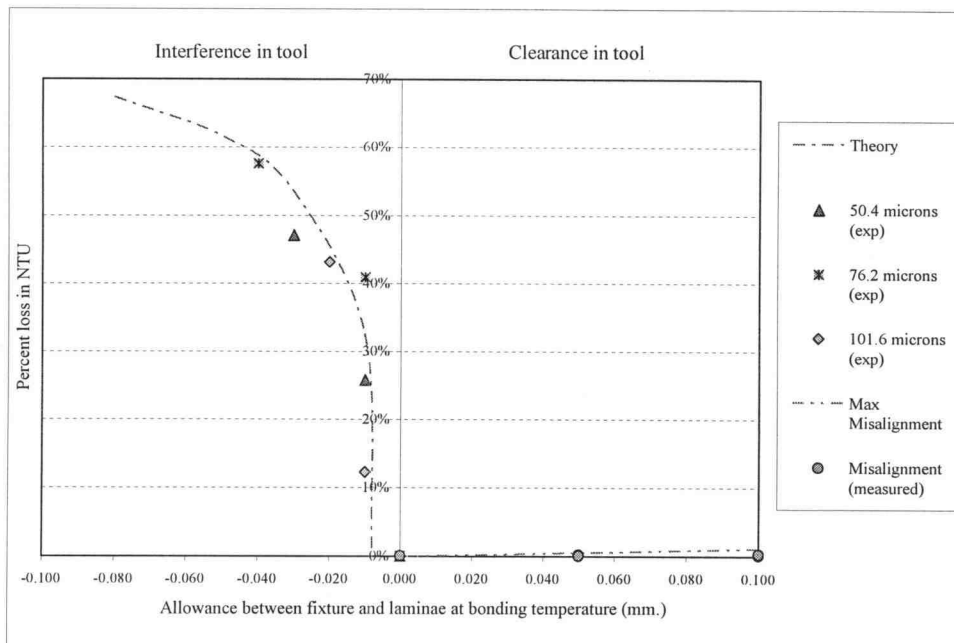
From Table 3-2, it appears that the use of adhesive tape results in a significant effect on the variation of alignment. When the three layers of laminae were wrapped with the adhesive tape, the movement was secured during bonding up to the point where the adhesive tape was burnt away. As a result, a plausible outcome of misalignment ranged from 7 to 15 μm and less variation between windows was achieved. This investigation suggests that securing the laminae before bonding may provide better results when the tolerance of the fixture is not tight. However, at this point, wrapping laminae with tape prior to bonding requires pre-alignment, which may not be economical. Further investigation should be

pursued to investigate an effective way to achieve precise and consistent pre-bonding alignment for multilayer microlamination.

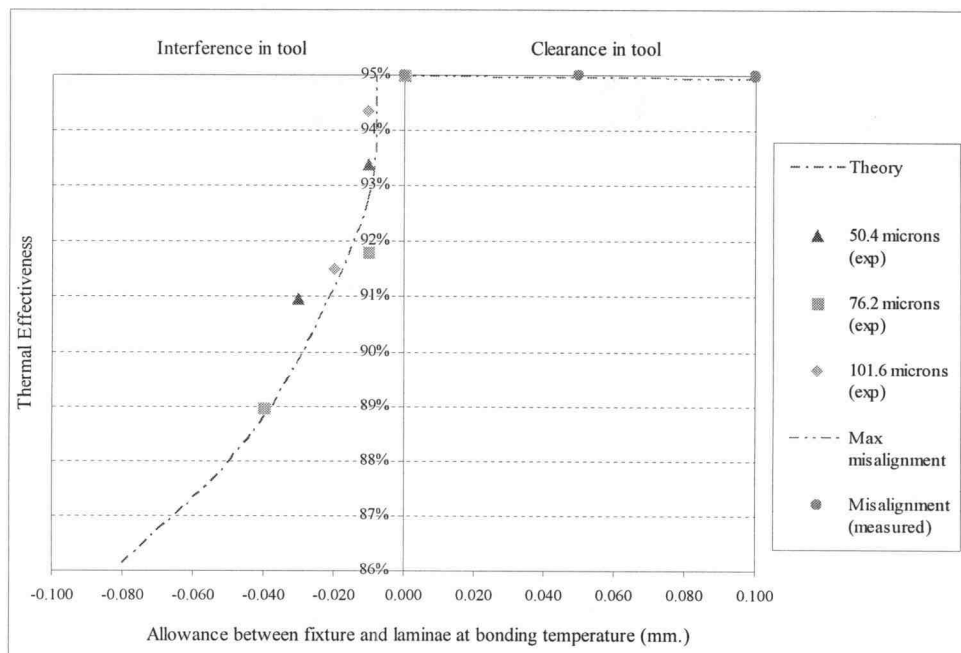
3.5.3 The Relationship of Both Fin Buckling and Channel Misalignment to Device Performance

Figure 3-21 represents the reduction in the heat exchanger performance due to both misalignment and fin warpage nonuniformity with respect to a variation in allowance between laminae and fixture at the bonding temperature, based on the same base case heat exchanger unit discussed in Chapter 2. As shown on this graph, as soon as the interference exceeded 10 μm , the reduction of NTU increased exponentially to over 30% and further to 60% when the interference reached 50 μm . In agreement with Chapter 2, fin warpage dominates the efficiency of the device. With very small interference between the laminae and the bonding fixture, warpage due to buckling is generated and results in a high reduction of NTU. Figure 3-21 (b) shows the conversion of the percent reduction in NTU into the average effectiveness of the nominal heat exchanger. See Appendix N for further information on the evaluation of this relation.

As fin buckling contributes to the penalty of thermal performance of microchannel heat exchangers, knowing the critical buckling point can help manufacturers evaluate the limitation of fin dimensions or the fixture tolerances for the TEER process. For instance, for the limitation of materials with thicknesses below 0.11 mm (such as the material for this study), the tolerance limit of the fixture needs to be smaller than 8 μm , while the limit can be increased to 40 μm as the fin thickness increases to 0.254 mm.



(a)



(b)

Figure 3-21. Effect of fin buckling on a nominal heat exchanger performance in terms of (a) percent loss in NTU, (b) thermal effectiveness at different amounts of allowance between laminae and fixture at elevated temperature

3.6 Conclusions

Microlamination of metal structures for MECS devices requires high temperature bonding. The TEER technique has been developed for precise alignment and bonding in the microlamination process. This research has been conducted to investigate the tolerance limits in a TEER bonding fixture for the purpose of minimizing the shape variation due to misregistration and fin buckling caused by excessive registration force during microlamination. Both analytical and experimental results are in good agreement within 95% confidence interval. Furthermore, it is evident that there are some tolerance limits in the TEER fixture that allows high-temperature microlamination to generate the multilayer structure with the minimal amount of shape variation. With respect to the nominal dimension specified in this study, the tolerance limit of 10 μm (interference) is where the fin starts to buckle, while the limit in misalignment is proportional to the clearance at the bonding temperature. The average channel-to-channel misalignment within this tolerance limit was about 6 μm . It was also shown that pre-alignment of the laminae may be a viable alternative to the TEER method. Finally, it was shown that the fixture tolerance has a finite fixed lower limit based on the elastic limit of the material. Therefore, as the thickness of laminae continues to decrease, the fixture tolerances will not need to continue to decrease below this lower limit.

3.7 References

- The Online Materials Information Resource. "Physical and Thermal Properties of 304 Stainless Steel.", 2002 Available: www.matweb.com.
- Toyo Tanso USA, Inc. "Physical and Thermal Properties of Graphite.", 2002 Available: www.ttu.com.
- ALSC, *Stainless Steel Handbook*. Pittsburgh, Pennsylvania: Allegheny Ludlum Steel Corporation, 1956.
- Ashley, S., "Turbines on a dime," *Mechanical engineering*, vol. 119, pp. 78-81, 1997.
- ASM, *Source Book on Stainless Steels*. Metals Park, Ohio: The Periodical Publication Department, American Society for Metals, 1976.
- ASTM, "The Elevated-Temperature Properties of Stainless Steels," in *ASTM Data Series Publication DS 5 - S1*, 1965.
- ASTM, "An Evaluation of the Yield, Tensile, Creep, and Rupture Strengths of Wrought 304, 316, 321, and 347 Stainless Steels at Elevated Temperatures," in *ASTM Data Series DS 5S2*, 1969.
- Brooks, K. P., Martin, P. M., Drost, M. K., and Call, C. J., "Mesoscale Combustor/Evaporator Development," presented at ASME IMECE Conference, Nashville, TN, 1999.
- Chavez, S. A., Korth, G. E., and Harper, D. M., "High-temperature tensile and creep data for Inconel 600, 304 stainless steel and SA106B carbon steel," *Nuclear Engineering and Design*, vol. 148, pp. 351-363, 1994.
- Daymo, E. A., VanderWiel, D. P., Fitzgerald, S. P., Wang, Y., Rozmiarek, R. T., LaMont, M. J., and Tonkovich, A. L. Y., "Microchannel Fuel Processing for Man Portable Power," presented at AIChE 2000 Spring National Meeting, Atlanta, GA, 2000.
- Drost, M. K. and Friedrich, M., "Miniature Heat Pumps for Portable and Distributed Space Conditioning Applications," presented at Proceedings of IECEC, 1997.
- Drost, M. K., Friedrich, M., Martin, C., Martin, J., and Cameron, R., "Recent Developments in Microtechnology-Based Chemical Heat Pumps,"

presented at 3rd International Conference on Microreaction Technology, Frankfurt, Germany, 1999.

Drost, M. K., Wegeng, R. S., Martin, P. M., Brooks, K. P., Martin, J. L., and Call, C., "MicroHeater," presented at AIChE 2000 Spring National Meeting, Atlanta, GA, 2000.

Gere, J. M. and Timoshenko, S. P., *Mechanics of materials*. Boston: PWS-KENT Pub. Co., 1997.

Lohner, K. A., Chen, K.-S., Ayon, A. A., and Spearing, S. M., "Microfabricated Silicon Carbide Microengine Structures," *Proceeding of Material Resource Society Symposium*, vol. 546, pp. 85-90, 1999.

London, A. L., "Laminar Flow Gas Turbine Regenerators--The Influence of Manufacturing Tolerances," *Transactions of ASME: Journal of Engineering for Power*, vol. 92, pp. 46-56, 1970.

Mantell, C. L., *Carbon and Graphite Handbook*. New York: Interscience Publishers, 1968.

Martin, P. M., Bennett, W. D., and Johnson, J. W., "Microchannel heat exchangers for advanced climate control," presented at Proceedings of SPIE, 1995.

Martin, P. M., Matson, D. W., and Bennett, W. D., "Microfabrication Methods For Microchannel Reactors and Separations Systems," *Chemical Engineering Communications*, vol. 173, pp. 245-254, 1999.

Martin, P. M., Matson, D. W., Bennett, W. D., Stewart, D. C., and Bonham, C. C., "Laminated Ceramic Microfluidic Components for Microreactor Applications," presented at AiChE 2000 Spring National Meeting, Atlanta, GA, 2000.

Matson, D. W., Martin, P. M., and Bennett, W. D., "Laser micromachined microchannel solvent separator," presented at Proceedings of SPIE, 1997.

Mondt, J. R., "Effects of Nonuniform Passages on Deepfold Heat Exchanger Performance," *Transactions of ASME: Journal of Engineering for Power*, vol. 99, pp. 657-663, 1977.

Paul, B. K., Dewey, T., Alman, D., and Wilson, R. D., "Intermetallic Microlamination for High-Temperature Reactors," presented at 4th International Conference on Microreaction Technology, Atlanta, GA, 2000.

- Stewart, J., *Single Variable Calculus: Early Transcendentals*. New York: Brooks/Cole Publishing Company, 1995.
- Thomas, J. "Establishing Thermally Enhanced Edge Registration (TEER) as a Feasible Alignment Technique for Metallic Laminated Devices." *M.S. Thesis*, Industrial Engineering: Oregon State University, 2001.
- Tonkovich, A. L. Y., Zilka, J. L., Jimenez, D. M., LaMont, M. J., and Wegeng, R. S., "Microchannel Chemical Reactors for Fuel Processing," presented at AIChE 1998 Spring National Meeting, New Orleans, 1998.
- Wangwatcharakul, W. and Paul, B. K., "Development of Passive Micro-ball valve," in *in press*, 2001.

CHAPTER 4

USE OF COMPLIANCE IN HIGH-VOLUME METAL MICROLAMINATION TO REDUCE SHAPE VARIATION DUE TO FIN BUCKLING

4.1 Abstract

Microtechnology-based energy and chemical systems (MECS) is a new generation of devices with critical feature sizes in the meso-scale on the order of tens to hundreds of micrometers. MECS devices generally deal decreasing the length-scale of energy, chemical, and biological systems through the improved heat and mass transfer found in high surface area-to-volume ratio microchannels. The benefits of this miniaturization are the ability to decentralize and make portable otherwise centralized systems such as heat pumps, waste processing and hydrogen separation for fuel cells. MECS devices are fabricated using microlamination techniques involving three steps: laminae patterning, registration, and bonding. Microchannels are formed between alternating fin layers. A Thermally-Enhanced Edge Registration (TEER) technique has been developed for precision aligning large numbers of laminae in diffusion bonding processes. By implementing the difference in thermal expansion between a graphite fixture and the metallic laminae, high temperature registration for all layers can be achieved. Furthermore, with a clearance at room temperature, this technique permits easy loading. However, fixture tolerances necessary to promote buckle-free TEER bonding have been found to be very small (below 10 μm). This research focuses on the development of a new approach based on fixture compliance to improve the robustness of the TEER method. An analysis based on both fin buckling behavior and the compliance of the fixture is implemented to investigate the tolerance limit of a compliant TEER fixture. Experiments are conducted to verify the theoretical

model. Results show that a compliant fixture can yield a plausible tolerance limit in TEER.

4.2 Introduction

The miniaturization of energy, chemical and biological systems for distributed and portable applications is realized by the enhancement in heat and mass transfer performance with high surface-to-volume ratio microchannels. Some MECS applications include: microelectronic cooling systems (Kawano, et al., 1998), chemical reactors (Martin, et al., 1999; Martin, et al., 1999; Matson, et al., 1999), fuel processing (Tonkovich, et al., 1998; Daymo, et al., 2000), and heat pumps (Drost, et al., 1997; Drost, et al., 2000). Most of these devices include unit operations such as microchannel arrays, fluid mixers, micropumps, microvalves, and reaction chambers. In all, multi-scale thermal and fluid systems have been constructed in a wide array of materials including copper, stainless steel, intermetallic and various polymers with embedded features as small as tens of micrometers.

Microlamination is the patterning and bonding of thin layers of material, called laminae, into a monolithic device. This process dominates the manufacturing of MECS devices in which embedded features range from 25 to 200 micrometers. Microlamination involves three steps: (1) laminae patterning, (2) laminae registration, and (3) laminae bonding to produce a monolithic device. Figure 4-1 shows the microlamination of a general-purpose microchannel array, which could be used as a heat or mass transfer application in MECS.

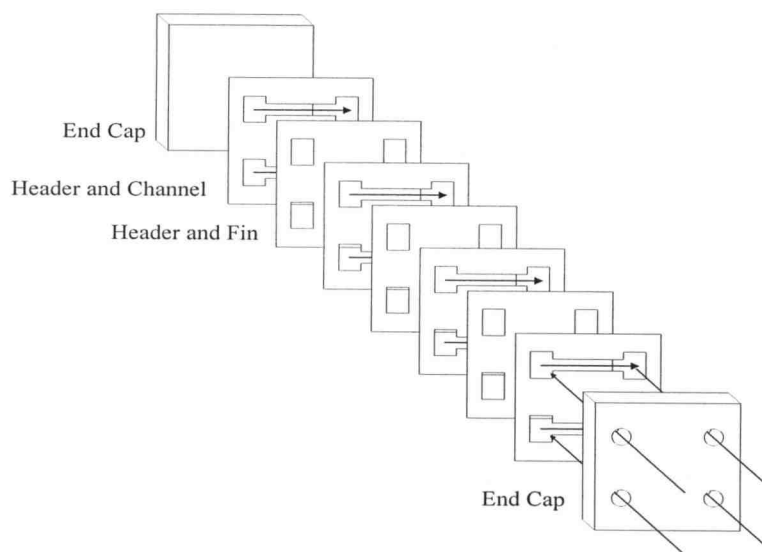


Figure 4-1. Microlamination scheme used to fabricate a dual microchannel array (arrows represent direction of flow)

One method for registering laminae is called TEER or thermally-enhanced edge registration (Thomas, 2001). This technique is used for high temperature diffusion bonding of polycrystalline metals and applies the concept of the difference in coefficient of thermal expansion (CTE) between the bonding fixture and the laminated material to produce a registration force at high temperatures for bonding multiple layers of laminae. The technique has the advantage of permitting easy loading at room temperature. TEER has proved to provide high precision alignment, and time and cost savings, for registering large numbers of laminae (Thomas, 2002).

For metallic microlamination, the diffusion bonding temperature can be as much as a thousand degrees Celsius. As the bonding temperature increases, the amount of registration force is increased as well, for a given laminae-fixture configuration. If this registration force is higher than the critical point of buckling

of the microchannel fin, the fin will buckle, as discussed in Chapter 3 and illustrated in Figure 4-2.

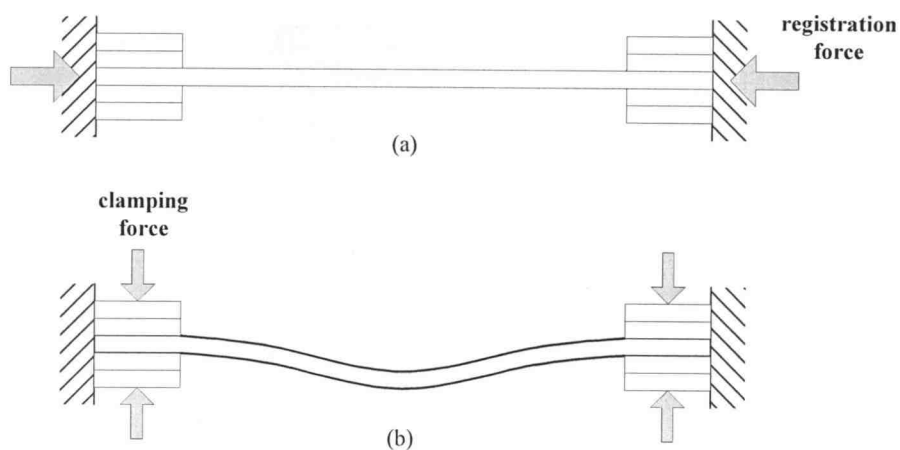


Figure 4-2. Schematic of fin buckling due to excessive registration force

When buckling happens, flow channels that are separated by the buckled fin are no longer uniform and this results in lower efficiency of the laminated MECS device. Figure 4-3 shows the results of fin buckling within a microchannel array.

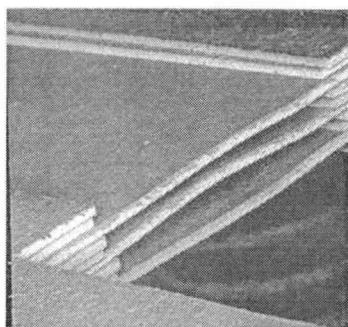
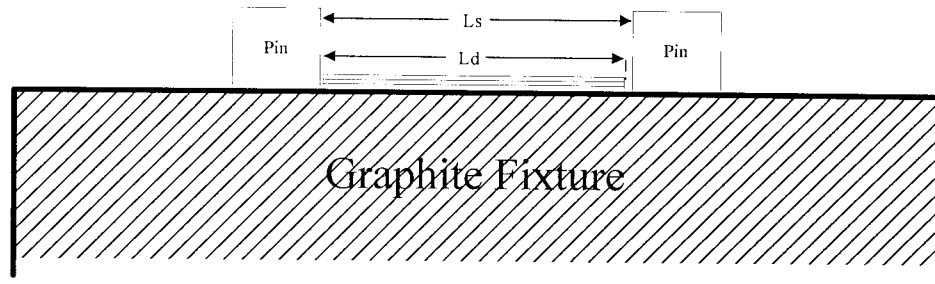


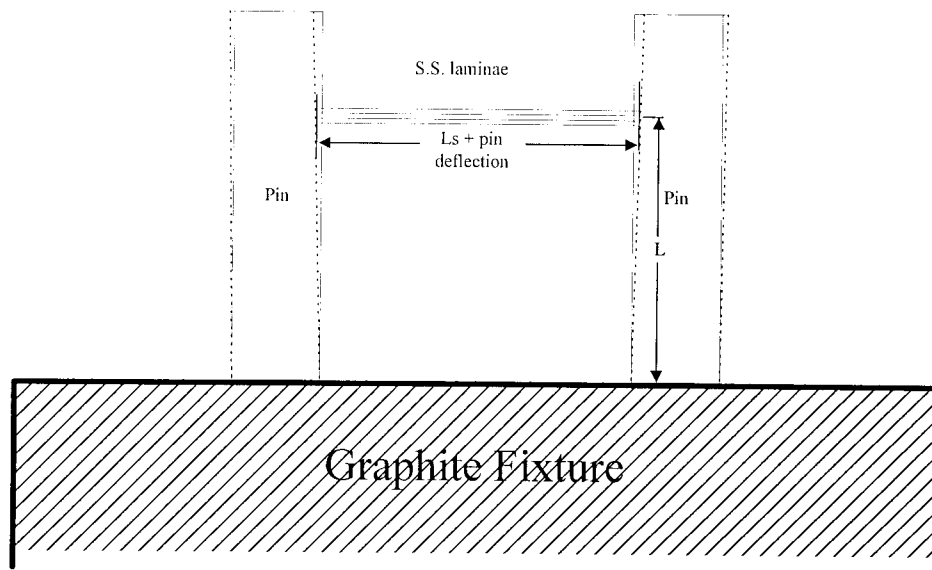
Figure 4-3. Microchannel heat exchanger with nonuniform flow channels due to fin buckling

According to the preceding investigation (Chapter 3), the tolerance limit for alignment fixtures of fins with thicknesses ranging from 0.0508 to 0.1016 mm is less than 10 μm . This limit is practically exceeds the tolerance limits in most conventional machine tools used to produce the alignment fixtures. One way to overcome these issues is to use compliance within the fixture. Many manufacturing applications have used compliance between a tool and a device to improve the accuracy of assembly or alignment (Jackman, et al., 1994; Saxena, et al., 1998; Edmondson, et al., 2001). When a TEER fixture is used in the laminae registration and bonding process, the edges of the laminae interact with the fixture pins in order to generate a registration force at elevated temperature. Figure 4-4 illustrates two schematics of a TEER fixture for high volume microlamination. Figure 4-4 (a) depicts a TEER fixture where the stack of laminae is aligned with the bottom of the fixture pins. In contrast, the schematic in Figure 4-4 (b) shows that the placement of the stack is moved up to a specific height above the bottom plate. In the second case, an insert plate is used to provide the support and bring the specimens up to the specific height. The dotted lines displayed in Figure 4-4 (b) represent the compliance of the fixture due to the deflection of pins.

The compliance of the TEER fixture helps reduce the excessive force from registration so that fin buckling can be avoided or minimized. As shown in Figure 4-4 (b), these pins function as a cantilever to absorb some of the registration force. Because the amount of pin deflection is proportional to the location where the pins interact with the specimen, both beam bending and buckling theory are helpful to develop a predictive model for this approach.



(a)



(b)

Figure 4-4. A schematic of TEER fixture (a) original concept, (b) with the implementation of the compliance of fixture

4.3 Theoretical Models

A theoretical model was developed to evaluate the critical point of fin buckling based on the amount of pin deflection. First the fin buckling analysis is discussed, and then the concept of beam bending is used to evaluate the compliance

of the fixture pin. During the development of predictive model, the following assumptions were made as a part of the buckling evaluation.

- Before the load is applied, fin layer is perfectly straight.
- The buckling force is uniformly applied to the fin along the axis.
- The cross-section and the moment of inertia of the fin are assumed to be constant, thereby the fin buckling can be treated as a column buckling.
- Fin material is assumed to be linearly elastic and the elastic limit is constant for every fin sample.
- The scope of investigation in fin buckling is still under small deflection conditions.
- With the clamping force applied to both ends of the fin layer, the mode shape of fin buckling is derived from fixed-ended support condition.
- The bonding fixture is assumed to have a perfect rigidity when the placement of the sample is at the bottom level.

4.3.1 Fin Warpage Analysis

Figure 4-5 illustrates the schematic of uniform and nonuniform channel due to fin buckling. L_f indicates the channel width and cn denotes the channel height.

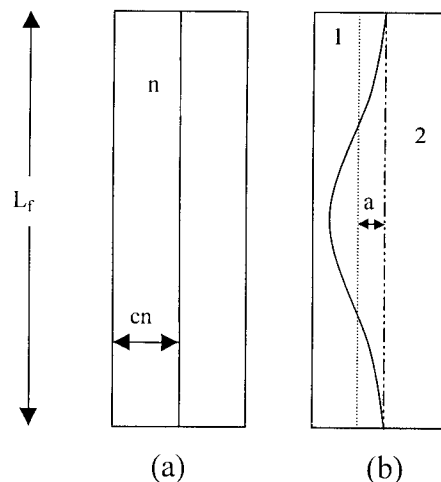


Figure 4-5. Geometry of (a) uniform flow channels, (b) nonuniform fin buckling

The calculation of the deviation of flow channels (δ_c) is based on the investigation by London (1970) and Mondt (1977) on the nonuniformity of the flow channel in a heat exchanger (London, 1970; Mondt, 1977). The channel deviation due to fin buckling is calculated from $\delta_c = \frac{a}{cn}$, where a , as shown in Figure 4-6 (b), is the distance from the original position of the fin before buckling to the average position of the fin after buckling. Since the support boundary condition for TEER process is a fixed-ended (Figure 4-6), 'a' will be half the distance between the original position and the peak of the deflection.

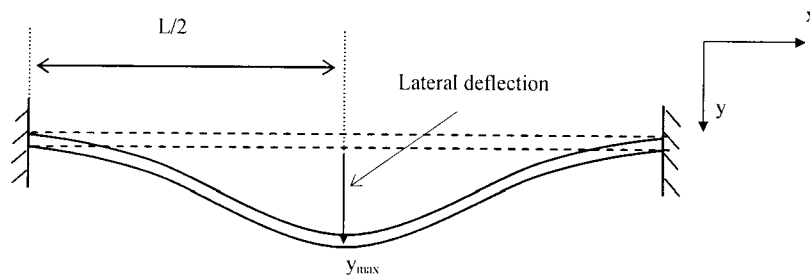


Figure 4-6. Column buckling behavior for fixed-ended boundary condition

The force that can cause the fin to buckle needs to be higher than the critical point of buckling, and the stress at this buckling point need to be smaller than the yield point of the material. If the buckling stress is larger than the yield strength, the fin will yield in compression instead of buckling (Gere, et al., 1997). For the fixed-ended boundary condition, the critical point of buckling and the critical stress is calculated from:

$$P_c = \frac{4 \cdot \pi^2 \cdot E \cdot I}{L^2}, \sigma_c = \frac{P_c}{A} = \frac{4 \cdot \pi^2 \cdot E \cdot I}{A \cdot L^2} \quad (1)$$

Secondly, we need to evaluate the registration force of TEER. This evaluation is based on the different in CTE. This force is denoted as P_t . P_t needs to be larger than P_c to realize the fin buckling. The force due to the difference in CTE can be calculated from:

$$P_t = E \cdot A \cdot (\alpha_1 - \alpha_2) \cdot \Delta T \quad (2)$$

In this investigation, α_1 is the CTE of stainless steel and α_2 is the CTE of graphite, while ΔT is the different between room temperature and the bonding temperature. As the thermal loading stress, caused by the CTE mismatch, exceeds the proportional limit of elastic property, the fin buckling will be permanently deformed. The buckling deflection can be calculated based on the geometry of fixed-ended buckling geometry:

$$y = A_{mp} \cdot \left(1 - \cos\left(\frac{2 \cdot \pi \cdot x}{L}\right) \right) \quad (3)$$

The maximum deflection, caused by fin buckling, can be calculated from the amplitude of the buckling deflection function based on the fin width (L_f') and the fixture slot (L_s') at the bonding temperature, by applying the arc length formula:

$$L1 = \int_0^{l.2} \sqrt{1 + \left(\frac{dy}{dx}\right)^2} dx \quad (4)$$

However, since the buckling form of the substituted equation does not have a closed-form anti-derivation, the evaluation of fin amplitude is based on the approximation equation:

$$L1 = \int_0^{l.2} \sqrt{1 + \left(\frac{dy}{dx}\right)^2} dx \approx \int_0^{l.2} \left\{ 1 + \frac{\left(\frac{dy}{dx}\right)^2}{2} \right\} dx \quad (5)$$

Amplitude can be calculated when substitute function of fin buckling (4) into (5), which yields: $L1 = L2 + \frac{\pi^2 \cdot A_{mp}^2}{L2}$, so the maximum deflection of the fin

$$(2 \cdot A_{mp}) \text{ is: } D_{\max} = \frac{2}{\pi} \cdot \sqrt{L2 \cdot (L1 - L2)} \text{ or } \frac{2}{\pi} \cdot \sqrt{L2 \cdot Inf} \quad (6)$$

where $L2$ is the width of the fixture slot at the bonding temperature and $L1 - L2$ is the amount of the interference between the laminae and the fixture at the bonding temperature, Inf .

4.3.2 The Compliance of the TEER Fixture

The final tolerance in a compliant fixture is dependent upon the maximum amount of deflection, δ_{\max} , of the fixture pins prior to fin buckling. When the specimens are placed at a specific height above the bottom plate of the fixture, the edge alignment features or pins are allowed to deflect upon excessive registration force due to the interference between the fin width and slot width at the elevated temperature. With respect to this interaction, the compliance of the pins can provide additional displacement for test specimens before the actual buckling starts, and once the buckling starts the relation between interference can still be used to evaluate the magnitude of fin warpage (equation 5). To evaluate the pin deflection due to registration force, the beam bending theory is applied. The amount of pin deflection (δ) depends on the distance from the fixed end of the pin to the point where the interaction happens (L), as shown in Figure 4-5 (b). The equation for pin deflection can be stated as:

$$\delta = \frac{F \cdot L^3}{3 \cdot E \cdot I} \quad (7)$$

where F is the registration force acting against the pin, L is the length of the pin from the fixed end, E is the Young's modulus of the fixture material, and I is the

moment of inertia of the pin. The force F in the equation above can be evaluated from the force due to the difference in CTE of graphite and stainless steel, which in this study are the fixture and laminae base material, presented in equation (2).

When substituting an appropriate specification, the amount of fixture compliance based on pin deflection can be stated as:

$$\delta = \frac{64 \cdot A_f \cdot E_{ss} \cdot (\alpha_{ss} - \alpha_g) \cdot \Delta T \cdot L^3}{3 \cdot E_g \cdot \pi \cdot D^4} \quad (8)$$

Alternatively, if we substitute the specified amount of pin deflection into equation (7), the height of the insert plate can be calculated. This specific amount of pin deflection can be used as a tolerance limit of the compliant TEER, which indicates the allowable interference limit for fin buckling. As mentioned previously, the greater the deflection, the larger the space for the specimen to expand before it starts to buckle. Consequently, the compliance of the fixture can be applied to reduce the amount of shape variation by improving the tolerance limit of the fixture.

For this study, the condition we are particularly interested in is the height “ L ” under the condition where δ equal to an amount at the critical point of buckling or the allowable machining tolerances of the fixture— δ_{max} . As a result, the height of the insert can be calculated from:

$$L = \sqrt[3]{\frac{\delta_{max} \cdot 3 \cdot n \cdot E_g \cdot \pi \cdot D^4}{64 \cdot L_{ch} \cdot t \cdot E_{ss} \cdot (\alpha_{ss} - \alpha_g) \cdot \Delta T}} \quad (9)$$

where n is the number of pair of the pin in the TEER fixture.

With additional deflection due to fixture compliant, the fin will not buckle (zero deflection) until the interference between the laminae and the compliance TEER exceeds the amount of this pin deflection (δ_{max}). Once the interference becomes greater than δ_{max} , the magnitude of fin buckling can be calculate from equation (6), but the term Inf is now equal to $L1-L2-\delta_{max}$. See the calculation note

for the evaluation of the compliance of the fixture and the relation between insert thickness and the amount of pin deflection in Appendix J.

4.4 Experimental

The main purpose of this work was to determine whether the buckling behavior of the test specimen follows the theoretical prediction based on both buckling theory and the bending concept, as well as to investigate the factors affecting the magnitude of the warpage. Experiments were conducted using the fixture with a graphite insert to take advantage of the pins compliance. The width of the fin was varied to evaluate the effect of interference on the magnitude of buckling. In addition, the results should verify that within the specified tolerance limit the minimum amount of fin buckling can be achieved.

The evaluation of the difference between theory and experiment was performed by the paired t-test under the null hypothesis that the mean of the difference is zero with alpha equal to 0.05. In addition, if both theoretical and experimental results are equal, a 95% confidence interval for the mean difference must include zero. Then a multifactor ANOVA (Type III Sums of Squares) was implemented to evaluate main effects such as fin thickness and allowance on the magnitude of misalignment. A significant effect must have a p-value less than 0.05.

The following is the description of the test fixture, test specimen and the experimental procedure in this study, including the measurement technique for laminate characterization.

The bonding fixture and the insert plate were fabricated from a graphite block using a Computer Numerical Control (CNC) milling machine in order to achieve high dimensional accuracy. This fixture assembly was designed to align laminae in one dimension to simplify experimentation and modeling. Test

specimens as shown in Figure 4-7 were used for these experiments. Each specimen consists of two channel layers and a fin lamina. As mentioned previously, fin width and thickness of the specimen were crucial for buckling behavior; therefore, both parameters were treated as a factor to evaluate the relationship between the interference at bonding temperature and the shape variation due to fin buckling.

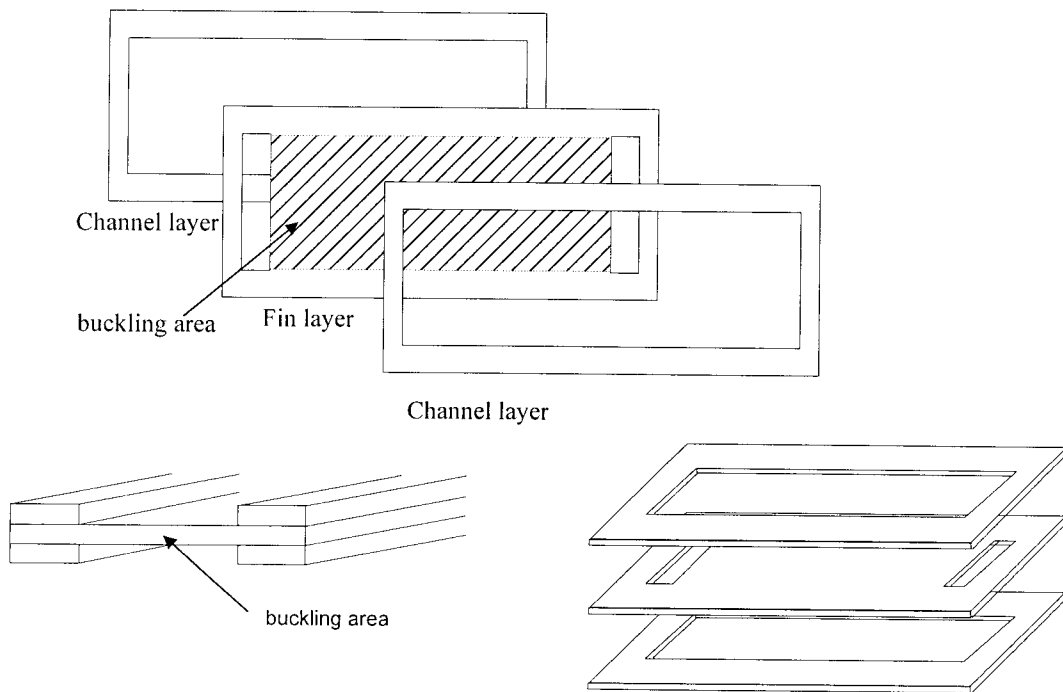


Figure 4-7. Geometry of the test specimen in this study

Figure 4-7 also highlights the buckling area that might be generated if the registration force exceeds the critical buckling force as well as if the stress of this reaction is over the proportional limit in yield strength. The loading of test specimen on the compliant TEER fixture is illustrated in Figure 4-8. The clearance

between the laminae and the TEER fixture at room temperature permits easy loading.

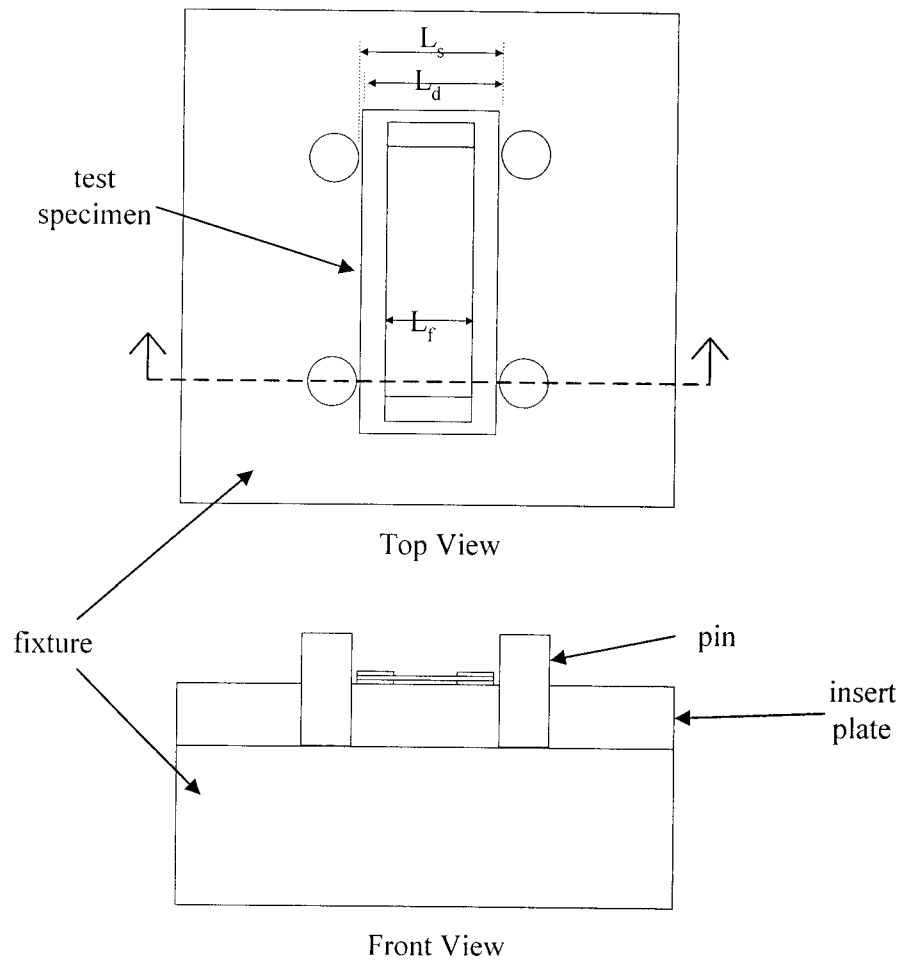


Figure 4-8. Loading of the test specimen laminae onto the TEER fixture

To verify the relation between fin thickness and the limitation of bonding fixture, three thicknesses of 304 stainless steel shims were used: 0.0508 mm, 0.0762 mm and 0.1016 mm. A total of 20 specimens (8 for both 0.0508 mm and 0.1016 mm, and 4 for 0.0762 mm thick stainless steel) were tested in this

experiment. The test specimens were patterned into specific designs (fin or channel layer) by a Nd:YAG laser operating at the fourth harmonic (266 nm) wavelength. In an effort to remove the slag and ejecta, all patterned laminae were polished with an ultra fine 3M Scotch-Brite hand pad and cleaned in an ultrasonic cleaner with a 50% concentration of Citranox for 20 minutes. Next, the fin lamina was taken from the set and measured by a Dektak3 surface profiler to verify the flatness characteristics. This profiler is capable of making vertical measurements up to 2 mm with a 1 nm, standard deviation for step height repeatability. A 12.5- μm diamond-tipped stylus was used to perform surface topography measurement. Flatness measurements were taken at four locations for each fin specimen: the left side, two near the middle of the fin, and the right end of the fin area. Then, all laminae were rinsed with Acetone, Ethanol, and De-ionized water (AED) before loading on the bonding fixture.

After stacking all laminae in the fixture, the fixture assembly was put in a vacuum hot press chamber, and the bonding step began. The bonding process for this experiment involved pumping down the chamber to achieve a satisfactory vacuum (approximately 10^{-4} mbar), and then heating the system to the bonding temperature. The clamping pressure was applied to the fixture when the temperature inside the chamber reached the bonding temperature. At the end of the bonding cycle, the clamping force was removed from the laminate to allow uniform contraction. The bonding conditions for this experiment were set at 750 °C with 5 MPa applied pressure for one hour. After cool down to room temperature, the laminate was cleaned with AED and then the warpage characteristic were measured at four different locations. The fin deflection after bonding was also measured by the Dektak3 surface profiler. The average maximum deflection and standard deviation of each sample were then calculated.

Experimental methodology based on a factorial design was implemented in this study to verify the minimum fin buckling condition and validation of tolerance limits of the bonding fixture upon the compliance of the fixture. Prior to the actual

test, a preliminary experiment was conducted to verify the location where the fin and fixture starts to interfere at the elevated temperature. A variety of test coupons with different width spans (in 10- μm step increments) were tested on the bonding fixture to calibrate the expansion of stainless steel associated with the high temperature dimensions of the graphite fixture. The point of calibration used to calibrate the device was the critical point of buckling. The point at which buckling of the fin began provided a reference as to how much interference existed between the laminae and the fixture. Repeatability of the process was verified by running the same dimension sample several times to check the consistency of the test results. It was found that the test fixture used in this experiment caused buckling in stainless steel laminae beyond 14.81 mm in width (at room temperature, without the graphite insert).

4.5 Results and Discussion

The following sections describe the relation of the interference between the laminae and the bonding fixture and the magnitude of fin buckling based on the theoretical predictions and experimental results. In addition, the variation between both results is discussed as well as the effect of the fin buckling on the performance of a MECS device.

4.5.1 The Relationship between Tolerance Limit and Fin Buckling

To simplify the experiment, it was desirable to use an insert with a constant height. According to equation (8), the pin deflection is proportional to the thickness of the fin. Therefore variations in pin deflection were controlled by laminae thickness. In this study, a specific level of tolerance limit was set equal to

the fin thickness ($\delta = t$) in order to calculate the height of the graphite insert. The procedure with the graphite insert for this experiment was called compliant TEER.

Experiments were conducted to verify the theoretical model of fin buckling on the compliant TEER. The variety of fin thicknesses and fin widths of the specimen were tested (total of 20 specimens) and the data was collected. The results of buckling characteristic of test specimens from the experiment are presented in Figure 4-9, along with the analytical model. The error bars in Figure 4-9 describes 95% confidence interval of the measured data. Each side of the interval equals to $2 * S_m$, where S_m is the standard error calculated from the variation of the warpage measurement at 4 locations.

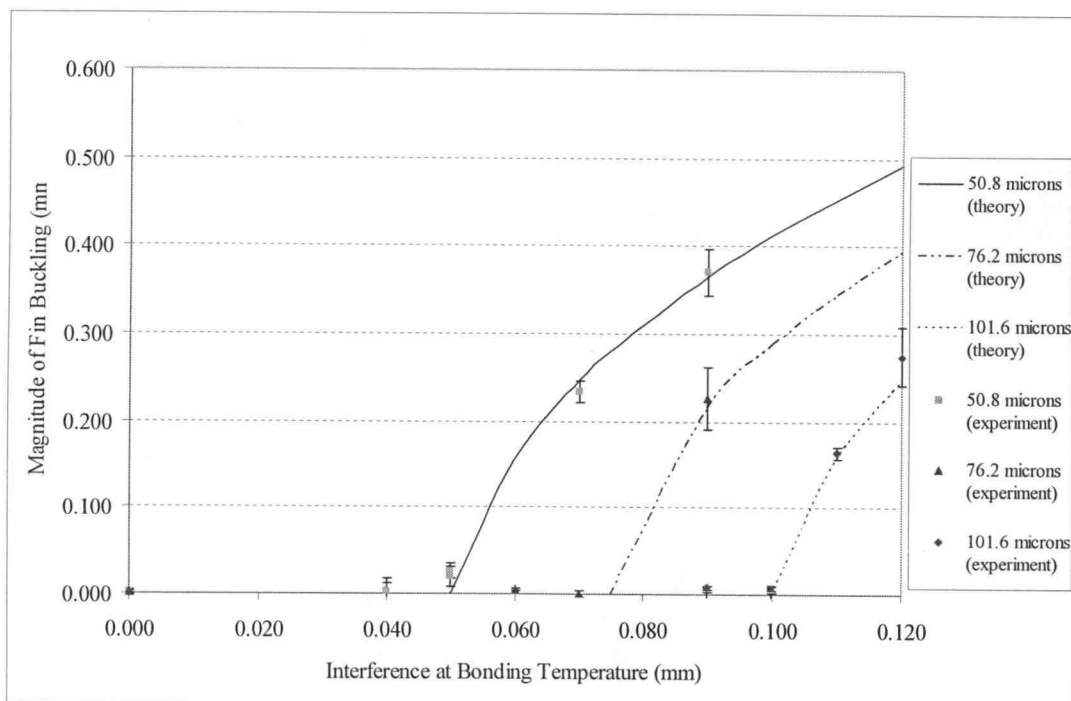


Figure 4-9. Magnitude of fin buckling versus interference between fixture and laminae at bonding temperature with 95% confidence interval of standard deviation

According to an ANOVA, there was conclusive evidence to indicate that the mean warpage depended on both fin thickness and the amount of allowance (p-value < 0.05), but not on the location of the measurement on the fin (p-value = 0.176), as expected from the buckling and the bending behavior as mentioned in equations (6) and (9). Moreover, there is evidence that the experiment results and the theoretical model are in good agreement (t-stat = 1.34, df = 19). The 95% confidence interval of the mean difference in both results ranged from -1.93 to 8.76, which includes zero.

However, there was some variation of fin deflection between experimental and the theoretical calculation. According to Figure 4-9, the magnitude of fin warpage at the allowance close to the critical point of permanent buckling (tolerance limit) was supposed to be zero because the registration force did not exceed the critical point of buckling yet. As can be seen from the graph, the deflection of the fin at these locations could be as high as 0.026 mm. This variation might relate to the characteristics of the shim we used such as the residual stress or the initial imperfection. Furthermore, it was found that thinner specimen contributed the greater amount of this variation based on the information of pre-bonding fin flatness measurement as shown on Table 4-1.

Table 4-1. The average initial deflection of fin lamina of a variety of shim thickness

Thickness	# of sample	Location				Average
		Loc 1	Loc 2	Loc 3	Loc 3	
50.4 μm	8	14.18	15.73	20.13	19.54	17.39
76.2 μm	4	11.62	14.49	18.30	13.58	14.50
101.6 μm	8	9.57	11.43	10.51	10.33	10.46

Since the shim stock used in this experiment was a cold-roll material, the residual stress in the structure might induce a deflection during the bonding process. The thinner the fin, the greater the amount of residual stress exists due to a greater amount of thickness reduction. Figure 4-10 presents deflection characteristics of a 0.0508-mm thick fin before and after buckling when the interference is 90 μm . Notice that the fin already contained some amount of deflection prior to the experiment. This amount of pre-warpage was removed from the post bonding warpage prior to plotting Figure 4-9. This pre-warpage might also have reduced the magnitude of the critical load for buckling causing additional deviations from theoretical.

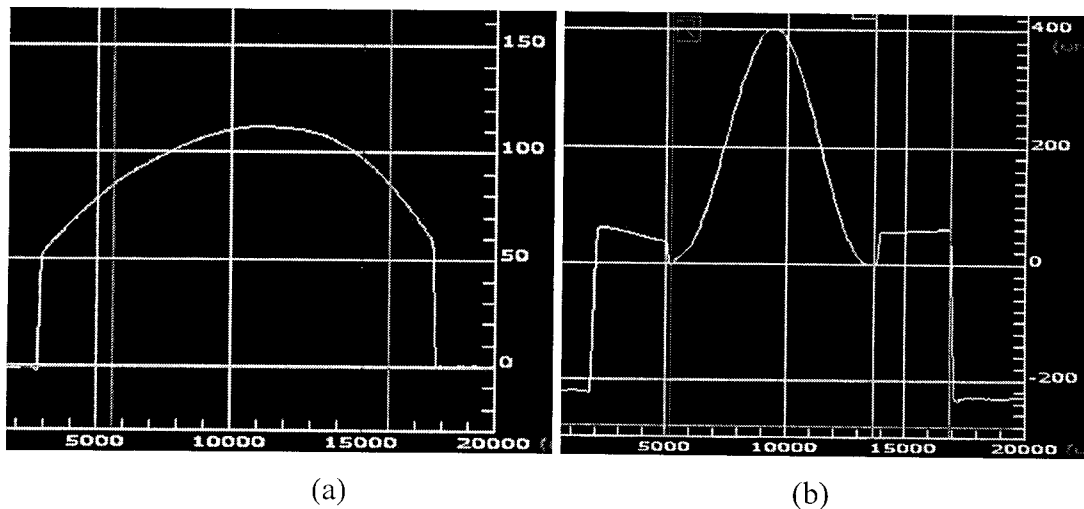


Figure 4-10. Deflection profiles of laminate (a) prior to bonding, (b) after bonding measured by Dektak3 surface profiler

Another hypothesis would be the proportional limit of stainless steel. For the theoretical calculation, the proportional limit of yield strength was based on that from the literature (ASTM, 1965; Chavez, et al., 1994). It is possible that the actual proportional limit of the stainless steel tested in this experiment might

deviate from the standard, so that warpage could be encountered earlier before the critical point of buckling. In addition, the variation of fin dimension can play a key role here as well. Even though the laser micromachining is considered to be a very accurate machining process, only a few microns difference from the desired specification would make a difference in the results, especially when this variation is close to the critical point of buckling.

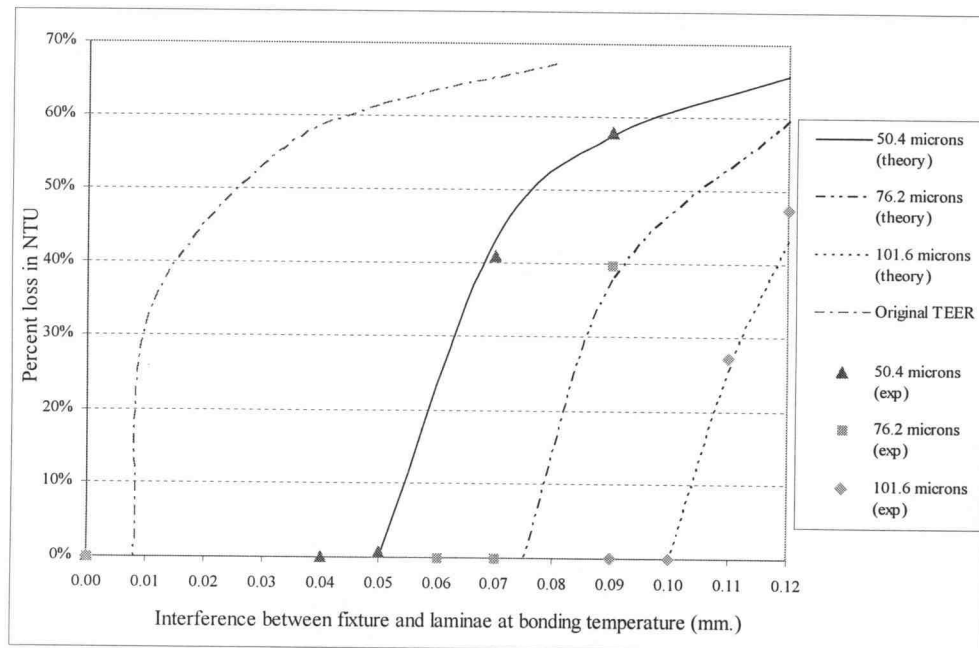
The time dependent deformation is also another concern in this study. Therefore, this issue has been analyzed and presented in Appendix P. The deformation mechanism map and inelastic deformation equation (Frost, et al., 1982; Stouffer, et al., 1996) were used to evaluate the effect of this mechanism based on the bonding parameters of this experiment: time, temperature, and pressure. Based on the result of this investigation, it is concluded that the effect of time dependent mechanism was negligible (less than 0.5 $\mu\text{m/hr}$).

4.5.2 The Relationship between Fin Buckling and Device Performance

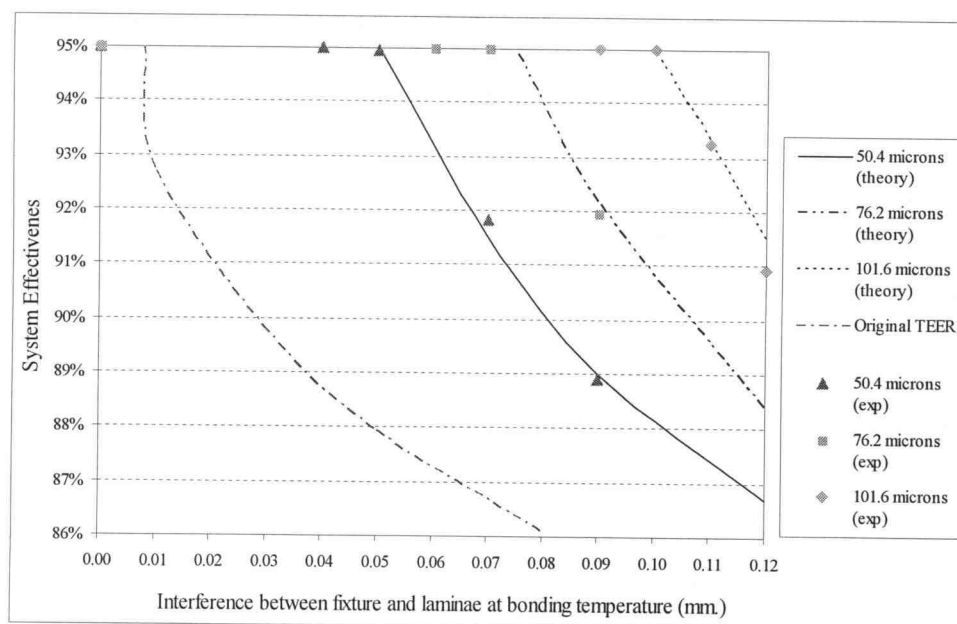
Figure 4-11 shows the reduction in a nominal heat exchanger performance due to fin warpage nonuniformity, based on the same base case heat exchanger unit discussed in Chapter 2. The graph is presented in terms of a variation in allowance between laminae and fixture at the bonding temperature based on both analytical and experimental results. For the comparison reason, the reduction in NTU in the case of the original TEER is also included.

Regarding the results from Chapter 3 in which the original TEER was investigated, the fin was buckled at a small amount of interference; therefore, the reduction in device performance is larger than the compliant TEER in which the concept of pin deflection was applied. With respect to the nominal counter-flow heat exchanger discussed in Appendix N, it was found that if the tolerance limit was less than 50 μm in interference, the effect of shape variation was no longer

significant. The amount of interference needs to exceed $75\ \mu\text{m}$ in order to make the effectiveness of a heat exchanger with 0.0504-mm thick decrease below 90%, while over $100\ \mu\text{m}$ interference are needed for the 0.1016-mm thick fin, as shown in Figure 4-11 (b). In contrast, the laminate fabricated by original TEER can suffer over 62% reduction in NTU (or below 88% thermal effectiveness) as soon as the interference reaches $50\ \mu\text{m}$.



(a)



(b)

Figure 4-11. Effect of fin buckling on a nominal heat exchanger performance in terms of (a) percent loss in NTU, (b) thermal effectiveness at different amounts of allowance between laminae and fixture at elevated temperature

Since the evaluation of the pin deflection is based on the location where the laminae interact with the pin edge, if large numbers of multiple layer of fin are fabricated on this fixture, the interaction due to registration force will rely solely on the bottom fin next to the graphite insert. As a result, the upper laminae can be out of alignment, which could lead to laminae misalignment or leakage. Figure 4-12 illustrates the relationship between the amount of pin deflection and the allowable misalignment. With respect to relative triangles as shown in the detailed drawing (in the center), the ratio of pin deflection (δ) over the insert height (L) is equal to the ratio of the allowable misalignment (δm) and the height of the laminae stack (H). If we know δm , the maximum height of the device can be calculated from:

$$H = \frac{\delta m}{\delta} * L \quad (10)$$

For instance, if 0.1016-mm thick laminae is used ($\delta = t$) and δm is set at 50 μm , the maximum device thickness will be $(0.05 * 10.2 / 0.1016)$ 5 mm, which converts into a total of $(5 / 0.1016)$ 49 layers. Since the number of allowable laminae was involved, these relations should be evaluated before the height of insert was specified to allow TEER bonding of high number of laminated layers without fin buckling and channel leakage.

Another implication from the relation in equation (10) is that we can calculate the size of the fixture slot as a function of the height of the insert, where the total height of the stack is specified. Since the slot size ($L2$) is equal the fin length ($L1$) at bonding temperature plus the tolerance limit of the fixture (δ), and this δ is also a function of L as mentioned in equation (10); therefore, the relation

$$\text{between slot size and the insert height is: } L2 = L1 + \left(\frac{\delta m}{H}\right) * L \quad (11)$$

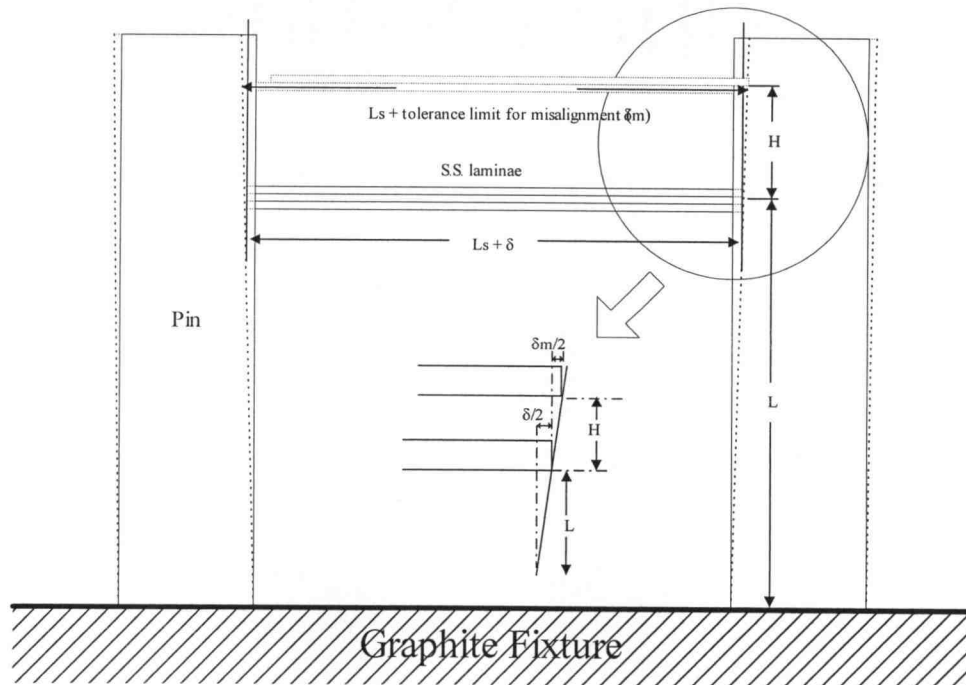


Figure 4-12. Relationship between the pin deflection and tolerance limit for misalignment

4.6 Conclusions

An investigation on the development of the bonding fixture for high-volume metal microlamination based on TEER was carried out in order to reduce fin buckling and attain the maximum performance of the MECS device. The compliant TEER technique can provide a better bonding result in the microlamination process. It was found that fixture tolerances can be measured from 8 μm to over 50 μm with the use of compliant pins for the cases studied. This brings the tolerances of TEER fixtures well within conventional machining tolerances and makes the process more economical. The results also show that the theoretical predictions and experimental data are in good agreement within a 95% confidence interval. As expected, there is conclusive evidence that the magnitude of warpage depends on both fin thickness and the amount of interference. In this study, the tolerance limit was set equal to the fin thickness, therefore the tolerance limits of 0.0504, 0.0762, and 0.1016 mm can be achieved when using a fin thickness of those relative limits. At these tolerance limits, conventional machining tools can be used to fabricate the bonding fixture, which increase the flexibility of microlamination. The compliant TEER also maintains the efficiency of the MECS devices by enabling the fabrication of buckle-free devices to avoid the effect of channel deviation on NTU reduction. In addition, the evaluation of the limitations on the allowable laminate thickness relative to the compliance of the fixture was discussed showing that for 50 μm allowable misalignment, a device with 100 μm laminae could have as many as 49 laminae based on the specific insert used in this study.

4.7 References

- ASTM, "The Elevated-Temperature Properties of Stainless Steels," in *ASTM Data Series Publication DS 5 - S1*, 1965.
- Chavez, S. A., Korth, G. E., and Harper, D. M., "High-temperature tensile and creep data for Inconel 600, 304 stainless steel and SA106B carbon steel," *Nuclear Engineering and Design*, vol. 148, pp. 351-363, 1994.
- Daymo, E. A., VanderWiel, D. P., Fitzgerald, S. P., Wang, Y., Rozmiarek, R. T., LaMont, M. J., and Tonkovich, A. L. Y., "Microchannel Fuel Porcessing for Man Portable Power," presented at AIChE 2000 Spring National Meeting, Atlanta, GA, 2000.
- Drost, M. K. and Friedrich, M., "Miniature Heat Pumps for Portable and Distributed Space Conditioning Applications," presented at Proceedings of IECEC, 1997.
- Drost, M. K., Wegeng, R. S., Martin, P. M., Brooks, K. P., Martin, J. L., and Call, C., "MicroHeater," presented at AIChE 2000 Spring National Meeting, Atlanta, GA, 2000.
- Edmondson, N. F. and Redford, A. H., "A compliance device for flexible close tolerance assembly," *Industrial Robot*, vol. 28, pp. 54-62, 2001.
- Frost, H. J. and Ashby, M. F., *Deformation-Mechanism Maps: The Plasticity and Creep of Metals and Ceramics*. New York: Pergamon Press, 1982.
- Gere, J. M. and Timoshenko, S. P., *Mechanics of materials*. Boston: PWS-KENT Pub. Co., 1997.
- Jackman, J., Deng, J.-J., Ahn, H.-i., Kuo, W., and Vardeman, S., "Compliance measure for the alignment of cylindrical part features," *IIE Transactions*, vol. 26, pp. 2-10, 1994.
- Kawano, K., Minakami, K., Iwasaki, H., and Ishizuka, M., "Micro Channel Heat Exchanger for Cooling Electrical Equipment," *ASME (HTD) -- Proceeding of the ASME Heat Transfer Division*, vol. 361-3, pp. 173-180, 1998.
- London, A. L., "Laminar Flow Gas Turbine Regenerators--The Influence of Manufacturing Tolerances," *Transactions of ASME: Journal of Engineering for Power*, vol. 92, pp. 46-56, 1970.

- Martin, P. M., Matson, D. W., and Bennett, W. D., "Microfabrication Methods For Microchannel Reactors and Separations Systems," *Chemical Engineering Communications*, vol. 173, pp. 245-254, 1999.
- Martin, P. M., Matson, D. W., Bennett, W. D., Stewart, D. C., and Lin, Y., "Laser Micromachined and Laminated Microfluidic Components for Miniaturized Thermal, Chemical and Biological Systems," presented at Proceeding of SPIE -- the International Society for Optical Engineering, 1999.
- Matson, D. W., Martin, P. M., Stewart, D. C., Tonkovich, A. L. Y., White, M., Zilka, J. L., and Roberts, G. L., "Fabrication of Microchannel Chemical Reactors Using a Metal Lamination Process," presented at Third International Conference on Microreaction Technology, Frankfurt, Germany, 1999.
- Mondt, J. R., "Effects of Nonuniform Passages on Deepfold Heat Exchanger Performance," *Transactions of ASME: Journal of Engineering for Power*, vol. 99, pp. 657-663, 1977.
- Paul, B. K., Dewey, T., Alman, D., and Wilson, R. D., "Intermetallic Microlamination for High-Temperature Reactors," presented at 4th International Conference on Microreaction Technology, Atlanta, GA, 2000.
- Saxena, A. and Kramer, S. N., "Simple and accurate method for determining large deflections in compliant mechanisms subjected to end forces and moments," *Journal of Mechanical Design, Transactions of the ASME*, vol. 120, pp. 392-400, 1998.
- Stouffer, D. C. and Dame, L. T., *Inelastic Deformation of Metals: Models, Mechanical Properties, and Metallurgy*. New York: John Wiley & Sons, Inc., 1996.
- Thomas, J. "Establishing Thermally Enhanced Edge Registration (TEER) as a Feasible Alignment Technique for Metallic Laminated Devices." *M.S. Thesis*, Industrial Engineering: Oregon State University, 2001.
- Thomas, J. and Paul, B. K., "Thermally-Enhanced Edge Registration (TEER) for Aligning Metallic Microlaminated Devices," presented at Transactions of NAMRC XXX, West Lafayette, IL, 2002.
- Tonkovich, A. L. Y., Zilka, J. L., Jimenez, D. M., LaMont, M. J., and Wegeng, R. S., "Microchannel Chemical Reactors for Fuel Processing," presented at AIChE 1998 Spring National Meeting, New Orleans, 1998.

CHAPTER 5

USE OF BUCKLING THEORY TO CONTROL FIN WARPAGE IN METALLIC MICROLAMINATED HEAT EXCHANGERS

5.1 Abstract

Microchannel arrays are used to dissipate or deliver heat within compact, portable systems, such as those needed for microelectronic cooling systems and automotive fuel processors. One fabrication technique for producing these microchannel arrays is microlamination. Microlamination consists of patterning thin material shims and stacking and bonding these shims into a monolithic device. However, shape variation or irregularity in the microchannel geometry after microlamination can lower the performance of the device or even lead to functional failure due to nonuniform flow distribution or the reduction of the number of transfer units. Buckling warpage on microchannel fins has been shown to significantly reduce the effectiveness of microchannel heat exchangers. However, if buckling can be controlled to produce higher modes in a predictable fashion, the magnitude and effect of fin warpage can be minimized. Hence, this research investigates a microlamination method for inducing higher modes of fin buckling in the preferred manner. A Thermally-Enhanced Edge Registration (TEER) procedure is used to align laminae and to induce lateral buckling within microchannel arrays. The buckling theory is used to predict how to achieve higher modes of buckling, thereby reducing the overall microchannel deviation. A constraining technique is introduced for encouraging the fin geometry to produce higher modes of buckling. A rudimentary experiment was conducted to present the feasibility of this technique to form higher modes of buckling.

5.2 Introduction

Microtechnology-based energy and chemical systems (MECS) is a new generation of devices with critical feature sizes in the meso-scale. Microchannel arrays are normally embedded in MECS devices. The microchannel arrays studied in this research are also considered to be mesoscale, in which the dominated structures or flow channels are in the order of tens to hundreds of micrometers, but the entire dimension is over a millimeter in range. Devices in this scale have been shown to have a significant advantage for heat transfer applications over conventional heat exchangers due to the large surface-to-volume ratio of the transfer area (Wegeng, et al., 1999; Ameel, et al., 2000). Implementing microchannel arrays for microfluidic systems allows decentralization and portability of energy and chemical systems by shortening the diffusional distances and providing high rates of heat and mass transfer. Because microchannel arrays operate within small volumes, excellent temperature control, easy operation at high pressure and rapid temperature changes are also beneficial. Because of these benefits, MECS applications that implement microchannel arrays include portable power generators (Wegeng, et al., 1999), portable heat, ventilation and air conditioning (Martin, et al., 1995; Drost, et al., 1997; Drost, et al., 1999), microreactors and fuel processors (Tonkovich, et al., 1998), dechlorinators (Jovanovic, 2001) or solvent extractors (Matson, et al., 1997; Martin, et al., 1999), etc.

Several manufacturing techniques can be used to fabricate microchannel arrays depending on the design geometry and base material. For a metallic structure, microlamination is a well-known technique (Matson, et al., 1999; Paul, et al., 1999). Microlamination involves three major steps: laminae patterning, registration, and bonding. Figure 5-1 shows an exploded view of a microlaminated, two-fluid counter-flow microchannel array, which could be used for mesoscale heat and mass transfer applications. For this specific design, fin and channel layers are

normally alternated in order to generate the passage of hot and cold fluid streams for heat transfer applications.

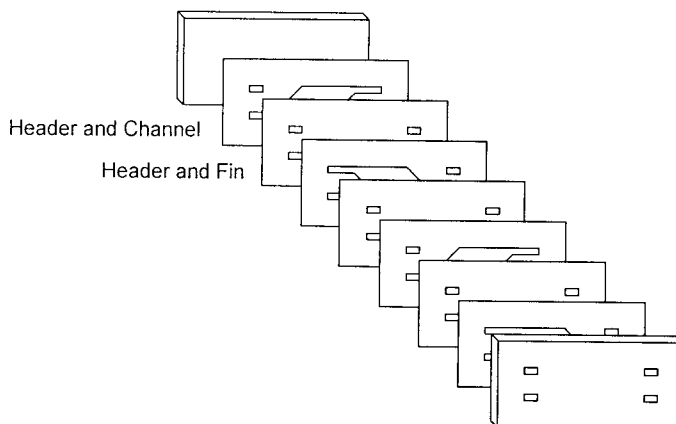


Figure 5-1. A schematic of microlamination procedure for two-fluid counter-flow microchannel array

This research is focused on the fabrication of microchannel arrays that can be used in a two-fluid counter-flow heat exchanger, in which laminar is the flow scheme. It was found that the flow distribution of two fluids influences the efficiency of this type of heat transfer device (Kaka, et al., 1983).

Shape variation, or irregularity in the geometry of a device can be introduced during the fabrication of the device. Shape variation can happen in any step of microlamination, but the alignment and bonding steps have been found to generate major variations in the final result. When the shape variation exists in the microchannel arrays, the thermal efficiency of the heat exchanger will be lowered or the device may not function properly, depending on the degree of the variations.

As mentioned in the second step of microlamination, alignment techniques are used to properly register layers of patterned shims prior to the bonding step. Alignment is achieved mechanically through the use of pin or edge registration within a bonding fixture. The registration technique that was applied in this study

was based on TEER (Thomas, 2001). This technique is used for the high-temperature diffusion bonding of polycrystalline metals and employs the difference in thermal expansion coefficients between the bonding fixture and the laminated material to produce a registration force on the laminae at the bonding temperature. By making the bonding fixture from a material that has a lower coefficient of thermal expansion (CTE) than the laminae, a clearance will exist between the tooling and the laminae at room temperature, which makes the loading of laminae easier than for other mechanical alignment methods. The benefits of TEER include high precision alignment, and time and cost savings, because large numbers of laminae can be automatically registered in the fixture without the requirement of any specific aligning tool while still achieving an accuracy of below 5 microns after bonding (Thomas, 2002).

However, if the registration force generated during TEER is higher than the critical point of buckling of the microchannel fin, buckling of the fin will occur. This is demonstrated in Figure 5-2. When buckling happens, flow channels that are separated by the buckled fin are no longer uniform. Figure 5-3 shows nonuniform microchannels produced as a result of fin buckling.

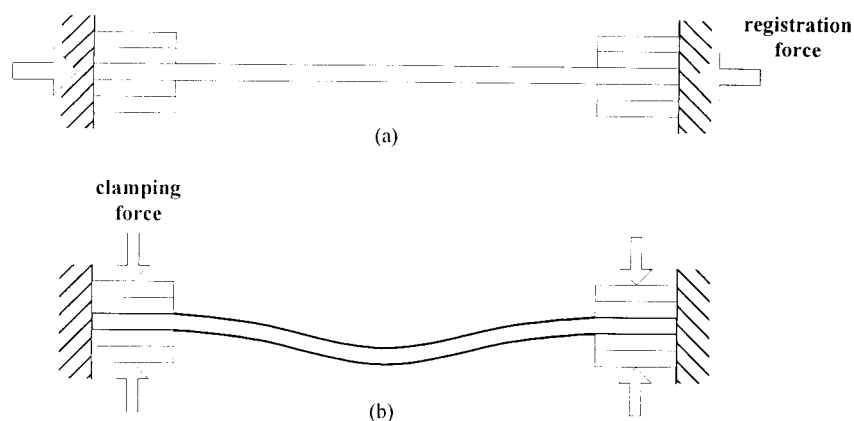


Figure 5-2. Schematic of fin buckling due to excess registration force

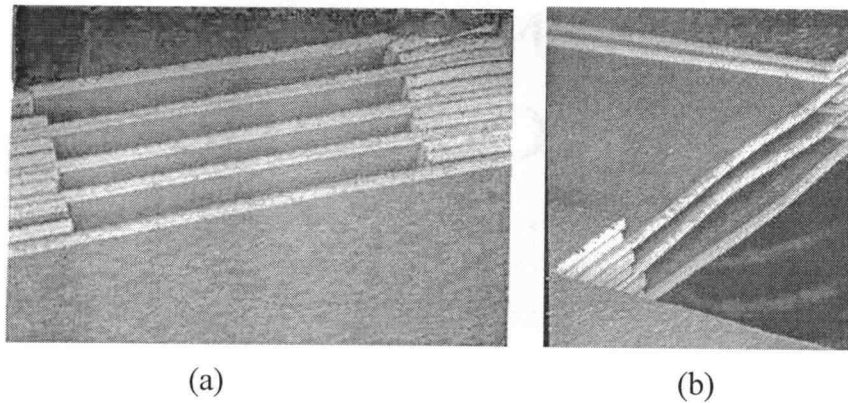


Figure 5-3. SEM micrographs of a microchannel heat exchanger with nonuniform flow channels (a) before and (b) after fin buckling

As discussed in Chapter 2, warpage due to fin buckling denotes a significant effect on the thermal effectiveness of heat exchangers. One possible way to minimize this effect is to induce a higher mode of buckling. With a greater number of mode deflection, the nonuniformity of the channel will be reduced.

In order to induce the higher mode of buckling, a constraining technique can be implemented. This technique aims to manipulate the buckling mechanism of the fin to form mode 2 or higher in order to reduce the channel nonuniformity that can lessen the performance of the heat exchanger. With a placement of constraints at specific locations, the fin deflection at those points is prevented and causes the fin to buckle in another position (Shames, 1989).

In 1999, Hexiang et al. presented a numerical procedure for modeling the instability of radially constrained plates subjected to in-plane, circumferential loading resulting from thermal expansion. The authors investigated the analytical evaluation of mode 2 buckling behavior formed by the constraining technique and showed that the shape of buckling depended on the location of the constrained structure. Accurate placement was required to achieve symmetry in mode 2 buckling geometry. Their results also showed that when the constrained location

was not symmetrical, the buckling plate could jump into other buckled configurations, where the critical load was smaller, such as a fundamental mode or another asymmetric form (Hexiang, et al., 1999).

Forming higher mode buckling has also been discussed in other literature on elastic stability and buckling (Simitses, 1976; Allen, et al., 1980; Shames, 1989; Mai, 1991; Alfutov, 2000; Bloom, et al., 2000). According to the literature, in order to attain higher modes of buckling, we need to apply lateral constraints at a specific location to prevent any vertical motion of the beam there. As shown in Figure 5-4, constraints are placed at the midpoint of the plate, so that mode 2 buckling can be formed. Similarly, for higher modes of buckling, $(n-1)$ constrained locations are required, where n represents the mode number. For instance, two locations on the plate need to be constrained to induce mode 3 buckling, as shown on Figure 5-5. In addition, the external restraints can be provided by the walls of the cavity as shown on Figure 5-6.

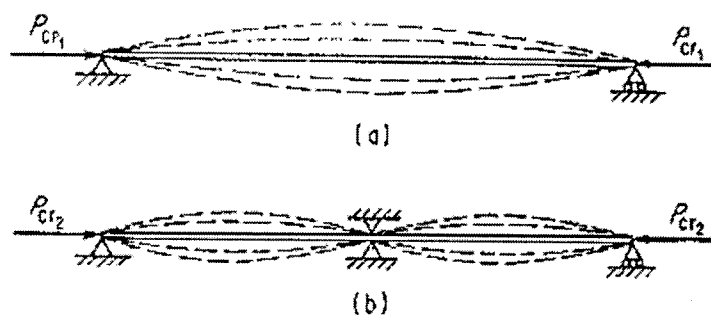


Figure 5-4. First and second buckling modes (Shames, 1989)

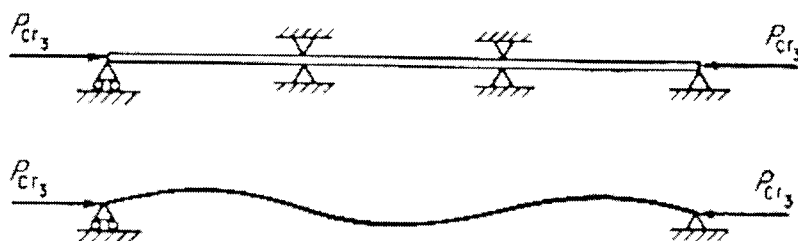


Figure 5-5. Formation of mode 3 buckling (Shames, 1989)

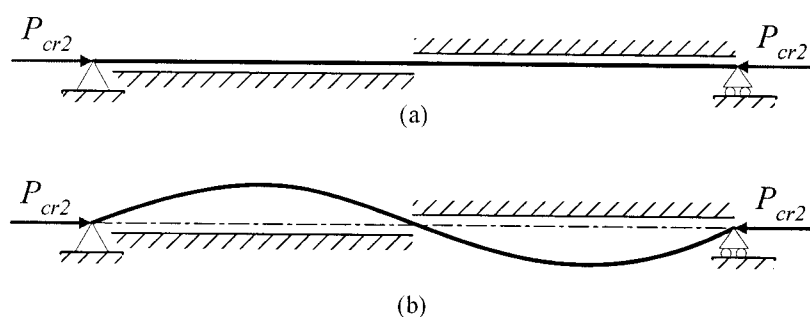


Figure 5-6. Mode 2 buckling formation by external restraint (Hexiang, 1999)

This investigation focuses on the development of preferential buckling geometry for the fin layer that can be achieved with high-temperature microlamination, as well as the implementation of the buckling theory to predict the configuration of the higher buckling mode structure. A rudimentary experiment was carried out to demonstrate the characteristics of the higher mode of buckling. The experimental result also showed that controlling the buckling mode of the fin was possible by using the TEER fixture. As a result, the knowledge developed in this study will be useful for future development of high performance MECS devices.

5.3 Theoretical Models

A schematic for illustrating channel nonuniformity due to fin buckling in mode 1 and higher modes is presented in Figure 5-7.

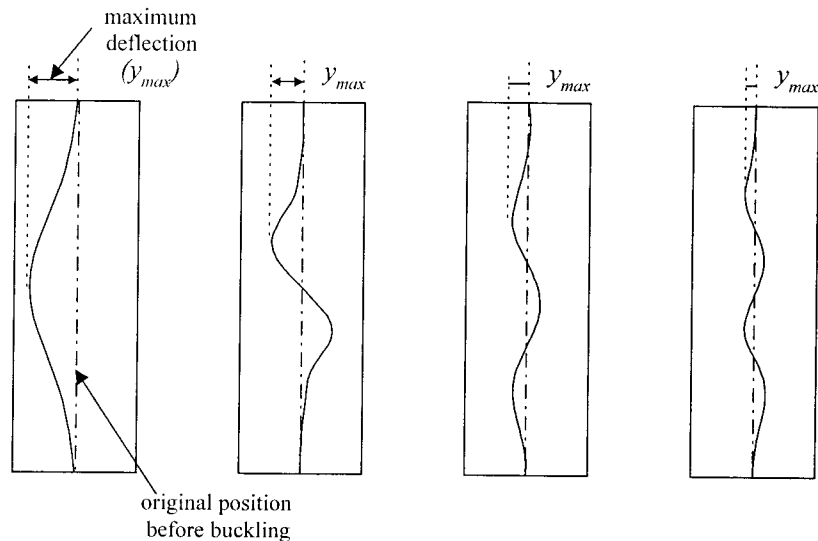


Figure 5-7. Geometry of fin warpage induced by buckling from mode 1 to mode 4

To determine if a fin will buckle, the mode of failure needs to be confirmed by calculating the stress at the critical point of buckling. This critical stress needs to be smaller than the yield stress of the fin material; otherwise, the plate will yield before it buckles (Gere, et al., 1997). For the fixed-ended boundary condition, the critical stress can be calculated from:

$$\sigma_c = \frac{P_c}{A} = \frac{4 \cdot \pi^2 \cdot E \cdot I}{A \cdot L^2} \quad (1)$$

For mode 2 buckling, equation (1) will change to:

$$\sigma_c = \frac{P_c}{A} = \frac{8.18 \cdot \pi^2 \cdot E \cdot I}{A \cdot L^2} \quad (2)$$

For buckling geometries higher than mode 2, the fin is assumed to buckle similar to a simply-support condition; therefore, the critical stress will be calculated from:

$$\sigma_c = \frac{P_c}{A} = \frac{n^2 \cdot \pi^2 \cdot E \cdot I}{A \cdot L^2} \quad (3)$$

where n is the mode number.

The second consideration is the force due to thermal expansion (P_t). As long as P_t is larger than the critical load of buckling (P_c), the fin layer will buckle. The force due to the difference in the CTE can be calculated from:

$$P_t = A \cdot E \cdot (\alpha_1 - \alpha_2) \cdot \Delta T \quad (4)$$

In this investigation, α_l is the CTE of the laminae and α_2 is the CTE of the bonding fixture, while ΔT is the difference between room temperature and diffusion temperature.

As the thermal loading stress caused by the temperature changes reaches the plastic strength of the base material, the buckling fin will be permanently deformed. When buckling happens, the buckling theory can be used to evaluate the change in the fin geometry such as the maximum deflection.

The deflection function of mode 1 buckling is described by:

$$y = A_{mp} \cdot \left(1 - \cos\left(\frac{2 \cdot \pi \cdot x}{L}\right) \right) \quad (5)$$

while the deflection function of mode 2 buckling is

$$y = A_{mp} \cdot \left[\sin(\mu \cdot x) - \mu \cdot x - \frac{\mu \cdot L}{2} \cdot (\cos(\mu \cdot x) - 1) \right] \quad (6)$$

For a buckling geometry higher than mode 2, a sine-form function:

$$y = A_{mp} \cdot \sin\left(\frac{n \cdot \pi \cdot x}{L}\right) \quad (7)$$

will be used to approximate the deflection geometries. The implementation of these buckling shapes is also discussed in detail in Appendix E.

The maximum deflection caused by fin buckling can be calculated based on the geometry of the buckling deflection function. Since the fin width and the fixture slot at the elevated temperature can be calculated (L_f' and L_s'), the arc length formula is applied to solve for the magnitude of fin buckling:

$$L1' = \int_0^{L2'} \sqrt{1 + \left(\frac{dy}{dx}\right)^2} dx \quad (8)$$

The fin deflection from either equation (5), (6), or (7) will be substituted into equation (8) to solve for amplitude, which is dependent on the mode of buckling. However, since the buckling form of equations (5) to (7) do not have a closed-form anti-derivation, approximation methods need to be implemented. According to previous investigations (Chapter 3 and 4), the following approximation equation can be applied:

$$L1' = \int_0^{L2'} \sqrt{1 + \left(\frac{dy}{dx}\right)^2} dx \approx \int_0^{L2'} \left\{ 1 + \frac{\left(\frac{dy}{dx}\right)^2}{2} \right\} dx \quad (9)$$

5.4 Preliminary Experiment

5.4.1 Mode 1 and Mode 2 Buckling

To present the implication of the buckling theory in order to predict the formation of a preferential buckling geometry, a rudimentary experiment was conducted. The constraining technique has been implemented to generate the higher mode buckling structure. The specimen consists of two features: channel layers and a fin plate as shown in Figure 5-8. All layers were cut from a 0.1778-mm thick 304 stainless steel shim using a milling machine within an accuracy of ± 0.025 -mm tolerance. Figure 5-8 also highlights the area that buckling is expected

to be induced by excessive thermal expansion force. The dimension of this buckling area was assumed to have the same deflection as the nominal geometry stated in Appendix E.

After patterning, laminae were cleaned by rinsing the shims with Acetone, Ethanol alcohol, and De-ionized water (AED), and then put into the alignment fixture to be diffusion-bonded in a vacuum hot press. The bonding conditions for this experiment were set at 820 °C with 5 MPa applied pressure for one hour. Bonding pressure was applied only after the specimens had reached the thermal equilibrium at the bonding temperature and was released during the cool-down cycle so that the laminate could contract uniformly without inducing any stress. The loading of the test specimen onto the TEER fixture is presented in Figure 5-9. With larger CTE, the width of the specimen was slightly smaller than the fixture slot at room temperature for easy loading.

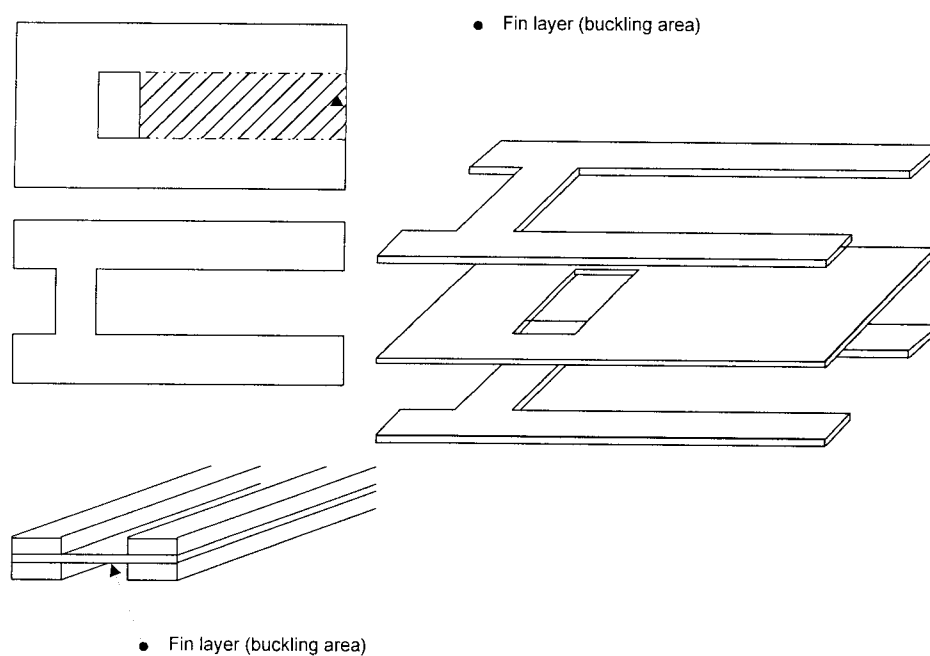


Figure 5-8. Geometry of test specimen for rudimentary experiment

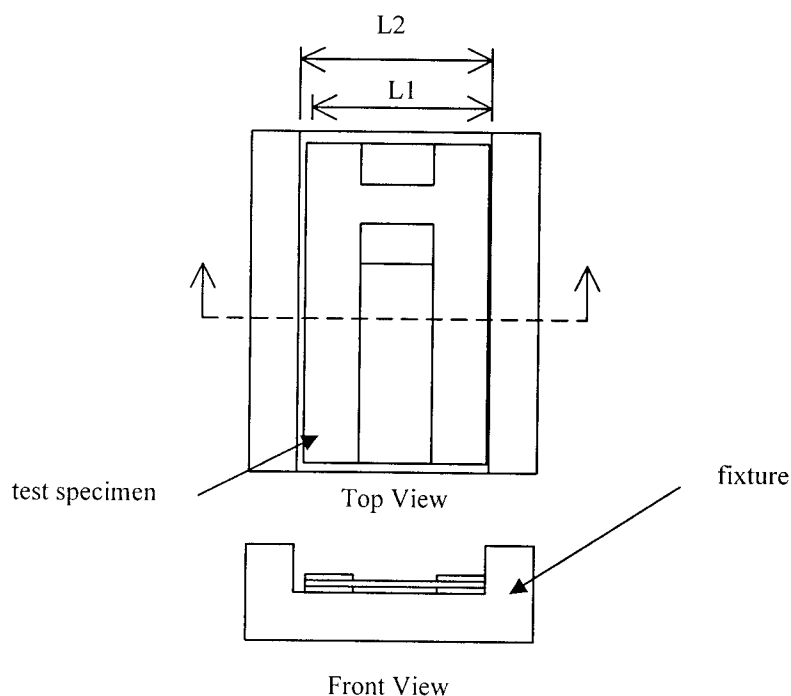


Figure 5-9. Loading of the test specimen laminae onto the TEER fixture

The contact profilometer used to measure the fin deflection in this study was the Dektak3 Surface Profiler from VEECO Metrology Group, Inc. This equipment is capable of surface measurement with nanometer resolution. More equipment descriptions are presented in Appendix H.

For this study, the experiment was divided into 2 sets: mode 1 buckling and mode 2 buckling. Both tests were based on the same initial laminae geometry, only the fin from the second set was intentionally induced to form mode 2 buckling. In addition, to be able to promote the mode 2 structure on the second specimen, the constraints were placed against the midpoint of the fin width, using two graphite laces, to restrain the fin buckling at that location, as mentioned previously.

5.4.2 Mode 10 Buckling

An additional experiment on mode 10 buckling has been conducted based the constraining technique as shown on Figure 5-6. A constraint fixture was fabricated from graphite block to provide the external restraint on the fin to prevent the fundamental buckling during microlamination as well as to manipulate the fin to buckle into mode 10 geometry. Configuration of this fixture is presented in Appendix H. In this experiment, in stead of using 0.1778-mm thick stainless steel, a 0.0508 mm 304 stainless steel was used as the fin layer. With thinner material, the registration force forming during thermal expansion is able to exceed the critical point of buckling of mode 10. The fin width was set up to be 20 mm and the bonding conditions were set at 800 °C, 5 MPa applied pressure, and one hour dwell time. The other experimental procedures were the same as the first experimental setup.

5.5 Results and Discussion

The following sections represent both the analytical evaluation of nonuniform flow passage due to fin buckling in different modes and the results from the preliminary experiment.

5.5.1 Analytical Results for Various Modes of Buckling

This section presents the analytical evaluation of higher modes buckling based on the nominal dimension of a heat exchanger where specimens were induced to form a various mode of fin buckling (mode 1, mode 2, and mode 10) based on 50 μm interference between the laminae and bonding fixture at the

bonding temperature. Assuming that the registration force is exceeded a critical load of buckling and fin buckling becomes the mode of failure.

The arc length formula and the approximation technique were used to determine the maximum deflection of the buckled fin. Figure 5-10 illustrates the relationship of the maximum deflection generated by mode 1, mode 2 and mode 10 buckling to the interference between the fixture and the laminae at bonding temperature. Notice that higher modes of buckling resulted in a smaller maximum deflection, and the magnitude of this deflection was also a function of the mode number. For example, mode 2 deflection is about one-half of a fundamental mode warpage, while mode 10 deflection is about 10 times smaller than the magnitude of warpage from mode 1.

However, to be able to form a higher mode of buckling, registration force needs to be greater than the critical buckling load. Regarding the fin geometry for the first set of the experiment (thickness = 0.1778 mm), the analysis showed that mode 2 buckling can happen only when the interference is equal to or greater than 50 μm interference, whereas mode 10 could not happen under this experimental condition since the critical load was larger than the registration force. Nonetheless, changing fin thickness or adjusting the testing condition would allow the induction of this mode if that registration force exceeds the mode of failure. This is the reason that the author decided to change the thickness of material from 0.1778 mm to 0.0508 mm to permit fin buckling into mode 10 geometry.

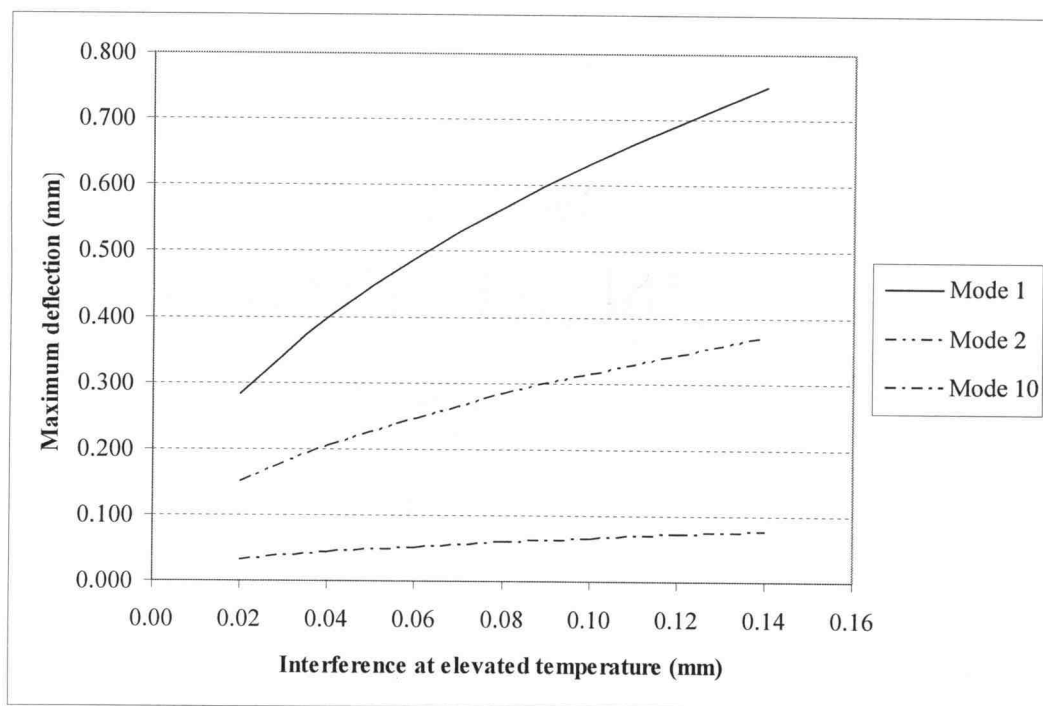


Figure 5-10. Magnitude of buckling of a fin layer at different amounts of clearance between the laminae and fixture

5.5.2 Experimental Results

The microlaminated devices from the first test setup (mode 1 and mode 2) are presented in Figure 5-11. Figure 5-11 (a) represents the test specimen from mode 1 buckling, while Figure 5-11 (b) displays the mode 2 buckling structure. Correspondingly, the buckling characteristics of both tests measured by the Dektak3 surface profiler are illustrated in Figure 5-12.

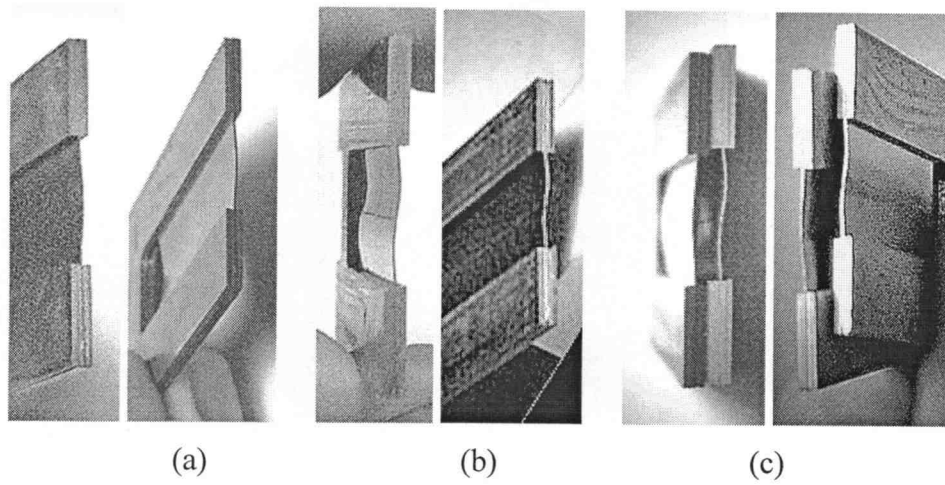


Figure 5-11. Photographs of laminate from (a) mode 1 and (b) mode 2 buckling

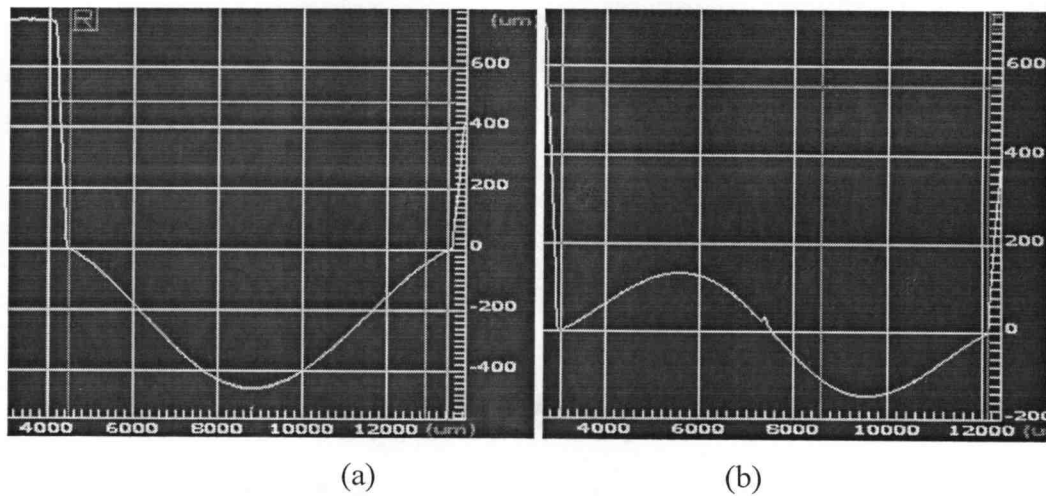


Figure 5-12. Deflection profiles of laminate from (a) mode 1 buckling, (b) mode 2 buckling

According to the measurement, the magnitude of warpage from mode 1 buckling ranged from 0.025 to 0.460 mm (from left to right). When comparing this mode 1 result to Figure 5-10, it shows that the experimental result at the maximum

magnitude is close to the theoretical prediction (0.438 mm). On the other hand, the maximum warpage from the mode 2 buckling specimen ranged from 0.12 to 0.16 mm, which is smaller than the analytical value (0.21 mm). Moreover, it was observed that the magnitude of deflection in opposite directions in vertical axis was not the same. Sources of the experimental error that could contribute to the deviation from the theoretical model might include the asymmetrical geometry of the test specimens, the variation of laminae dimension, the property of the fin material, or the precision of constraint placement, among others.

First of all, when machining the laminae with the milling machine, burrs might be encountered and could make the fin behave differently during buckling. The other error might be the design of test specimen. As can be seen in Figure 5-8, the design of the specimen is not symmetrical (from left to right). This asymmetrical geometry could cause the buckling deflection at the other end to be larger than in the position next to the stiffed area. This might be the reason why we see the variation of the maximum of buckling from both laminates. In addition, the registration force to cause a fin to buckle was very close to the critical load for mode 2 formation. This would affect the buckling of mode 2, in which some part of the fin was resist to buckling but other parts has already warped; therefore, the final warpage result ended up with smaller deflection than the one from the theory. In addition, the effect of inaccurate placement of the constraints might have caused an asymmetric buckling of mode 2 between the peak and valley of deflection. Last but not least, residual stress might play a key role for this variation as well. The stainless steel shims used in this experiment were fabricated by a cold work process. Therefore, residual stress of cold work shim might prevent the stainless steel laminae from expanding freely during diffusion bonding.

The result from mode 10 buckling is presented in Figure 5-13 and 5-14. Figure 5-13 shows the photograph of the actual specimen when the fin was induced to form mode 10 buckling. The deflection profile of this specimen is shown in Figure 5-14. This measurement was performed on a Dektak3 surface profiler.

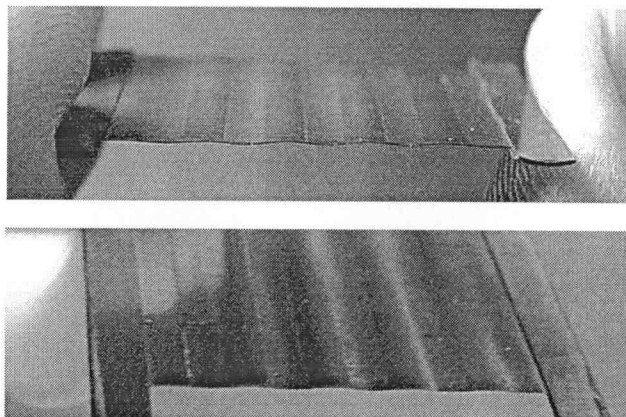


Figure 5-13. Photographs of laminate from mode 10 buckling

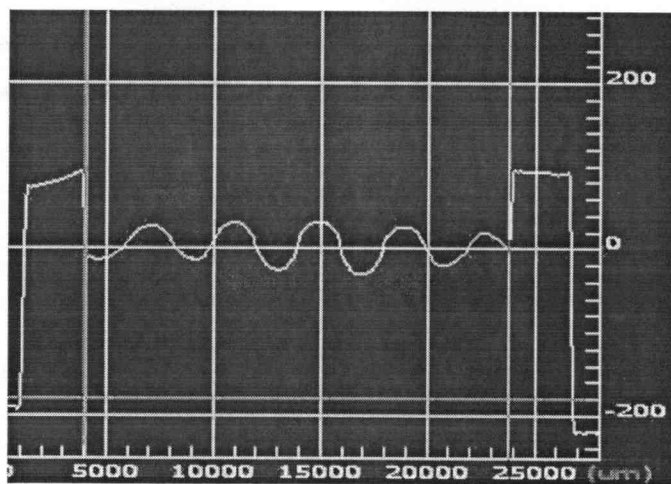


Figure 5-14. Deflection profiles of mode 10 buckling

As can be seen on the profile graph, the magnitude of mode 10 deflection was about 70 - 80 μm . The magnitude of deflection from theoretical calculations for this configuration was equal 100 μm . Furthermore, it was observed that the magnitude of deflection from all ten of them were not exactly the same. Sources of variation could be the property of the fin material and the accuracy of the fixture.

As mentioned previously, the material used in this experiment is cold-rolled. It might contain residual stress that can affect the buckling behavior of the fin layer, which can result in the variation in the magnitude of deflection. In addition, the constraints insert for this experiment were fabricated from a conventional milling machine; therefore, there might be some variation in the fixture that could induce nonuniform buckling geometry as in Figure 5-14.

5.6 Conclusions

It is evident that buckling nonuniformity has a significant effect on the performance of the heat transfer device due to flow maldistribution from a nonuniform channel. Induction of the higher mode of buckling makes it feasible to decrease this nonuniformity as well as the impact of channel deviation on heat transfer performance. A constraining technique was implemented to encourage higher modes of fin buckling. This technique prevents the fin from deflecting into a fundamental mode, but allows it to buckle into a chosen mode with respect to the location of constraints.

A rudimentary experiment was performed to verify the buckling formation of mode 1, mode 2, and mode 10. The experimental results demonstrated that a higher mode of buckling can be controlled, but the experimental measurements showed some deviation of the magnitude of buckling from the analytical predictions. The sources of error have been discussed, which potentially included accuracy of the machine tool, material property, and specimen design. Further work should include higher modes buckling formation with uniform deflection. In addition, intentional buckling of a higher mode based on other techniques should be studied to find an effective procedure to reduce the effect of flow maldistribution as well as to maximize the performance of the meso-scale heat exchanger.

5.7 References

- Alfutov, N. A., *Stability of Elastic Structures*. New York: Springer, 2000.
- Allen, H. G. and Bulson, P. S., *Background to buckling*. London, New York: McGraw-Hill Book Co., 1980.
- Ameel, T. A., Papautsky, I., Warrington, R. O., Wegeng, R. S., and Drost, M. K., "Miniaturization Technologies for Advanced Energy Conversion and Transfer Systems," *Journal of Propulsion and Power*, vol. 16, pp. 577-582, 2000.
- Bloom, F. and Coffin, D., *Handbook of thin plate buckling and postbuckling*. Boca Raton, FL: Chapman & Hall/CRC, 2000.
- Drost, M. K. and Friedrich, M., "Miniature Heat Pumps for Portable and Distributed Space Conditioning Applications," presented at Proceedings of IECEC, 1997.
- Drost, M. K., Friedrich, M., Martin, C., Martin, J., and Cameron, R., "Recent Developments in Microtechnology-Based Chemical Heat Pumps," presented at 3rd International Conference on Microreaction Technology, Frankfurt, Germany, 1999.
- Gere, J. M. and Timoshenko, S. P., *Mechanics of materials*. Boston: PWS-KENT Pub. Co., 1997.
- Hexiang, L., Minghui, F., Lark, R. J., and Williams, F. W., "The Calculation of Critical Buckling Loads for Externally Constrained Structures," *Communications in Numerical Methods in Engineering*, vol. 15, pp. 193-201, 1999.
- Jovanovic, G. "Chemical and Reactor-based Systems.", 2001 Available: www.me.orst.edu/research/mecs/projects/.
- Kaka, S., Shah, R. K., and Bergles, A. E., *Low Reynolds number flow heat exchangers : advanced study institute book*. Washington: Hemisphere Pub. Corp., 1983.
- Mai, W.-a. "Buckling analysis of timoshenko beam/column." *Master of Science Thesis*, Civil Engineering: Cleveland State University, 1991.

- Martin, P. M., Bennett, W. D., and Johnson, J. W., "Microchannel heat exchangers for advanced climate control," presented at Proceedings of SPIE, 1995.
- Martin, P. M., Matson, D. W., and Bennett, W. D., "Microfabrication Methods For Microchannel Reactors and Separations Systems," *Chemical Engineering Communications*, vol. 173, pp. 245-254, 1999.
- Matson, D. W., Martin, P. M., and Bennett, W. D., "Laser micromachined microchannel solvent separator," presented at Proceedings of SPIE, 1997.
- Matson, D. W., Martin, P. M., Stewart, D. C., Tonkovich, A. L. Y., White, M., Zilka, J. L., and Roberts, G. L., "Fabrication of Microchannel Chemical Reactors Using a Metal Lamination Process," presented at Third International Conference on Microreaction Technology, Frankfurt, Germany, 1999.
- Paul, B. K. and Peterson, R. B., "Microlamination for Microtechnology-based Energy, Chemical, and Biological System," presented at ASME IMECE, Nashville, Tennessee, 1999.
- Shames, I. H., *Introduction to solid mechanics*. Englewood Cliffs, NJ: Prentice-Hall, 1989.
- Simitses, G. J., *An Introduction to the Elastic Stability of Structures*. Englewood Cliffs, New Jersey: Prentice-Hall, Inc., 1976.
- Thomas, J. "Establishing Thermally Enhanced Edge Registration (TEER) as a Feasible Alignment Technique for Metallic Laminated Devices." *M.S. Thesis*, Industrial Engineering: Oregon State University, 2001.
- Thomas, J. and Paul, B. K., "Thermally-Enhanced Edge Registration (TEER) for Aligning Metallic Microlaminated Devices," presented at Transactions of NAMRC XXX, West Lafayette, IL, 2002.
- Tonkovich, A. L. Y., Zilka, J. L., Jimenez, D. M., LaMont, M. J., and Wegeng, R. S., "Microchannel Chemical Reactors for Fuel Processing," presented at AIChE 1998 Spring National Meeting, New Orleans, 1998.
- Wegeng, R. S., Drost, M. K., and Brenchley, D. L., "Process Intensification Through Miniaturization of Chemical and Thermal Systems in the 21st Century," *Pacific Northwest National Laboratory*, 1999.

CHAPTER 6

CONCLUSIONS AND RECOMMENDATIONS

6.1 Summary

An investigation of the effect of shape variation in the metallic microlaminated device has been presented. It was found that the major shape variation happens primarily during the aligning and bonding process. Two types of shape variations were discussed in this dissertation: fin buckling and channel misalignment. Furthermore, the thermal performance of the heat exchanger was chosen to be the criteria to evaluate the impact of these two types of shape variation. It has been shown that fin warpage can lower the thermal performance of the device by inducing flow maldistribution between consecutive flow channels. On the other hand, channel misalignment causes minor reduction to the heat effectiveness of the device with respect to the change in the heat transfer area. According to the base case heat exchanger discussed in Chapter 2, a microlaminated device with fin buckling could cause over 60% reduction in the number of transfer units (NTU) or about a threefold increase in heat transfer area needed to compensate this loss. One suggestion to mitigate the problem is to induce higher modes of fin buckling, which can result in smaller average channel deviation as well as flow maldistribution. For the system of interest, the result of flow maldistribution becomes insignificant when the fin is induced beyond mode 10 buckling.

In order to fabricate the precision metal microlaminated device, the bonding fixture is required. A thermally-enhanced edge registration (TEER) has been implemented for aligning laminate structure for high-temperature microlamination.

Using the difference in thermal expansion between aligned materials and a bonding fixture, TEER is able to precisely manufacture the laminated structure with micron-scale misalignment. However, fin buckling can be generated easily if the registration force between the fixture and the laminae exceeds the critical buckling load as well as the elastic limit of deformation. Buckling theory was implemented to predict the tolerance limits on the TEER fixture. With respect to both theoretical and experimental results, it was found that beyond 10 μm interference at the bonding temperature, the fin started to buckle. In the mean time, the amount of misalignment was found proportional to the clearance of the fixture at the bonding temperature. The parameter that controls the amount of misalignment might be related to surface roughness and pressure which may be an interesting area for future investigation.

In addition, there is evidence that pre-orientation of the laminae plays a key role in the variation of the misalignment at different locations of the specimen. According to the additional experiment, constraining the laminae with adhesive tape showed the reduction in variations among different locations of misalignment measurement. From this study, the average misalignment achieved at tight tolerance was about 6 μm . The author also presented an analytical evaluation of the critical point of fin buckling as a function of fin thickness. The relationship between fin stiffness or thickness and the critical load or interference has been derived, thus the critical point of fin buckling could be estimated for other configurations of the microchannel device.

As we found that fin buckling is more important than channel misalignment, and the tolerance limit of the bonding fixture is very tight, the study was then focused on the technique to reduce or control fin buckling during high-temperature microlamination. First, the concept of fixture compliance and beam bending were applied to TEER for the purpose of increasing the tolerance limit for fin warpage. The tolerance limit in the compliant TEER can be preset so that its limit was proportional to the height of the fixture insert. Experimental study was

presented and was found to be in agreement with theoretical analysis. ANOVA also showed that both fin thickness as well as interference between fin width and fixture slot affect the magnitude of fin buckling. For thick lamina, the fin layer not only is robust for buckling, but also able to generate a greater amount of fixture compliance (or reduce the amount of interference) and extend the limitation of the fixture tolerance. Sources of error during experiment have been investigated and discussed. It was found that fabrication of laminae and fixtures can contribute to variation of interference displacement and vary the result of fin buckling. With respect to this new approach, the tolerance limits have been improved and was found to be well within the tolerance limits of the conventional machine tools.

Regarding the last part of this dissertation, investigation on intentional buckling has been discussed. By constraining a vertical movement of fin during buckling at specific locations, the fin could be induced to buckle into a preferred manner. As discussed earlier in the prior section, the effect of flow maldistribution due to channel nonuniformity becomes smaller when the number of buckling modes is increased. The relationship between the interference and the magnitude of buckling has been presented theoretically. As we expected, the magnitude of fin warpage was indirectly proportional to the mode number of buckling. Once a buckling geometry reached mode 10, the deflection magnitude was only about one-tenth of mode 1 buckling magnitude. This explains why the effect of fin buckling in the higher mode is no longer significant to the device performance.

6.2 Recommendations for Future Work

In regards to the effect of flow maldistribution, nonuniform flow channels should be avoided. This dissertation has presented two strategies to reduce the channel deviation due to fin buckling shape variation: modification of bonding fixture and intentional buckling laminate. Though the experimental results were in

agreement with theoretical prediction, there were some variations of fin warpage, especially where this deflection was supposed to be zero. Further study needs to be done in order to identify the source of error, whether it relates to the material property or the bonding condition for microlamination. In fact, it is possible that there is a limit in miniaturization in terms of fin thickness or the device geometry. Also, since specific application in MECS might require a specific material, materials other than stainless steel should be tested to verify that the experimental results still behave similarly to the theory for a variety of materials, and to bring the effect of material property into the picture.

In the last chapter, only one technique to induce a higher mode buckling has been discussed, the constraining technique. Future research should continue to verify that other techniques such as notching could be used to induce the preferential buckling. Moreover, additional experiment on higher modes fin buckling induction should be conducted to better understand and access the difference between the theoretical prediction and the experimental result. In addition, the performance of devices based on this structure could be tested in comparison to the fundamental mode of buckling. It might be possible that forming of multi-mode fins to separate two consecutive channels not only would reduce the effect of channel deviation, but also increase the overall efficiency of the counterflow heat exchanger due to the increase in heat transfer area.

This dissertation also included some suggestions on high-volume microlamination. In chapter 3, the discussion was presented that securing the laminae together proved that the consistent misalignment can be achieved at an acceptable precision level. This strategy should be implemented into a practical technique so that multiple numbers of laminae could automatically be pre-aligned before bonding. Instead of using an adhesive tape, stainless steel foils could be used to restrain the stack of laminae during microlamination. With the same CTE between the laminae and the foil, the whole assembly might not encounter fin buckling due to the excessive registration during the bonding cycle. But with the

restriction in movement and rotation, precision alignment could be achieved. Last but not least, an approach to supply both registration and clamping force to the bonding laminae should be investigated. We should be able to apply the clamping force to the laminate by the use of the difference in CTE. The future goal is to be able to manufacture the microlaminated device with a mass production process such as a conveyORIZED APCVD reactor, but still achieve a device with buckle-free and precise alignment similar to the results from the compliant TEER.

BIBLIOGRAPHY

- Alfutov, N. A., *Stability of Elastic Structures*. New York: Springer, 2000.
- Allen, H. G. and Bulson, P. S., *Background to buckling*. London, New York: McGraw-Hill Book Co., 1980.
- ALSC, *Stainless Steel Handbook*. Pittsburgh, Pennsylvania: Allegheny Ludlum Steel Corporation, 1956.
- Ameel, T. A., Papautsky, I., Warrington, R. O., Wegeng, R. S., and Drost, M. K., "Miniaturization Technologies for Advanced Energy Conversion and Transfer Systems," *Journal of Propulsion and Power*, vol. 16, pp. 577-582, 2000.
- Ameel, T. A., Warrington, R. O., Wegeng, R. S., and Drost, M. K., "Miniaturization Technologies Applied to Energy Systems," *Energy Conversion and Management*, vol. 38, pp. 969-982, 1997.
- Ashby, M. F., *Materials selection in mechanical design*. Oxford ; Boston: Butterworth-Heinemann, 1999.
- Ashley, S., "Turbines on a dime," *Mechanical engineering*, vol. 119, pp. 78-81, 1997.
- ASM, *Source Book on Stainless Steels*. Metals Park, Ohio: The Periodical Publication Department, American Society for Metals, 1976.
- ASTM, "The Elevated-Temperature Properties of Stainless Steels," in *ASTM Data Series Publication DS 5 - S1*, 1965.
- ASTM, "An Evaluation of the Yield, Tensile, Creep, and Rupture Strengths of Wrought 304, 316, 321, and 347 Stainless Steels at Elevated Temperatures," in *ASTM Data Series DS 5S2*, 1969.
- Bier, W., Keller, W., Linder, G., Seidel, D., and Schubert, K., "Manufacturing and Testing of Compact Micro Heat Exchangers with High Volumetric Heat Transfer Coefficients," *ASME: DSC series*, vol. 19, pp. 189-197, 1990.
- Bloom, F. and Coffin, D., *Handbook of thin plate buckling and postbuckling*. Boca Raton, FL: Chapman & Hall/CRC, 2000.

- Brenchley, D. L., "Applications for Micro Chemical and Thermal Systems," presented at IMRET 5 2001 International Conference on Microreaction Technology, Strasbourg, France, 2001.
- Brenchley, D. L. and Wegeng, R. S., "Status of Microchemical Systems Development in the United States of America," presented at AIChE 1998 Spring National Meeting, New Orleans, 1998.
- Brooks, K. P., Martin, P. M., Drost, M. K., and Call, C. J., "Mesoscale Combustor/Evaporator Development," presented at ASME IMECE Conference, Nashville, TN, 1999.
- Chavez, S. A., Korth, G. E., and Harper, D. M., "High-temperature tensile and creep data for Inconel 600, 304 stainless steel and SA106B carbon steel," *Nuclear Engineering and Design*, vol. 148, pp. 351-363, 1994.
- Chowdhury, K. and Sarangi, S., "Effect of Flow Maldistribution on Multipassage Heat Exchanger Performance," *Heat transfer engineering*, vol. 6, pp. 45-54, 1985.
- Christenson, T. R. and Schmale, D. T., "A Batch Wafer Scale LIGA Assembly and Packaging Technique Via Diffusion Bonding," presented at The Twelfth IEEE international conference on Micro Electro Mechanical Systems, 1999.
- Cuta, J. M., Bennett, W. D., McDonald, C. E., and Ravigururaran, T. S., "Fabrication and Testing of Micro-Channel Heat Exchangers," presented at SPIE proceedings, 1995.
- Daymo, E. A., VanderWiel, D. P., Fitzgerald, S. P., Wang, Y., Rozmiarek, R. T., LaMont, M. J., and Tonkovich, A. L. Y., "Microchannel Fuel Processing for Man Portable Power," presented at AIChE 2000 Spring National Meeting, Atlanta, GA, 2000.
- Drost, M. K. and Friedrich, M., "Miniature Heat Pumps for Portable and Distributed Space Conditioning Applications," presented at Proceedings of IECEC, 1997.
- Drost, M. K., Friedrich, M., Martin, C., and Martin, J., "Mesoscopic Heat-Actuated Heat Pump Development," presented at ASME IMECE Conference, Nashville, TN, 1999.
- Drost, M. K., Friedrich, M., Martin, C., Martin, J., and Cameron, R., "Recent Developments in Microtechnology-Based Chemical Heat Pumps," presented at 3rd International Conference on Microreaction Technology, Frankfurt, Germany, 1999.

- Drost, M. K., Wegeng, R. S., Martin, P. M., Brooks, K. P., Martin, J. L., and Call, C., "MicroHeater," presented at AIChE 2000 Spring National Meeting, Atlanta, GA, 2000.
- Edmondson, N. F. and Redford, A. H., "A compliance device for flexible close tolerance assembly," *Industrial Robot*, vol. 28, pp. 54-62, 2001.
- Fang, W., Lee, C.-H., and Hu, H., -H., "On the buckling behavior of micromachined beams," *Journal of Micromechanical and Microengineering*, vol. 9, pp. 236-244, 1999.
- Fang, W. and Wickert, J. A., "Post buckling of micromachined beams," *Journal of Micromechanical and Microengineering*, vol. 4, pp. 116-122, 1994.
- French, P. J., "Integration of MEMS devies," *Proceeding of SPIE -- the International Society for Optical Engineering*, vol. 3892, pp. 39-48, 1999.
- Frost, H. J. and Ashby, M. F., *Deformation-Mechanism Maps: The Plasticity and Creep of Metals and Ceramics*. New York: Pergamon Press, 1982.
- Gere, J. M. and Timoshenko, S. P., *Mechanics of materials*. Boston: PWS-KENT Pub. Co., 1997.
- Hexiang, L., Minghui, F., Lark, R. J., and Williams, F. W., "The Calculation of Critical Buckling Loads for Externally Constrained Structures," *Communications in Numerical Methods in Engineering*, vol. 15, pp. 193-201, 1999.
- Jackman, J., Deng, J.-J., Ahn, H.-i., Kuo, W., and Vardeman, S., "Compliance measure for the alignment of cylindrical part features," *IIE Transactions*, vol. 26, pp. 2-10, 1994.
- Jovanovic, G., Chaplen, F., McFadden, P., Plant, T., Trempey, J., Paul, B. K., and Liburdy, J. "Environmental Testing and High-Throughput Screening Devices.", 2001 Available: www.me.orst.edu/research/mecs/projects/.
- Kaka, S., Shah, R. K., and Bergles, A. E., *Low Reynolds number flow heat exchangers : advanced study institute book*. Washington: Hemisphere Pub. Corp., 1983.
- Kanlayasiri, K., Wattanatchariya, W., and Paul, B. K., "ASPECT RATIO LIMITS IN MICROLAMINATION DUE TO MACHINING METHODS," *Journal of Manufacturing Science and Engineering (To be published)*, 2001.

- Kawano, K., Minakami, K., Iwasaki, H., and Ishizuka, M., "Micro Channel Heat Exchanger for Cooling Electrical Equipment," *ASME (HTD) -- Proceeding of the ASME Heat Transfer Division*, vol. 361-3, pp. 173-180, 1998.
- Kays, W. M. and Crawford, M. E., *Convective heat and mass transfer*. New York: McGraw-Hill, 1993.
- Kitto, J. B. and Robertson, J. M., "Effects of Maldistribution of Flow on Heat Transfer Equipment Performance," *Heat transfer engineering*, vol. 10, pp. 18-25, 1989.
- Krause, V., Treusch, H.-G., Loosen, P., Kimpel, T., Biesenbach, J., Kosters, A., Robert, F., Oestreicher, H., Marchiano, M., and DeOdorico, B., "Microchannel Coolers for High Power Laser Diodes in Copper Technology," *Proceeding of SPIE -- the International Society for Optical Engineering*, vol. 2148, 1994.
- Lalot, S., Florent, P., Lang, S. K., and Bergles, A. E., "Flow maldistribution in heat exchangers," *Applied Thermal Engineering*, vol. 19, pp. 847-863, 1999.
- Lohner, K. A., Chen, K.-S., Ayon, A. A., and Spearing, S. M., "Microfabricated Silicon Carbide Microengine Structures," *Proceeding of Material Resource Society Symposium*, vol. 546, pp. 85-90, 1999.
- London, A. L., "Laminar Flow Gas Turbine Regenerators--The Influence of Manufacturing Tolerances," *Transactions of ASME: Journal of Engineering for Power*, vol. 92, pp. 46-56, 1970.
- Mai, W.-a. "Buckling analysis of timoshenko beam/column." *Master of Science Thesis*, Civil Engineering: Cleveland State University, 1991.
- Mantell, C. L., *Carbon and Graphite Handbook*. New York: Interscience Publishers, 1968.
- Martin, P. M., Bennett, W. D., Hammerstrom, D. J., Johnson, J. W., and Matson, D. W., "Laser micromachined and laminated microchannel components for chemical sensors and heat transfer applications," presented at Proceedings of SPIE, 1997.
- Martin, P. M., Bennett, W. D., and Johnson, J. W., "Microchannel heat exchangers for advanced climate control," presented at Proceedings of SPIE, 1995.
- Martin, P. M., Matson, D. W., and Bennett, W. D., "Microfabrication Methods For Microchannel Reactors and Separations Systems," *Chemical Engineering Communications*, vol. 173, pp. 245-254, 1999.

- Martin, P. M., Matson, D. W., Bennett, W. D., and Hammerstrom, D. J., "Fabrication of plastic microfluidic components," presented at Proceedings of SPIE, 1998.
- Martin, P. M., Matson, D. W., Bennett, W. D., Stewart, D. C., and Bonham, C. C., "Laminated Ceramic Microfluidic Components for Microreactor Applications," presented at AiChE 2000 Spring National Meeting, Atlanta, GA, 2000.
- Martin, P. M., Matson, D. W., Bennett, W. D., Stewart, D. C., and Lin, Y., "Laser Micromachined and Laminated Microfluidic Components for Miniaturized Thermal, Chemical and Biological Systems," presented at Proceeding of SPIE -- the International Society for Optical Engineering, 1999.
- Matson, D. W., Martin, P. M., and Bennett, W. D., "Laser micromachined microchannel solvent separator," presented at Proceedings of SPIE, 1997.
- Matson, D. W., Martin, P. M., Stewart, D. C., Tonkovich, A. L. Y., White, M., Zilka, J. L., and Roberts, G. L., "Fabrication of Microchannel Chemical Reactors Using a Metal Lamination Process," presented at Third International Conference on Microreaction Technology, Frankfurt, Germany, 1999.
- McDonald, C. F., "Low-cost compact primary surface recuperator concept for microturbines," *Applied Thermal Engineering*, vol. 20, pp. 471-497, 2000.
- Minoshima, K., Inoute, S., Terada, T., and Komai, K., "Influence of Specimen Size and Sub-Micron Notch on the Fracture Behavior of Single Crystal Silicon Microelements and Nanoscopic AFM Damage Evaluation," presented at Material Research Society Symposium Proceedings, Boston, MA, 1998.
- Mondt, J. R., "Effects of Nonuniform Passages on Deepfold Heat Exchanger Performance," *Transactions of ASME: Journal of Engineering for Power*, vol. 99, pp. 657-663, 1977.
- Mueller, A. C., "Effects of Some Types of Maldistribution on the Performance of Heat Exchangers," *Heat transfer engineering*, vol. 8, pp. 75-86, 1987.
- Mueller, A. C. and Chiou, J. P., "Review of Various Types of Flow Maldistribution in Heat Exchangers," *Heat transfer engineering*, vol. 9, pp. 36-50, 1988.
- Papautsky, I., Gale, B. K., Mohanty, S., Ameel, T. A., and Frazier, A. B., "Effects of rectangular microchannel aspect ratio on laminar friction constant," presented at SPIE proceedings, 1999.

- Paul, B. K., Dewey, T., Alman, D., and Wilson, R. D., "Intermetallic Microlamination for High-Temperature Reactors," presented at 4th International Conference on Microreaction Technology, Atlanta, GA, 2000.
- Paul, B. K., Hasan, H., Thomas, J., Wilson, R. D., and Alman, D., "Limits on Aspect Ratio in Two-Fluid Micro-Scale Heat Exchangers," *in press*, 2000.
- Paul, B. K. and Peterson, R. B., "Microlamination for Microtechnology-based Energy, Chemical, and Biological System," presented at ASME IMECE, Nashville, Tennessee, 1999.
- Paul, B. K., Peterson, R. B., and Wattanuchariya, W., "The Effect of Shape Variation in Microlamination on the Performance of High-Aspect-Ratio, Metal Microchannel Arrays," presented at Proceedings of the third international conference on microreaction technology, 1999.
- Paul, B. K. and Terhaar, T., "Comparison of two passive microvalve designs for microlamination architectures," *Journal of Micromechanical and Microengineering*, vol. 10, pp. 15-20, 2000.
- Peng, X. F. and Peterson, G. P., "Convective heat transfer and flow friction for water flow in microchannel structures," *International Journal of Heat and Mass Transfer*, vol. 39, pp. 2599-2608, 1996.
- Peterson, R. B., "Small Package," *Mechanical Engineering*, 2001.
- Pfahler, J., Harley, J., and Bau, H., "Liquid Transport in Micron and Submicron Channels," *Sensors and Actuators A*, vol. 21-23, pp. 431-434, 1990.
- Pfahler, J., Harley, J., Bau, H., and Zemel, J. N., "Gas and Liquid Flow in Small Channels," *Micromechanical Sensors, Actuators, and Systems--Transaction of the ASME: DSC*, vol. 32, 1991.
- Popov, E. P., *Engineering mechanics of solids*. Upper Saddle River, N.J.: Prentice Hall, 1999.
- Pottenger, M. and Eyre, B., "MEMS: The maturing of a new technology," *Solid State Technology*, vol. 40, pp. 89-94, 1997.
- Qin, D., Xia, Y., Rogers, J. A., Jackman, R. J., Zhao, X.-M., and Whitesides, G. M., "Microfabrication, Microstructures and Microsystems," *Topics in Current Chemistry*, vol. 194, pp. 1-20, 1998.
- Saxena, A. and Kramer, S. N., "Simple and accurate method for determining large deflections in compliant mechanisms subjected to end forces and moments,"

- Journal of Mechanical Design, Transactions of the ASME*, vol. 120, pp. 392-400, 1998.
- Shah, R. K. and London, A. L., *Laminar flow forced convection in ducts : a source book for compact heat exchanger analytical data*. New York: Academic Press, 1978.
- Shah, R. K. and London, A. L., "Effects of Nonuniform Passages on Compact Heat Exchanger Performance," *Transactions of ASME: Journal of Engineering for Power*, vol. 102, pp. 653-659, 1980.
- Shames, I. H., *Introduction to solid mechanics*. Englewood Cliffs, NJ: Prentice-Hall, 1989.
- Simitses, G. J., *An Introduction to the Elastic Stability of Structures*. Englewood Cliffs, New Jersey: Prentice-Hall, Inc., 1976.
- Spearing, S. M., "Materials Issues in Microelectromechanical Systems (MEMS)," *ACTA material*, vol. 48, pp. 179-196, 2000.
- Stampfl, J., Liu, H.-C., Nam, S. W., Kang, S., and Prinz, F. B., "Rapid Prototyping of Mesoscopic Devices," *Proceeding of Micromaterials 2000*, pp. 1-6, 2000.
- Stewart, J., *Single Variable Calculus: Early Transcendentals*. New York: Brooks/Cole Publishing Company, 1995.
- Stouffer, D. C. and Dame, L. T., *Inelastic Deformation of Metals: Models, Mechanical Properties, and Metallurgy*. New York: John Wiley & Sons, Inc., 1996.
- TeGrotenhuis, W. E., Cameron, R., Butcher, M. G., Martin, P. M., and Wegeng, R. S., "Microchannel Devices for Efficient Contacting of Liquids in Solvent Extraction," presented at AIChE 1998 Spring National Meeting, New Orleans, 1998.
- Thomas, J. "Establishing Thermally Enhanced Edge Registration (TEER) as a Feasible Alignment Technique for Metallic Laminated Devices." *M.S. Thesis*, Industrial Engineering: Oregon State University, 2001.
- Thomas, J. and Paul, B. K., "Thermally-Enhanced Edge Registration (TEER) for Aligning Metallic Microlaminated Devices," presented at Transactions of NAMRC XXX, West Lafayette, IL, 2002.
- Timoshenko, S., *Theory of Elastic Stability*. New York, Toronto, London: McGraw-HILL Book Company, 1961.

- Tonkovich, A. L. Y., Zilka, J. L., Jimenez, D. M., LaMont, M. J., and Wegeng, R. S., "Microchannel Chemical Reactors for Fuel Processing," presented at AIChE 1998 Spring National Meeting, New Orleans, 1998.
- van den Berg, A. and Lammerink, T. S. J., "Micro Total Analysis Systems: Microfluidic Aspects, Integration Concept and Applications," *Topics in Current Chemistry*, vol. 194, pp. 21-49, 1998.
- Wangwatcharakul, W. and Paul, B. K., "Development of Passive Micro-ball valve," *in press*, 2001.
- Weck, M., Fischer, S., and Vos, M., "Fabrication of microcomponents using ultraprecision machine tools," *Nanotechnology*, vol. 8, pp. 145-148, 1997.
- Wegeng, R. S., Drost, M. K., and Brenchley, D. L., "Process Intensification Through Miniaturization of Chemical and Thermal Systems in the 21st Century," *Pacific Northwest National Laboratory*, 1999.
- Weigl, B. H. and Yager, P., "Microfluidic Diffusion-Based Separation and Detection," *Science*, vol. 283, pp. 346-347, 1999.
- Welty, J. R., Wicks, C. E., and Wilson, R. E., *Fundamentals of momentum, heat, and mass transfer*. New York: Wiley, 1984.
- White, F. M., *Fluid Mechanics*, 3rd ed: McGraw-Hill, 1994.
- Wu, P. and Little, W. A., "Measurement of the heat transfer characteristics of gas flow in fine channel heat exchangers used for microminiature refrigerators," *Cryogenics*, vol. 23, pp. 273-277, 1983.

APPENDICES

APPENDIX A

Aspect Ratio Limits In Microlamination Due To Machining Methods

Kannachai Kanlayasiri, Wassanai Wattanutchariya
Graduate Student
Brian K. Paul
Associate Professor

Department of Industrial and Manufacturing Engineering
118 Covell Hall, Oregon State University, Corvallis, OR 97331, USA

In general, it is desirable to minimize the pressure drop within microchannels used for energy system miniaturization. For microchannels fabricated by microlamination methods, some minimum aspect ratio limit exists at which the surface roughness on the endwalls of microchannels no longer significantly affects pressure drop. The major influencing factor on endwall surface roughness is the machining method used. Therefore, this paper delineates the influence of machining methods on the pressure drop in 76.2 μm high stainless steel microchannels and seeks to establish a minimum aspect ratio limit at which this influence is no longer significant. Microchannels are formed by diffusion bonding micromachined laminae between thick end caps. Laminae are machined by deep UV laser micromachining and electrochemical micromachining (EMM). Microchannel widths are varied from 225 μm to 1296 μm . Flow testing is performed on the microchannels to determine pressure drop across the channel. Results show that EMM provides microchannels with less friction coefficient than those machined by the deep UV laser micromachining. Further, the influence of machining method is no longer significant beyond an aspect ratio between 9:1 and 14:1.

1 Introduction

Microchannel devices are well known for their superior performance in heat and mass transport applications (Pfahler et al., 1990b, Pfahler et al., 1991). Much of this is due to the large surface area to volume ratios made possible by the high-aspect-ratio (HAR) microchannels within these devices. In order for these HAR devices to be efficient, pressure drop through these devices must be minimized. Past research has shown that as the channel size decreases within microchannels, the fluid flow behavior within the laminar flow regime of the channel begins to deviate from the traditional Navier-Stokes theory (Pfahler et al., 1990, Rahman and Gui, 1993, Zemel et al. 1994). Wu and Little (1983) and Peng et al. (1994) both found that the wall effect in microchannels had a significant impact on the laminar

flow behavior within the microchannels. Parameters given for influencing the wall effect included the method used to form microchannel walls.

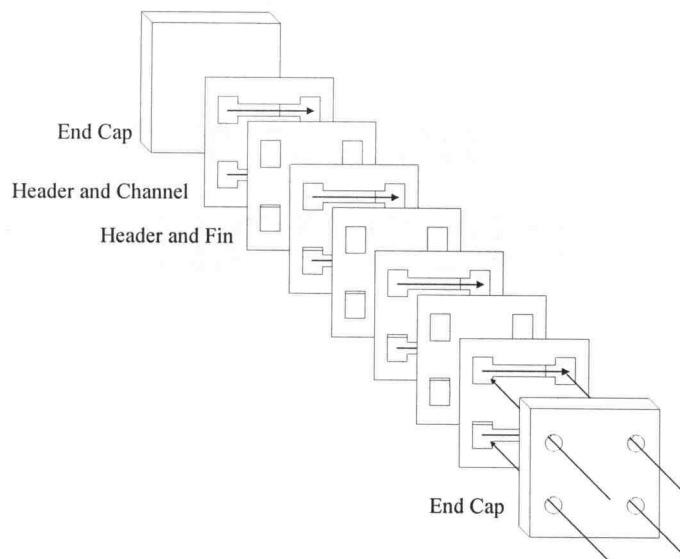


Figure 1. Microlamination scheme used to fabricate a dual microchannel array. Arrows show direction of flow.

One economical method for fabricating HAR microchannel devices is microlamination. Figure 1 is a schematic of a microlamination approach to making a HAR microchannel array. The three steps involved with microlamination are lamina patterning, alignment and bonding to form monolithic microchannel device (Paul and Peterson, 1999). Typically, in metal microlamination, the device is formed from cold-rolled shim stock, which possesses a very smooth surface finish. Therefore, sidewall geometries in metal microlaminated structures are not expected to play a large role in the microfluidic wall effect. However, as shown in Figure 2, a microchannel formed by microlamination may have significant endwall surface roughness depending upon the method of machining used during the lamina patterning step.

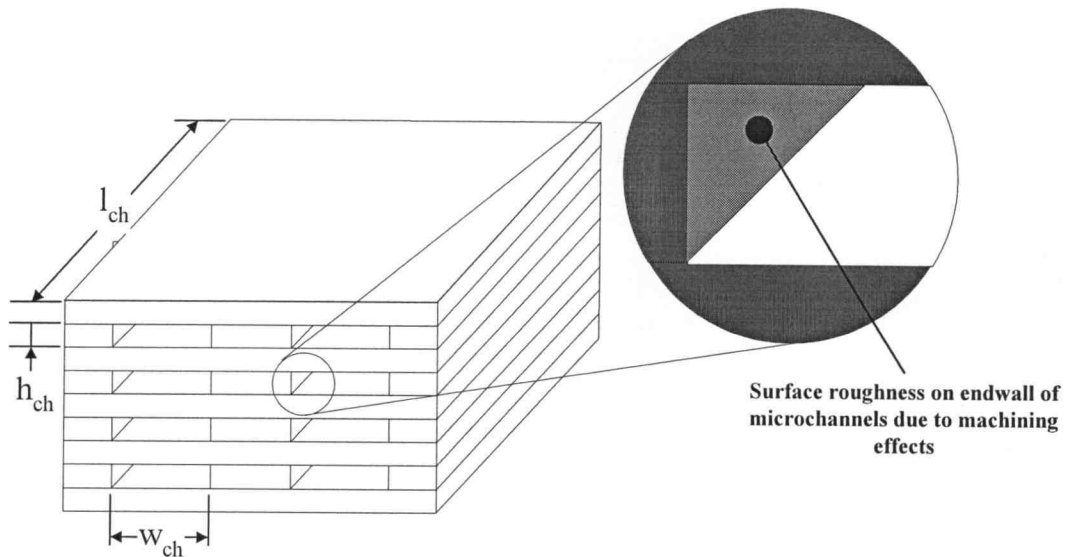


Figure 2. Schematic defining terms associated with a microlaminated geometry.

Many techniques have been used for lamina patterning including laser micromachining, photochemical etching, and electrochemical machining (Wegeng et al. 1996, Paul et al. 1999). Laser micromachining has been used to form microchannels for microlamination because of its ability to quickly adapt to complex geometry. However, the endwalls formed by the laser micromachining process are known to be rough. Photochemical etching has been used in microlamination due to its relatively low cost when compared with laser machining. Matson et al. (1997) used photochemical etching to pattern highly complex stainless steel shims to fabricate laminated microchannel chemical reactors with a relatively low cost per shim (less than US\$1). However, in photochemical etching processes, the costs of waste treatment and disposal can be greater than the processing costs (Datta and Harris, 1997). An alternative process with fewer waste disposal problems is electrochemical micromachining (EMM). EMM is a well-established technique that has been used in the electronics industry to machine thick and thin films. This method is known to provide a very smooth endwall surface.

It is expected that for microlaminated channels there exists an aspect ratio limit at which the method of lamina patterning no longer significantly influences the microchannel pressure drop. Knowledge of this limit would be beneficial for device designers of cross-flow and counter-flow microchannel devices where maximum aspect ratio limits are known to exist (Paul et al., 2001). In this paper, stainless steel microchannels with various aspect ratios are fabricated with machining techniques resulting in both good (EMM) and poor (deep UV laser micromachining) surface finish. Pressure drop is then tested across the microchannels. The results are compared to see whether there is a difference in the

pressure drop performance of the microchannels due to these two machining methods and at what aspect ratio the difference becomes insignificant.

2 Theoretical

For fluid flow in a channel, it has been well known that the friction factor is not only a function of Reynolds number, but it also depends on the shape of the channel cross section. With the same flow area, the friction factors are different if the channel cross sections are different. Surface roughness of the channel is another important factor for flow in the micro channels because of large relative roughness although the effect is negligible in macro scale fluid (Wu and Little, 1983, White, 1994).

In this experiment, two different shapes of the channel cross section are considered--rectangle and trapezoid. The difference in the shapes of cross section is caused by different machining methods used in the experiment. The EMM process provides a trapezoidal cross section with smooth end walls whereas laser machining gives a rectangular cross section with rougher end walls.

In this study, we set up the range of the volumetric flow rate Q for the microchannel test, and measured the pressure drop Δp across the test module, which has a specific cross-section area A , and channel length L . The results are presented in form as a friction factor f and hydraulic diameter D_h . The friction factor is defined as:

$$f = \left(\frac{2\Delta p A^2}{\rho L Q^2} \right) D_h \quad (1)$$

where ρ is the density of liquid and the hydraulic diameter D_h can be calculated from:

$$D_h = \frac{4 \cdot A}{\text{Wetted Perimeter}} \quad (2)$$

For laser micromachining, the cross-section area is rectangular, so the hydraulic diameter is equal to $D_h = \frac{4(W \cdot H)}{2(W + H)}$, where W and H are the channel width and

channel height, respectively. On the other hand, the EMM product generated the trapezoidal cross-section. We can calculate the hydraulic diameter in Eq. (2) by substituting the cross-sectional area and the wetted perimeter of this trapezoidal structure. The cross-sectional area of this structure is equal to the average of the top width a and bottom width b of the channel multiplied by the channel height H , or $A = \left(\frac{a+b}{2} \right) H$, where the wetted perimeter will equal to $a + b + 2 \cdot \sqrt{H^2 + \frac{(a-b)^2}{4}}$.

The Reynolds number, Re , can be calculated from

$$Re = \frac{Q D_h}{A \nu} \quad (3)$$

where ν is the dynamic viscosity of the liquid.

As stated in the Moody chart for the laminar flow regime, the relationship of the friction factor in laminar flow, and the Reynolds number is linear, $f = C_f/Re$, where C_f is the friction coefficient for the system.

In this paper, we will verify whether these friction coefficients are still valid within the range of our experiment, or the effect of the surface roughness generated by different fabrication technique can generate the potential of the error in these coefficients.

3 Experimental Details

3.1 Specimen Preparation. In this experiment, a batch of stainless steel shims was machined by one-sided through mask EMM. Each shim was cleaned with acetone-methanol-deionized water (AMD) to remove grease from the surface and was treated through a photolithography process. The shim was coated with a positive photoresist approximately 2 μm thick on both sides (one side was used as an insulator). A photomask with the microchannel features was registered on the front side and then photoresist was exposed to a UV source and developed to define the patterns. On the back side, a small circle area was left from the photoresist to allow for electrical contact to the stainless steel shim. The important parts of the patterns were 3000 μm in diameter sumps and microchannel. The channel widths and depths are shown in Table 1. To machine the shim, it was connected to the anode of the EMM cell so that it was dissolved electrochemically. In the EMM cell, 5 M NaCl was used as the electrolyte and pumped through the electrodes at a flow rate of 2.0 l/min. In this experiment, the stainless steel shims were set to be machined in the transpassive regime of the electrochemical system to provide a smooth finish. A stainless steel cathode was spaced 1 mm from the anode with 12 V applied potential, 2.64 A/cm² average current density, and 10% duty cycle with 10 ms pulse on time. After machining, the photoresist mask and insulator were stripped out of the shim by using AMD.

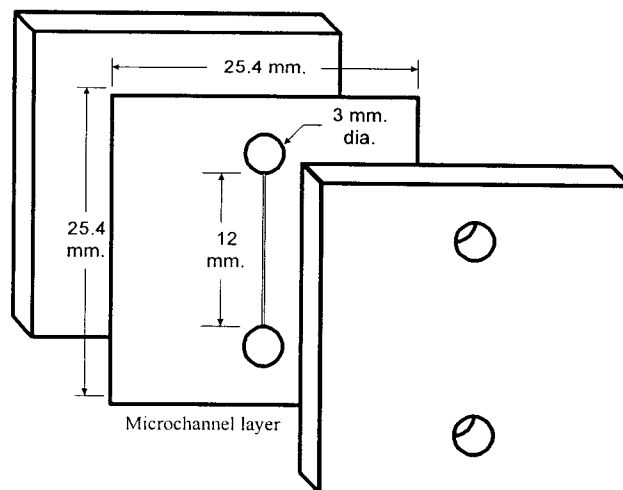


Fig. 3. Schematic of a microchannel layer and end caps

In the laser micromachining technique, the stainless steel shim was fabricated into shape by an ESI Nd:YAG laser (266 nm) with an average power of 300 mW and 4.5 kHz repetition rate. After the microchannel layer has been cut out of the stainless shim, it was cleaned in the ultrasonic cleaner with 20 % Citranox detergent for 15 minutes to remove the re-deposited material on the cut pattern.

3.2 Diffusion Bonding. Each machined lamina was then diffusion bonded with two 3 mm thick stainless steel end caps with mirror-like finishes ($R_a = 0.2 \mu\text{m}$). Both end caps were polished to provide extremely smooth surfaces for the bonded microchannel to minimize the effect of sidewall friction. Diffusion bonding conditions used in bonding laminae were 3,000 N at 800°C with a dwell time of 2 hours and 1.33×10^{-5} Pa vacuum.

3.3 Pressure Drop Testing. The bonded microchannels were pressure drop tested at various flow rates in the laminar flow regime. According to Wu and Little (1983) and Peng et al. (1994), the transition zone from laminar flow to turbulent flow in microchannels occurs much earlier than conventional values. They reported that for different test devices with hydraulic diameters ranging from 0.1 to 0.3 mm, the transition zone varies from 200 to 900 at Reynolds numbers. In this study, the maximum Reynolds number was kept no more than 200, which was still in the laminar flow regime.

A schematic of the experimental apparatus used to investigate pressure drop across the test channel is shown in Fig. 4. The de-ionized (DI) water was used as the working fluid in this flow loop. Water was pumped from the inlet reservoir, which is filled with half air and half deionized water. In order to keep contaminants out of the system and to prevent clogging of internal passages, a $5 \mu\text{m}$ filter was installed in the flow loop.

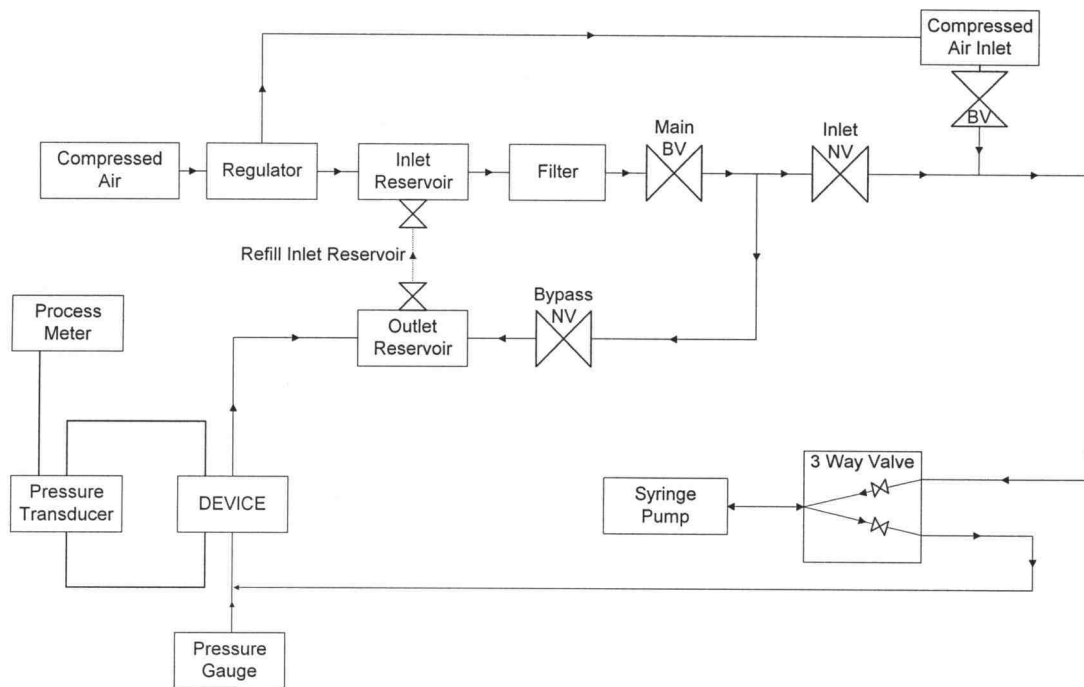


Fig. 4. The schematic diagram of the test loop

A syringe pump was used to provide DI water to the test channel, which was held between tooling plates, which directed the fluid in and out of the channel. A separate tooling plate was designed for each specific microchannel. Each tooling plate included two plenums (one inlet and one outlet) that were made large enough to simulate the fluid entering the microchannel from a static reservoir. Gaskets were inserted between the tooling plate and the test channel to keep the device from leaking.

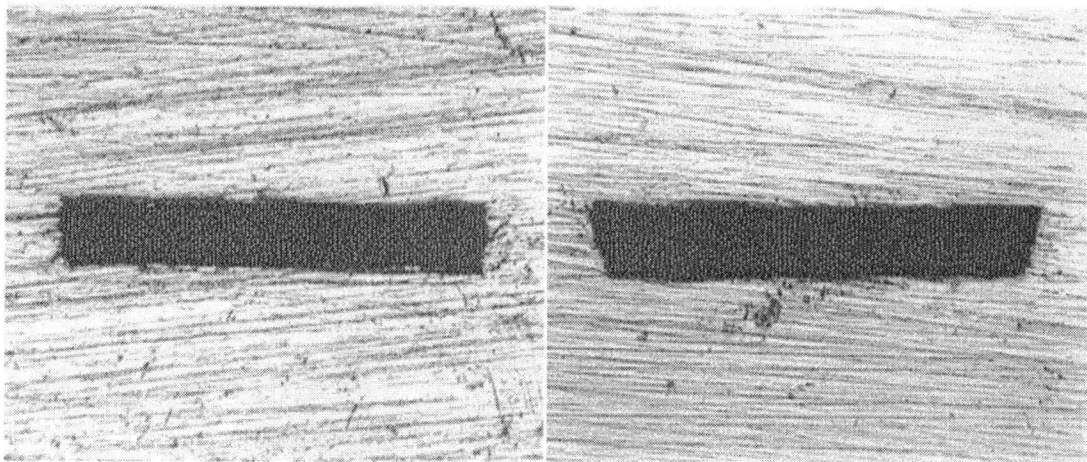
In order to measure the pressure drop across the microchannel, a wet/wet differential pressure transducer was employed. The maximum differential pressure the transducer reads is 172 kPa. The accuracy of the transducer is 0.25% of full scale at constant temperature.

3.4 Dimensional Validation. There is a possibility that dimensions of the microchannel are changed due to severe bonding conditions during diffusion bonding. To obtain the true microchannel dimensions, the test devices were cut and then the cross-section of the microchannels was measured. The measured dimensions are used to calculate the friction coefficient if they are different from the nominal values. Table 1 shows dimensions and theoretical friction coefficients of each experimental channel. The values of theoretical friction coefficient in the table are from Shah and London (1978).

Table 1. Dimensions and Friction Coefficient of experimental channels

Channel No.	Machining Method	Top Width (micron)	Bottom Width (micron)	Depth (micron)	Length (micron)	Hydraulic Diameter (micron)	Theoretical C_f
1	Laser	225.4	225.4	78.2	12000	116.1	67.7
2	Laser	319.3	319.3	77.2	12000	124.3	73.5
3	Laser	474.1	474.1	72.3	12000	125.5	80.0
4	Laser	563.8	563.8	74.3	12000	131.2	81.7
5	Laser	678.4	678.4	74.3	12000	133.9	83.8
6	Laser	1037.0	1037.0	77.2	12000	143.4	87.3
7	EMM	277.2	162.8	76.2	12000	106.3	62.8
8	EMM	372.2	306.8	74.3	12000	119.9	72.0
9	EMM	507.7	454.2	74.3	12000	127.6	80.0
10	EMM	591.3	510.5	75.3	12000	130.3	76.0
11	EMM	656.2	656.2	78.2	12000	139.7	82.9
12	EMM	1296.3	1111.1	73.4	12000	133.7	84.0

Fig. 5 represents the cross-section views of the diffusion bonded test devices of channel number 3 and 9, which were fabricated by laser micromachining and by electrochemical micromachining respectively.

**A) Laser Micromachining****B) EMM****Figure 5. Cross section of test device at 100X**

4 Results and Discussion

From the results, the friction coefficients of microchannels with various aspect ratios showed deviations from theoretical values. The values of friction coefficients of both laser machined channels and electrochemically machined channels are greater than the corresponding theoretical values and the differences from theory are more obvious for laser machined channels. From Figure 12, at 2:1

aspect ratio microchannels, the friction coefficient of the one machined by laser micromachining differs by about 40% from that of EMM machined microchannel, as the aspect ratio of the microchannels increases, the difference in friction coefficient decreases and when the aspect ratio reaches 9:1, the value of friction coefficient became almost the same value. From the results, it indicates that the machining methods have a major impact on the behavior of fluid flow in the microchannels since they are directly related to surface roughness of the microchannels, which is associated with the flow behavior. However, this indicates that the effect of the machining method on fluid flow behavior is no longer significant if the aspect ratio of the microchannel is not less than about 9:1.

From the results, for the channels machined by laser, the friction coefficient of low aspect ratio channels is greater than theoretical values as the aspect ratio increases, the difference between experimental and theoretical decreases, but this characteristic is not found in electrochemically machined channels. For the channels machined by EMM, the difference between theoretical and experimental is not significant at low aspect ratios, but obvious at an aspect ratio of 15:1. These phenomena can be explained by noting that at low aspect ratios, where the end walls have strong influence, the surface roughness of end walls dominates pressure drop across the channel. Since laser machining is known to provide a rough surface finish than EMM, the difference between theoretical and experimental friction coefficient for laser-machined channels is greater than that of channels machined by EMM. For EMM channels, at high aspect ratio the deviation from theoretical friction coefficient was greater than expected. This might be explained by the increasingly important role the side wall effect at larger aspect ratios. As shown in Figure 13, investigation of channel number 12 (for which the deviation exists) showed a slight deflection in the side wall. These types of anomalies are expected to happen in increasing friction coefficient at higher aspect ratios. This suggests that at aspect ratios above 10:1, side wall deflection appears a more dominant constraint to aspect ratio than machining method.

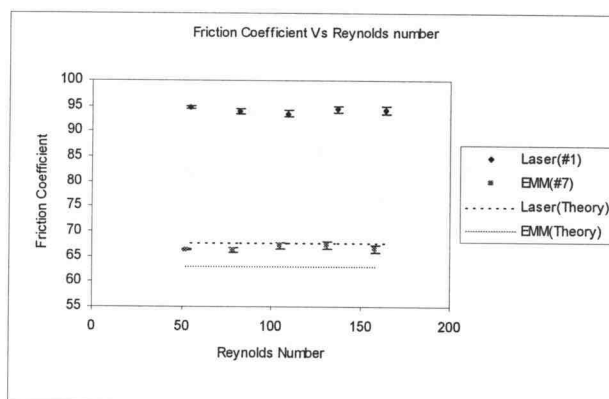


Figure 6. Friction coefficient and Reynolds number (Re) of channel number 1 (aspect ratio 3:1) and channel number 7 (aspect ratio 2:1)

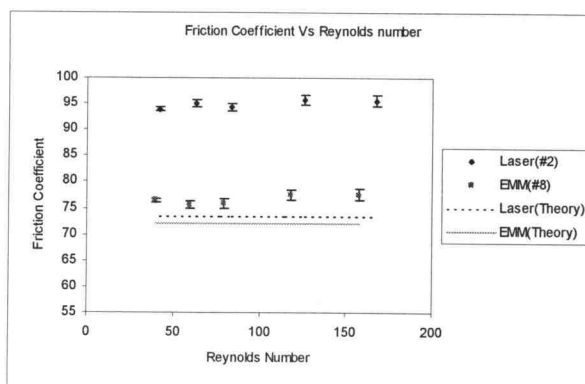


Figure 7. Friction coefficient and Re of channel number 2 (aspect ratio 4:1) and channel number 8 (aspect ratio 4:1)

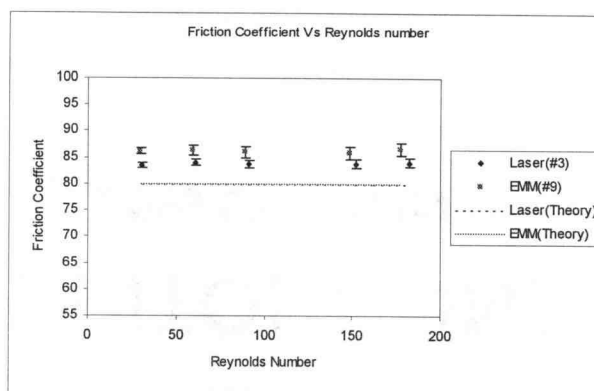


Figure 8. Friction coefficient and Re of channel number 3 (aspect ratio 7:1) and channel number 9 (aspect ratio 6:1)

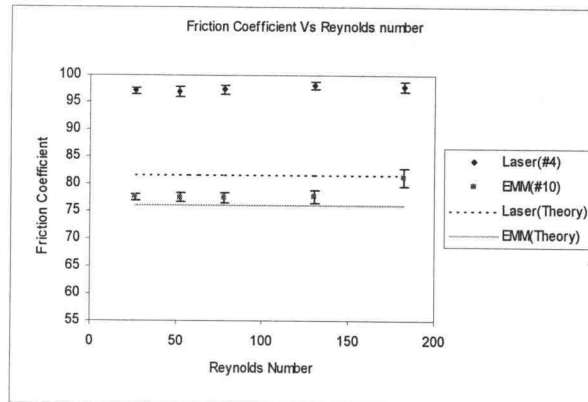


Figure 9. Friction coefficient and Re of channel number 4 (aspect ratio 8:1) and channel number 10 (aspect ratio 7:1)

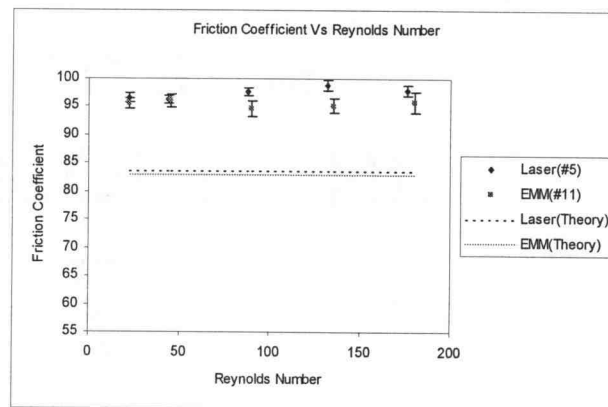


Figure 10. Friction coefficient and Re of channel number 5 (aspect ratio 9:1) and channel number 11 (aspect ratio 8:1)

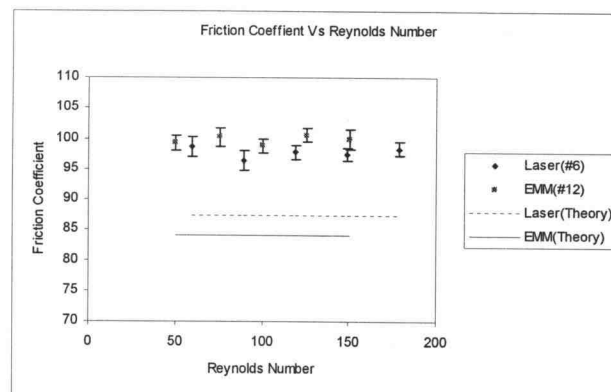


Figure 11. Friction coefficient and Re of channel number 6 (aspect ratio 13:1) and channel number 12 (aspect ratio 15:1)

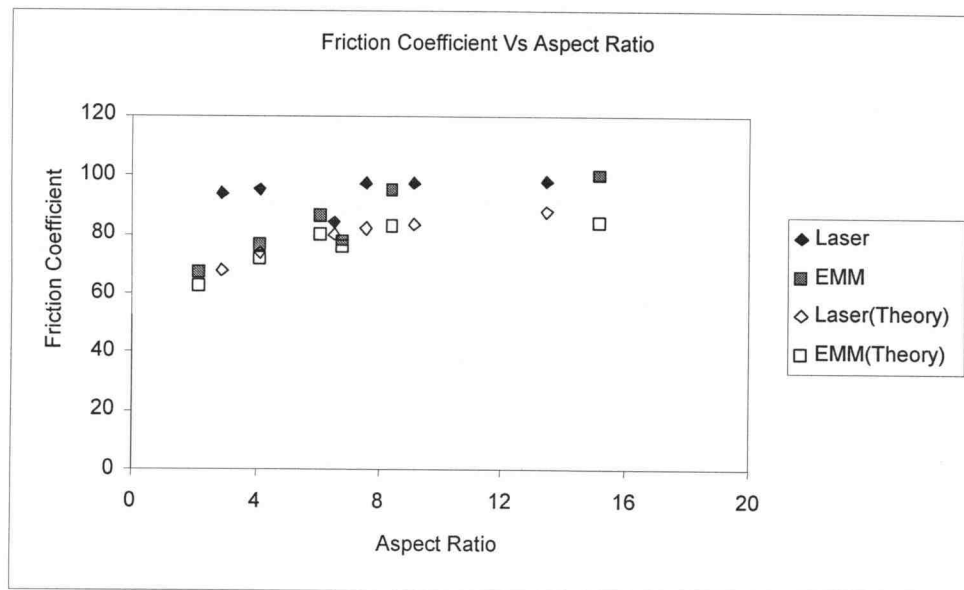


Figure 12. Average friction coefficient and aspect ratios of the microchannels

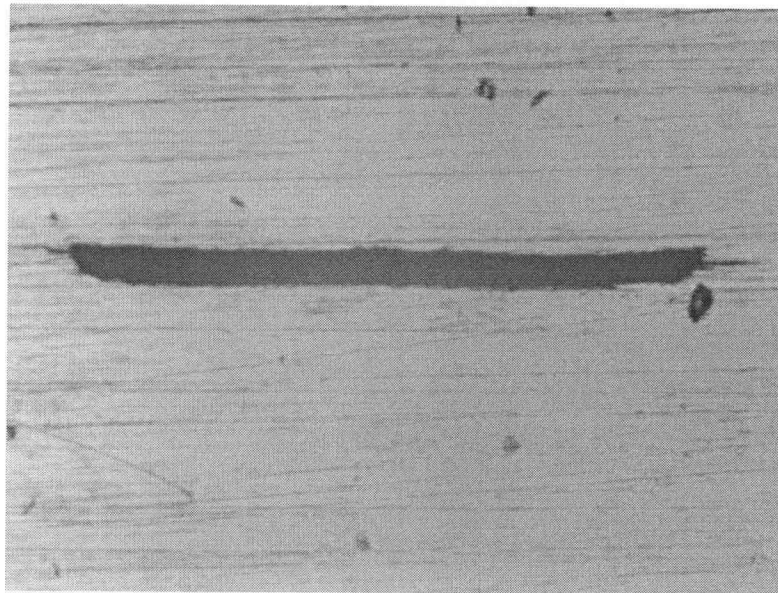


Figure 13. Cross section of channel number 12

5 Conclusions

From this study, it is found that there is no significant difference in the value of friction coefficient of stainless steel microchannels machined by deep UV laser micromachining and EMM when the aspect ratio is greater than about 9:1. As

a result, it is expected that machining methods do not have a major significance to microchannels having aspect ratios greater than 20:1, which is typical within the literature. Side wall effects such as fin deflection seem to be more important above about 9:1. However, the result from this study could be more significant for cross-flow and counterflow microchannel devices where aspect ratios have been found to be limited below 10:1. The effect of machining methods should be considered in the design and fabrication of these devices.

6 Acknowledgment

This work was funded by the Office of Naval Research.

7 References

- Datta, M., and Harris, D., 1997, "Electrochemical Micromachining: An Environmentally Friendly, High Speed Processing Technology," *Electrochimica Acta*, Vol. 42, Nos. 20-22, pp. 3007-3013.
- Matson, D.W., Martin, P.M., Bennett, W.D., Stewart, D.C., and Johnston, J.W., 1997, "Laser Micromachined Microchannel Solvent Separator," *Proceedings of Micromachining and Microfabrication Process Technology III*, Austin, TX, September 29-30.
- Paul, B.K. and Peterson, R.B., 1999, "Microlamination for Microtechnology-based Energy, Chemical, and Biological Systems," *ASME IMECE*, Nashville, Tennessee, November 15-20, 1999.
- Paul, B.K., Peterson, R.B., and Wattanuchariya, W., 1999, "The Effect of Shape Variation in Microlamination on the Performance of High-Aspect-Ratio, Metal Microchannel Arrays," *Proceedings of the Third International Conference on Microreaction Technology*, Frankfurt, Germany.
- Paul, B.K., Hasan, H., Thomas, J., Wilson, R.D., and Alman, D., 2001, "Limits on Aspect Ratio in Two-Fluid Micro-Scale Heat Exchangers," *Transactions of NAMRI/SME*, Vol. 29, in press.
- Peng, X.F., Peterson, G.P., and Wang, B.X., 1994, "Frictional Flow Characteristics of Water Flowing Through Rectangular Microchannels," *Experimental Heat Transfer*, Vol. 7, pp. 249-264.
- Pfahler, J., Harley, J., and Bau, H., 1990a, "Liquid Transport on Micron and Submicron Channels," *Sensors and Actuators*, A21-A23, pp. 431-434.
- Pfahler, J.N., Harley, J., Bau, H.H., and Zemel, J., 1990b, "Liquid and Gas Transport in Small Channels," *Proc. ASME Winter Meeting*, Vol. DSC-19, pp. 149-

157.

Pfahler, J., Harley, J., Bau, H.H., and Zemel, J., 1991, "Gas and Liquid Flow in Small Channels," in D. Cho et al. (eds.), *Micromechanical Sensors, Actuators, and Systems*, ASME Vol. DSC-32, pp. 49-60.

Rahman, M.M., and Gui, F., 1993, "Experimental Measurements of Fluid Flow and Heat Transfer in Microchannel Cooling Passages in a Chip Substrate," *EEP*, Vol. 4-2, *Advances in Electronic Packaging*, ASME, pp. 685-692.

Shah, R.K., and London, A.L., 1978, "*Laminar Flow Forced Convection in Ducts: A Source Book for Compact Heat Exchanger Analytical Data*," Academic Press, New York.

Wegeng, R.S., Call, C.J., and Drost, M.K., 1996, "Chemical System Miniaturization," *Proceedings of the 1996 Spring National Meeting of AIChE*, New Orleans, LA, February 25-29.

White, F.M., 1994, *Fluid Mechanics*, 3th edition, McGraw Hill, Singapore.

Wu, P., and Little, W.A., 1983, "Measurement of Friction Factors for the Flow of Gases in Very Fine Channels Used for Microminiature Joule-Thomson Refrigerators," *Cryogenics*, pp. 273-277.

Zemel, J.N., Harley, J.C., Pfahler, J.N., Urbanek, W., and Bau, H.H., 1994, "Fluid Transport in Microchannels," *Proceedings of the Symposium on Microstructures and Microfabricated Systems*, Vol. 94-14, pp. 210-219.

APPENDIX B

Derivation of Equations for LONDON MODEL and Implementation to Fin Warpage Nonuniformity

The following summary presents the derivation of the London model that is used to evaluate the effect of channel nonuniformity on the performance of the heat exchanger discussed in Chapter 2. Figure B-1 represents the channel geometry used to evaluate the irregularity of the flow channel inside the heat exchanger. Later, the implementation of warpage nonuniformity as shown on Figure 2-4 will be discussed.

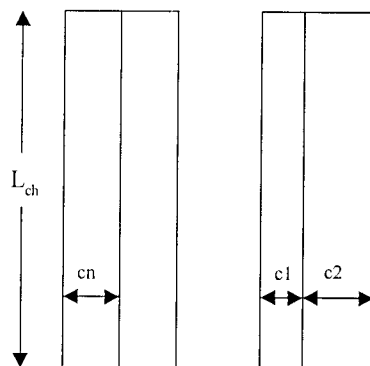


Figure B-1 Flow channel geometry for (a) uniform channel (b) nonuniform channel due to different in cross-sectional area of flow channel

Flow distribution

At the steady state, the pressure drop across channel (1) and (2) is presumed to be the same, whether the channel geometry is uniform or not.

$$\Delta P = f_1 \left[\rho \cdot \frac{(V_1)^2}{2 \cdot g_c} \right] \cdot \left(\frac{L}{r_{h,1}} \right) = f_2 \left[\rho \cdot \frac{(V_2)^2}{2 \cdot g_c} \right] \cdot \frac{L}{r_{h,2}} \quad (\text{B1})$$

The term f from this equation is the fanning friction factor, which is related to the Reynolds number by relation:

$$f = \frac{C_f}{\text{Re}} \quad (\text{B2})$$

where C_f (or sometimes use $f\text{Re}$) is a constant term which depends only on the geometry of the channel. The Reynolds number is calculated from

$$\text{Re} = \frac{V \cdot 4 \cdot rh}{\nu} \quad (\text{B3})$$

When substituting the relation of the friction factor (B2) and the Reynolds number (B3) into the pressure drop relation (B1), the velocity ratio between two channels will be:

$$\frac{V_1}{V_2} = \left(\frac{f\text{Re}_2}{f\text{Re}_1} \right) \cdot \left(\frac{r_{h,1}}{r_{h,2}} \right)^2 \quad (\text{B4})$$

Based on the continuity equation: $W = \rho \cdot A \cdot V$ (B5)

so the equation (B4) will become:

$$\frac{W_1}{W_2} = \left(\frac{fRe_2}{fRe_1} \right) \left(\frac{r_{h,1}}{r_{h,2}} \right)^2 \left(\frac{A_1}{A_2} \right) \quad (B6)$$

Since we assume that the sum of the flow through both channels are the same at transient state whether the channel geometry is uniform or not, we can write this relation that $W_1 + W_2 = 2 \cdot W_n$. Defining $\omega_1 + \omega_2 = 1$ where; $\omega_i = \frac{W_i}{2 \cdot W_n}$; therefore, the equation (B6) can be represented as equation (4) of Chapter 2 based on the relation of mass flow rate ratio between both sides of the heat exchanger.

Based on the relation in equation (4), the The hydraulic radius (rh) is a passage area over the wetted parameter (A/P). Because the wetted parameters of both channels are the same in fin warpage case, this relation will change to:

$$\frac{\omega_1}{\omega_2} = \left(\frac{fRe_2}{fRe_1} \right) \left(\frac{A_1}{A_2} \right)^3 \quad (B7)$$

Based on the relation that $A_1 = An - Aa$, and $A_2 = An + Aa$, the flow distribution ratio can be written as the equation (5) in Chapter 2. In addition, the fRe term of each side of channel can be calculated from the following equation (based on laminar flow scheme):

$$fRe = 24 \cdot \left(1 - 1.3553\alpha - 1.9467\alpha^2 + 1.7012\alpha^3 + 0.9564\alpha^4 - 0.2537\alpha^5 \right) \quad (B8)$$

where α is the ratio of channel width over channel height or cn/L_s

Effectiveness-NTU Relations

The number of transfer units (NTU) is related to the Stanton Number and the ratio of channel length and hydraulic radius as: $NTU = St * \frac{L}{rh}$ (B9)

where the Stanton number is defined as: $St = \frac{Nu}{Re * Pr}$ (B10)

Substituting the Stanton number in terms of Re , Nu , and Pr , the NTU equation (B9)

will become: $NTU = \frac{Nu}{Re * Pr} * \frac{L}{rh}$ (B11)

Then the Reynolds number is replaced by equation (B3) and (B5), thus NTU

relation can be rewritten as: $NTU = \frac{Nu * A}{W * rh^2} * \frac{L}{4 * Pr}$ (B12)

Since L and Pr are common to both channels whether they are uniform or not, the ratio of the number of transfer units of any i -th channel to a uniform channel can be represented in equation (6) of Chapter 2.

From the relation of NTU_i and NTU_n in equation (6), the hydraulic radius can be normalized in terms of area and wetted parameter as:

$$\frac{NTU_i}{NTU_n} = \left(\frac{Nu_i}{Nu_n} \right) \left(\frac{\omega_n}{\omega_i} \right) \left(\frac{A_n}{A_i} \right) \left(\frac{P_i}{P_n} \right)^2$$

For fin warpage nonuniformity, $P_i = L_s + L_f + 2*cn$, and $P_n = 2*L_s + 2*cn$, the equation above can be written as equation (7) of Chapter 2. (B13)

However, the area of each channel in nonuniform channel is not the same. This equation depends on what the ratio of NTU of which side of channel will be solved. If it is the ratio of NTU_1 over NTU_n , $A_1 = An - Aa$ is substituted, but if it is the ratio of NTU_2 over NTU_n , $A_2 = An + Aa$ will be used. In addition, the Nusselt number of each side of channel can be calculated from the following equation (based on the laminar flow scheme):

$$Nu = 8.235 + 2.0421\alpha + 3.0853\alpha^2 + 2.4765\alpha^3 + 1.0578\alpha^4 + 0.1861\alpha^5 \quad (B14)$$

Now, the relation of NTU and the effectiveness (ϵ) of each channel will be determined based on the flow distribution, in order to balance the effectiveness for the combined heat exchanger. This relation can be written as: $\epsilon_{avg} = \omega_1 \cdot \epsilon_1 + \omega_2 \cdot \epsilon_2$, where

$$\epsilon_1 = \frac{NTU_1}{1 + NTU_1} \quad \epsilon_2 = \frac{NTU_2}{1 + NTU_2} \quad (B15)$$

Therefore, the effective NTU and the percent loss of NTU due to the nonuniformity can be represented as equation (10) and (11) of Chapter 2.

Pressure Drop Relations

When flow maldistribution occurs, the pressure drop will be decreased (or sometimes called gain). Based on the relation of pressure drop of both sides of the channel-equation (B1), a ratio of pressure drop between the nonuniformity flow channel and uniformity channel can be rewritten as:

$$\frac{\Delta P_i}{\Delta P_n} = \left(\frac{f_i}{f_n} \right) * \left(\frac{V_i}{V_n} \right)^2 * \left(\frac{rh_n}{rh_i} \right) \quad (B16)$$

From continuity equation (B5), and the Reynolds number (B3), this equation can be transformed into equation (14) in Chapter 2. Therefore, the percent reduction (gain) in the pressure drop when flow maldistribution happens can be calculated from equation (15), where ΔP_i to be used in this equation is the pressure drop of the larger side.

APPENDIX C

Evaluation of Overall Number of Transfer Units and Transfer Areas

The nominal dimension of the heat exchanger in this study is specified in order to present the numerical results of the influence of the warpage nonuniformity.

$$\begin{array}{ll}
 L_{ch} = 30 & \text{mm} \\
 cn = 0.5 & \text{mm} \\
 L_s = 10 & \text{mm} \\
 \Delta T_m = 3 & ^\circ\text{C} \\
 T_{hi} = 100 & ^\circ\text{C}
 \end{array}
 \qquad
 \begin{array}{ll}
 T_{ci} = & 39 \text{ } ^\circ\text{C} \\
 k = & 30\text{E-3 W/m K} \\
 W = & 0.07 \text{ g/s} \\
 cp = & 1009 \text{ J/kg K} \\
 \varepsilon = & 0.95
 \end{array}$$

Verification of NTU from ε - NTU relation

Since air is the working fluid for both the hot and cold streams of this

counter-flow heat exchanger, the formula to calculate NTU is: $NTU = \frac{\varepsilon}{1 - \varepsilon}$ (C1)

Which is equal to 19 for this nominal dimension and condition.

Similarly, NTU can also be defined as $\frac{U * Ah}{W * cp}$ (C2)

In case of the similar fluid, $U = \frac{h}{2}$ (C3)

From relation: $Nu = \frac{h * 4 * rh}{k}$ (C4)

equation (C3) can be rewritten as $U = \frac{k * Nu}{8 * rh}$ (C5)

The Nusselt number can be solved from:

$$Nu = 8.235 + 1.20421\alpha - 3.0853\alpha^2 - 2.4765\alpha^3 + 1.0578\alpha^4 - 0.1861\alpha^5 \quad (C6)$$

when $\alpha = 0.05$, Nu is equal to 7.455. $rh = A/P = \frac{L_s * cn}{2 * L_s + 2 * cn} = 0.238 \text{ mm}$.

Therefore, $h = 234.84 \text{ W/m}^2 \text{ K}$, and $U = 117.42 \text{ kg/s}^3 \text{ K}$.

From equation (C2), the heat transfer area is equal to $\frac{NTU * W * cp}{U} = 11.43 \times 10^3 \text{ mm}^2$.

Assuming that each channel has the heat transfer area of $(2 * L_s * L_{ch})$ 600 mm^2 (2-sided), the total number of channel that will be needed for this heat exchanger will be $(\frac{Ah}{2 * L_s * L_{ch}})$ 19 channels in order to satisfy the effectiveness

of 95% as specified. Figure below illustrates the schematic of the counter flow heat exchanger with air as the working fluid.

Check the flow scheme of the heat exchanger

$$\text{From the Reynolds number equation: } Re = \frac{4 * \rho * V * rh}{\mu} \quad (C7)$$

$$\text{when substituting } V = \frac{W}{\rho * A} \quad \text{and} \quad rh = \frac{Ls * cn}{2 * Ls + 2 * cn} \quad (C8)$$

$$\text{equation (C7) will become} \quad Re = \frac{4 * W}{\mu * (2 * Ls + 2 * cn)} \quad (C9)$$

For air at 350 K, $\mu = 208.2 \times 10^{-4}$ g/m s, so the Reynolds number is 640.4, which is considered to be the laminar flow scheme.

Pressure drop calculation

$$\text{From} \quad \Delta P = f * \rho * V^2 * \frac{L_{ch}}{2 * rh} \quad (C10)$$

and $f = fRe/Re$ where fRe can be calculated from relation:

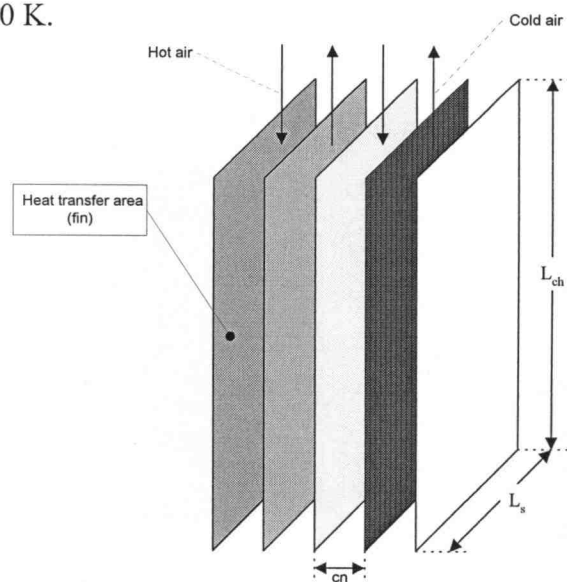
$$fRe := 24 * (1 - 1.3553\alpha + 1.9467\alpha^2 - 1.7012\alpha^3 + 0.9564\alpha^4 - 0.2537\alpha^5) \quad (C11)$$

Substituting Re from equation (C9) and fRe from equation (C11) into equation (C10), the pressure drop in this system is 414.98 Pa or about 0.06 PSI with the volumetric flow rate of (W/ρ) 70.352 mL/s.

The pumping power (W_p) required for this heat exchanger is 0.03 W, based on relation:

$$W_p = \frac{W * \Delta P}{\rho} \quad (C12)$$

when the density is 0.995 kg/m³ at 350 K.



APPENDIX D

Evaluation of the Heat Transfer Performance and Pressure Drop Relationship Based on Channel Deviation

Given $L_s/cn = 20.100$ $Ntu-n = 19$ $L_f = 10$ mm $L_s = 10.05$ mm
 $fRe-n = 22.499$ $Nu-n = 7.459$ $cn = 0.5$ mm $Lch = 30$ mm

delta c	alpha1	alpha2	An	Aa	fRe1	fRe2	Nu-1	Nu-2	$\omega1/\omega2$	$\omega1$	$\omega2$
0	0.050	0.050	5.025	0.000	22.492	22.492	7.459	7.459	1.000	0.500	0.500
0.05	0.047	0.052	5.025	0.251	22.563	22.423	7.495	7.423	0.736	0.424	0.576
0.1	0.045	0.055	5.025	0.503	22.634	22.353	7.531	7.388	0.541	0.351	0.649
0.15	0.042	0.057	5.025	0.754	22.705	22.285	7.568	7.352	0.396	0.284	0.716
0.2	0.040	0.060	5.025	1.005	22.777	22.216	7.605	7.317	0.289	0.224	0.776
0.25	0.037	0.062	5.025	1.256	22.849	22.148	7.642	7.283	0.209	0.173	0.827
0.3	0.035	0.065	5.025	1.508	22.922	22.081	7.679	7.248	0.150	0.131	0.869
0.35	0.032	0.067	5.025	1.759	22.996	22.014	7.717	7.214	0.107	0.097	0.903
0.4	0.030	0.070	5.025	2.010	23.070	21.948	7.755	7.180	0.075	0.070	0.930
0.45	0.027	0.072	5.025	2.261	23.144	21.882	7.793	7.147	0.052	0.049	0.951
0.5	0.025	0.075	5.025	2.513	23.219	21.817	7.832	7.113	0.035	0.034	0.966
0.55	0.022	0.077	5.025	2.764	23.295	21.752	7.871	7.080	0.023	0.022	0.978
0.6	0.020	0.080	5.025	3.015	23.371	21.687	7.910	7.047	0.014	0.014	0.986
0.65	0.017	0.082	5.025	3.266	23.448	21.623	7.950	7.015	0.009	0.009	0.991
0.7	0.015	0.085	5.025	3.518	23.525	21.560	7.990	6.983	0.005	0.005	0.995
0.75	0.012	0.087	5.025	3.769	23.603	21.497	8.030	6.950	0.003	0.003	0.997

Ntu1*	Ntu2*	delta P2*	$\epsilon1$	$\epsilon2$	ϵ -avg	Ntu-eff	%Loss in Ntu	%Gain-P	% change in Area	# Channel Needed
1.000	1.000	1.000	0.950	0.950	0.950	19.000	0.00%	0.00%	0%	19.0
1.247	0.823	0.992	0.960	0.940	0.948	18.305	3.66%	0.82%	4%	19.8
1.598	0.694	0.969	0.968	0.929	0.943	16.557	12.86%	3.12%	15%	21.9
2.103	0.598	0.933	0.976	0.919	0.935	14.426	24.07%	6.72%	32%	25.1
2.842	0.527	0.887	0.982	0.909	0.925	12.417	34.65%	11.34%	53%	29.1
3.945	0.472	0.834	0.987	0.900	0.915	10.740	43.47%	16.65%	77%	33.7
5.625	0.430	0.777	0.991	0.891	0.904	9.415	50.45%	22.34%	102%	38.4
8.244	0.397	0.719	0.994	0.883	0.894	8.391	55.84%	28.14%	126%	43.1
12.436	0.370	0.661	0.996	0.875	0.884	7.600	60.00%	33.85%	150%	47.6
19.359	0.347	0.607	0.997	0.868	0.875	6.985	63.24%	39.33%	172%	51.8
31.224	0.329	0.555	0.998	0.862	0.867	6.499	65.79%	44.47%	192%	55.7
52.488	0.313	0.508	0.999	0.856	0.859	6.109	67.85%	49.24%	211%	59.2
92.755	0.300	0.464	0.999	0.851	0.853	5.788	69.54%	53.61%	228%	62.5
174.510	0.288	0.424	1.000	0.845	0.847	5.519	70.95%	57.59%	244%	65.6
356.251	0.277	0.388	1.000	0.840	0.841	5.289	72.16%	61.19%	259%	68.4
813.018	0.267	0.356	1.000	0.835	0.836	5.088	73.22%	64.44%	273%	71.1

APPENDIX E

Evaluation of Channel Deviation Due To Fin Buckling

This section discusses the procedure to evaluate the channel nonuniformity based on a different mode of buckling, which consists of 3 parts: (1) verification of buckling phenomenon, (2) calculation of maximum deflection of fin buckling, and (3) evaluation of the channel deviation due to fin buckling. First of all, some assumptions are specified for this evaluation.

- Laminae are made from stainless steel and the holding fixture is made from graphite.
- Based on the different of coefficient of thermal expansion (CTE) of both laminae and fixture, when both objects are put together and heated up to diffusion temperature, the laminae will be constrained in the fixture because stainless steel has a higher thermal expansion rate than graphite.
- There is no initial deflection in the laminae prior to the bonding step.
- There is no other source of warpage that contributes to buckling in this case, other than the force from the difference of the thermal expansion.

The following dimensions and properties are the nominal value for the heat exchanger and the holding fixture used in this evaluation.

L_{ch}	=	30 mm	t	=	0.1778 mm
L_f	=	10 mm	E	=	200 GPa
L_s	=	10.05 mm	α_g	=	6.25E-6 K ⁻¹
cn	=	0.5 mm	α_{ss}	=	18.7E-6 K ⁻¹
ΔT	=	800 °C	σ_y	=	517 MPa
T_{dif}	=	820 °C			

Case 1: Mode 1 Buckling

1. Verification of buckling phenomenon

In the first step, verification that buckling is the limiting mode of failure in our study needs to be performed. In order to verify the mode of failure, the buckling stress (σ_c) of the fin will be compared with the yield strength (σ_y) of the

stainless steel plate. The buckling stress is calculated from $\sigma_c = \frac{P_c}{A_f}$ (E1)

where

$$P_c = \frac{4 * \pi^2 * E * I}{L^2} \quad (E2)$$

is the critical load of fixed-ended boundary condition. Since buckling occurs at the diffusion temperature, the actual length at that temperature or L_s' will be substituted

for L to evaluate this buckling stress. L_s' will be calculated based on the slot size of the fixture because this length represents the allowance of the fixture slot at the diffusion temperature. By applying a linear thermal expansion equation for the graphite fixture at diffusion temperature, L_s' will equal to: $L_s' = L_s * (1 + \alpha_g * \Delta T)$ (E3) When the laminae are 10 mm wide and slot size is 10.05 mm (0.05 mm is the clearance between the fixture and the laminae), the slot size at the diffusion temperature based on equation (E3) is 10.10 mm.

From equation (D2), I or the moment of inertia is calculated from $L_{ch} * t^3 / 12$, which equals 0.014 mm^4 . A_f is the cross sectional area of the fin in the clamping direction which is calculated from $L_{ch} * t$. When substituting E , I , L_s' back in equation (E2) and (E1), $P_c = 1.09 \text{ kN}$, and $\sigma_c = 204 \text{ MPa}$. Since the buckling stress is lower than the yield strength ($\sigma_c < \sigma_y$), buckling is the mode of failure in this case.

The next step is to check whether or not the force generated by thermal expansion during diffusion bonding (P_t) is high enough to cause the fin to buckle. During the diffusion bonding cycle, the force due to thermal expansion happens after the laminae have touched the fixture. Hence, the actual difference of temperature between the point that laminae touch fixture until the temperature reaches the diffusion point (ΔT_{eff}) is required.

With a clearance of 0.05 mm between fixture and laminae at room temperature, it will take some amount of temperature ($\Delta T'$), in order to bring both structures into a contact. When both structures are touching, it means that $L_s' = L_f'$ at that point. Since $L_s' = L_s * (1 + \alpha_g * \Delta T')$ and $L_f' = L_f * (1 + \alpha_{ss} * \Delta T')$, we can solve $\Delta T'$ from

$$\Delta T' = \left(\frac{L_s - L_f}{\alpha_{ss} * L_f - \alpha_g * L_s} \right) \quad (E4)$$

$$\text{and } \Delta T_{eff} = \Delta T - \Delta T' \quad (E5)$$

From equation (E4), $\Delta T'$ is 402.617 K, therefore, ΔT_{eff} is 397.383 K.

Now, the force due to thermal expansion can be calculated from

$$P_t = A_f * E * (\alpha_{ss} - \alpha_g) * \Delta T_{eff} \quad (E6)$$

P_t from the above equation is 5.28 kN. Since this clamping force is higher than the critical buckling load ($5.28 \text{ kN} > 1.09 \text{ kN}$), the fin will buckle.

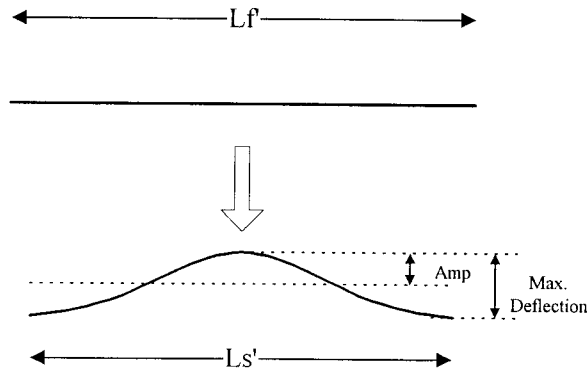
Now as we know that the column is buckled by the difference in CTE between laminae and fixture, the calculation of the maximum deflection and the evaluation of the deviation of the channel due to this buckle deflection will be discussed.

2. Calculation of the maximum deflection of the fin buckling

Based on the elastic buckling equation of a fin that is clamped at both ends, or also referred to as a fixed-ended boundary condition, the buckling shape or the displacement function of mode 1 buckling are designated by equation:

$$y = A_{mp} \cdot \left(1 - \cos \left(\frac{2 \cdot \pi \cdot x}{L_f} \right) \right) \quad (E7)$$

where A_{mp} is the amplitude of the buckling shape. For a fundamental buckling, the amplitude is half of the maximum deflection, and x is the distance from one side of the column to any position on the column, as shown in the picture below.



According to this picture, buckling occurs because the lamina expands into L_f , but the slot size of the fixture is only L_s' (L_s' less than L_f), so the lamina is axially constrained, causing the fin to buckle in lateral direction.

In order to calculate the maximum deflection and the channel deviation, the amplitude is required. Because the fin and slot width at room temperature and at the diffusion temperature can be calculated based on linear thermal expansion, the amplitude of the buckling form can be solved by implementing the arc length formula to the buckling deflection equation.

Arc length formula: $L_1 = \int_0^{L_2} \sqrt{1 + \left(\frac{d-y}{dx} \right)^2} dx \quad (E8)$

Substituting the buckling deflection shape from equation (E7) and changing L_1 to L_f' and L_2 to L_s' , equation (E8) becomes:

However, this function does not have a closed-form antiderivative (the

$$\begin{aligned} L_f' &= \int_0^{L_s'} \left[\sqrt{1 + \left(\frac{d}{dx} \left[A_{mp} \cdot \left(1 - \cos \left(\frac{2 \cdot \pi \cdot x}{L_s'} \right) \right) \right] \right)^2} \right] dx \\ &= \int_0^{L_s'} \left[\sqrt{1 + \left(2 \cdot A_{mp} \cdot \sin \left(2 \cdot \pi \cdot \frac{x}{L_s'} \right) \cdot \frac{\pi}{L_s'} \right)^2} \right] dx \end{aligned} \quad (E9)$$

result is in a form of elliptic integral), so approximation methods will be used to calculate the arc length, and solve for the maximum deflection. There are two approximation methods that we can apply (1) Simpson approximation technique and (2) Integration-square root approximation.

I. Simpson approximation technique

This technique involves dividing the arc length into subsection and then combines the subsection length to evaluate the overall length. Simpson's Rule is stated as:

$$\int_a^b f(x) dx = \frac{\Delta x}{3} \cdot (f(x_0) + 4 \cdot f(x_1) + 2 \cdot f(x_2) + 4 \cdot f(x_3) + \dots + 2 \cdot f(x_{n-2}) + 4 \cdot f(x_{n-1}) + f(x_n)) \quad (E10)$$

where $\Delta x = (b-a)/n$. For our case, $b-a$ is the fin width and n is the number of subsection to be integrated to solve for the fin length based on the slot size. This approximation is performed using the EXCEL program, which is presented in Appendix F. By guessing the value of amplitude that make the right side of the approximation equation equal to the fin length, the final result of A_{mp} is equal to 0.226 mm, thus the maximum deflection = 0.452 mm.

II. Integration-square root approximation

According to the arc length formula from equation (E8), the integration-square root approximation changes this equation into:

$$L1 = \int_0^{L2} \left[1 + \frac{\left(\frac{d}{dx} y \right)^2}{2} \right] dx \quad (E11)$$

When substituting the buckling deflection shape from equation (E7) and changing L_1 to L_s and L_2 to L_f , the above equation becomes:

$$\begin{aligned} Lf &= \int_0^{Ls'} \left[1 + \frac{\left(2 \cdot \text{Amp} \cdot \sin \left(2 \cdot \pi \cdot \frac{x}{Ls'} \right) \cdot \frac{\pi}{Ls'} \right)^2}{2} \right] dx \\ &= \frac{1}{Ls'} \cdot (Ls'^2 + \pi^2 \cdot \text{Amp}^2) \end{aligned} \quad (E12)$$

and the amplitude can be calculated from:

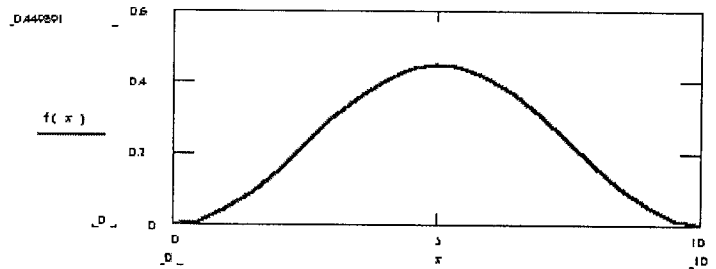
$$\text{Amp} = \sqrt{\frac{Ls' \cdot (Lf - Ls')}{\pi^2}} \quad (E13)$$

which results in $A_{mp} = 0.225$ mm. Therefore the maximum deflection based on this approximation method is 0.45 mm.

Both approximation techniques show that the calculated amplitude is very similar (0.226 vs. 0.225 mm). However, since the second approximation technique does not require any trial-and-error during the calculation, this later one is preferred.

The picture below is the X-Y graph of the fin geometry under the fundamental mode buckling (mode 1). x is the slot length (from 0 to Ls') and y is

the deflection curve. The maximum deflection (y-max) occurs at the middle of the slot length or fin length, which is equal to 0.45 mm.



3. Evaluation of the channel deviation due to fin buckling

The equation to evaluate the deviation of the channel (δ_c) is a/cn . For fundamental mode buckling, $a = A_{mp}$, so $\delta_c = A_{mp}/cn$. From the previous section, as $A_{mp} = 0.225$ mm, the channel deviation is 0.45 mm.

Case 2: Mode 2 Buckling

In this section the evaluation of the channel deviation due to mode 2 buckling will be discussed. The procedure will follow the same order as presented in Case 1.

1. Verification of buckling phenomenon

Verification is required to demonstrate that the clamping force due to thermal expansion is still higher than the critical load of buckling for mode 2 and the stress due to this mode of buckling will stay in the proportional limit of the yield stress. The critical stress of mode 2 for fixed-ended boundary condition is

$$\sigma_c = \frac{P_c}{A_f} = \frac{8.18 \cdot \pi^2 \cdot E \cdot I}{A_f \cdot L_f^2} \quad (E14)$$

For this case, $P_c = 2.22$ kN and $\sigma_c = 417$ MPa. With the clamping force of 5.28 kN, and the yield strength of 517 MPa. It shows that this fin can buckle into mode 2 shape and the elastic buckling equation can be implemented.

The next part represents the technique to evaluate the channel deviation of mode 2 based on half section of the total length. In fact, since the channel is symmetrical at half-length, evaluation of the top or bottom section of this mode demonstrates the same result.

2. Calculation of the maximum deflection of the fin buckling

Based on the fixed-ended boundary condition, the buckling of the second mode shape or the displacement function can be calculated from

$$y = A_{mp} \cdot \left[\sin(\mu \cdot x) - \mu \cdot x - \frac{\mu \cdot L_s}{2} \cdot (\cos(\mu \cdot x) - 1) \right] \quad (E15)$$

where A_{mp} is the amplitude of the column, and x is the distance from one side of the column to any position on the fin, and $\mu = 4.493 \cdot 2/L_s$. In this case, the buckling happens because the fin width at the elevated temperature (L_f') is longer than the slot size of the fixture (L_s).

Similarly to Case 1, the arc length formula will be implemented to solve for the amplitude of this fin buckling. From equation (E8), when substituting the buckling deflection shape from equation (E15) and changing L_f to L_f' and L_s to L_s' , equation (E8) becomes:

$$\begin{aligned} L_f' &= \int_0^{L_s'} \left[1 + \left(\frac{d}{dx} \left[\text{Amp} \cdot \left[\sin(\mu \cdot x) - \mu \cdot x - \frac{L_s'}{2} \cdot (\cos(\mu \cdot x) - 1) \right] \right) \right)^2 \right] dx \\ &= \int_0^{L_s'} \left[1 + \left(\text{Amp} \cdot \mu \cdot \cos(\mu \cdot x) - \text{Amp} \cdot \mu + \frac{1}{2} \cdot \text{Amp} \cdot \mu^2 \cdot L_s' \cdot \sin(\mu \cdot x) \right)^2 \right] dx \quad (E16) \end{aligned}$$

However, this function does not have a closed-form antiderivative, both approximation techniques previously stated in mode 1 buckling will be used to calculate the arc length and solve for the maximum deflection for this buckling shape.

I. Simpson Approximation

Based on Simpson's Rule presented in equation (E10), when substituting mode 2 buckling shape from equation (E15) and using the EXCEL program, the amplitude that satisfies both sides of the Simpson approximation method is 0.035 mm. (See Appendix F)

II. Integration-square root approximation

According to the integration-square root approximation (E11), when substituting the buckling deflection shape from equation (E15) and changing L_s to L_s' and L_f to L_f' , the above equation becomes:

$$\begin{aligned} L_f' &= \int_0^{L_s'} \left[1 + \frac{\text{Amp}^2 \cdot \left(\mu \cdot \cos(\mu \cdot x) - \mu + \frac{1}{2} \cdot \mu^2 \cdot L_s' \cdot \sin(\mu \cdot x) \right)^2}{2} \right] dx \\ &= L_s' + \text{Amp}^2 \cdot \left(\frac{1}{16} \cdot \mu^4 \cdot L_s'^3 + \frac{1}{4} \cdot \mu \cdot \cos(\mu \cdot L_s') \cdot \sin(\mu \cdot L_s') - \frac{1}{2} \cdot \mu^2 \cdot L_s' \cdot \mu \cdot \sin(\mu \cdot L_s') \right) \\ &\quad - \text{Amp}^2 \cdot \left(\frac{1}{4} \cdot \mu^2 \cdot L_s' \cdot \cos(\mu \cdot L_s')^2 + \frac{1}{2} \cdot \mu^2 \cdot L_s' \cdot \cos(\mu \cdot L_s') \cdot \frac{1}{16} \cdot \mu^3 \cdot L_s'^2 \cdot \cos(\mu \cdot L_s') \cdot \sin(\mu \cdot L_s') \right) \quad (E17) \end{aligned}$$

and the amplitude can be calculated from:

$$\text{Amp} = \sqrt{\frac{(L_f - L_s')}{\left(\frac{1}{16} \cdot \mu^4 \cdot L_s'^3 + \frac{1}{4} \cdot \mu \cdot \cos(\mu \cdot L_s') \cdot \sin(\mu \cdot L_s') - \dots - \frac{1}{16} \cdot \mu^3 \cdot L_s'^2 \cdot \cos(\mu \cdot L_s') \cdot \sin(\mu \cdot L_s')\right)}} \quad (E18)$$

The amplitude from this equation is similar to the result from the Simpson approximation (0.035 mm); therefore, instead of Simpson approximation that involves trial and error of amplitude value, this integration-square root approximate will be applied to solve for the amplitude of the buckling deflection in order to evaluate the maximum deflection and channel deviation.

However, the maximum deflection is not directly proportional to the amplitude. In order to find this value, the point where the fin has a slope equal to zero (except at $x = 0$ or L_s') needs to be calculated to solve for the maximum deflection of mode 2 buckling.

Using differential equation of deflection equation of mode 2 buckling and set this equation to zero, the point in which the slope is zero, x^* can be identified. The differential of equation (E15) is:

$$\frac{d}{dx} y = \text{Amp} \cdot \mu \cdot \cos(\mu \cdot x) - \text{Amp} \cdot \mu + \frac{1}{2} \cdot \text{Amp} \cdot \mu^2 \cdot L_s' \cdot \sin(\mu \cdot x)$$

$$\text{Set this equation} = 0; \quad \text{Amp} \cdot \mu \cdot \cos(\mu \cdot x) - \text{Amp} \cdot \mu + \frac{1}{2} \cdot \text{Amp} \cdot \mu^2 \cdot L_s' \cdot \sin(\mu \cdot x) = 0$$

$$\text{or} \quad \cos(\mu \cdot x) = 1 + \frac{\mu \cdot L_s'}{2} \cdot \sin(\mu \cdot x) = 0$$

$$\text{From relation;} \quad \cos^2(a) + \sin^2(a) = 1$$

$$\sqrt{1 - \sin^2(\mu \cdot x)} = 1 + \frac{\mu \cdot L_s'}{2} \cdot \sin(\mu \cdot x) = 0$$

$$\sqrt{1 - \sin^2(\mu \cdot x)} = 1 - \frac{\mu \cdot L_s'}{2} \cdot \sin(\mu \cdot x)$$

$$1 - \sin^2(\mu \cdot x) = \left(1 - \frac{\mu \cdot L_s'}{2} \cdot \sin(\mu \cdot x)\right)^2$$

$$\mu \cdot L_s' \cdot \sin(\mu \cdot x) = \sin^2(\mu \cdot x) \cdot \left[1 + \left(\frac{\mu \cdot L_s'}{2}\right)^2\right]$$

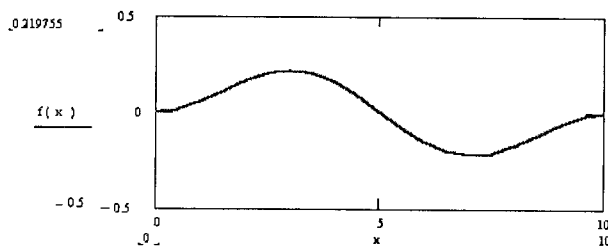
$$\sin(\mu \cdot x) = \frac{\mu \cdot L_s'}{1 - \left(\frac{\mu \cdot L_s'}{2}\right)^2}$$

Since sine-form equation can exist in both quadratic 1 and 2 (the angle can be just x where x is within 90 degree (quadratic 1), or x can be more than 90 degree (180- x degree)-quadratic 2. Thus, the above equation can be rewritten into two equations:

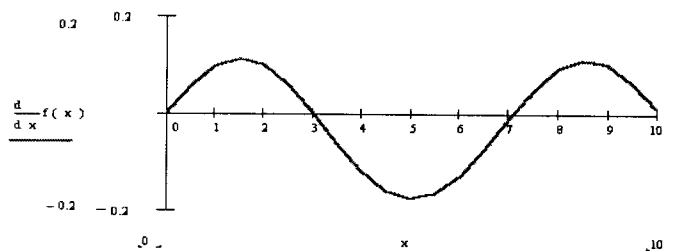
$$x = \frac{1}{\mu} \cdot \sin^{-1} \left[\frac{\mu \cdot L_2'}{1 + \left(\frac{\mu \cdot L_2'}{2}\right)^2} \right] \quad \text{or} \quad x = \frac{1}{\mu} \left[\pi - \sin^{-1} \left[\frac{\mu \cdot L_2'}{1 + \left(\frac{\mu \cdot L_2'}{2}\right)^2} \right] \right] \quad (E19)$$

From both equations, the resulting x can be either 0.492 or 3.039 mm. Since, there is a possibility that the fin slope can become zero more than one point, so we need to find just the point that generates the maximum deflection between both points. Hence, both points of x are substituted back in equation (E15), which then results in the deflection peak of 0.014 and 0.22 mm, respectively. In conclusion, the maximum deflection happens at 3.04 mm from the end of the fin, and its value is 0.22 mm.

The graph below represents the fin geometry based on mode 2 buckling. x is the slot length (from 0 to L_s') and y or $f(x)$ is the deflection curve.



The following picture is the x-y plot of the derivation of the graph above. The point where the bottom graph cross the x-axis or when $y = 0$ indicates that the slope from the above graph is equal zero, or the point where local maximum or minimum happens. As summarized earlier, the maximum deflection happens at 3.04 mm from the end of the fin (either from the left or the right end).



3. Evaluation of the channel deviation due to fin buckling

The equation to evaluate the deviation of the channel (δc) is d/cn , where d can be calculated from integration of deflection function from 0 to $L_s'/2$.

$$d = \frac{1}{X} \int_0^X F_x dx \tag{E20}$$

When substituting the buckling curve equation and $X = L_s'/2$, equation (E20) becomes:

$$d = \frac{1}{X} \int_0^X \text{Amp} \cdot \left[\sin(\mu \cdot x) - \mu \cdot x - \mu \cdot \frac{L_s'}{2} \cdot (\cos(\mu \cdot x) - 1) \right] dx$$

$$d = \frac{1}{(4 \cdot L_s')} \cdot \text{Amp} \cdot \left(\frac{8 \cdot \cos\left(\frac{1}{2} \cdot \mu \cdot L_s'\right) - \mu^2 \cdot L_s'^2 - 4 \cdot \mu \cdot L_s' \cdot \sin\left(\frac{1}{2} \cdot \mu \cdot L_s'\right) + 8}{\mu} \right) \tag{E21}$$

After substituting $A_{mp} = 0.035$ mm, d is equal to 0.122 mm, thus the channel deviation for mode 2 buckling (δc) is 0.245.

Case 3: Higher Modes Buckling

As soon as the mode of buckling gets higher (ex: mode 3, 4, etc.), the deflection of the buckling geometry of a fixed-ended boundary condition will be similar to a simply-support condition, in which sine-form function can be implemented to evaluate the buckling deflection curve. This section will demonstrate the implementation of sine-form into the buckling at higher modes. For example, mode 3 buckling will be evaluated based on sine-function deflection curve. The calculation of maximum deflection and the channel deviation will be performed.

Sine-form buckling geometry denotes by equation:

$$y = A_{mp} \cdot \sin\left(\frac{n \cdot \pi \cdot x}{L}\right) \quad (E22)$$

where n is the mode number (or number of half wave).

The following evaluation steps are similar to Case 1 and Case 2, except that the sine-wave equation will be implemented to characterize the fin buckling in higher modes.

1. Verification of buckling phenomenon

For mode n buckling, the stress equation (E14) based on simply-supported condition will be: $\sigma_c = \frac{P_c}{A_f} = \frac{n^2 \cdot \pi^2 \cdot E \cdot I}{A_f \cdot L_f^2}$ (E23)

Then we need to verify that the clamping force is larger than the critical load and the stress cause by this force is still smaller than the yield strength. Next section will explain the calculation of deflection when the fin is buckle into Mode n .

2. Calculation of the maximum deflection of the fin buckling

When applying the arc length equation to this sine function, the equation is: This equation does not have an antiderivative form, thus the approximation

$$L^f = \int_0^{Ls'} \left[\sqrt{1 + \left[\frac{d}{dx} \left(\text{Amp} \cdot \sin\left(\frac{n \cdot \pi \cdot x}{Ls'}\right) \right) \right]^2} \right] dx \quad (E24)$$

method is required in order to find the amplitude value.

Since the integration-square root approximation technique appears to be the preferable and reliable technique as mentioned in the previous cases, the amplitude would be solved based on the following:

$$L_f = \int_0^{L_s'} \left[1 + \frac{\left[\frac{d}{dx} \left(\text{Amp} \cdot \sin \left(\frac{n \cdot \pi \cdot x}{L_s'} \right) \right) \right]^2}{2} \right] dx$$

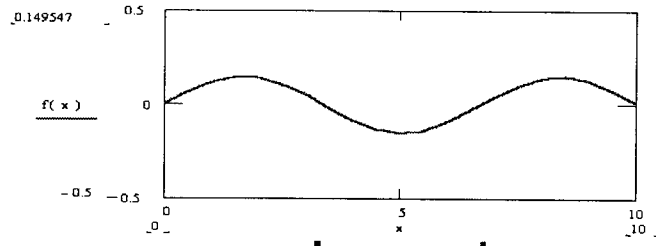
$$= \frac{1}{4} \frac{\left(4 \cdot L_s'^2 + n \cdot \pi \cdot \text{Amp}^2 \cdot \cos(n \cdot \pi) \cdot \sin(n \cdot \pi) + \text{Amp}^2 \cdot n^2 \cdot \pi^2 \right)}{L_s'} \quad (E25)$$

Therefore:

$$\text{Amp} := 2 \cdot \sqrt{\frac{L_s' \cdot (L_f - L_s')}{n \cdot \pi \cdot \cos(n \cdot \pi) \cdot \sin(n \cdot \pi) + n^2 \cdot \pi^2}} \quad (E26)$$

and we can solve for the amplitude when number of mode is substituted. For example, when mode 3 is chosen, the value of amplitude is 0.15 mm.

The characteristic of mode 3 buckling when plotted by a simulation program is shown below. As can be seen, the maximum deflection of this buckling curve is the amplitude of the equation and it occurs every one-sixth of the fin length.



3. Evaluation of the channel deviation due to fin buckling

The equation to evaluate the deviation of the channel (δ_c) is similar to Case 2, in which $\delta_c = d/cn$, except that the integration of deflection function will be evaluated from 0 to $L_s'/3$ because there are 3 loops in this buckling shape.

From equation (D20), when substituting the buckling curve equation and $X = L_s'/3$, this equation becomes:

$$d = \frac{1}{X} \int_0^X \text{Amp} \cdot \sin \left(\frac{3 \cdot \pi \cdot x}{L_s'} \right) dx$$

$$d = \frac{1}{(3 \cdot X)} \cdot L_s' \cdot \text{Amp} \cdot \frac{\left(\cos \left(3 \cdot \pi \cdot \frac{X}{L_s'} \right) - 1 \right)}{\pi} \quad (E27)$$

After substituting $A_{mp} = 0.15$ mm, d is equal to 0.096 mm, thus the channel deviation for Mode 2 buckling (δ_c) is 0.191.

APPENDIX F

Simpson Approximation for Calculation of Arc Length Equation

MODE 1 Buckling

Simpson's Approximation:
$$\int_a^b f(x) dx = \frac{\Delta x}{3} (f(x_0) + 4 \cdot f(x_1) + 2 \cdot f(x_2) + 4 \cdot f(x_3) + \dots + 2 \cdot f(x_{n-2}) + 4 \cdot f(x_{n-1}) + f(x_n))$$

$$y = A_{up} \cdot \left(1 - \cos \left(\frac{2 \cdot \pi \cdot x}{L_f} \right) \right)$$

where $L_s' = 10.10$ $\Delta x = 1.01$

Use trial and error to find the value of Amp that yield the arc length (L_f) = 10.15 mm

Amp	x	f(x)	F(x)	coeff	coeff*F(x)
Guessing 0.226	0	0	1	1	1
	1.01	0.0068292	1.0034088	4	4.013635
	2.02	0.0178791	1.00889996	2	2.0178
	3.03	0.0178791	1.00889996	4	4.0356
	4.04	0.0068292	1.0034088	2	2.006818
	5.05	0	1	4	4
	6.06	0.0068292	1.0034088	2	2.006818
	7.07	0.0178791	1.00889996	4	4.0356
	8.08	0.0178791	1.00889996	2	2.0178
	9.09	0.0068292	1.0034088	4	4.013635
	10.1	0	1	1	1
			Sum =		30.14771
			Delta x/3 =		0.336667
			Result =		10.150

MODE 2 buckling

where $L_s' = 10.10$ $\Delta x = 1.01$ $\mu = 0.889703$

Use trial and error to find the value of Amp that yield the arc length (L₁) = 10.149

Amp	x	f(x) ^{0.5}	F(x)	coeff	coeff*F(x)
Guessing 0.035	0	0	1	1	1
	1.01	0.0977248	1.00476372	4	4.019055
	2.02	0.0982101	1.00481104	2	2.009622
	3.03	0.0010896	1.00000059	4	4.000002
	4.04	-0.120351	1.0072161	2	2.014432
	5.05	-0.174473	1.01510636	4	4.060425
	6.06	-0.120438	1.00722656	2	2.014453
	7.07	0.0009807	1	4	4.000002
	8.08	0.0981619	1.00480632	2	2.009613
	9.09	0.0977737	1.00476848	4	4.019074
	10.1	0.0001092	1.00000001	1	1
			Sum =		30.14668
			Delta x/3 =		0.336667
			Result =		10.149

x-max	Max deflec	delta c	cn (mm)	d
3.04	0.2199	0.2446	0.5	0.12228

APPENDIX G

Conversion of NTU into a Compensated Area or Number of Channels

As mentioned in equation (C2) of Appendix C, NTU is equal to $\frac{U * Ah}{W * cp}$,

which means that if U , W , and cp are kept constant, NTU should be changed in the proportion to Ah or the heat transfer area. With respect to a nominal microchannel heat exchanger, NTU of a uniform case (NTU_o) is 19, and its corresponding Ah is $11.43 \times 10^3 \text{ mm}^2$. At this point the heat exchanger has the heat effectiveness of 95%. If assume the channel encounters the deviation of 45% in channel width, its NTU changes to 7 (NTU'). As a result, the heat transfer area must decrease at the same rate as the NTU- Ah relationship. However, instead of solving for the loss of NTU, transforming this reduction into an additional of heat transfer needed to compensate for this NTU reduction would be a better indicator for the manufacturing perspective. To increase the performance of a nonuniform channel heat exchanger, the compensated area is derived from the ratio of an original NTU over the deviated NTU or NTU_o/NTU' . Therefore, percent increase in area to

compensate for the loss due to channel deviation is: $\frac{NTU_o}{NTU'} - 1 * (100\%)$. (G1)

According to this relationship, the increase in the number of channel to compensate for the loss can be solved by multiplying the number of the original channel needed in the uniform case with the result of equation (G1). For example, for $NTU' = 7$, the percent change in compensated area = $\frac{19}{7} - 1 \times 100\% = 172\%$, and a total of 52 channels will be needed in this nonuniform heat exchanger.

For the counter-flow heat exchanger that encounters the channel misalignment, NTU of the misaligned channel will proportional to the decreased heat transfer area, Ah' , where $Ah' = L_{ch} * L_c$. Therefore, equation (G1) can be rewritten in case of channel misalignment as:

$$\left(\frac{Ah}{Ah'} - 1 = \frac{L_{ch} * L_f}{L_{ch} * L_c} - 1 = \frac{L_f}{L_f - x} - 1 \right) = \frac{x}{L_f - x} * (100\%) \quad (G2)$$

where x is the amount of misalignment between consecutive channels.

APPENDIX H

Measuring Equipment Summaries, Test specimen, and Fixture Configurations

Optical Microscope and Video Measurement System

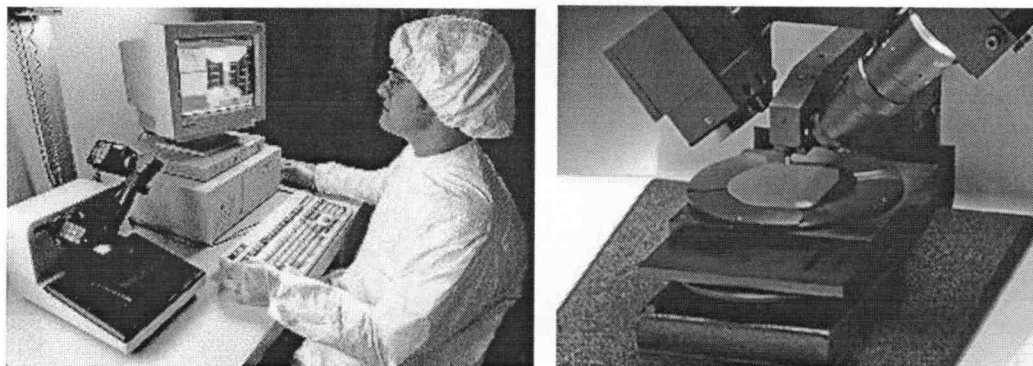
Misalignment and fin buckling geometry can be measured by a LEICA DML microscope and a video measurement system (VIA-100). The entire system provides flexibility and accuracy for specimen's dimensional inspection because its features include X, Y or point to point measurement, an easy calibration procedure, and 50X-2000X magnification within submicron scale resolution. Thickness measurements can be carried out over a 5-cm range and within submicron resolution. Not only is the video measurement system available in the laboratory, a computer unit can be connected to capture the digital image of specimen characteristics using a FlashBus FBG program.

As stated previously, the optical microscope is mainly used for direct visual observation, or preliminary observation for final characterization. In conjunction with a measurement system, this device provides the capability for two-dimension and rough thickness measurement within micron resolution. It is an accessible and affordable device for a typical laboratory. However, it still has many limitations within the range of measurement or resolution, including limited magnification, lack in three-dimensional analysis or surface topography. Hence, other measurement techniques, such as an electron microscope or surface-measuring device, are necessary to facilitate the micro-scale characterization.

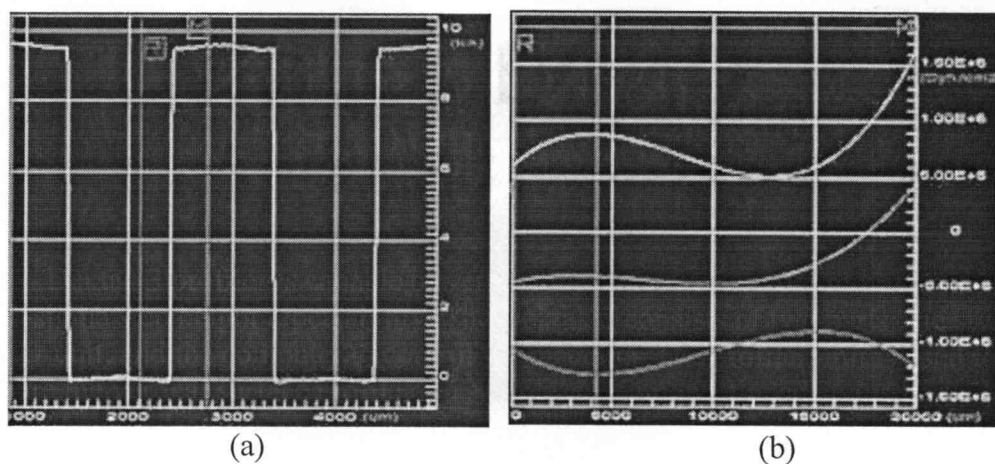
Contact profilometer

This device applies a contact measurement technique to inspect the surface profile of the microstructure. The instrument uses a probe or a stylus to run along the surface of interest to evaluate the surface profile and projects on the device's monitor or plots on a graph-sketching machine. Some profilometer uses special tools such as diamonds to identify the characteristics of that profile within nanometer resolution. In general, profilometer uses a transducer inside the system to convert the traced result into numerical data or graph on the monitor or other output devices.

The contact profilometer that will be used to verify the experimental result in this study is the DEKTAK 3 Surface Profiler from VEECO Metrology Group, Inc. Pictures below show the Dektak 3 system currently used in micro manufacturing laboratory at Oregon State University.



Dektak 3 profiler is capable of vertical measurement up to 2 mm with a 1 nm, 1-sigma step height repeatability. The Dektak 3 consists of two parts: the stylus profiler unit, and the computer to control the machine. The profiler unit is used to measure the vertical surface profile of a sample. A diamond-tipped stylus is lowered onto the sample, and the stage is slowly translated, causing the stylus to move up and down vertically as it moves along the surface. The vertical motion of the stylus is measured electrically and converted to a digital format. The profile can be viewed on the screen and saved to disk to be printed. With this capability, topography of fin laminae before and after buckling can be accurately verified. For instance pictures of step height measurement (a) and the measurement of substrate waviness (b) are shown below.



The specimen and fixture configuration used in the study of chapter 3 and 4 are presented on the following pages.

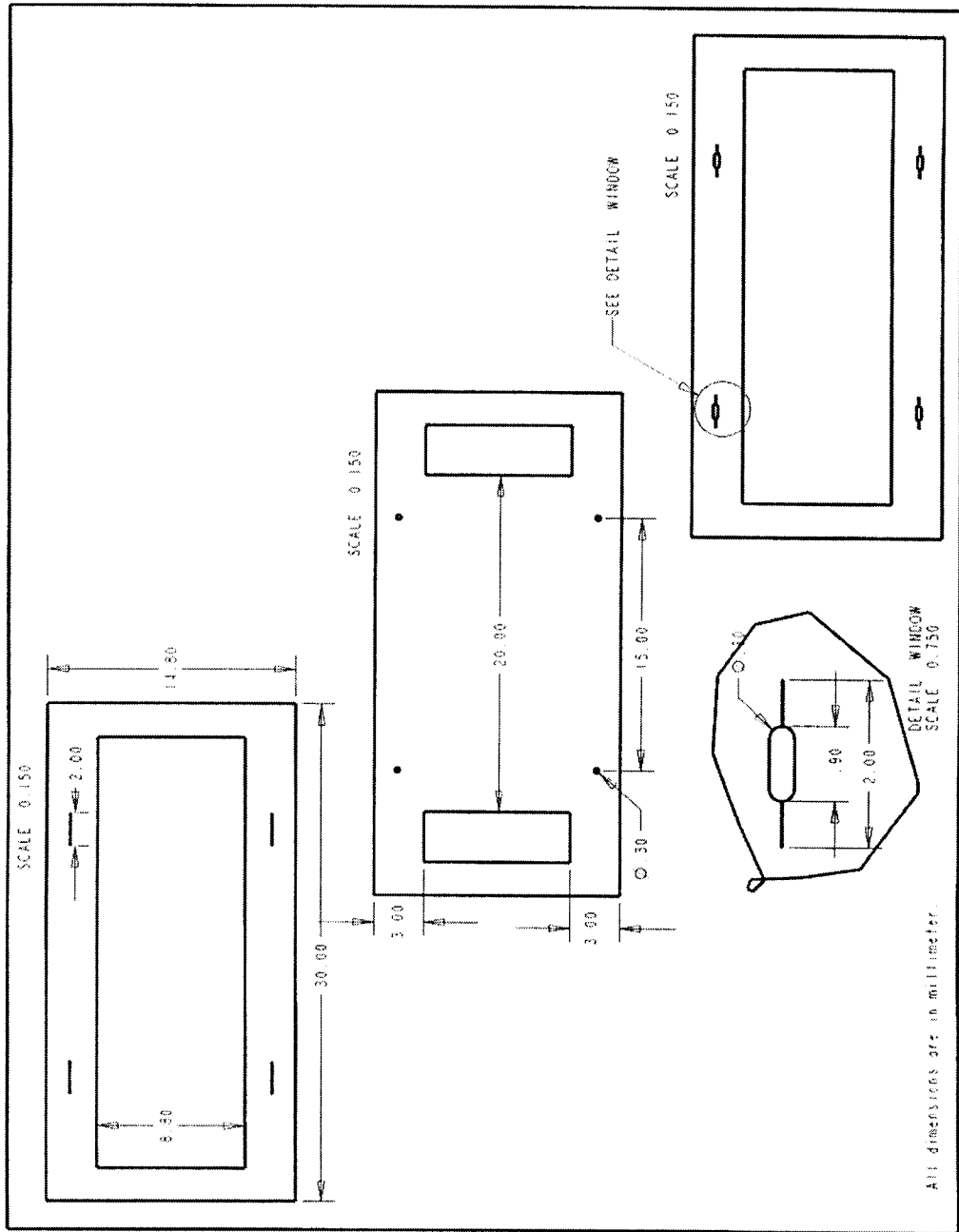


Figure H-1. Specification of the test specimen

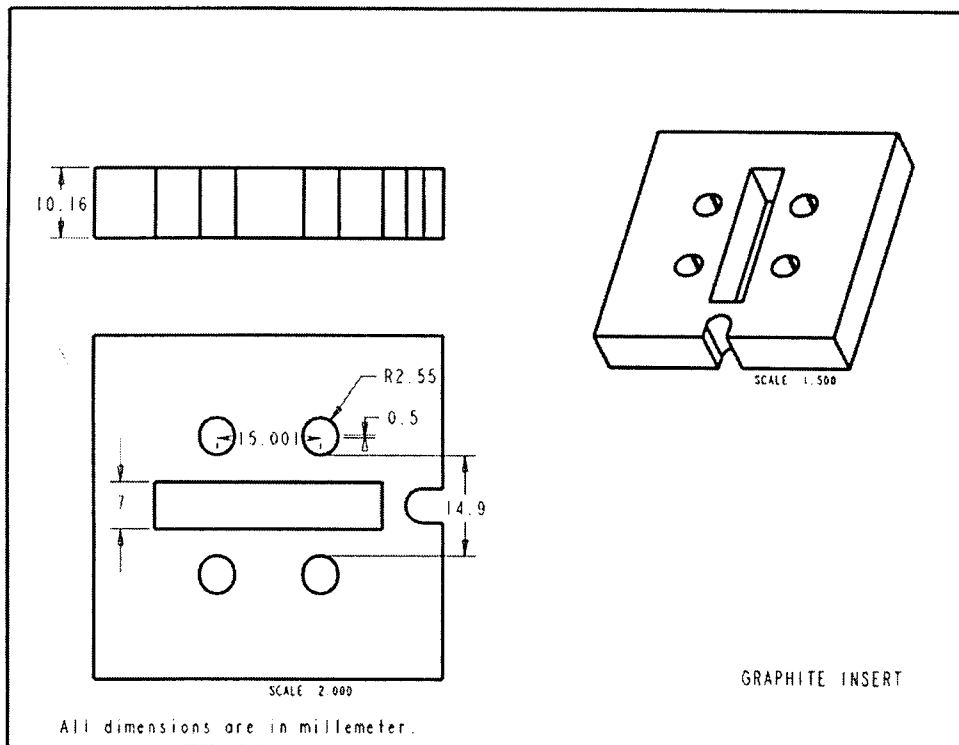
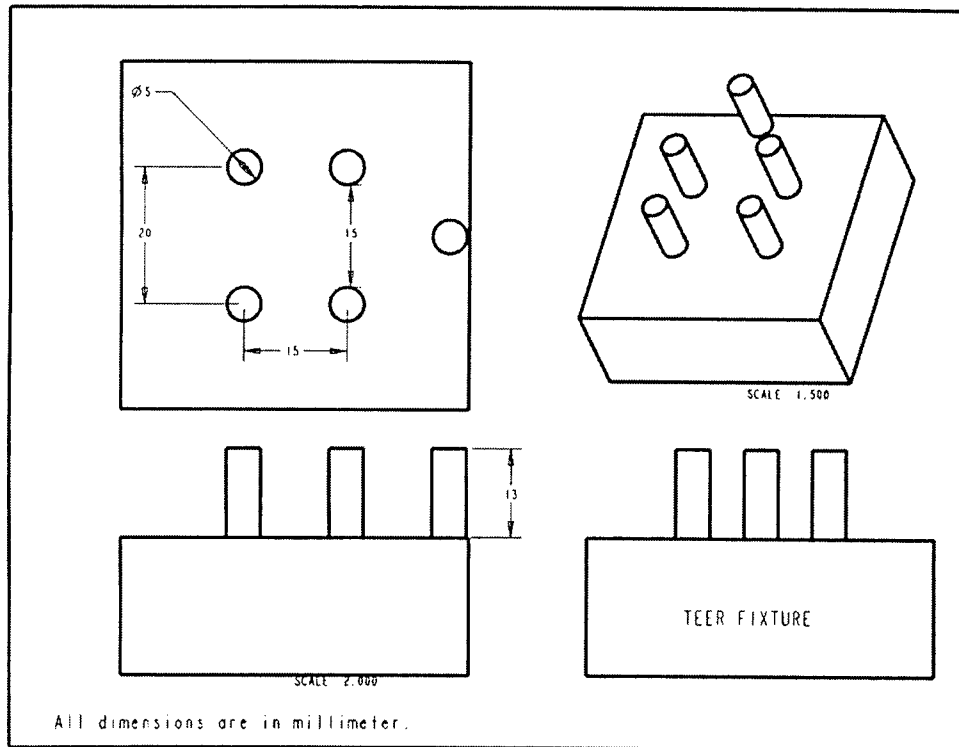


Figure H-2. Specifications of the TEER fixture and the graphite insert

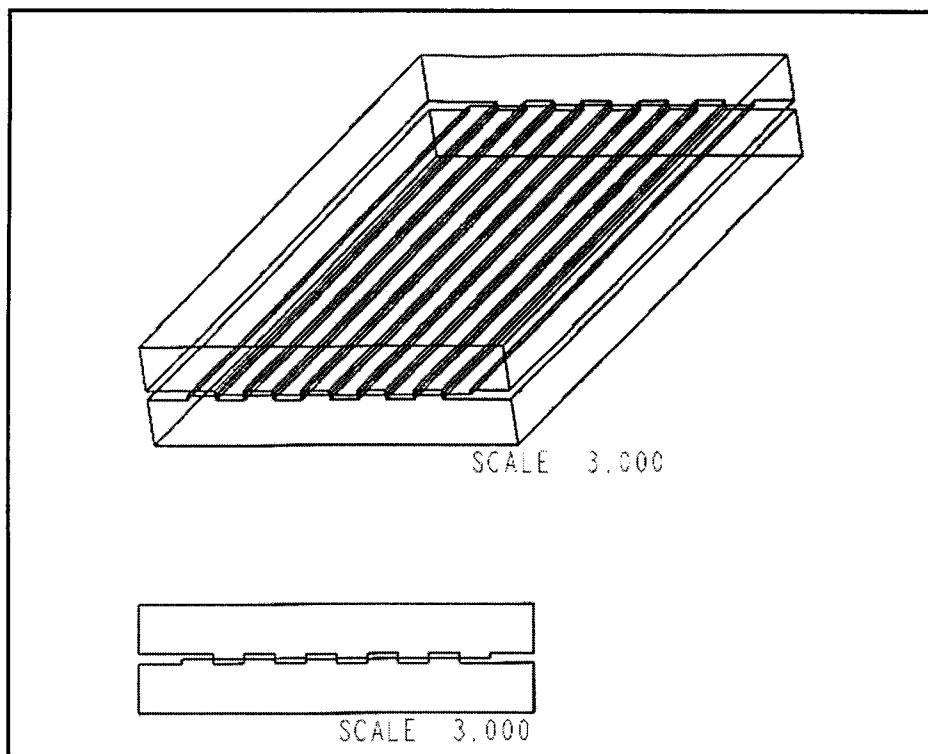
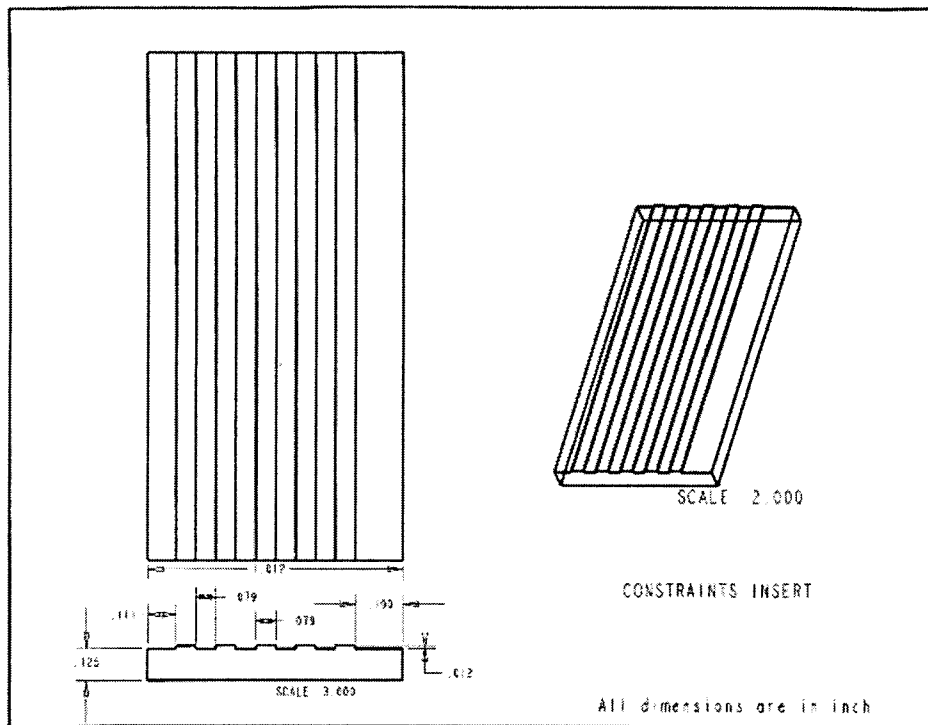


Figure H-3. Specifications of the constraints insert for mode 10 buckling induction

APPENDIX I

Experimental Procedure Details for Patterning, Bonding and Measurement of Microlaminated Specimens

1. Patterning Step
 - a. Create a patterning program on the SmartCAM software and export into the code file for ESI 4420 laser micromachining format.
 - b. Place stainless steel shim with specified thickness on the stage of ESI 4420 laser unit and turn on the vacuum stage to hold the shim.
 - c. Focus the top surface of shim using illumination system and the video screen.
 - d. Set the tool path parameters depending on the pattern needed to cut. For cut-through pattern, set the following conditions:
 - Profile speed = 2.0 mm/sec
 - Rep Rate = 4000 Hz
 - Bite size = 0.5 micron
 - Num Repeat = 3 (for 0.0508-mm shim), 6 (for 0.0762-mm shim), and 12 (for 0.1016-mm shim)
 - Current = 22.75 A (laser power ~ 300 mW)For line marker, the parameters are changed to:
 - Profile speed = 0.9 mm/sec
 - Rep Rate = 6000 Hz
 - Bite size = 0.15 micron
 - Num Repeat = 1
 - Current = 19.5 A (laser power ~ 50 mW)
 - e. Execute the patterning program.
2. Pre-Bonding Measurement Step
 - a. Polish the patterned shims with 3M Ultrafine handpad Scotch-Brite to remove ejecta from laser machining process.
 - b. Clean polished shims with 50% concentrate Citranox in the ultrasonic cleaner for 20 minutes.
 - c. Rinse the shims with water.
 - d. Take the fin lamina from the set to measure on the Dektak3 profilometer
 - e. Hold the fin lamina on the stage with scotch tape on both ends.
 - f. Position the stylus near the edge of the lamina.
 - g. Run the scan file to measure the initial flatness of the lamina across its width.

- h. Collect analyzed data of maximum deflection (TIR) at four locations of each specimen (from left to right).
3. Bonding Step
- a. Wash all shims with acetone, ethanol and de-ionized water (AED) and blow dry with pressurized air.
 - b. Clean the graphite fixture and apply a thin layer of magnesium hydroxide on the fixture and let it dry.
 - c. Stack the laminae in the prearranged order against one side of the pin.
 - d. Place the fixture assembly in the hot press and close the chamber.
 - e. Program the hot press for bonding cycle with a ramping rate of 35 °C/min to target temperature of 750 °C and dwell time of 1 hour.
 - f. Turn on the mechanical pump and rough valve to pre-pump the chamber.
 - g. Turn the diffusion pump and the chiller on.
 - h. Switch to diffusion pump when the vacuum reaches 100 mTorr by closing the rough valve and open the fore line valve and gate valve.
 - i. Run the program for bonding cycle when the vacuum has reached 1×10^{-4} mbar.
 - j. Apply the clamping load to the fixture when the temperature in the cycle reaches 750 °C (about 25 minutes from the beginning).
 - k. Retract the clamping load at the end of dwell cycle and let the system cool down.
 - l. Take the fixture out of the hot press at the end of cycle, when the temperature inside the chamber is down to room temperature.
 - m. Wash the laminate with AED and blow dry with pressurized air.
4. Post-Bonding Measurement
- * For Buckling Measurement
 - a. Place the laminate on the Dektak profiler stage and hold it down with scotch tape at both ends.
 - b. Run the scan file across the laminate to measure the surface profile.
 - c. Record the maximum deflection (TIR) data at four locations.

* For Alignment Measurement

According to Chapter 3, the misalignment measuring features has been included in the pattern program as shown on Figure 3-15. These features are located at four corners of the laminate. The steps to measure misalignment are as follows:

- a. Place the laminate on the optical microscope with measuring features appear on the top.
- b. Turn on the microscope and the video measurement system.
- c. Turn on the computer and execute FlashBus FBG program.
- d. Select the measure command to enter the XY measurement mode.

- e. Locate the misalignment measuring features on the screen.
- f. Use 200X magnification with resolution of 0.3-0.5 micron to measure the misalignment.
- g. Use one measurement line as a reference datum and another line to measure the displacement, by positioning one line at the bottom of the screen and another on the edge of the feature of interest. (See Figure 1)
- h. Identify the center of the reference line by positioning the measurement line at the top edge of the reference line and record the number. (See Figure 1(a))
- i. Move that measurement line to the bottom edge of the reference line and record the number. The center of the reference line will be the average of those two numbers. (See Figure I-1(b))
- j. Identify the center of the line marker using the same step as step h., but position the measurement line at the top and the bottom of the line marker instead. (See Figure 1(c) and (d))
- k. Deduct the average center of the reference line from the line marker to achieve the misalignment value at that location. (for Figure 1, the misalignment is $\{(150+123.5)/2 - (138.8+111.8)/2\}$ 11.45 microns.)
- l. Follow step g to j for the other three locations.

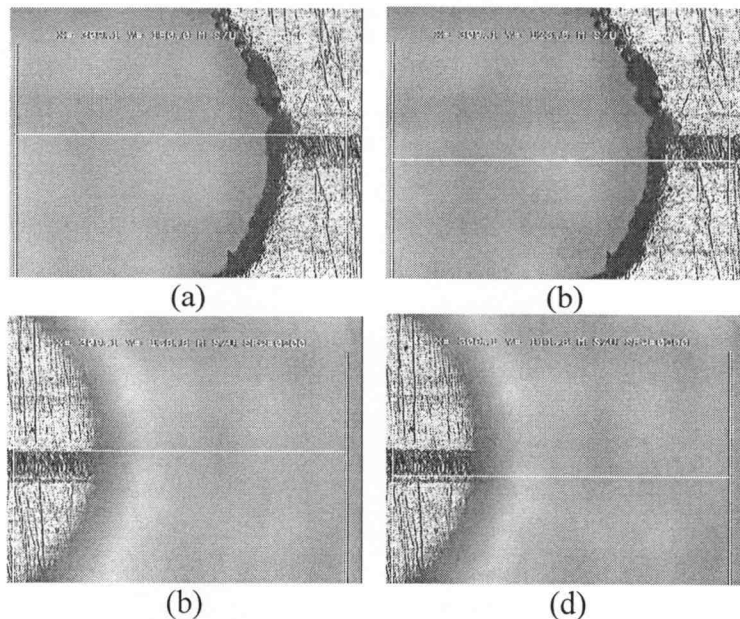


Figure I-1. Measurement of misalignment using optical microscope

According to previous investigation, Scanning Electron Microscope has been used to validate the results from this measurement technique, which is proved to be a reliable process.

APPENDIX J

Nominal Evaluation of Fin Buckling Based on Original and Modified TEER

Case 1: Graphite fixture has a perfect rigidity

Assumption: the graphite fixture is rigid, and it won't be complied by the registration force that come from the difference in the thermal expansion between the fin and the fixture

Graphite property

$$\alpha\Delta := 0.004 \quad \Delta T := 730\text{K} \quad E_g := 13.2 \cdot 10^9 \text{Pa}$$

Fixture spec

$$\alpha_g := \frac{\alpha\Delta}{\Delta T} \quad \alpha_g = 5.479 \times 10^{-6} \text{K}^{-1}$$

$\phi_p := 5.05 \text{mm}$ $L_{pp} := 25.05 \text{mm}$ $L_s := L_{pp} - 2 \cdot \phi_p$ $L_s = 14.95 \text{mm}$
SS fin property

For $t := 0.0508 \text{mm}$ (2 mil S.S.) $E := 200 \cdot 10^9 \text{Pa}$ $E' := 135 \cdot 10^9 \text{Pa}$

$$\alpha_{ss} := 19.8 \cdot 10^{-6} \text{K}^{-1} \quad L_{ch} := 20 \text{mm} \quad L_e := 3 \text{mm} \quad L_g := 2 \text{mm}$$

$$L_s' := L_s (1 + \alpha_g \cdot \Delta T) \quad L_s' = 15.01 \text{mm} \quad L_c' := L_s' - 2 \cdot L_e \quad I := \frac{L_{ch} \cdot t^3}{12}$$

$$A_f := L_{ch} \cdot t \quad A_f' := A_f (1 + \alpha_{ss} \cdot \Delta T)$$

$$L_{d0} := \frac{L_s'}{(1 + \alpha_{ss} \cdot \Delta T)} \quad L_{d0} = 14.8 \text{mm}$$

The fin will buckle when the force due to thermal expansion is higher that the critical load of buckling and the stress due to this registration force must higher than the proportional limit strength ($\sigma_p \sim 74 \text{MPa}$)

Critical point of buckling

$$P_c := \frac{4 \cdot \pi^2 \cdot E' \cdot I}{L_c^2} \quad P_c = 14.345 \text{N}$$

Proportional limit stress (after this point, the fin will permanently buckle)

$$\sigma_p := 73.6 \cdot 10^6 \text{Pa} \quad P_t := \sigma_p \cdot A_f'$$

Therefore the force to cause the fin to permanently buckle is $P_t = 75.858 \text{N}$

Since this force is already higher than critical load, we will use this force to evaluate the minimum fin size that can create the fin warpage after bonding.

$$P_t := A_f' \cdot E' \cdot (\alpha_{ss} - \alpha_g) \cdot \Delta T_{eff} \quad \text{So} \quad \Delta T_{eff} := \frac{\sigma_p}{E' \cdot (\alpha_{ss} - \alpha_g)}$$

$$\Delta T_{eff} = 38.07 \text{K} \quad \Delta T_{eff0} := \Delta T_{eff}$$

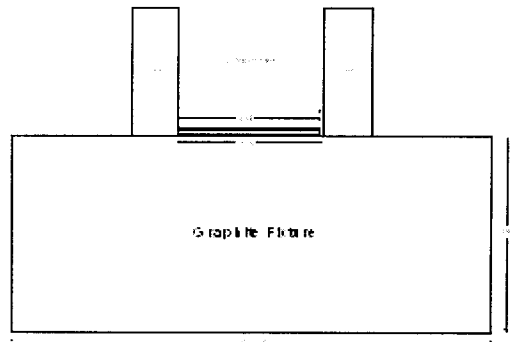
$$\Delta T' := \Delta T - \Delta T_{eff} \quad \Delta T' = 691.93 \text{K}$$

$$L_d := L_s \left(\frac{1 + \alpha_g \cdot \Delta T'}{1 + \alpha_{ss} \cdot \Delta T'} \right) \quad L_d = 14.8 \text{mm} \quad L_{db} := L_d$$

The oversize amount from the perfect spec is $Ov_0 := L_{db} - L_{d0} \quad Ov_0 = 7.926 \times 10^{-3} \text{mm}$

The fin need to be about 8 microns oversize from the perfect spec in order to generate the permanent warpage.

Case 2: Laminae are at the bottom of the fixture and the fixture is comply to the registration force (Original TEER)



$$\begin{aligned}
 hf &:= 29.72\text{mm} & Lf &:= 51.90\text{mm} \\
 AF &:= hf \cdot Lf & AF &= 1.542 \times 10^3 \text{mm}^2 & \text{(Cross section area of the fixture)} \\
 \Delta F' &:= AF \cdot (1 + \alpha_g \cdot \Delta T)^2 & \Delta F' &= 1.555 \times 10^3 \text{mm}^2 & E_g = 1.32 \times 10^{10} \text{Pa}
 \end{aligned}$$

From, the preceding section, when the fin is about 8 micron oversize, the force due to thermal expansion will reach the proportional limit and make the pin to permanently buckle

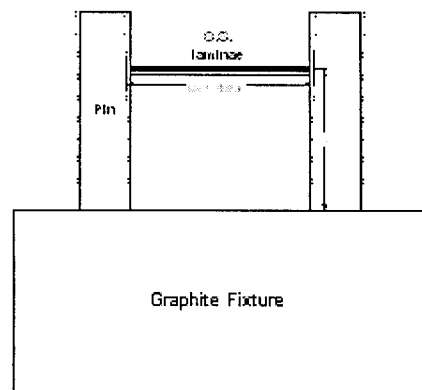
But, as we put the specimen to bond together in the fixture, the actual force that act against the pin will be based on the cumulative of 3 layers. So we need to evaluate this force (Pr).

The real cross section area that create the registration force will include the cross section of the fin itself plus the cross-section area at the edge of all three structures.

$$\begin{aligned}
 A3 &:= Af + 6 \cdot Lg \cdot t & A3 &= 1.64 \text{mm}^2 \\
 Pr &:= \sigma_p \cdot A3 & Pr &= 120.725\text{N} \\
 \epsilon_f &:= \frac{Pr}{\Delta F' \cdot E_g} & \epsilon_f &= 5.882 \times 10^{-6} & \text{(Strain of fixture due to this registration force)} \\
 \delta_f &:= \epsilon_f \cdot L_s & \delta_f &= 8.79 \times 10^{-5} \text{mm}
 \end{aligned}$$

The fixture will comply less than 0.1 micron upon registration force due to thermal expansion (when stack laminae in the original TEER)

Case 3 The fin is at some height from the bottom of the fixture, and we consider the graphite pins as cantiliver beams (Modified TEER)



Beam bending equation

$$\delta := \frac{F \cdot L^3}{3 \cdot E \cdot I} \qquad I := \frac{\pi \cdot \phi^4}{64} \qquad \delta := \frac{64 \cdot F \cdot L^3}{3 \cdot E_g \cdot \pi \cdot \phi^4}$$

Now, if we make the graphite fixture to be able to expand by the force due to this registration force, so that the fin will not warp at this amount of this interference (just 8 micron).

Consider the graphite fin as the cantilever which is applied by the load due to registration force, Pt.

If set the maximum displacement of the pin to withstand the registration force (σ_y) to be 50.8 micron (fin thickness)

$$t = 0.0508 \text{ mm} \quad t1 := t \quad \delta1 := t$$

Solve for the length of the pin (from the bottom plate) that allow this max displacement based on this critical registration force where the fin start to permanently warp.

From Cantilever equation:

$$\delta := \frac{64 \cdot F \cdot L^3}{3 \cdot E_g \cdot \pi \cdot \phi p^4}$$

This equation is based on one pair of pin, but we have two pair of pin to support this registration force, therefore we need to divide the above equation by 2

$$\delta := \frac{64 \cdot F \cdot L^3}{6 \cdot E_g \cdot \pi \cdot \phi p^4}$$

Solve for L

$$L := \left(\frac{6 \cdot E_g \cdot \pi \cdot \phi p^4 \cdot \delta}{64 \cdot F} \right)^{\frac{1}{3}}$$

Since we have 3-layer structure, we need to add the cross sectional area of the top & bottom plate to evaluate the real registration force against the pin.

Check the registration force up to the point that the stress is over the proportional limit

$$A_f := Lch \cdot t \quad A_f := A_f \cdot (1 + \alpha_{ss} \cdot \Delta T) \quad A_3 := A_f + 6 \cdot Lg \cdot t$$

$$A_f = 1.031 \text{ mm}^2 \quad A_3 = 1.64 \text{ mm}^2 \quad \sigma_p = 7.36 \times 10^7 \text{ Pa}$$

$$\Delta T_{eff} := \frac{\sigma_p}{E' \cdot (\alpha_{ss} - \alpha_g)} \quad \Delta T_{eff} = 38.07 \text{ K}$$

$$P_{t3} := A_3 \cdot E' \cdot (\alpha_{ss} - \alpha_g) \cdot \Delta T_{eff} \quad P_{t3} = 120.725 \text{ N}$$

$$\delta := \delta1 \quad L := \left(\frac{6 \cdot E_g \cdot \pi \cdot \phi p^4 \cdot \delta}{64 \cdot P_{t3}} \right)^{\frac{1}{3}} \quad L = 10.209 \text{ mm} \quad L1 := L$$

Example Let $L_d := 14.86 \text{ mm}$

$$CL := L_s - L_d \quad CL = 0.09 \text{ mm} \quad L_d' := L_d \cdot (1 + \alpha_{ss} \cdot \Delta T) \quad L_d' = 15.075 \text{ mm}$$

$$\Delta T' := \frac{CL}{(\alpha_{ss} \cdot L_d - \alpha_g \cdot L_s)} \quad \Delta T' = 423.908 \text{ K}$$

$$\Delta T_{eff} := \Delta T - \Delta T' \quad \Delta T_{eff} = 306.092 \text{ K}$$

$$\delta \Gamma1 := \delta$$

$$Inf3 := L_d' - L_s' - \delta \Gamma1 \quad Inf3 = 0.014 \text{ mm} \quad L_x := L_c' + Inf3$$

$$Amp3 := \sqrt{\left(\frac{L_x \cdot Inf3}{\pi^2} \right)} \quad Amp3 = 0.114 \text{ mm} \quad MaxW := 2 \cdot Amp3 \quad MaxW = 0.228 \text{ mm}$$

$$MaxW' := \frac{MaxW}{(1 + \alpha_{ss} \cdot \Delta T)} \quad MaxW' = 0.225 \text{ mm}$$

Apply the same evaluation for 4-mil thick specimen

Note: For thicker material, the force will be greater and the amount of deflection will be proportional to the thickness

$$t := 0.1016 \text{ mm} \quad (4 \text{ mil})$$

$$A_f := L_{ch} \cdot t \quad A_f' := A_f (1 + \alpha_{ss} \cdot \Delta T) \quad A_f' = 2.061 \text{ mm}^2$$

At the same amount of interference to cause the fin to permanent warpage

$$A_3 := A_f' + 6 \cdot L_g \cdot t \quad A_3 = 3.281 \text{ mm}^2$$

$$\Delta T_{eff} := \frac{\sigma_p}{E' (\alpha_{ss} - \alpha_g)} \quad \Delta T_{eff} = 38.07 \text{ K}$$

$$P_{t3} := A_3 \cdot E' (\alpha_{ss} - \alpha_g) \cdot \Delta T_{eff} \quad P_{t3} = 241.45 \text{ N}$$

$$L := L_1$$

$$\delta := \frac{64 \cdot P_{t3} \cdot L^3}{6 \cdot E_g \cdot \pi \cdot \phi_p^4} \quad \delta = 0.102 \text{ mm}$$

Example

$$L_{et} \quad L_{d} := 14.90 \text{ mm}$$

$$C_L := L_s - L_d \quad C_L = 0.05 \text{ mm} \quad L_{d'} := L_d (1 + \alpha_{ss} \cdot \Delta T) \quad L_{d'} = 15.115 \text{ mm}$$

$$I_{nf} := L_{d'} - L_s' \quad I_{nf} = 0.106 \text{ mm}$$

Since we know that the fixture will expand at least 100 micron before the specimen starts to buckle

$$\delta_{T2} := \delta$$

$$I_{nf4} := L_{d'} - L_s' - \delta_{T2} \quad I_{nf4} = 3.965 \times 10^{-3} \text{ mm} \quad L_x := L_c' + I_{nf4}$$

$$A_{mp4} := \sqrt{\left(\frac{L_x \cdot I_{nf4}}{\pi^2} \right)} \quad A_{mp4} = 0.06 \text{ mm} \quad \text{Max}W := 2 \cdot A_{mp4} \quad \text{Max}W = 0.12 \text{ mm}$$

$$\text{Max}W' := \frac{\text{Max}W}{(1 + \alpha_{ss} \cdot \Delta T)} \quad \text{Max}W' = 0.119 \text{ mm}$$

Apply the same evaluation for 3-mil thick specimen

If

$$t := 0.0762 \text{ mm} \quad (3 \text{ mil}) \quad L_{ch} = 20 \text{ mm}$$

$$A_f := L_{ch} \cdot t \quad A_f' := A_f (1 + \alpha_{ss} \cdot \Delta T) \quad A_f' = 1.546 \text{ mm}^2$$

At the same amount of interference to cause the fin to permanent warpage

$$A_3 := A_f' + 6 \cdot L_g \cdot t \quad A_3 = 2.46 \text{ mm}^2$$

$$\Delta T_{eff} = 38.07 \text{ K}$$

$$P_{t3} := A_3 \cdot E' (\alpha_{ss} - \alpha_g) \cdot \Delta T_{eff}$$

$$P_{t3} = 181.087 \text{ N}$$

Set

$$L := L_1$$

$$\delta := \frac{64 \cdot P_{t3} \cdot L^3}{6 \cdot E_g \cdot \pi \cdot \phi_p^4} \quad \delta = 0.076 \text{ mm}$$

APPENDIX K

**Experimental Results of Fin Buckling and Channel Misalignment for
Chapter 3**

1. Fin Buckling Results

Thickness	Initial status				Avg	SD
2	32.08	33.45	33.47	42.70	35.43	4.89
	19.44	20.32	33.60	32.11	26.37	7.52
	18.65	18.84	13.94	14.38	16.45	2.65
Average	23.39	24.20	27.00	29.73	26.08	2.88
3	13.02	14.00	18.24	22.07	16.83	4.16
	7.13	9.12	10.85	6.29	8.35	2.05
	2.72	14.76	12.22	4.65	8.59	5.81
Average	7.62	12.63	13.77	11.00	11.26	2.67
4	4.11	6.31	9.55	13.16	8.28	3.95
	4.89	7.50	7.62	9.45	7.37	1.88
	5.71	8.53	9.64	6.03	7.48	1.92
Average	4.90	7.45	8.94	9.55	7.71	2.07

Thickness (mil)	Inf (micron)	Results/Location				Average	SD
		1	2	3	4		
2	0	21.67	19.44	26.84	27.70	23.91	4.00
	10	147.61	200.35	197.47	188.39	183.46	24.43
	30	313.18	285.25	280.16	278.38	289.24	16.22
3	0	22.59	24.83	23.39	22.68	23.37	1.04
	10	286.77	266.54	235.61	176.54	241.37	48.07
	40	394.66	387.12	362.48	358.10	375.59	18.02
4	0	9.03	7.95	8.70	6.71	8.10	1.03
	10	119.14	99.27	99.17	99.04	104.16	9.99
	20	275.96	264.87	250.57	226.10	254.38	21.53

The following pictures present the measurement of fin after the bonding cycle ranged from 50.8- μm , 76.2- μm , and 101.6- μm thick. Each profile was measured at the center of the fin for a variety of interference.

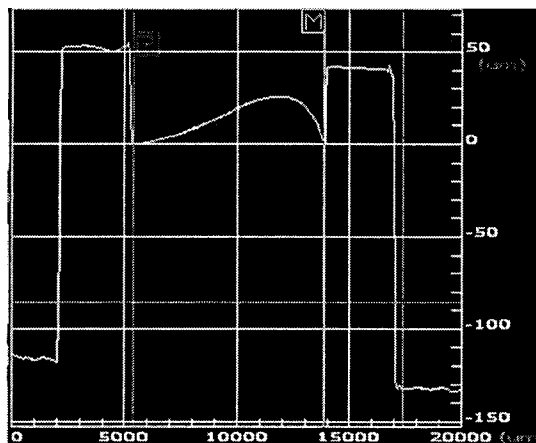


Fig K-1. Surface profile of 50.4- μm fin laminate at 0- μm interference

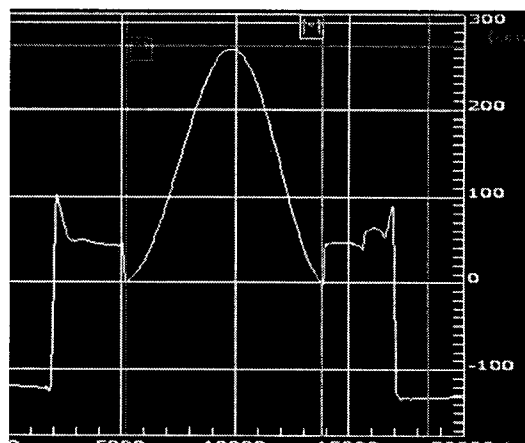


Fig K-3. Surface profile of 50.4- μm fin laminate at 30- μm interference

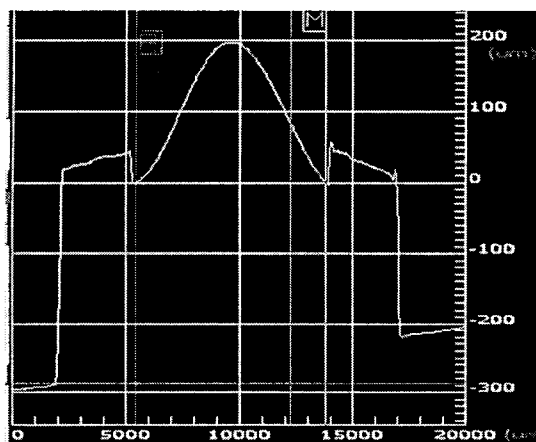


Fig K-2. Surface profile of 50.4- μm fin laminate at 10- μm interference

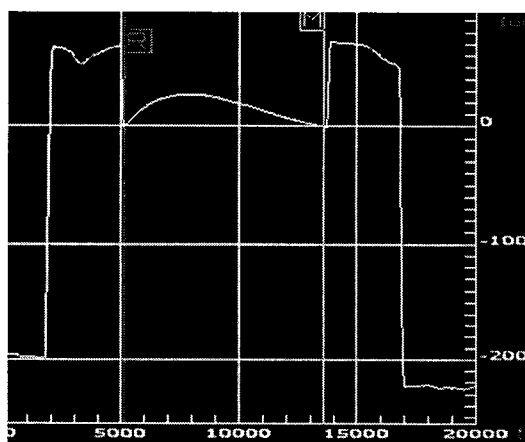


Fig K-4. Surface profile of 76.2- μm fin laminate at 0- μm interference

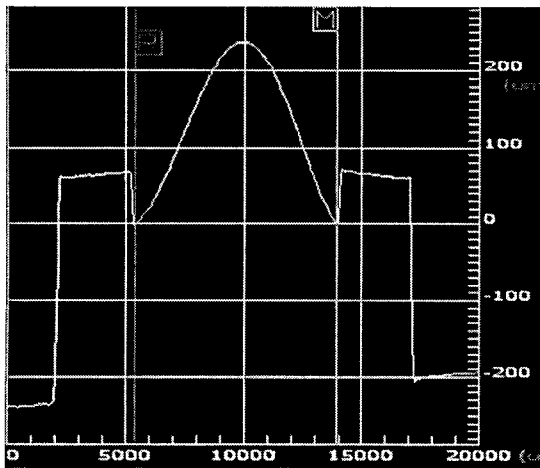


Fig K-5. Surface profile of 76.2- μm fin laminate at 10- μm interference

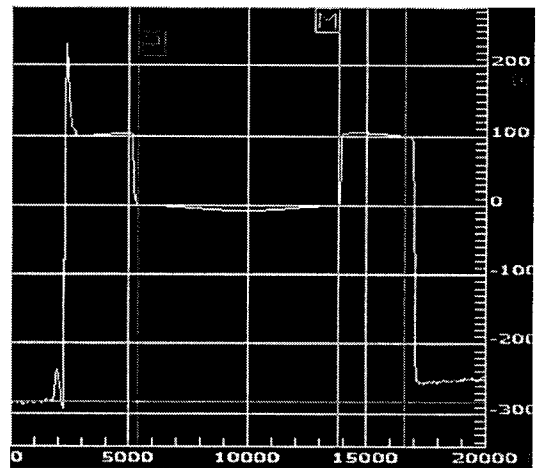


Fig K-7. Surface profile of 101.6- μm fin laminate at 0- μm interference

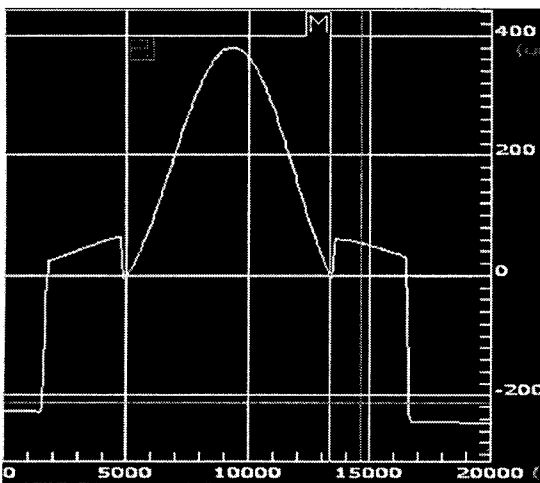


Fig K-6. Surface profile of 76.2- μm fin laminate at 40- μm interference

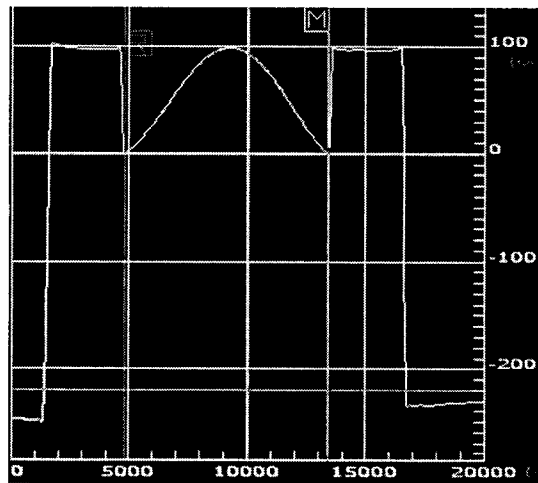


Fig K-8. Surface profile of 101.6- μm fin laminate at 10- μm interference

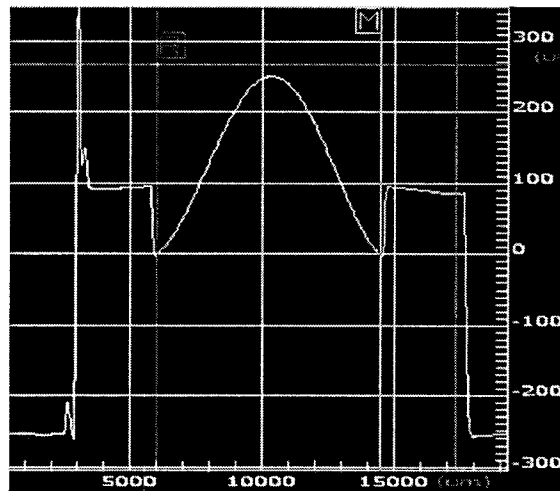


Fig K-9. Surface profile of 101.6- μm fin laminate at 20- μm interference

2. Misalignment Results

Inspector 1

Thickness (micron)	Allowance (micron)	Window				Average Misalignment
		1	2	3	4	
50.8	0	9.65	6.50	3.25	1.00	5.10
	50	5.75	23.90	6.50	16.65	13.20
	100	4.75	28.40	12.50	13.50	14.79
	-10	12.90	12.50	14.75	8.15	12.08
	-30	4.70	5.50	3.75	16.70	7.66
76.2	0	5.75	2.00	13.65	2.50	5.98
	50	8.90	22.15	16.95	35.55	20.89
	100	7.95	20.90	8.75	30.10	16.93
	-10	7.70	10.90	17.15	11.00	11.69
	-40	14.40	30.90	7.35	30.10	20.69
101.6	0	4.50	12.45	2.50	2.50	5.49
	50	10.40	12.65	1.50	2.00	6.64
	100	2.00	49.80	1.75	49.80	25.84
	-10	10.45	31.80	14.00	6.75	15.75
	-20	3.00	6.25	12.75	4.70	6.68

Inspector 2

Thickness (micron)	Allowance (micron)	Window				Average Misalignment	Total Average
		1	2	3	4		
50.8	0	9.75	7.70	4.20	1.50	5.79	5.444
	50	5.45	25.15	6.50	17.40	13.63	13.413
	100	5.25	28.65	11.90	14.45	15.06	14.925
	-10	10.40	10.25	11.75	8.25	10.16	11.119
	-30	4.50	10.65	6.75	18.90	10.20	8.931
76.2	0	5.95	1.20	9.95	6.40	5.88	5.925
	50	10.95	24.60	16.50	37.30	22.34	21.613
	100	5.90	21.40	7.50	18.40	13.30	15.113
	-10	5.65	7.95	7.45	6.50	6.89	9.288
	-40	16.90	22.20	12.40	31.65	20.79	20.738
101.6	0	5.15	11.20	6.20	1.75	6.08	5.781
	50	11.15	13.65	3.50	1.90	7.55	7.094
	100	2.25	50.25	3.50	51.50	26.88	26.356
	-10	8.45	28.60	20.00	4.80	15.46	15.606
	-20	2.50	9.00	9.75	3.95	6.30	6.488

- Adhesive Tape Test

Inspector 1

Thickness (micron)	Allowance (micron)	Window				Average Misalignment
		1	2	3	4	
76.2	20	14.90	14.45	5.40	11.40	11.54
	50	12.75	6.50	20.40	25.15	16.20
	100	8.45	3.25	25.55	13.65	12.73
	> 100	5.95	6.95	12.45	4.25	7.40
	> 100	6.70	5.00	9.20	6.25	6.79

Inspector 2

Thickness (micron)	Allowance (micron)	Window				Average Misalignment
		1	2	3	4	
76.2	20	11.90	11.95	4.00	8.65	9.13
	50	10.90	5.50	19.90	18.45	13.69
	100	6.15	5.25	30.30	12.00	13.43
	> 100	6.45	8.15	7.25	7.20	7.26
	> 100	12.40	6.70	7.25	4.70	7.76

APPENDIX L

Experimental Results of Fin Buckling for Chapter 4

Fin Buckling Results

Thickness	Initial status				Avg	SD
50.4 μm	29.81	11.49	15.31	17.11	18.43	7.94
	8.87	13.29	20.58	23.91	16.66	8.58
	23.28	28.35	33.88	42.00	31.88	8.02
	6.21	12.25	19.45	31.14	17.26	10.72
	7.67	14.76	14.43	13.17	12.51	3.30
	10.08	25.86	23.49	13.69	18.28	7.59
	3.84	5.85	11.21	6.40	6.83	3.00
	23.66	13.99	22.66	8.86	17.29	7.10
Average	14.18	15.73	20.13	19.54	17.39	7.03
76.2 μm	8.28	3.85	6.34	2.52	5.25	2.57
	4.67	6.11	7.10	7.23	6.28	1.18
	22.00	29.33	38.75	27.04	29.28	7.02
	11.54	18.65	21.00	17.52	17.18	4.03
Average	11.62	14.49	18.30	13.58	14.50	3.70
101.6 μm	6.21	10.29	9.25	6.41	8.04	2.04
	4.11	6.31	9.55	13.16	8.28	3.95
	2.43	3.01	3.65	4.09	3.30	0.73
	12.41	16.10	12.45	13.69	13.66	1.73
	22.19	19.53	20.45	21.42	20.90	1.16
	9.60	6.97	1.65	3.38	5.40	3.57
	13.94	13.58	11.89	10.73	12.54	1.50
	5.64	15.63	15.18	9.76	11.55	4.76
Average	9.57	11.43	10.51	10.33	10.46	2.43

Thickness (mil)	Inf (micron)	Set#	Results/Location				Average	SD	
			1	2	3	4			
2	0	1	16.62	18.52	22.53	21.72	19.85	2.76	
		2	11.98	13.10	10.91	13.56	12.39	1.19	
		AVG	14.30	15.81	16.72	17.64	16.12	1.97	
	40	1	7.76	17.74	41.01	50.12	29.16	19.73	
		2	19.11	13.35	14.36	34.40	20.31	9.73	
		AVG	13.44	15.55	27.69	42.26	24.73	14.73	
	50	1	22.24	24.86	35.24	47.54	32.47	11.51	
		2	33.88	41.34	47.89	54.85	44.49	8.97	
		AVG	28.06	33.10	41.57	51.20	38.48	10.24	
	70	1	223.43	239.24	253.28	244.42	240.09	12.53	
	90	1	352.89	393.71	415.97	386.25	387.21	26.13	
	3	0	1	7.15	8.41	9.59	8.05	8.30	1.01
		60	1	10.85	11.43	11.18	12.86	11.58	0.89
70		1	24.63	27.14	30.31	34.18	29.07	4.13	
90	1	192.29	246.93	267.65	268.70	243.89	35.83		
4	0	1	7.29	4.99	10.00	10.83	8.28	2.66	
		2	8.17	7.13	6.70	7.35	7.34	0.62	
		AVG	7.73	6.06	8.35	9.09	7.81	1.64	
	90	1	10.53	8.86	11.01	13.86	11.07	2.08	
		2	10.43	8.42	9.16	18.86	11.72	4.83	
		AVG	10.48	8.64	10.09	16.36	11.39	3.46	
	100	1	9.30	12.56	14.99	25.86	15.68	7.18	
		2	10.28	10.30	12.67	16.38	12.41	2.88	
		AVG	9.79	11.43	13.83	21.12	14.04	5.03	
	110	1	165.88	178.69	178.18	182.18	176.23	7.13	
	120	1	277.11	245.58	324.03	302.88	287.40	33.84	

The following pictures present the measurement of fin after the bonding cycle ranged from 50.8- μm , 76.2- μm , and 101.6- μm thick. Each profile was measured at the center of the fin for a variety of interference.

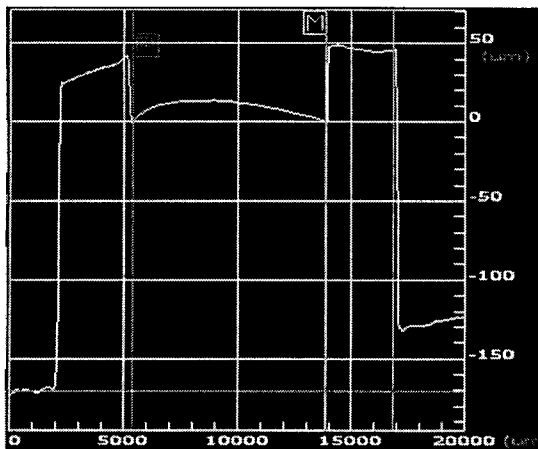


Fig L-1. Surface profile of 50.4- μm fin laminate at 0- μm interference

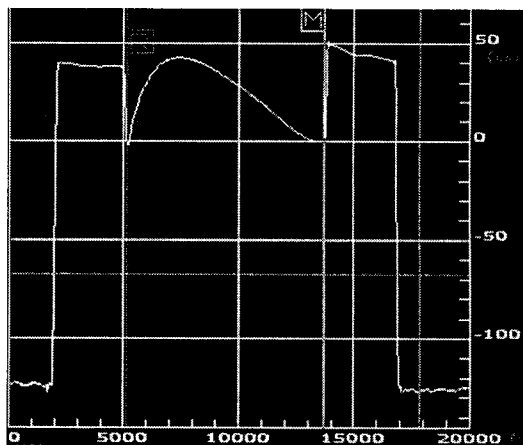


Fig L-3. Surface profile of 50.4- μm fin laminate at 50- μm interference

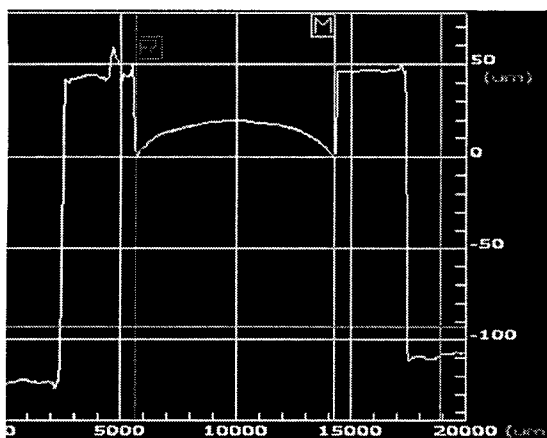


Fig L-2. Surface profile of 50.4- μm fin laminate at 40- μm interference

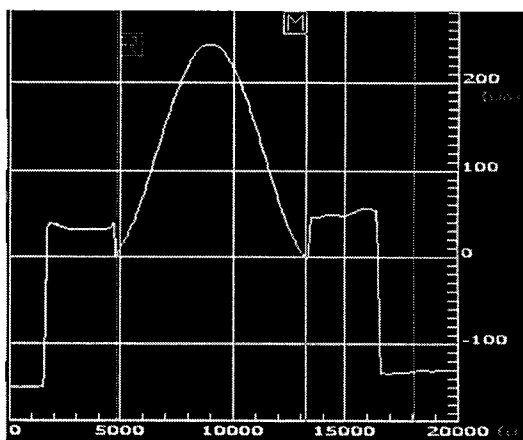


Fig L-4. Surface profile of 50.4- μm fin laminate at 70- μm interference

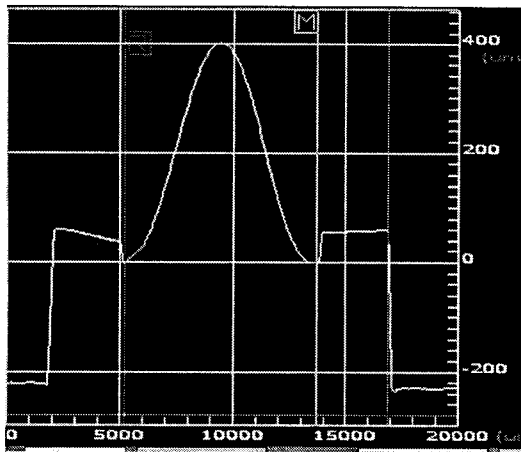


Fig L-5. Surface profile of 50.4- μm fin laminate at 90- μm interference

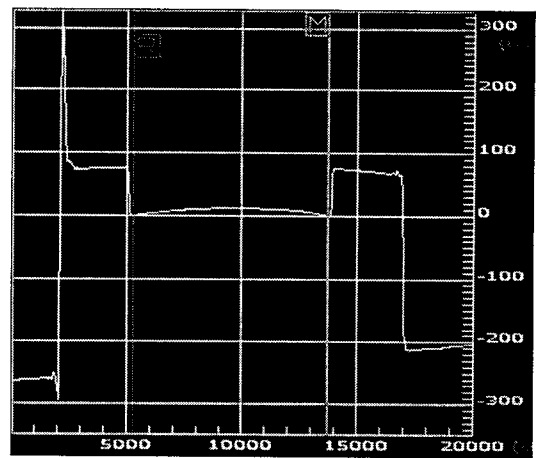


Fig L-7. Surface profile of 76.2- μm fin laminate at 60- μm interference

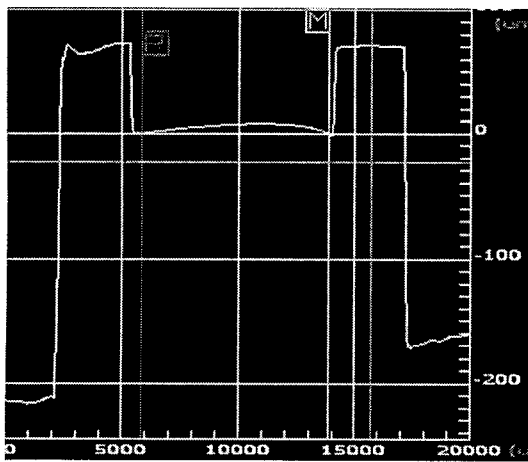


Fig L-6. Surface profile of 76.2- μm fin laminate at 0- μm interference

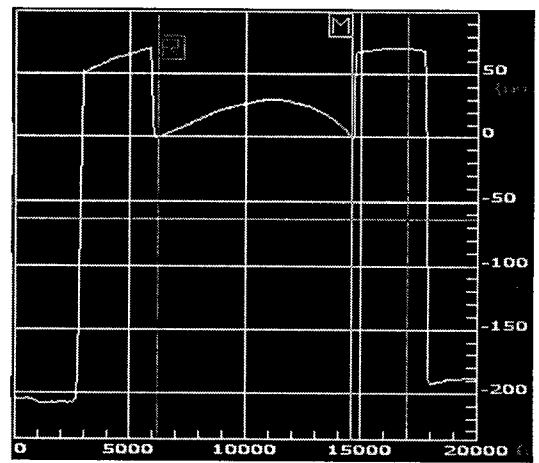


Fig L-8. Surface profile of 76.2- μm fin laminate at 70- μm interference

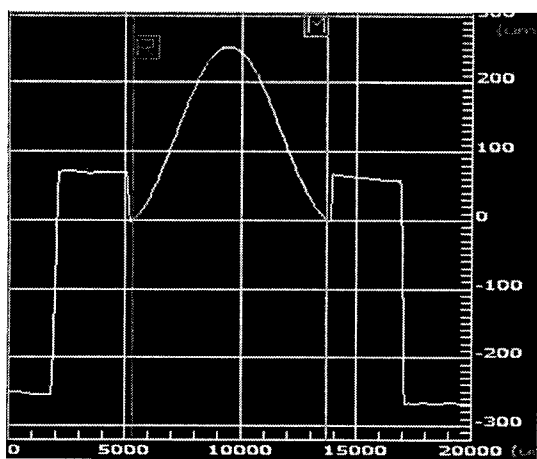


Fig L-9. Surface profile of 76.2- μm fin laminate at 90- μm interference

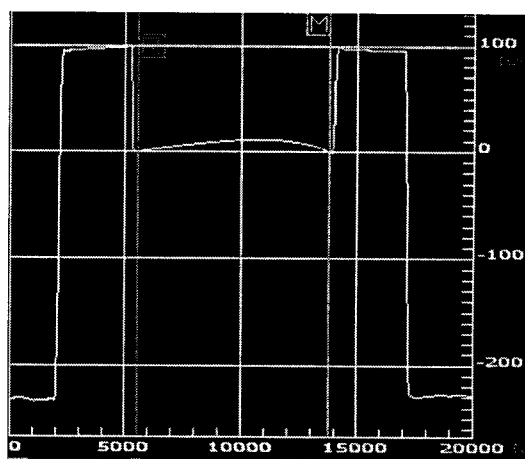


Fig L-11. Surface profile of 101.6- μm fin laminate at 90- μm interference

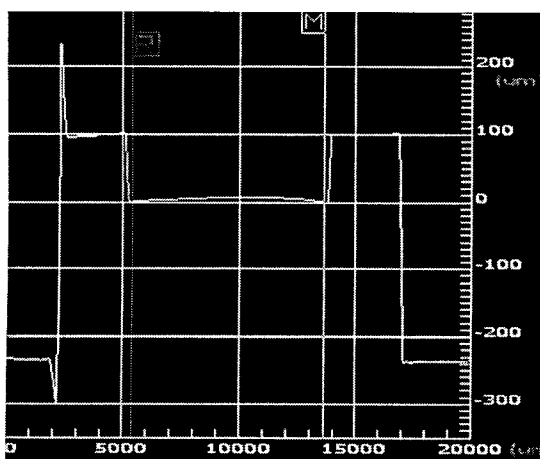


Fig L-10. Surface profile of 101.6- μm fin laminate at 0- μm interference

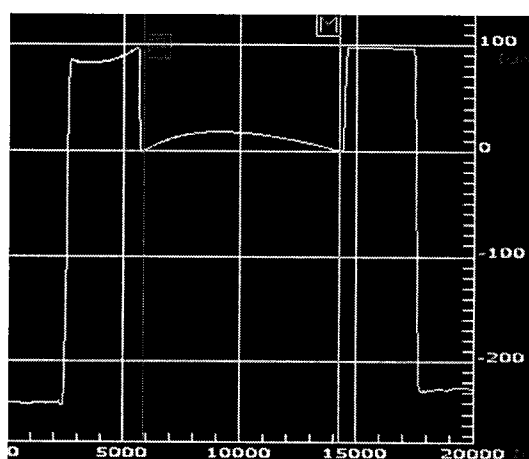


Fig L-12. Surface profile of 101.6- μm fin laminate at 100- μm interference

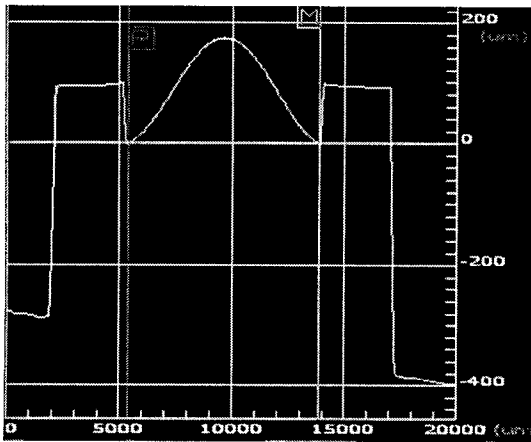


Fig L-13. Surface profile of 101.6- μm fin laminate at 110- μm interference

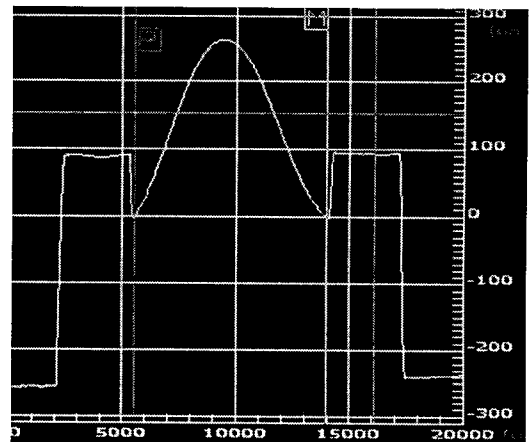


Fig L-14. Surface profile of 101.6- μm fin laminate at 120- μm interference

APPENDIX M

Statistical Evaluations

Chapter 3

1. Significance of Thickness effect on the first set of the experiment in Chapter 3

Multifactor ANOVA - Experiment

Analysis of Variance for Experiment - Type III Sums of Squares

Source	Sum of Squares	Df	Mean Square	F-Ratio	P-Value
MAIN EFFECTS					
A:Thickness	0.004075	2	0.0020375	0.99	0.5029
B:Interference	0.037446	1	0.037446	18.16	0.0509
RESIDUAL	0.004123	2	0.0020615		
TOTAL (CORRECTED)	0.045644	5			

All F-ratios are based on the residual mean square error.

The StatAdvisor

The ANOVA table decomposes the variability of Experiment into contributions due to various factors. Since Type III sums of squares (the default) have been chosen, the contribution of each factor is measured having removed the effects of all other factors. The P-values test the statistical significance of each of the factors. Since no P-values are less than 0.05, none of the factors have a statistically significant effect on Experiment at the 95.0% confidence level.

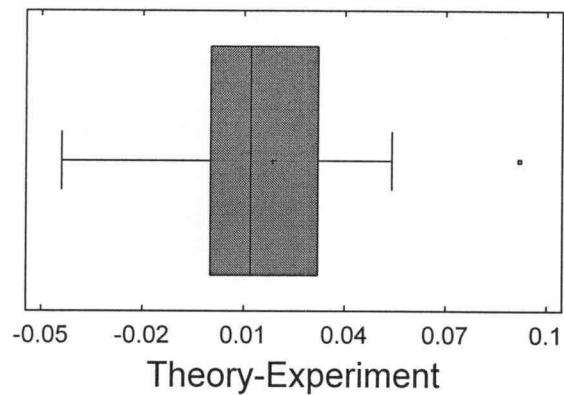
2. Paired t-test for Theoretical and Experimental Results

Paired Samples - Theory & Experiment

Summary Statistics for Theory-Experiment

Count = 9
 Average = 0.0183333
 Variance = 0.001493
 Standard deviation = 0.0386394
 Minimum = -0.044
 Maximum = 0.092
 Range = 0.136
 Std. skewness = 0.617433
 Std. kurtosis = 0.640713

Box-and-Whisker Plot



Confidence Intervals for Theory-Experiment

```
-----
95.0% confidence interval for mean: 0.0183333 +/- 0.0297009  [-
0.0113676,0.0480342]
95.0% confidence interval for standard deviation: [0.0260992,0.0740241]
The StatAdvisor
-----
```

This pane displays 95.0% confidence intervals for the mean and standard deviation of Theory-Experiment. The classical interpretation of these intervals is that, in repeated sampling, these intervals will contain the true mean or standard deviation of the population from which the data come 95.0% of the time. In practical terms, we can state with 95.0% confidence that the true mean Theory-Experiment is somewhere between -0.0113676 and 0.0480342, while the true standard deviation is somewhere between 0.0260992 and 0.0740241.

Hypothesis Tests for Theory-Experiment

Sample mean = 0.0183333

t-test

Null hypothesis: mean = 0.0
Alternative: not equal

Computed t statistic = 1.42342
P-Value = 0.192422

Do not reject the null hypothesis for alpha = 0.05.

The StatAdvisor

This pane displays the results of three tests concerning the center of the population from which the sample of Theory-Experiment comes. The first test is a t-test of the null hypothesis that the mean Theory-Experiment equals 0.0 versus the alternative hypothesis that the mean Theory-Experiment is not equal to 0.0. Since the P-value for this test is greater than or equal to 0.05, we cannot reject the null hypothesis at the 95.0% confidence level.

3. ANOVA for Misalignment Results

Multifactor ANOVA - Misalignment

Analysis Summary

Dependent variable: Misalignment

Factors:

Allowance
Thickness
Inspector
Window

Number of complete cases: 120

The StatAdvisor

This procedure performs a multifactor analysis of variance for Misalignment. It constructs various tests and graphs to determine which factors have a statistically significant effect on Misalignment. It also tests for significant interactions amongst the factors, given sufficient data. The F-tests in the ANOVA table will allow you to identify the significant factors. For each significant factor, the Multiple Range Tests will tell you which means are significantly different from which others. The Means Plot and Interaction Plot will help you interpret the significant effects. The Residual Plots will help you judge whether the assumptions underlying the analysis of variance are violated by the data.

Analysis of Variance for Misalignment - Type III Sums of Squares

Source	Sum of Squares	Df	Mean Square	F-Ratio	P-Value

MAIN EFFECTS					
A:Allowance	2869.35	6	478.225	5.95	0.0000
B:Thickness	104.46	2	52.2301	0.65	0.5241
C:Inspector	1.27102	1	1.27102	0.02	0.9002
D:Window	2330.34	3	776.779	9.67	0.0000
RESIDUAL	8598.35	107	80.3584		

TOTAL (CORRECTED)	14087.3	119			

All F-ratios are based on the residual mean square error.

The StatAdvisor

The ANOVA table decomposes the variability of Misalignment into contributions due to various factors. Since Type III sums of squares (the default) have been chosen, the contribution of each factor is measured having removed the effects of all other factors. The P-values test the statistical significance of each of the factors. Since 2 P-values are less than 0.05, these factors have a statistically significant effect on Misalignment at the 95.0% confidence level.

Chapter 4

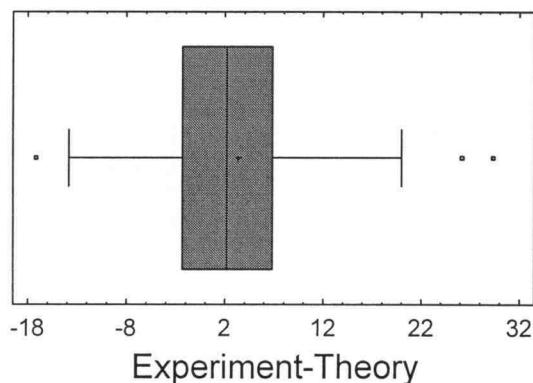
1. Paired t-test for Theoretical and Experimental Results

Paired Samples - Experiment & Theory

Summary Statistics for Experiment-Theory

Count = 20
 Average = 3.4115
 Variance = 130.482
 Standard deviation = 11.4229
 Minimum = -17.17
 Maximum = 29.34
 Range = 46.51
 Stnd. skewness = 1.32616
 Stnd. kurtosis = 0.940349

Box-and-Whisker Plot



Confidence Intervals for Experiment-Theory

 95.0% confidence interval for mean: 3.4115 +/- 5.34607 [-1.93457,8.75757]
 95.0% confidence interval for standard deviation: [8.68698,16.6839]
 The StatAdvisor

 This pane displays 95.0% confidence intervals for the mean and standard deviation of Experiment-Theory. The classical interpretation of these intervals is that, in repeated sampling, these intervals will contain the true mean or standard deviation of the population from which the data come 95.0% of the time. In practical terms, we can state with 95.0% confidence that the true mean Experiment-Theory is somewhere between -1.93457 and 8.75757, while the true standard deviation is somewhere between 8.68698 and 16.6839.

Hypothesis Tests for Experiment-Theory

Sample mean = 3.4115

t-test

 Null hypothesis: mean = 0.0
 Alternative: not equal

Computed t statistic = 1.33563
P-Value = 0.197451

Do not reject the null hypothesis for alpha = 0.05.

The StatAdvisor

This pane displays the results of three tests concerning the center of the population from which the sample of Experiment-Theory comes. The first test is a t-test of the null hypothesis that the mean Experiment-Theory equals 0.0 versus the alternative hypothesis that the mean Experiment-Theory is not equal to 0.0. Since the P-value for this test is greater than or equal to 0.05, we cannot reject the null hypothesis at the 95.0% confidence level.

2. ANOVA for Buckling Results

Multifactor ANOVA - Warpage

Analysis of Variance for Warpage - Type III Sums of Squares

Source	Sum of Squares	Df	Mean Square	F-Ratio	P-Value
MAIN EFFECTS					
A:Allowance	870158.6	8	108769.8	403.0	0.0000
Residual	6477.53	24	269.90		
B:Location	4268.49	3	1422.83	4.08	0.1760
Residual	814.13	2.34	348.32		
C:Thickness	322123.5	2	161061.8	577.3	0.0000
Residual	1673.94	6	278.99		
INTERACTIONS					
D:Allowance*Location	6477.53	24	269.90	1.21	0.4060
Residual	1932.85	8.65	223.53		
E:Allowance*Thickness	267324.6	3	89108.2	430.3	0.0000
Residual	1863.84	9	207.09		
F:Location*Thickness	1673.94	6	278.99	1.29	0.3530
Residual	1903.05	8.79	269.90		

All F-ratios are based on the individual residual mean square error.

The StatAdvisor

The ANOVA table decomposes the variability of Warpage into contributions due to various factors. Since Type III sums of squares (the default) have been chosen, the contribution of each factor is measured having removed the effects of all other factors. The P-values test the statistical significance of each of the factors. Since 2 P-values are less than 0.05, these factors have a statistically significant effect on Warpage at the 95.0% confidence level.

APPENDIX N

Effect of Fixture Allowance on the Magnitude of Buckling and Misalignment and Device Performance

1. Fin Buckling (original TEER)

Theory:		Experiment																							
Thickness (µm)	Allowance (mm)	Interference (mm)	Max.deflect (mm)	Delta C (mm)	b1*	b2*	An	Au	Re1	Re2	Nu1*	Nu2*	w1*	w1*Aw1*	w2*	Nu1*	Nu2*	e1	e2	e-ave	Nu-eff	%Loss in Area	% increase in Area		
50.4	-0.080	0.080	0.531	37.498	11.498	4.4	2.335	23.165	21.409	7.804	6.952	0.027	0.026	0.170	0.152	0.348	0.450	0.989	0.978	0.986	0.861	0.910	10.050	47.10%	89%
	-0.050	0.050	0.418	30.237	12.412	4.4	1.839	21.662	21.662	7.706	7.035	0.065	0.061	0.179	0.152	0.348	0.450	0.989	0.978	0.986	0.861	0.910	10.050	47.10%	89%
	-0.030	0.030	0.327	26.153	13.263	4.4	1.439	21.822	21.704	7.638	7.035	0.103	0.111	0.189	0.166	0.348	0.450	0.989	0.978	0.986	0.861	0.910	10.050	47.10%	89%
76.2	-0.010	0.010	0.189	21.609	14.804	4.4	0.831	21.596	22.001	7.512	7.209	0.319	0.236	0.468	0.359	0.500	0.500	0.950	0.950	0.950	0.918	0.918	11.225	40.92%	69%
	-0.030	0.030	0.327	26.153	13.263	4.4	1.439	21.822	21.704	7.638	7.035	0.103	0.111	0.189	0.166	0.348	0.450	0.989	0.978	0.986	0.861	0.910	10.050	47.10%	89%
	-0.068	0.068	0.600	17.600	17.600	4.4	0.000	22.295	22.295	7.358	7.358	0.000	0.000	0.500	0.500	0.500	0.500	0.950	0.950	0.950	0.950	19.000	0.00%	0%	

2. Fin Buckling (modified TEER)

Theory:		Experiment																							
Thickness (µm)	Allowance (mm)	Interference (mm)	Max.deflect (mm)	Delta C (mm)	b1*	b2*	An	Au	Re1	Re2	Nu1*	Nu2*	w1*	w1*Aw1*	w2*	Nu1*	Nu2*	e1	e2	e-ave	Nu-eff	%Loss in Area	% increase in Area		
50.4	-0.080	0.080	0.531	37.498	11.498	4.4	2.335	23.165	21.409	7.804	6.952	0.027	0.026	0.170	0.152	0.348	0.450	0.989	0.978	0.986	0.861	0.910	10.050	47.10%	89%
	-0.050	0.050	0.418	30.237	12.412	4.4	1.839	21.662	21.662	7.706	7.035	0.065	0.061	0.179	0.152	0.348	0.450	0.989	0.978	0.986	0.861	0.910	10.050	47.10%	89%
	-0.030	0.030	0.327	26.153	13.263	4.4	1.439	21.822	21.704	7.638	7.035	0.103	0.111	0.189	0.166	0.348	0.450	0.989	0.978	0.986	0.861	0.910	10.050	47.10%	89%
76.2	-0.010	0.010	0.189	21.609	14.804	4.4	0.831	21.596	22.001	7.512	7.209	0.319	0.236	0.468	0.359	0.500	0.500	0.950	0.950	0.950	0.918	0.918	11.225	40.92%	69%
	-0.030	0.030	0.327	26.153	13.263	4.4	1.439	21.822	21.704	7.638	7.035	0.103	0.111	0.189	0.166	0.348	0.450	0.989	0.978	0.986	0.861	0.910	10.050	47.10%	89%
	-0.068	0.068	0.600	17.600	17.600	4.4	0.000	22.295	22.295	7.358	7.358	0.000	0.000	0.500	0.500	0.500	0.500	0.950	0.950	0.950	0.950	19.000	0.00%	0%	

3. Fin Buckling (modified TEER)

Theory:		Experiment																							
Thickness (µm)	Allowance (mm)	Interference (mm)	Max.deflect (mm)	Delta C (mm)	b1*	b2*	An	Au	Re1	Re2	Nu1*	Nu2*	w1*	w1*Aw1*	w2*	Nu1*	Nu2*	e1	e2	e-ave	Nu-eff	%Loss in Area	% increase in Area		
50.4	-0.080	0.080	0.531	37.498	11.498	4.4	2.335	23.165	21.409	7.804	6.952	0.027	0.026	0.170	0.152	0.348	0.450	0.989	0.978	0.986	0.861	0.910	10.050	47.10%	89%
	-0.050	0.050	0.418	30.237	12.412	4.4	1.839	21.662	21.662	7.706	7.035	0.065	0.061	0.179	0.152	0.348	0.450	0.989	0.978	0.986	0.861	0.910	10.050	47.10%	89%
	-0.030	0.030	0.327	26.153	13.263	4.4	1.439	21.822	21.704	7.638	7.035	0.103	0.111	0.189	0.166	0.348	0.450	0.989	0.978	0.986	0.861	0.910	10.050	47.10%	89%
76.2	-0.010	0.010	0.189	21.609	14.804	4.4	0.831	21.596	22.001	7.512	7.209	0.319	0.236	0.468	0.359	0.500	0.500	0.950	0.950	0.950	0.918	0.918	11.225	40.92%	69%
	-0.030	0.030	0.327	26.153	13.263	4.4	1.439	21.822	21.704	7.638	7.035	0.103	0.111	0.189	0.166	0.348	0.450	0.989	0.978	0.986	0.861	0.910	10.050	47.10%	89%
	-0.068	0.068	0.600	17.600	17.600	4.4	0.000	22.295	22.295	7.358	7.358	0.000	0.000	0.500	0.500	0.500	0.500	0.950	0.950	0.950	0.950	19.000	0.00%	0%	

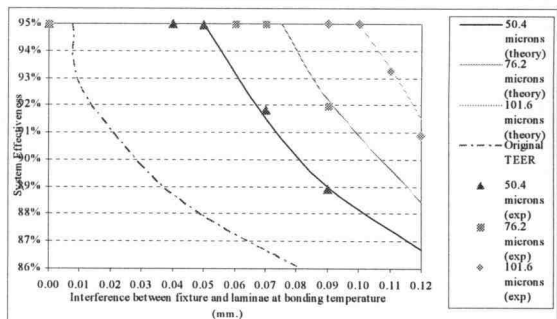
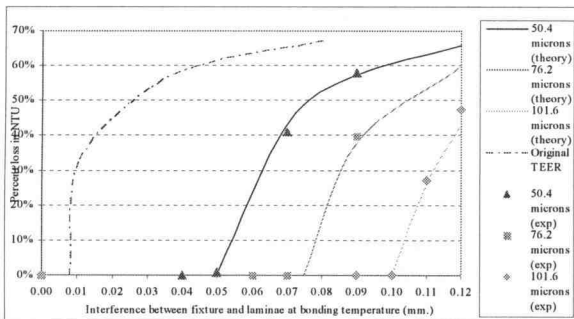
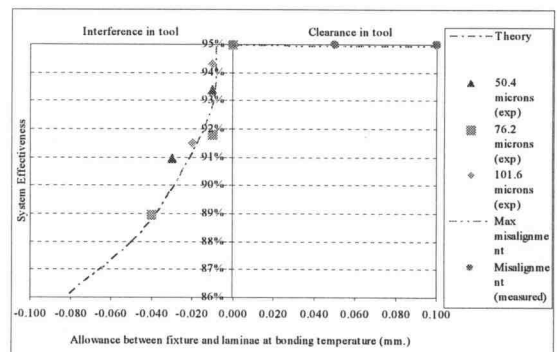
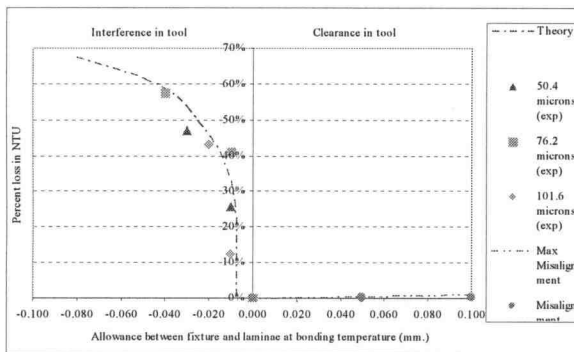
4. Fin Buckling (modified TEER)

Theory:		Experiment																							
Thickness (µm)	Allowance (mm)	Interference (mm)	Max.deflect (mm)	Delta C (mm)	b1*	b2*	An	Au	Re1	Re2	Nu1*	Nu2*	w1*	w1*Aw1*	w2*	Nu1*	Nu2*	e1	e2	e-ave	Nu-eff	%Loss in Area	% increase in Area		
50.4	-0.080	0.080	0.531	37.498	11.498	4.4	2.335	23.165	21.409	7.804	6.952	0.027	0.026	0.170	0.152	0.348	0.450	0.989	0.978	0.986	0.861	0.910	10.050	47.10%	89%
	-0.050	0.050	0.418	30.237	12.412	4.4	1.839	21.662	21.662	7.706	7.035	0.065	0.061	0.179	0.152	0.348	0.450	0.989	0.978	0.986	0.861	0.910	10.050	47.10%	89%
	-0.030	0.030	0.327	26.153	13.263	4.4	1.439	21.822	21.704	7.638	7.035	0.103	0.111	0.189	0.166	0.348	0.450	0.989	0.978	0.986	0.861	0.910	10.050	47.10%	89%
76.2	-0.010	0.010	0.189	21.609	14.804	4.4	0.831	21.596	22.001	7.512	7.209	0.319	0.236	0.468	0.359	0.500	0.500	0.950	0.950	0.950	0.918	0.918	11.225	40.92%	69%
	-0.030	0.030	0.327	26.153	13.263	4.4	1.439	21.822	21.704	7.638	7.035	0.103	0.111	0.189	0.166	0.348	0.450	0.989	0.978	0.986	0.861	0.910	10.050	47.10%	89%
	-0.068	0.068	0.600	17.600	17.600	4.4	0.000	22.295	22.295	7.358	7.358	0.000	0.000	0.500	0.500	0.500	0.500	0.950	0.950	0.950	0.950	19.000	0.00%	0%	

3. Channel Misalignment

Thickness (μm)	Allowance (mm)	Max Misalignment	% Loss in NTU	% Eff
50.4	0.1	0.1	1.14%	94.95%
	0.05	0.05	0.57%	94.97%
	0	0	0.00%	95.00%
76.2	0.1	0.1	1.14%	94.95%
	0.05	0.05	0.57%	94.97%
	0	0	0.00%	95.00%
101.6	0.1	0.1	1.14%	94.95%
	0.05	0.05	0.57%	94.97%
	0	0	0.00%	

Misalignment (measured) (mm)	% Loss in NTU	% Eff
0.015	0.17%	94.99%
0.013	0.15%	94.99%
0.005	0.06%	95.00%
0.015	0.17%	94.99%
0.022	0.25%	94.99%
0.006	0.07%	95.00%
0.026	0.30%	94.99%
0.007	0.08%	95.00%
0.006	0.07%	95.00%



APPENDIX P

Evaluation of Time Dependent (Creep) Deformation in Diffusion Bonding

This section presents an evaluation of creep deformation that sometimes happen in the process in high temperature environments, when the deformation of the structure also depends on time. Based on the assumption in Chapter 3, the bonding process takes place in the hot press chamber where the heating element provides the heat to the specimen up to 750 °C for an hour during diffusion-bonded step. Registration force and clamping force that are generated by the difference in thermal expansion between stainless steel specimen and graphite fixture for the prior case, and the load provides to the top fixture for the latter. The clamping - force will press all laminae together to allow diffusion-bonded among the layers. While the registration force is applied to the specimen, it will cause the specimen to deform either by realigning laminae together or cause the fin to warp if the force is too high. The magnitude of warpage can be evaluated based on the buckling equations discussed in Chapter 3. However, those buckling equations are based on elastic property as we assume that no creep is involved during the bonding step. The following section will introduce the technique to evaluate how much the creep might be, in order to confirm that the assumption is reliable.

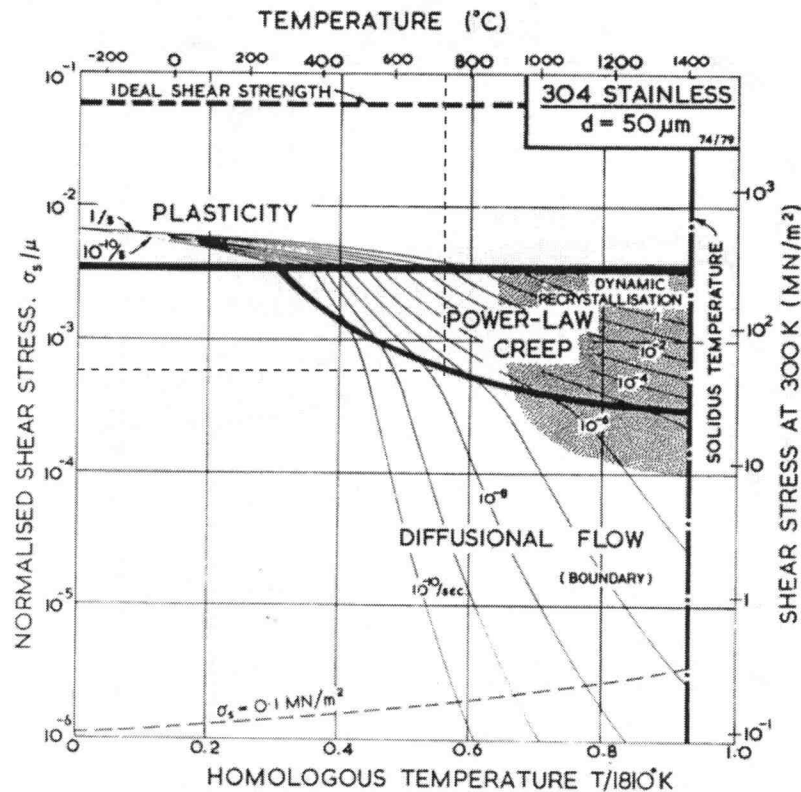
The following nominal dimensions of microchannel array and material properties were used to verify the theoretical approach presented in section 3.2.

L_{ch}	=	30	mm	T_r	=	300	K
σ_p	=	74	Mpa	T_m	=	1810	K
t_{diff}	=	60	min	T_{diff}	=	1023	K

1. Use the deformation mechanism map

Evaluation of creep mechanism can be identified by using the deformation mechanism map developed by Frost and Ashby¹ as shown on the next page.

¹ Frost, H. J. and M. F. Ashby (1982). Deformation-Mechanism Maps: The Plasticity and Creep of Metals and Ceramics. New York, Pergamon Press.



First, we need to calculate the normalized stress (σ_s / μ) to which it is subjected in order to use the deformation map for the 304 stainless steel. According to our setting, the normalized stress is equal to 7.986×10^{-4} (see calculation on the next page). At 750°C , the deformation falls at the boundary of power-law creep and diffusional flow, with the shear strain rate around 2×10^{-8} per second. When converting this shear strain rate into compression strain rate, it is around 4×10^{-5} per second. With fin width of 9 mm, this can lead to only 0.4 micron per hour, which is not significant to take effect on this experiment.

2. Use creep equation

In order to provide the precise result from the graph, the calculation of creep information has been performed based on both power-law creep and diffusional flow evaluation. MathCAD program has been used to calculate the result of both boundary, which show that the strain rate from the experiment is still around 5×10^{-5} per second or less than 0.5 micron per hour. This confirms that inelastic property due to creep deformation does not have any significant effect to the result of the experiment conduct in this research. The calculation notes by MathCAD program are presented on the next page.

Evaluate creep deformation

$$T := 1023\text{K} \quad T_M := 1810\text{K} \quad T_r := 300\text{K}$$

$$\mu_0 := 8.1 \cdot 10^{10} \text{Pa} \quad T_m := -0.85$$

$$\mu := \mu_0 \left[1 + \left(\frac{T - T_r}{T_M} \right) \cdot T_m \right] \quad \mu = 5.35 \times 10^{10} \text{Pa} \quad \sigma_s := \frac{\sigma}{\sqrt{3}} \quad \dot{\gamma}' := \sqrt{3} \cdot \dot{\epsilon}'$$

Let $\sigma_p = \sigma = 74 \text{ MPa}$ (proportional limit stress)

$$\sigma := 74 \cdot 10^6 \text{Pa}$$

$$\sigma_s := \frac{\sigma}{\sqrt{3}} \quad \sigma_s = 4.272 \times 10^7 \text{Pa}$$

Normalized shear stress (σ_s/μ) OR χ

$$\chi := \frac{\sigma_s}{\mu} \quad \chi = 7.986 \times 10^{-4}$$

At 750 C, the shear strain rate falls in between the diffusion flow area and the power law creep boundary in the area between 10^{-8} to 10^{-7} per second

First, try diffusional flow equation to find the strain rate

$$\dot{\gamma}' := \frac{42 \cdot \sigma_s \cdot \Omega}{k \cdot T \cdot d^2} \cdot \text{Defl} \quad \text{Defl} := D_v \cdot \left(1 + \frac{\pi \cdot \delta}{d} \frac{D_b}{D_v} \right)$$

$$k := 1.381 \cdot 10^{-23} \frac{\text{J}}{\text{K}}$$

$$\Omega := 1.21 \cdot 10^{-29} \text{m}^3$$

$$d := 0.050 \text{mm}$$

$$R := 8.314 \frac{\text{J}}{\text{mol}} \text{K}^{-1}$$

$$T = 1.023 \times 10^3 \text{K}$$

$$\delta D_0 b := 2 \cdot 10^{-13} \frac{\text{m}^3}{\text{s}}$$

$$D_0 v := 3.7 \cdot 10^{-5} \frac{\text{m}^2}{\text{s}}$$

$$Q_b := 167 \cdot 10^3 \frac{\text{J}}{\text{mol}}$$

$$Q_v := 280 \cdot 10^3 \frac{\text{J}}{\text{mol}}$$

$$\delta D_b := \delta D_0 b \cdot e^{-\left(\frac{Q_b}{R \cdot T} \right)}$$

$$D_v := D_0 v \cdot e^{-\left(\frac{Q_v}{R \cdot T} \right)}$$

$$\text{Defl} := D_v \cdot \left(1 + \frac{\pi \cdot \delta D_b}{d \cdot D_v} \right)$$

$$\dot{\gamma}' := \frac{42 \cdot \sigma_s \cdot \Omega}{k \cdot T \cdot d^2} \cdot \text{Defl}$$

$$\dot{\gamma}' = 2.305 \times 10^{-8} \text{s}^{-1}$$

For diffusional flow creep, we have the shear strain rate = 2.3×10^{-8} per sec

Now, try to use the power-law creep equation to find the strain rate

$$\dot{\gamma} := \frac{As \cdot \text{Def} \dot{\mu} \cdot b \left(\frac{\sigma}{\mu} \right)^n}{k \cdot T}$$

$$\text{Def} := Dv \left[1 + \frac{10 \cdot aDc}{b^2 \cdot Dv} \left(\frac{\sigma}{\mu} \right)^2 \right]$$

$$b := 2.58 \cdot 10^{-10} \text{ m}$$

$$As := 1.5 \cdot 10^{12}$$

$$n := 7.5$$

Since there is no data on aDc0 and Qc, so I assume it is about the same as other existing info

$$aDc0 := 1 \cdot 10^{-23} \frac{\text{m}^4}{\text{s}} \quad Qc := 167 \cdot 10^3 \frac{\text{J}}{\text{mol}}$$

$$aDc := aDc0 \cdot e^{-\left(\frac{Qc}{R \cdot T} \right)}$$

$$\text{Def} := Dv \left[1 + \frac{10 \cdot aDc}{b^2 \cdot Dv} \left(\frac{\sigma}{\mu} \right)^2 \right]$$

$$\dot{\gamma} := \frac{As \cdot \text{Def} \dot{\mu} \cdot b \left(\frac{\sigma}{\mu} \right)^n}{k \cdot T} \quad \dot{\gamma} = 2.601 \times 10^{-8} \text{ s}^{-1}$$

For power-law creep, we have the shear strain rate = 2.6×10^{-8} per sec

Conclusion: Strain rate from both equations is about 2.3 - 2.6×10^{-8} per sec.

Let's use

$$\dot{\gamma} := 2.45 \cdot 10^{-8} \text{ s}^{-1}$$

$$\dot{\epsilon}' := \frac{\dot{\gamma}'}{\sqrt{3}} \quad \dot{\epsilon}' = 1.415 \times 10^{-8} \text{ s}^{-1}$$

If $t := 3600\text{s}$ $\epsilon := \dot{\epsilon}' \cdot t$ $\epsilon = 5.092 \times 10^{-5}$ Strain rate is about 0.005% per hour

For $L := 9\text{mm}$ $\delta := \epsilon \cdot L$ $\delta = 4.583 \times 10^{-4} \text{ mm}$ or about 0.5 micron per hour